Part 1:

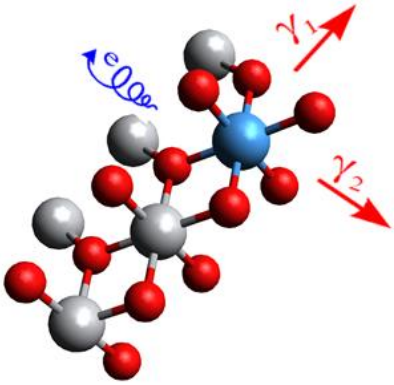
A particular EFG temperature dependence for $^{181}(TiO_2)$: An electron-gamma TDPAC study

Ian (Chang Jie), Yap

II. Physikalisches Institut, Georg-August Universität Göttingen

August 2022

Submitted as a requirement for the degree of Masters in Physics.



Supervised by:

Dr. Juliana Schell (SSP CERN-ISOLDE)

and

Prof Hans Christian Hofsäss (II. Physikalisches Institut, Georg-August Universität Göttingen)

CERN-THESIS-2022-405
//2022

Declaration of Authorship:

I hereby declare that I have written the present work independently and only using the sources and aids indicated. A significant part of this thesis is based on the paper published in Crystals, MDPI, that I also wrote: "Room-Temperature $^{181}Ta(TiO_2)$: An e-γ TDPAC Study", with the critique of my supervisors, alongside Dr Ulli Köster and two anonymous reviewers. They are reproduced in parts of this thesis under the Creative Commons 4.0 license.

The data analysis was done by myself, with the assistance of my supervisors and J. G. M. Correia. The measurement used to procure the data used for this work was carried out in both the Bonn Isotope Separator and the Isotope on-line device (ISOLDE).

Parts of this thesis are adopted and paraphrased from specific textbooks and papers for the literature review. Copyright licenses are obtained from the relevant publishers and with the citation appropriately placed throughout the thesis. Proof of the copyright licenses is found in Appendix F.

Acknowledgements:

This research was funded by the German Federal Ministry of Education and Research (BMBF) through grant No. 05K16PGA and the Foundation for Science and Technology FCT, Portugal, via Grant No. CERN-FIS-PAR-0005-2017.

We want to thank Thien Thanh Dang, Cornelia Noll, Reinhard Beck, Ulli Köster and Ronaldo Mansano as co-authors of the paper that leads to this thesis.

We acknowledge the financial support from our external funders and J. G. M. Correia for technical assistance during the e-γ experiments and pre-analysis of the data.

For the paper, we want to thank the AIP language services and their team of English language experts for their comprehensive review of the script. In addition, we would like to thank the MDPI English language services team for post-processing the manuscript, alongside their excellent suggestions to make the writing more readable to the audience.

We highly appreciate the criticism and comments both anonymous reviewers posted, who have contributed to the final version of this thesis.

I thank J. G. M. Correia for his expert assistance with Gfit19 and Interlude and his indirect mentorship that complements J.S. Schell and H.C. Hofsäss.

I thank my parents for their sacrifices and support thus far. They have supplied me with the necessary funds and equipment for this project.

This thesis was written with the support of Grammarly.

Abstract:

The hyperfine parameters of the ^{181}Ta trace impurities in the rutile structure of the TiO_2 single crystals (denoted ^{181}Ta(TiO_2)) are studied mainly using the time differential e-γ perturbed angular correlation (e-γ TDPAC) technique by the ion-implanted ^{181}Hf tracers that decays to ^{181}Ta. The experiments are performed in the air, with a temperature range of $50 - 427\ K$. It is found that with significant annealing (5hr 15mins at a temperature of $873.15\ K$) of the ^{181}Ta(TiO_2) sample, the ^{181}Ta trace impurities are mainly found in the main interstitial Ti site. This allows for the precise measurement of the largest electric field gradient (V_{zz}), asymmetry parameter (η), and orientation (θ & ϕ) of the interstitial ^{181}Ta trace impurities surrounded by the octahedral-like TiO_2 host matrix surroundings.

The $R(t)$ signal and the experimental parameters resulting from the e-γ TDPAC spectroscopy agree with that of the γ-γ TDPAC spectroscopy (in both our experiment and literature) at room temperature. However, we detected a non-linear increase of V_{zz} (with a positive curvature) at the low-temperature regime ($50 - 293\ K$), as opposed to the linear increase at the high-temperature regime (600-1200 K) as suggested by the literature. We also suspected that at a specific temperature of around $500\ K$, there might be a V_{zz} maxima. Though precise ab-initio methods modelled the linear increase at the high-temperature regime, such techniques are lacking for the low-temperature regime. Hence, our next step would be doing Density Functional Theory (DFT) calculations on the Ta(TiO_2) over a broad temperature range of $0 - 1200\ K$ to obtain more profound insight into the particular temperature dependence of our experimentally measured V_{zz} in the theoretical part of this thesis (Part 2).

Contents:

0) Preface: Personal/Professional Motivation……7

1) Introduction and overview of BONIS and ISOLDE……8

1.1) TDPAC and Nuclear Solid-State Physics……8

1.2) BONIS and ISOLDE……9

2) Nuclear Properties of the Probe Atom……13

2.1) The Operators of the Total Angular Momentum $\hat{I}$ and Magnetic Moment $\hat{\mu}$……13

2.2) Electrical Quadrupole Moment……14

2.3) The Hyperfine structure and the interactions of an external electric field……18

2.3.1) Electric Interactions……18

2.3.2) Special case for which $\eta = 0$ and $I = 5/2$……24

2.3.3) General case for η, with $I = 5/2$……25

3) Principles of Time-Dependent Perturbed Angular Correlation (TDPAC)……29

3.1) Nuclear γ-decay……29

3.2) Radial Angular Distribution……32

3.3) Theory for Unperturbed $\gamma - \gamma$ Angular Correlation……36

3.3.1) Special case in which the z-axis is aligned with detector 1 and with only a single multipole transition……37

3.3.2) General case of PAC……39

3.4) Theory of Time-Dependent Perturbed Angular Correlation (TDPAC)……42

3.4.1) TDPAC Angular Correlation $W(\vec{k}_1, \vec{k}_2, t)$……42

3.4.2) Analysis of the interaction Hamiltonian $\widehat{H}_I$……44

3.4.3) Properties of the Unitary Matrix U and the Perturbation $G_{k_1,k_2}^{N_1,N_2}(t)$ under the influence of the static electric quadrupole interactions (Summary)……47

4) Working Principles of TDPAC: The Relevance of $R(t)$……50

4.1) Expressions of $G_{k_1,k_2}^{N_1,N_2}(t)$ and $G_{kk}(t)$……50

4.2) The count rate ratio $R(t)$ and the polycrystalline experimental observable $A_2(\gamma_1)A_2(\gamma_2)G_{22}(t)$ in data acquisition and computation……53

4.3) Experimental imperfections and the implementation of the time resolution function and the Lorentzian/Gaussian function……56

4.4) Miscellaneous section on experimental TDPAC spectroscopy……57

4.4.1) Fundamental frequency……57

4.4.2) Geometry……57

5) Working Principles of TDPAC: The γ-γ and e-γ TDPAC setup……59

5.1) From γ-γ to e-γ correlations……59

5.2) The γ-γ and e-γ TDPAC setup……61

6) Properties of rutile TiO_2 and $^{181}Hf(^{181}Ta)$ as a TDPAC probe nucleus and experimental details……65

6.1) Literature on TiO_2 and $^{181}Ta(TiO_2)$ γ−γ TDPAC Spectroscopy……65

6.1.1) State of the Art ($^{181}Ta(TiO_2)$ γ−γ TDPAC Spectroscopy)……66

6.1.2) Properties of rutile TiO_2……67

6.1.3) Motivation of applying the e−γ TDPAC Spectroscopy to the TiO_2 Material……68

6.2) $^{181}Hf(^{181}Ta)$ as a TDPAC probe……69

6.3) Experimental procedure for $^{181}Ta(TiO_2)$ γ−γ and e−γ TDPAC spectroscopy……70

6.3.1) $^{181}Hf(^{181}Ta)$ implantation process into rutile TiO_2……70

6.3.2) Data Acquisition of $^{181}Ta(TiO_2)$ γ−γ and e−γ TDPAC Spectroscopy……72

6.3.3) X-ray Diffraction of the $^{181}Ta(TiO_2)$ Sample after the γ−γ and e−γ TDPAC Spectroscopy……73

6.3.4) Expectations from $^{181}Ta(TiO_2)$ γ-γ and e-γ TDPAC Spectroscopies……73

7) γ-γ and e-γ TDPAC results……74

7.1) γ-γ TDPAC spectroscopy setup……74

7.2) e-γ TDPAC spectroscopy setup……78

7.3) X-ray Diffraction of the $^{181}Ta(TiO_2)$ Sample after the γ−γ and e−γ TDPAC Spectroscopy……88

8) Interpretation of γ-γ and e-γ TDPAC results……90

8.1) Room Temperature results……91

8.1.1) γ-γ TDPAC spectroscopy setup……91

8.1.2) e-γ TDPAC spectroscopy setup……92

8.2) Temperature-dependent e−γ TDPAC results……100

8.3) X-ray Diffraction of the $^{181}Ta(TiO_2)$ Sample after the γ−γ and e−γ TDPAC Spectroscopy……107

9) Conclusion……109

Appendix A: Analytical solution to the eigenvalue equation (2.57)……111

Appendix B: Butz's derivation of the properties of $G_{k_1,k_2}^{N_1,N_2}(t)$ (And some comments on the unitary matrix $\overleftrightarrow{U}$) ……116

Appendix C: Explicit expression of the unitary matrix $\overleftrightarrow{U}$ for $I = 5/2$ as given by Butz……121

Appendix D: Geometry between the Different Detector Planes……124

Appendix E: Literature Review of Ion Implantation Damage to the Host Semiconductor……129

Appendix F: Proof of the Copyright Licenses Agreement……131

References……135

0) Preface: Personal/Professional Motivation

This thesis (part 1 of the duo/trio-logy) deals with the experimental part of the temperature-dependent spectroscopic technique of e-γ time differential perturbed angular correlation (TDPAC) to $^{181}Hf \rightarrow {}^{181}Ta$ probe nuclei incorporated into single crystal rutile TiO_2 as a host material. From now on, it will be referred to as $^{181}Ta(TiO_2)$ e-γ TDPAC spectroscopy.

I have been part of the Solid-State Physics group in ISOLDE, CERN [1] since 2016, first as a CERN summer school student, after which I was admitted to the Universität Göttingen Physics Master's Program in 2019, where I was given the data of $^{181}Ta(TiO_2)$ e-γ TDPAC spectroscopy to analyse for my Masters Project. In a sense, the master's thesis was due to be published in 2021 but was ultimately delayed by a year or two due to two factors.

The first is due to the 2020 Corona Pandemic, which inhibited my and my supervisors' ability to work and communicate. The second is due to the surprising trend discovered over the $^{181}Ta(TiO_2)$ e-γ TDPAC spectroscopy data analysis, in which sophisticated techniques such as Density Functional Theory have to be employed to pinpoint the exact origins of this phenomena. The issue of accurately simulating the electric field gradient of a material over a varying temperature is a complex open problem. Hence, the overall project is not fully concluded as of this writing and will be split into two/more different parts.

As mentioned above, part 1, the master's thesis, deals with the experimental part, where the relevant concept of TDPAC spectroscopy will be discussed. After which, the results for the room temperature $^{181}Ta(TiO_2)$ e-γ TDPAC spectroscopy will be compared with the established $^{181}Ta(TiO_2)$ γ-γ TDPAC spectroscopy from the literature. Temperature-dependent $^{181}Ta(TiO_2)$ e-γ TDPAC spectroscopy results will be presented, and the particular unusual trend will be highlighted and discussed.

Part 2, an independent thesis, deals with the theoretical origin of the unusual temperature dependence of the electric field gradient of the foreign ^{181}Ta ion in the rutile TiO_2 matrix. As of this writing, particular progress has been made with the pure TiO_2 case, and in due time, we hope that at least some insights could be discovered following the successful simulation of $^{181}Ta(TiO_2)$.

Part of the $^{181}Ta(TiO_2)$ e-γ TDPAC spectroscopy results (About 50% of this master's thesis), precisely the room temperature results, have been communicated/published in the article "Room-Temperature $^{181}Ta(TiO_2)$: An e-γ TDPAC study" [2], in which certain sections and phases are republished under the Creative Commons CC BY 4.0 license. It is intended that the temperature-dependent $^{181}Ta(TiO_2)$ e-γ TDPAC spectroscopy results, alongside the corresponding DFT simulation, will be submitted and published under the title "Temperature-Dependent $^{181}Ta(TiO_2)$: An e-γ TDPAC study and ab-initio DFT analysis".

This work is long-standing and hence, part of my professional identity as a young physicist. It also serves as my desire to thread between theoretical, experimental, and mathematical physics. I hope that the theoretical origins of the unusual temperature dependence in the electric field gradient of the foreign Ta ion in the rutile TiO_2 will be unravelled in due time.

1) Introduction and overview of BONIS and ISOLDE

1.1) TDPAC and Nuclear Solid-State Physics

Time-Dependent Perturbed Angular Correlation (TDPAC) is a spectroscopic technique that incorporates the consecutive decays of specific nuclides to characterise the local electric and magnetic fields of the host material surrounding the abovementioned implanted nuclide. It is part of the broader family of nuclear solid-state physics methods, which is succinctly defined as an interdisciplinary study between two fields of physics (nuclear physics and solid-state physics), in which the properties of the nuclides are used to study specific complex systems as seen in solid-state physics.

One key advantage that nuclear physics brings into the field of solid-state physics is the access to the hyperfine interactions that are typically unavailable in conventional solid-state experiments. Hyperfine interactions (or hyperfine splits) are related to the hyperfine structure, a physical phenomenon in which the energy levels of the atom/molecule/ion, otherwise degenerate, are shifted and split by the multipole electromagnetic interactions between the nucleus and the electron clouds. Due to the small scale of the hyperfine interactions, they are often susceptible to the minute difference in the local configuration of the native ions in the host material. Examples of such nuclear hyperfine methods are Mössbauer spectroscopy (a well-known cousin of TDPAC), nuclear magnetic resonance (more well known as magnetic resonance imaging), and nuclear orientation [3].

In solid-state physics, chemical bonds between the nearest neighbouring ions serve as a foundation for building up the lattice structure of the host material. In this sense, as chemical bonds are interactions between the electric clouds of the atoms/ions, probing the local charge distribution and magnetic fields of the host material will allow for microscopic characterisation of the host material, which could be used to understand the corresponding macroscopic properties that could manifest in our everyday world.

Due to the sensitivity of the nuclear hyperfine methods, they could be used to study a wide variety of solid-state phenomena, including surface/interface states, defect states, and electronic interactions (excitations). Coupled with the advances in computational power and density functional theory (DFT) [4], one could combine the experimental results generated by nuclear hyperfine methods and the corresponding theoretical simulations of DFT to isolate the origins of the physical phenomenon that produces the abovementioned experimental results.

In this thesis, we will focus on the e-γ TDPAC spectroscopy, the sister of the more commonly used γ-γ TDPAC spectroscopy. Hence, for the rest of the thesis, we will only discuss TDPAC as a nuclear hyperfine method.

One further advantage that TDPAC brings to the field of solid-state physics is that only parts per billion in the number density of TDPAC nuclides (nuclear probes) are required for adequate characterisation, which will keep the electronic structure of the host material relatively unaltered.

1.2) BONIS and ISOLDE

Given the advantages that TDPAC (and other nuclear hyperfine methods) brings to solid-state physics, severe limitations prevent such practices from being widely adopted.

The most obvious limitation is in producing such (radioactive) nuclear probes that are used to facilitate the nuclear hyperfine methods. On the one hand, stringent safety protocols must be in place to prevent radiation poisoning and are often implemented at a federal (or even multinational) level. On the other hand, specialised equipment is needed to produce specific nuclear probes, thus inaccessible to a typical laboratory.

Thus, only a relatively limited number of research centres could conduct TDPAC spectroscopy over a wide range of nuclear probes. Two such places are the Bonn Isotope Separator (BONIS), located at the Helmholtz Institute for Radiation and Nuclear Physics (HISKP) [5], and the Isotope Mass Separator On-Line facility (ISOLDE) [6], housed at CERN.

ISOLDE is a premier isotope separator facility that can produce a wide variety of short-lived isotopes by focusing a 1.4 GeV proton beam (from the Proton Synchrotron Booster, the first of the accelerator circles that eventually leads to the Large Hadron Collider) onto an appropriate target.

The irradiation of the photon beam onto the target material produces various radioactive isotopes through various nuclear reactions, including nuclear spallation, fragmentation, and fission reactions. Different target material produces different isotopes, some of which are requested by experimentalists working on various nuclear experiments.

To obtain a high purity beamline of a specific isotope, the family of isotopes is first indiscriminately extracted by thermal diffusion from the bulk target material by heating the target material up to about 2000°C. Then, the specific isotope is filtered through by a mass separator (Either the General-purpose Separator (GPS), made of a dipole magnet, or the High-resolution separator (HRS), made up of a series of two magnetic dipoles) and directed to either one of the nuclear physics experiments (such as TDPAC spectroscopy), or an isotope-harvesting area.

Figure 1 shows the overall schematic of the mass separator at ISOLDE following the irradiation of the photon beam onto the target material [7].

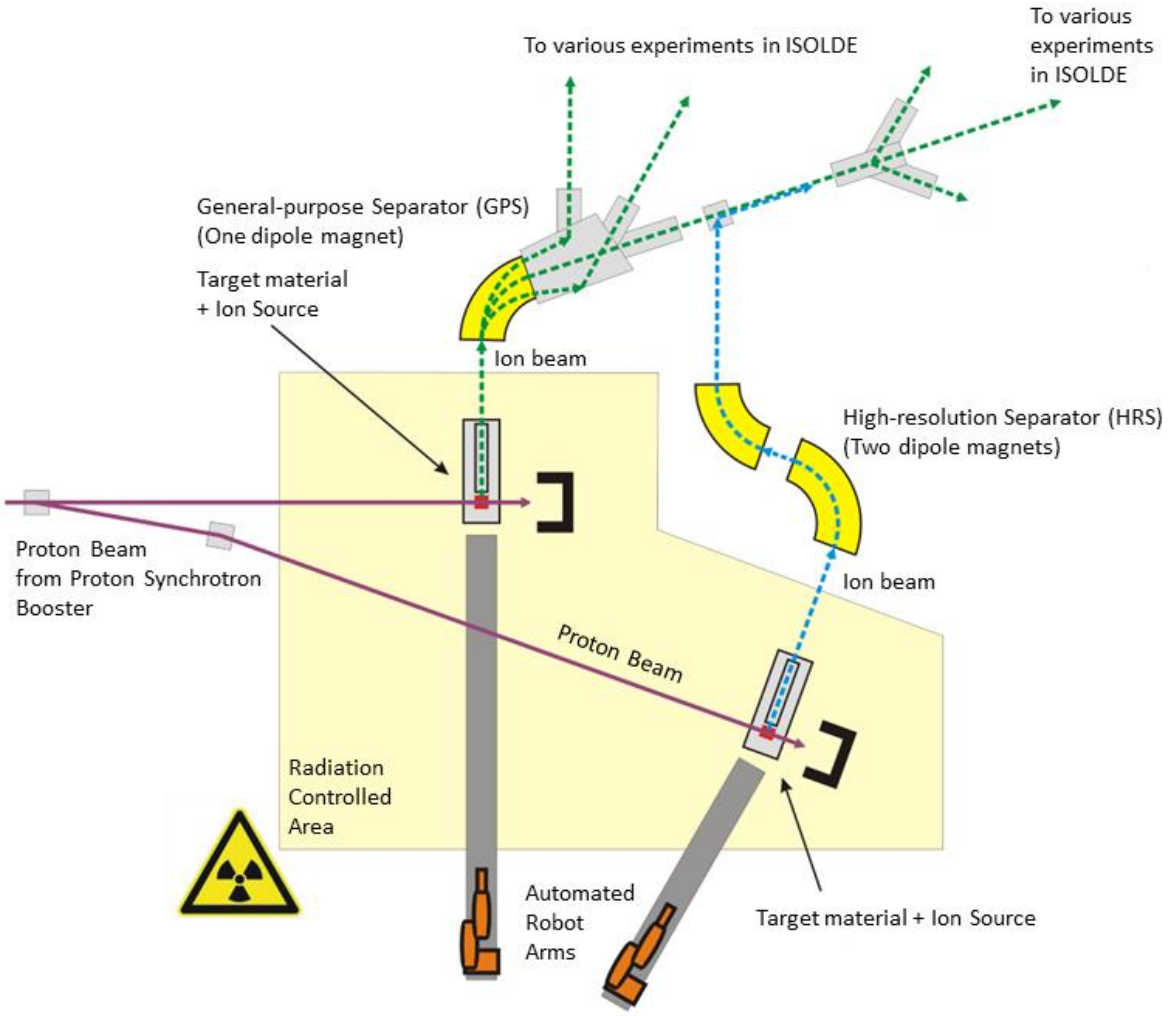


Figure 1: The overall schematic of the mass separator in ISOLDE. The 1.4 GeV Proton Beam from the Proton Synchrotron Booster irradiates the target material as an ion source, which is then separated by either the General-purpose Separator (GPS) or the High-resolution Separator (HRS), in which the magnetic dipoles are shown as the yellow curved shape. The above figure was adapted and translated from [7] under the Creative Commons CC0 1.0 Copyright Waiver license.

The ISOLDE facility is particularly well suited for TDPAC experiments because of its ability to produce several short-lived and exotic TDPAC nuclear probes such as ^{111m}Cd,^{119m}Hg, ^{204m}Pb, as well as various transition metal isotopes. This capability allows for the ISOLDE facility to be the largest (and premier) TDPAC facility in the world, with about 10 TDPAC instruments and counting, and with significant funding acquired from the German Federal Ministry of Education and Research (BMBF). Currently, the Solid-State Physics (SSP) group of ISOLDE occupies up to 20-25% of the ISOLDE's beam time, which underlies the TDPAC's significance in CERN.

However, as sophisticated as the ISOLDE facility in producing various TDPAC probes, some probes are 1) either not simply available at ISOLDE or 2) more economical to be produced at other research facilities. Figure 2 outlines ISOLDE's isotopes for TDPAC or Mössbauer spectroscopies.

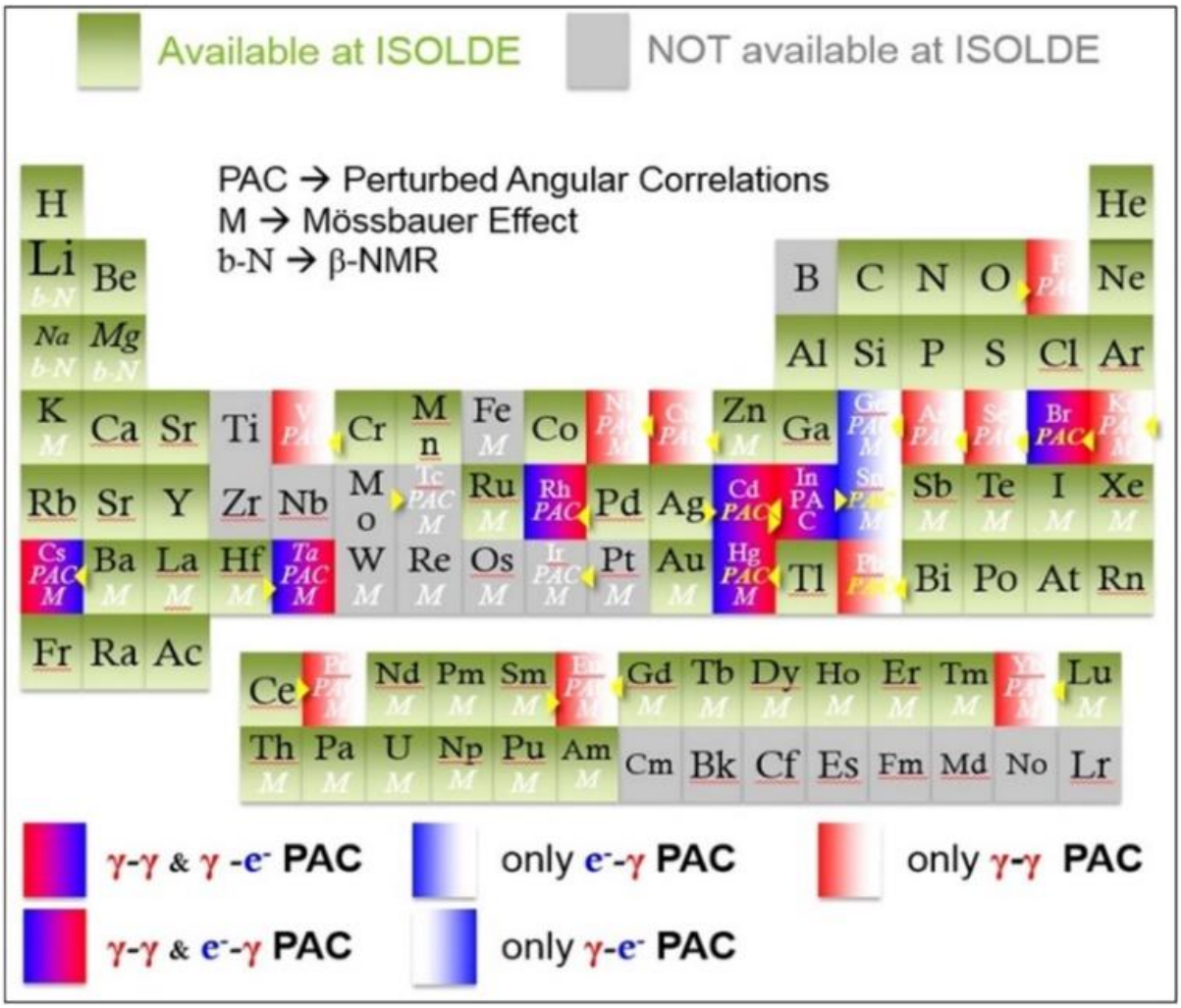


Figure 2: The list of isotopes that could be produced for Mössbauer/TDPAC experiments. Reproduced from [8] under the Creative Commons Attribution 3.0 International License. Copyright 2019 under Johnston, K. et al.

BONIS, like ISOLDE, is another isotope separator facility that incorporates the dipole magnet for high-purity mass separation (See Figures 3 and [9]). Specifically, reference [9] mentioned that the dipole magnet used to filter a specific isotope has a gap of 6m, a curvature of 1.5m, and a deflection angle of 55°. The maximum energy of the ion beam (sometimes referred to as the maximum acceleration voltage) is 160 keV, but the most often used energy configuration is 80 keV. For further purity of the beam, a diaphragm is used to filter out (by mass) all other irrelevant isotopes. Further technical details of BONIS are found in [9].

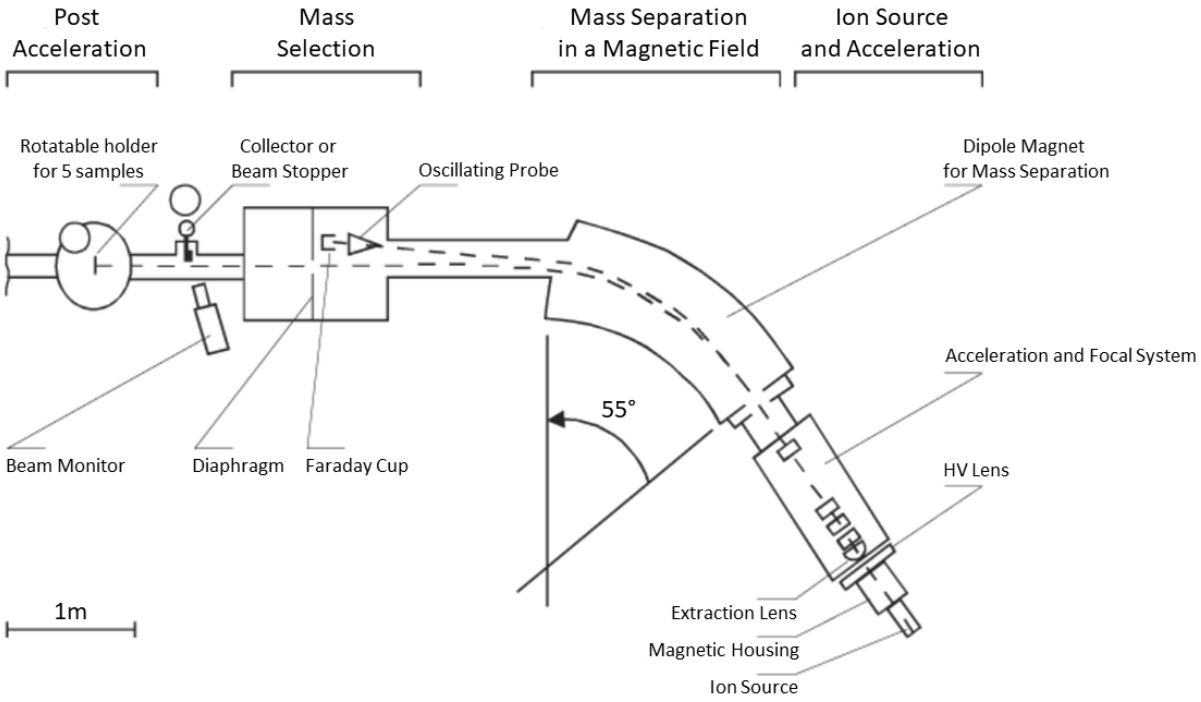


Figure 3: The schematic of BONIS. Like the working principles of ISOLDE, the thermally diffused cocktail of ions travels through the contraption, in which the dipole magnet and the diaphragm filter the relevant TDPAC probes to be implanted in the host material/sample. Adapted and translated from [10]. Technical details are found in [9].

For this $^{181}Ta(TiO_2)$ e-γ TDPAC spectroscopy, the BONIS facility is used to implant ^{181}Hf (→ ^{181}Ta) TDPAC nuclear probe into a single crystal TiO_2. The details of the implantation are elaborated in Chapter 6.

The e-γ TDPAC spectroscopy was established as far back as the 1970s when a group in HISKP conducted experiments on various metals [10-14]. Their e-γ spectrometer was significantly upgraded later and brought to its total capacity at SSP ISOLDE in the 1990s [15-17]. Recent experiments are using the modern e-γ TDPAC spectrometer, one involving a temperature- and "Si- and Zn-" dopant concentration-dependent study on $^{181}Ta(GaN)$ [18], in which the researchers have detected signals related to the recombination process (Details on the recombination process is elaborated in Chapter 5). With the help of DFT, researchers pinned the origin of this phenomenon to a variable range hopping in the low-temperature regime and thermally mobile electrons (electrons in the conduction band) in the high-temperature regime.

2) Nuclear Properties of the Probe Atom

The heart of the TDPAC spectroscopy lies in the hyperfine interactions between the nucleus and its electron cloud's electric/magnetic field, which could be affected by the local lattice environment of the host material. In this chapter, we will focus on the electric quadrupole moment of the electron cloud around the nucleus, which is then coupled to the nucleus itself. For TDPAC spectroscopy, the largest electric field gradient (EFG) and the asymmetry parameter will be derived in this chapter. We would also derive the eigenenergies of the Hamiltonian associated with the said electric quadrupole moment in terms of the largest EFG and the asymmetry parameter.

A significant part of the contents in this chapter is adapted with permission from Chapter 2.1 of Schatz's book [3]. Wiley retains copyright as the publisher.

2.1) The Operators of the Total Angular Momentum $\hat{I}$ and Magnetic Moment $\hat{\mu}$

In classical physics, the magnetic moment $\vec{\mu}$ of a body with charge q, mass m, and a total angular momentum $\vec{I}$ is given by:

$$\vec{\mu} = \gamma \vec{I}. \tag{2.1a}$$

γ is defined as the classical gyromagnetic ratio, given as:

$$\gamma = \frac{q}{2m}. \tag{2.1b}$$

Quantum mechanically, $\hat{\mu}$ and $\hat{I}$ are operators. From a typical undergraduate Quantum mechanics class (See Chapter 5 of Zettili's book [19]), the total angular momentum number I and the magnetic quantum number m, are good quantum numbers of $\hat{I}$ and $\hat{I}_z$, respectively. For a given system that has angular momentum symmetry, we can formulate the complete set of orthonormal bases of $\hat{I}$ and $\hat{I}_z$ as $\{|I, m\rangle\}$, where $m \in \{-I, -I+1, \dots, I-1, I\}$. Hence, the number of different $|I, m\rangle$ states amount to $2I + 1$ distinct values.

We note that $\hat{I}^2 = \hat{I}_x^2 + \hat{I}_y^2 + \hat{I}_z^2$ and based on the Casimir algebra [20], when $\hat{I}^2$ and $\hat{I}_z$ acts on $|I, m\rangle$, we have:

$$\hat{I}^2|I, m\rangle = I(I+1)\hbar^2|I, m\rangle, \tag{2.2a}$$

$$\hat{I}_z|I, m\rangle = m\hbar|I, m\rangle. \tag{2.2b}$$

Thus, we can define the magnetic moment of the z-component of $\hat{\mu}$ in the state $|I, m = I\rangle$ as μ, or in notation form:

$$\hat{\mu}_z \coloneqq \gamma \hat{I}_z, \tag{2.3a}$$

$$\mu \coloneqq \langle I, I|\gamma \hat{I}_z|I, I\rangle = \gamma \hbar I. \tag{2.3b}$$

The nuclear gyromagnetic ratio γ (not to be confused with the classical gyromagnetic ratio) is defined as:

$$\gamma = \frac{g\mu_N}{\hbar}. \tag{2.4a}$$

g is a dimensionless factor. The nuclear magnetron μ_N is a constant defined as:

$$\mu_N = \frac{e\hbar}{2m_p}. \tag{2.4b}$$

e is the elementary charge, and m_p is the mass of the proton.

In a nucleus (with spin), whose Hamiltonian can be commuted with $\hat{I}$ and subsequently, $\hat{\mu}$, we can write:

$$\hat{\mu} = g_L\hat{L} + g_s\hat{S}. \tag{2.5}$$

With $\hat{I} = \hat{L} + \hat{S}$. μ is written in terms of μ_N, and for I, L, S, in terms of $\hbar$. g_L and g_s are the g-factors for the orbital angular momentum $\hat{L}$ and spin angular momentum $\hat{S}$, and are determined experimentally. We will not go through $\hat{\mu}$ in further detail, as our TDPAC experiment in question does not use an external magnetic field. We would refer to [3] for a more thorough treatment.

2.2) Electrical Quadrupole Moment

Our $^{181}Ta(TiO_2)$ e-γ TDPAC setup displays evidence of an Electrical Quadrupole Interaction, and hence, it is imperative that we treat the Electrical Quadrupole Moment in sufficient theoretical detail here.

We would refer to Griffith's book [21] and Chapter 2.2 of Schatz's book [3].

Given a charge distribution of density $\rho(\vec{r})$, where $\vec{r}$ could be written in the standard reference frame as $\vec{r} = r_x\hat{x} + r_y\hat{y} + r_z\hat{z}$, it creates an electric potential $V(\vec{r})$ as a function of $\vec{r}$, given by (See Chapter 2.3.4 of [21]):

$$V(\vec{r}) = \frac{1}{4\pi\varepsilon_0}\int \frac{\rho(\vec{r}')}{|\vec{r} - \vec{r}'|}\,dV\,. \tag{2.6}$$

The meaning of $dV, \vec{r}$ and $\vec{r}'$ are encapsulated in Figure 4, shown below.

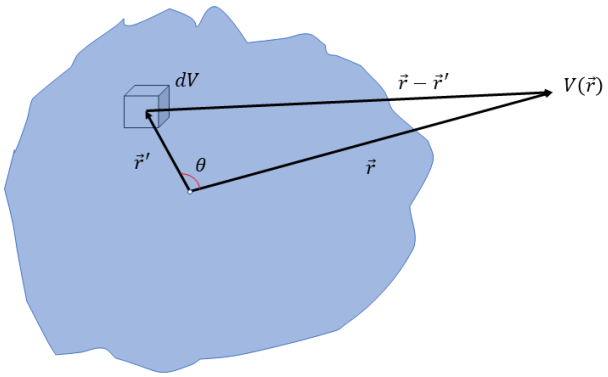


Figure 4: The physical manifestation of the electric potential on a continuous arbitrary charge. We note that the infinitesimal volume dV is represented as a cube inside the charge.

dV is the volume element of integration at the point $\vec{r}'$.

Using the spherical coordinates and doing the multipole expansion of equation (2.6) yields (See Chapter 3.3.2 and Chapter 3.4.1 of [21]):

$$V(\vec{r}) = \frac{1}{4\pi\varepsilon_0}\sum_{n=0}^{\infty}\frac{1}{r^{n+1}}\int (r')^n P_n(\cos\theta)\,\rho(\vec{r}')\,dV\,. \tag{2.7}$$

The angle between $\vec{r}$ and $\vec{r}'$ is defined to be θ, as shown in Figure 4. $r = |\vec{r}|$ is the scalar magnitude of the vector $\vec{r}$, and $P_n(x)$ are the Legendre Polynomials.

We want to extract the Quadrupole term by taking $n = 2$ only in the summation of equation (2.7). Noting that $P_2(x) = \frac{1}{2}(3x^2 - 1)$:

$$V_2(\vec{r}) = \frac{1}{4\pi\varepsilon_0}\left(\frac{1}{r^3}\int (\vec{r}')^2\,\frac{1}{2}(3\cos^2\theta - 1)\,\rho(\vec{r}')\,dV\right). \tag{2.8}$$

Noting that $\hat{r}.\vec{r}' = |\hat{r}||\vec{r}'|\cos\theta = |\vec{r}'|\cos\theta$,

$$V_2(\vec{r}) = \frac{1}{4\pi\varepsilon_0}\left(\frac{1}{r^3}\int \frac{1}{2}(3(\hat{r}.\vec{r}')^2 - (\vec{r}')^2)\,\rho(\vec{r}')\,dV\right). \tag{2.9}$$

At this point, we would like to take advantage of two identities: $(\vec{r}.\vec{r}')^2 = \left(\sum_{i=x,y,z} r_i r_i'\right)\left(\sum_{j=x,y,z} r_j r_j'\right)$ and $\vec{r}.\vec{r} = \sum_{i,j=x,y,z} r_i r_j \delta_{ij} = r^2$, with δ_{ij} as the Kronecker delta.

Thus, we define the Quadrupole moment Q_{quad} relative to the direction $\vec{r}'$ as:

$$Q_{quad} = \int \frac{1}{2}(3(\hat{r}.\vec{r}')^2 - (\vec{r}')^2)\,\rho(\vec{r}')\,dV = \frac{1}{r^2}\int \frac{1}{2}\left(3(\vec{r}.\vec{r}')^2 - (\vec{r}')^2(\vec{r}.\vec{r})\right)\rho(\vec{r}')\,dV$$
$$= \frac{1}{r^2}\sum_{i,j=x,y,z}\frac{1}{2}\int \left(3r_i' r_i r_j' r_j - (\vec{r}')^2 r_i r_j \delta_{ij}\right)\rho(\vec{r}')\,dV\,;$$

$$Q_{quad} = \sum_{i,j=x,y,z}\frac{1}{2r^2}\int \left(3r_i' r_j' - (\vec{r}')^2\delta_{ij}\right) r_i r_j\,\rho(\vec{r}')\,dV\,. \tag{2.10}$$

Consequently, we can define the symmetric quadrupole tensor Q_{ij}:

$$Q_{ij} \coloneqq \frac{1}{e}\int \left(3r_i' r_j' - (\vec{r}')^2\delta_{ij}\right)\rho(\vec{r}')\,dV. \tag{2.11}$$

And write:

$$Q_{quad} = \sum_{i,j=x,y,z}\frac{e}{2r^2}Q_{ij} r_i r_j\,, \tag{2.12}$$

$$V_2(\vec{r}) = \frac{1}{4\pi\varepsilon_0}\frac{e}{2r^5}\sum_{i,j=x,y,z} Q_{ij} r_i r_j\,. \tag{2.13}$$

In essence, the quadrupole moment of an atomic nucleus is the measure of the deformation from the ideal spherical shape, i.e., an ellipsoid, while maintaining its threefold axes of symmetry that intersect at the centre of the ellipsoid. We note that by definition, a perfectly spherical nucleus must have no quadrupole moment.

The magnitude and sign of the quadrupole moment reflect the physics that occurs between the neutrons and protons in the nucleus, characterised by $\rho(\vec{r}')$, along with the overall shape of the nucleus in general.

Since the z- direction is of importance in Quantum Mechanics; we choose our $\vec{r}$ to be $\hat{z}$. Thus, we then drop the "′" in $\vec{r}'$ for brevity and from equation (2.11), define the quadrupole moment of a nuclear state Q to be:

$$Q \coloneqq Q_{zz} = \frac{1}{e}\int (3z^2 - (\vec{r})^2)\,\rho(\vec{r})\,dV. \tag{2.14}$$

Q can be more than or less than 0. Elliptic Spheroids with $Q > 0$ are described to be prolate and oblate if $Q < 0$ (See Figure 5).

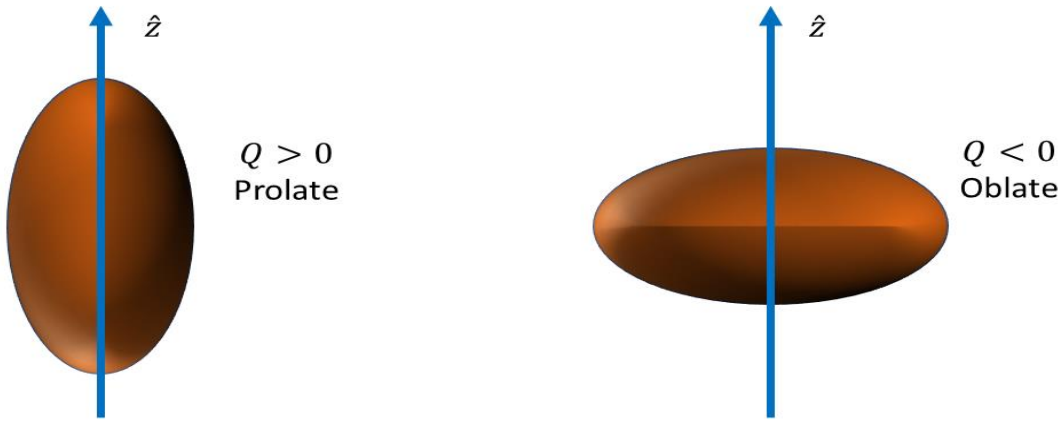


Figure 5: The orientation of the nucleus as an Elliptic Spheroids for the case $Q > 0$ & $Q < 0$.

Since we are using the spherical coordinates, we note that $z = r\cos\theta$, where θ is now the angle between $\hat{z}$ and $\vec{r}$. Therefore, from equation (2.14):

$$Q = \frac{1}{e}\int (3r^2\cos^2\theta - r^2)\rho(\vec{r})\,dV\,. \tag{2.15}$$

Furthermore, if we make use of the spherical harmonics:

$$Y_{20}(\theta,\varphi) = \sqrt{\frac{5}{16\pi}}(3\cos^2\theta - 1). \tag{2.16}$$

We have the alternate form for the expression of Q:

$$Q = \frac{1}{e}\sqrt{\frac{16\pi}{5}}\int r^2 Y_{20}(\theta,\varphi)\rho(\vec{r})\,dV\,. \tag{2.17}$$

Thus, we have the quantum-mechanical definition of Q, which follows in the exact analogue as μ in section 2.1, equation $(2.3a\ \&\ 2.3b)$:

$$Q \coloneqq \left\langle I, m = I\left|\sqrt{\frac{16\pi}{5}}Zr^2Y_{20}\right|I, m = I\right\rangle \coloneqq \langle\bar{Q}_{20}\rangle. \tag{2.18}$$

Z is the atomic number of the nucleus.

$Q_{20} = Zr^2Y_{20}$ is a tensor operator. By using Wigner-Eckart's Theorem (See [3], Chapter 2.2), we can express $\langle I, m|\bar{Q}_{20}|I, m\rangle$ as a product of $3j$-symbols (or equivalently, Clebsch-Gordan coefficients), alongside a reduced matrix element $\langle I||Q_2||I\rangle$:

$$\langle I, m|Q_{20}|I, m\rangle = (-1)^{I-m}\begin{pmatrix} I & 2 & I \\ -m & 0 & m \end{pmatrix}\langle I||Q_2||I\rangle. \tag{2.19}$$

We note that $\begin{pmatrix} I & 2 & I \\ -m & 0 & m \end{pmatrix}$ is a $3j$-symbol and is dependent on the geometry but not the dynamics (i.e., the orientation of the system with respect to the z-axis that defines the magnetic quantum numbers "m" and the "0", but not the total angular momentum number "I" and the "2" in $\langle\bar{Q}_{20}\rangle$) of the system.

We note that Q has dimensions of $[Length]^2$, i.e. the dimension of an $[Area]$, and due to the length scale of the nucleus, it is typically expressed in the units of barns:

$$1\ barn = 100\ fm^2 = 10^{-28}m^2. \tag{2.20}$$

To define Q_{ij} (Remember that $i, j \in \{x, y, z\}$, i.e. Cartesian coordinates), we note that in a complete vector space that is spanned by the Casimir elements $\{|I, m\rangle\}$, where $m \in \{-I, -I+1, \dots, I-1, I\}$, we cannot have a closed analytic form of Q_{ij} other than Q_{zz}, simply because $\hat{I}_x$ and $\hat{I}_y$ are not eigenoperators of $|I, m\rangle$. However, we can do two neat tricks, the first being shown right away in this section.

We refer to [22] for our first trick and note that the matrix element of any operator acting on the vector space of $\{|I, m\rangle\}$ must be formed from a (valid) linear combination of either $\hat{I}_x, \hat{I}_y, \hat{I}_z$ or $\hat{I}$. From our definition of the quadrupole moment (Equation (2.11)), the quadrupole operator $\overleftrightarrow{Q}\ (\hat{Q})$ has to be 1) Symmetric, 2) Traceless, 3) Rank 2 (I.e. a Matrix), and 4) expressed in terms of $\{\widehat{Id}, \hat{I}_x, \hat{I}_y, \hat{I}_z, \hat{I}\}$.

Thus, our ansatz for the general form of $\hat{Q}_{ij}$ must be in the form of:

$$\hat{Q}_{ij} = \frac{3C}{2}\left(\hat{I}_i\hat{I}_j + \hat{I}_j\hat{I}_i\right) - \delta_{ij}\hat{I}^2. \tag{2.21}$$

C is a constant that is yet to be determined. We anticipate that C must be expressed in terms of the total angular momentum number, I.

Since we have $\langle I, I|Q_{zz}|I, I\rangle = Q$, we have, recalling equation $(2.2a\ \&\ 2.2b)$:

$$\left\langle I, I\middle|\frac{3C}{2}\left(2\hat{I}_z\hat{I}_z\right) - \hat{I}^2\middle|I, I\right\rangle = C\langle I, I|3\left(\hat{I}_z\hat{I}_z - \hat{I}^2\right)|I, I\rangle = C\left(3I^2 - I(I+1)\right)\hbar^2 = Q,$$

$$C = \frac{Q}{I(2I-1)\hbar^2}. \tag{2.22}$$

Hence, we can write out the tensor components of $\overleftrightarrow{Q}$:

$$\hat{Q}_{ij} = \frac{Q}{I(2I-1)\hbar^2}\left[\frac{3}{2}\left(\hat{I}_i\hat{I}_j + \hat{I}_j\hat{I}_i\right) - \delta_{ij}\hat{I}^2\right]. \tag{2.23}$$

We will return to equation (2.23) later in section 2.3.1 once we have fleshed out the monopole term and the quadrupole term of the electric interactions.

2.3) The Hyperfine structure and the interactions of an external electric field

This section will introduce an external electric field, which will then be coupled to our probe nucleus in question. Such an interaction is called the "Hyperfine Interaction". By following a theoretical discourse of the hyperfine structure of our probe, we could understand the extensive effect of the external electrical field on the probe nucleus itself.

We would mainly refer to Chapter 3.2 of Schatz's book [3], up to a certain point. Then we would mainly rely on Butz's paper [23][1] for the detailed analysis (Reproduced with permission; copyright retained under Wiley and Springer Nature, respectively).

2.3.1) Electric Interactions

We start with a simple model of an arbitrary nuclear charge density $\rho(\vec{r})$, with a nuclear charge of Ze, along with an electrical potential $\Phi(\vec{r})$, with the centre of mass of the nuclear charge density set at the origin (As we do not want to introduce the $|\vec{r} - \vec{r}'|$ term, as per the previous sections; see figure 4).

The electrostatic energy is given by:

$$E = \int \rho(\vec{r})\, \Phi(\vec{r})\, dV. \tag{2.24}$$

Also:

$$\int \rho(\vec{r})\, dV = Ze. \tag{2.25}$$

Expanding $\Phi(\vec{r})$ in the multivariate Taylor expansion around $\vec{r} = 0$, we have:

$$\Phi(\vec{r}) = \Phi(\vec{0}) + \sum_{i=x,y,z} \left.\frac{\partial \Phi(\vec{r})}{\partial r_i}\right|_{\vec{r}=0} r_i + \frac{1}{2} \sum_{i,j=x,y,z} \left.\frac{\partial^2 \Phi(\vec{r})}{\partial r_i \partial r_j}\right|_{\vec{r}=0} r_i r_j + \cdots \tag{2.26}$$

This expansion means that we can split E in equation (2.24) as an infinite sum of terms, with each increasing term contributing a smaller amount to E:

$$E = E_0 + E_1 + E_2 + \cdots, \tag{2.27}$$

$$E_0 = \Phi(\vec{0}) \int \rho(\vec{r})\, dV, \tag{2.28}$$

$$E_1 = \sum_{i=x,y,z} \left.\frac{\partial \Phi(\vec{r})}{\partial r_i}\right|_{\vec{r}=0} \int r_i \rho(\vec{r})\, dV\,, \tag{2.29}$$

$$E_2 = \frac{1}{2} \sum_{i,j=x,y,z} \left.\frac{\partial^2 \Phi(\vec{r})}{\partial r_i \partial r_j}\right|_{\vec{r}=0} \int r_i r_j \rho(\vec{r})\, dV\,. \tag{2.30a}$$

[1] Be warned, however, that Butz's original paper contains mistakes, to which he had corrected it in the Erratum.

We analyse E_0, E_1 and E_2:

For E_0:

By equation (2.25), we have $E_0 = \Phi(\vec{0})Ze$. As $\Phi(\vec{0})$ is the potential at the origin $\vec{r} = 0$, E_0 is the Coulomb energy of a point charge in an external potential. This term contributes only to the system's potential energy and hence is the same for every isotope of the same element (so long as Z remains unchanged). Thus, E_0 cannot be distinguished by TDPAC experiments. In essence, we can set E_0 as 0.

For E_1:

From equation (2.29), we can write E_1 as:

$$E_1 = \left(\left.\frac{\partial \Phi(\vec{r})}{\partial x}\right|_{\vec{r}=0} \quad \left.\frac{\partial \Phi(\vec{r})}{\partial y}\right|_{\vec{r}=0} \quad \left.\frac{\partial \Phi(\vec{r})}{\partial z}\right|_{\vec{r}=0} \right) \begin{pmatrix} \int r_x \rho(\vec{r})\, dV \\ \int r_y \rho(\vec{r})\, dV \\ \int r_z \rho(\vec{r})\, dV \end{pmatrix}. \tag{2.31}$$

By definition, $\int r_i \rho(\vec{r})\, dV$ are the x, y, z-components for the electric dipole moment $\vec{\rho}$ respectively for $i = x, y, z$ and $\nabla\Phi = \left(\frac{\partial \Phi}{\partial x} \quad \frac{\partial \Phi}{\partial y} \quad \frac{\partial \Phi}{\partial z}\right) = -\vec{E}$ is the negative of the electrical field of the system. Thus:

$$E_1 = -\left(\vec{E}.\vec{\rho}\right)_{\vec{r}=0}. \tag{2.32}$$

E_1 describes the interaction energy of an electric dipole $\vec{\rho}$ of a nuclear charge distribution with an external field at the origin $\vec{r} = 0$. Due to the well-defined parity of the nuclear wave function, the electric dipole moment of the nuclear charge distribution is zero, and thus, $E_1 = 0$ as well.

For E_2:

To avoid the clutter of notation, we define $\left.\frac{\partial^2 \Phi(\vec{r})}{\partial r_i \partial r_j}\right|_{\vec{r}=0} = \Phi_{r_i r_j}$ for compact notation, which gives us:

$$E_2 = \frac{1}{2} \sum\nolimits_{i,j=x,y,z} \Phi_{r_i r_j} \int r_i r_j \rho(\vec{r})\, dV\,. \tag{2.30b}$$

Using $r^2 = x^2 + y^2 + z^2$, we could further express equation $(2.30b)$ as:

$$E_2 = \frac{1}{2} \sum\nolimits_{i,j=x,y,z} \Phi_{r_i r_j} \int \left(r_i r_j - \frac{r^2}{3} \delta_{ij} \right) \rho(\vec{r})\, dV + \frac{1}{6} \sum\nolimits_{i=x,y,z} \Phi_{r_i r_i} \int r^2 \rho(\vec{r})\, dV\,. \tag{2.33}$$

E_2 is split into the sum of two terms. We define the terms $E_{2,M}$ & $E_{2,Q}$:

$$E_{2,M} = \frac{1}{6} \sum\nolimits_{i=x,y,z} \Phi_{r_i r_i} \int r^2 \rho(\vec{r})\, dV\,, \tag{2.34a}$$

$$E_{2,Q} = \frac{1}{2}\sum_{i,j=x,y,z} \Phi_{r_i r_j} \int \left(r_i r_j - \frac{r^2}{3}\delta_{ij} \right) \rho(\vec{r})\, dV\,. \qquad (2.34b)$$

We further analyse $E_{2,M}$ and $E_{2,Q}$:

For $E_{2,M}$:

The electrostatic potential $\Phi(\vec{r})$ obeys Poisson's equation, which states that $\nabla^2\Phi = \frac{-\rho}{\varepsilon_0}$. Hence:

$$\nabla^2\Phi|_{\vec{r}=0} = \sum_{i=x,y,z} \Phi_{r_i r_i}\big|_{\vec{r}=0} = \frac{e\left|\Phi(\vec{0})\right|^2}{\varepsilon_0}. \qquad (2.35)$$

$\left|\Phi(\vec{0})\right|^2$ is the probability density of the electrons at the nucleus. $-e\left|\Phi(\vec{0})\right|^2 = \rho$ represents the charge density (It is non-zero only for s-electrons).

Furthermore, we define the mean square radius $\langle r^2 \rangle$, given by:

$$\langle r^2 \rangle = \frac{1}{Ze}\int r^2 \rho(\vec{r})\, dV. \qquad (2.36)$$

We thus have:

$$E_{2,M} = \frac{Ze^2}{6\varepsilon_0}\left|\Phi(\vec{0})\right|^2 \langle r^2 \rangle. \qquad (2.37)$$

$E_{2,M}$ is a monopole term that describes the electrostatic interaction of the expanded nucleus with electrons in the nuclear zone. It triggers a shift in the energy levels but does not induce the split of a degenerate set of states into different sub-levels. This shift gives rise to an isotope shift, a phenomenon that causes the Mössbauer shift in the energy lines between the excited state and ground state nucleus with different nuclear radii (which is then different for different isotopes). $E_{2,M}$ is more relevant for the Mössbauer Spectroscopy, and the TDPAC spectroscopy does not detect any Mössbauer shift.

For $E_{2,Q}$:

We are then left with $E_{2,Q}$. Recalling equation (2.11), we write:

$$E_{2,Q} = \frac{e}{6}\sum_{i,j=x,y,z} \Phi_{r_i r_j} Q_{ij}\,. \qquad (2.38a)$$

Or in the matrix form:

$$\overleftrightarrow{E_{2,Q}} = \frac{e}{6}\begin{pmatrix} \Phi_{xx}Q_{xx} & \Phi_{xy}Q_{xy} & \Phi_{xz}Q_{xz} \\ \Phi_{yx}Q_{yx} & \Phi_{yy}Q_{yy} & \Phi_{yz}Q_{yz} \\ \Phi_{zx}Q_{zx} & \Phi_{zy}Q_{zy} & \Phi_{zz}Q_{zz} \end{pmatrix}. \qquad (2.38b)$$

We can immediately see that $E_{2,Q}$ is a symmetric second-ranked tensor. We then attempt to diagonalise the matrix.

Physically, the act of diagonalisation transforms the coordinate system from the standard x, y, z-axis reference basis to the eigenvector basis in which the off-diagonal terms disappear.

Mathematically: The spectral theorem states that there exists an orthogonal matrix $\overleftrightarrow{O}$, which will turn the standard basis into the eigenvector basis. For clarity's sake, we will put a " ′ " on the transformed $E_{2,Q}$ only on the following equation, and write:

$$\overleftrightarrow{E}'_{2,Q} = \overleftrightarrow{O}^{-1}\overleftrightarrow{E}_{2,Q}\overleftrightarrow{O} = \frac{e}{6}\begin{pmatrix} \Phi_{xx}Q_{xx} & 0 & 0 \\ 0 & \Phi_{yy}Q_{yy} & 0 \\ 0 & 0 & \Phi_{zz}Q_{zz} \end{pmatrix}. \qquad (2.39a)$$

Or, in a compact notation:

$$E'_{2,Q} = \frac{e}{6}\sum_{i=x,y,z} \Phi_{r_i r_i} Q_{ii}\,. \qquad (2.39b)$$

We will work with the transformed $E_{2,Q}$, (i.e., only in the new eigenbasis) for the remainder of this section, and hence drop the " ′ " without inducing much confusion.

We then rewrite $\Phi_{r_i r_i} = V_{r_i r_i} + \frac{1}{3}\mathrm{Tr}\left(\overleftrightarrow{\Phi}\right)$, where $\mathrm{Tr}\left(\overleftrightarrow{\Phi}\right) = \sum_{i=x,y,z} \Phi_{r_i r_i}$, such that $\overleftrightarrow{V}$ is a traceless matrix. Since Q is a traceless second-ranked tensor (matrix) as well, and $\frac{1}{3}\mathrm{Tr}(\Phi)$ is simply just a constant, $\sum_{i=x,y,z} Q_{ii} = 0$ and:

$$\sum_{i=x,y,z} \frac{1}{3}\mathrm{Tr}\left(\overleftrightarrow{\Phi}\right) Q_{ii} = 0. \qquad (2.40)$$

We are left with the Electrical Field Gradient (See equation 2.1-2.8 in [24]):

$$E_{2,Q} = \frac{e}{6}\sum_{i=x,y,z} V_{r_i r_i} Q_{ii}\,. \qquad (2.41)$$

For the sake of brevity, in the subscript of the V in the equation (2.41), we will replace r_i with just i. V_{zz}, V_{yy}, V_{zz} form the x, y, z- principal components of the Electrical Field Gradient, abbreviated as "EFG". Only charge densities that are not at the nuclear site contribute to V_{xx}, V_{yy} and V_{zz}. The above implication means that in the TDPAC experiment, the configuration of the local lattice site of the host material surrounding the implanted TDPAC probe will affect the EFG of the mentioned probe.

For a particular case of spherically symmetric charged distributions (s-electrons, with $l = 0$ for example), $V_{xx} = V_{yy} = V_{zz} = 0$ and hence cannot contribute to $E_{2,Q}$. This result means that only p-electrons and above $(l \geq 1)$ can contribute to non-zero values of V_{xx}, V_{yy}, V_{zz} and hence $E_{2,Q}$.

V_{xx}, V_{yy}, V_{zz} are constrained by the following equation (Due to the trace-lessness of V):

$$\sum_{i=x,y,z} V_{ii} = 0. \qquad (2.42)$$

We have two degrees of freedom (parameters) for which we can choose our principal axis system. We also note that the TDPAC experiment does not impose a fixed geometry with

respect to the emission of the first γ-ray or e^- emission (See sections 3.3.2 and 3.4), thus allowing us to choose our principal axis system relative to the said emission.

Generally, we will take the principal axis system such that $|V_{zz}| \geq |V_{yy}| \geq |V_{xx}|$, and from the hints in our earlier definitions of Q (See equation (2.14)) and our general intuition of quantum mechanics, we chose to describe the EFG as a function of V_{zz} and our asymmetry parameter η:

$$\eta = \frac{|V_{yy}| - |V_{xx}|}{|V_{zz}|}. \tag{2.43}$$

One can see that the range of η is such that $0 \leq \eta \leq 1$.

η measures the deviation of the local charge distribution from the 3-axial symmetry around the origin point due to the influence of the electrical quadrupole interaction of the local lattice system (from the host environment) on the TDPAC probe.

Thus, E_Q is expressed as the product of the nuclear quadrupole moment Q_{ii} and the EFG (acting at the site of the nucleus) $V_{ii}, i \in \{x, y, z\}$. In the literature, E_Q is termed as the nuclear quadrupole interaction.

From equation (2.41), we can rewrite $E_{2,Q}$ in terms of V_{zz} and η explicitly. Using equation $(2.40, 2.42 \ \& \ 2.43)$, we have:

$$E_{2,Q} = \frac{e}{6}\left(V_{xx}Q_{xx} + V_{yy}Q_{yy} + V_{zz}Q_{zz}\right)$$

$$= \frac{e}{6}\Big(\left(V_{yy} - \eta V_{zz}\right)Q_{xx} + \left(V_{xx} + \eta V_{zz}\right)Q_{yy} + V_{zz}Q_{zz}\Big)$$

$$= \frac{e}{6}\Big(\left(-\eta V_{zz}Q_{xx} + \eta V_{zz}Q_{yy} + V_{zz}Q_{zz}\right) + \left(V_{yy}Q_{xx} + V_{xx}Q_{yy}\right)\Big)$$

$$= \frac{e}{6}\Big(\left(-\eta V_{zz}Q_{xx} + \eta V_{zz}Q_{yy} + 3V_{zz}Q_{zz}\right) + \left(-2V_{zz}Q_{zz} + V_{yy}Q_{xx} + V_{xx}Q_{yy}\right)\Big)$$

$$= \frac{e}{6}\Big(\left(\eta V_{zz}\left(Q_{yy} - Q_{xx}\right) + 3V_{zz}Q_{zz}\right) + \left(-2V_{zz}Q_{zz} - \left(V_{zz} + V_{xx}\right)Q_{xx} - \left(V_{zz} + V_{yy}\right)Q_{yy}\right)\Big)$$

$$= \frac{e}{6}\Big(\left(\eta V_{zz}\left(Q_{yy} - Q_{xx}\right) + 3V_{zz}Q_{zz}\right) - \Big(V_{zz}\left(Q_{xx} + Q_{yy} + Q_{zz}\right)\Big) - \left(V_{zz}Q_{zz} + V_{xx}Q_{xx} + V_{yy}Q_{yy}\right)\Big)$$

$$= \frac{e}{6}\left(\eta V_{zz}\left(Q_{yy} - Q_{xx}\right) + 3V_{zz}Q_{zz}\right) - E_{2,Q},$$

$$\widehat{H}_Q = E_{2,Q} = \frac{eV_{zz}}{12}\left(\eta\left(Q_{yy} - Q_{xx}\right) + 3Q_{zz}\right). \tag{2.44a}$$

Note that we have formulated $E_{2,Q}$ purely in terms of classical mechanics. By using Ehrenfest's Theorem and Bohr's correspondence principle (See section 3.8 of [19]), we can convert equation (2.44) into its quantum formulation, which will be characterised by the corresponding operator $\hat{Q}$ and hence, the total angular momentum operator $\hat{I}$.

By using equation (2.23):

$$\hat{Q}_{ii} = \frac{Q}{I(2I-1)\hbar^2}\left[3\hat{I}_i\hat{I}_i - \hat{I}^2\right],$$

We have:

$$\hat{H}_Q = \frac{eV_{zz}}{12}\frac{Q}{I(2I-1)\hbar^2}\left[9\hat{I}_z^2 - 3\hat{I}^2 + \eta\left(3\hat{I}_y^2 - \hat{I}^2 - 3\hat{I}_x^2 + \hat{I}^2\right)\right],$$

$$\hat{H}_Q = \frac{eV_{zz}Q}{4I(2I-1)\hbar^2}\left[3\hat{I}_z^2 - \hat{I}^2 + \eta\left(\hat{I}_y^2 - \hat{I}_x^2\right)\right]. \quad (2.44b)$$

Since we have the vector space of $\hat{H}_Q$ spanned by $\{|I,m\rangle\}$, where $m \in \{-I, -I+1, \dots, I-1, I\}$, and $\hat{H}_Q$ is expressed by $\hat{I}_x$,$\hat{I}_y$, $\hat{I}_z$ or $\hat{I}$, we will make use of the Ladder algebra, which is our second trick. We define the ladder operators:

$$\hat{I}_+ = \hat{I}_x + i\hat{I}_y, \quad (2.45a)$$

$$\hat{I}_- = \hat{I}_x - i\hat{I}_y, \quad (2.45b)$$

We then have:

$$\hat{I}_+^2 = \hat{I}_x^2 + i\hat{I}_y\hat{I}_x + i\hat{I}_x\hat{I}_y - \hat{I}_y^2, \quad (2.46a)$$

$$\hat{I}_-^2 = \hat{I}_x^2 - i\hat{I}_y\hat{I}_x - i\hat{I}_x\hat{I}_y - \hat{I}_y^2. \quad (2.46b)$$

$$\hat{I}_x^2 - \hat{I}_y^2 = \frac{1}{2}\left(\hat{I}_+^2 + \hat{I}_-^2\right). \quad (2.46c)$$

Thus, we have the final form of $\hat{H}_Q$ as:

$$\hat{H}_Q = \frac{eV_{zz}Q}{4I(2I-1)\hbar^2}\left[3\hat{I}_z^2 - \hat{I}^2 - \frac{\eta}{2}\left(\hat{I}_+^2 + \hat{I}_-^2\right)\right]. \quad (2.47)$$

With the ladder operators, we can see three distinct features:

1) The matrix representation of $\hat{H}_Q$ in the space spanned by $\{|I,m\rangle\}$, where $m \in \{-I, -I+1, \dots, I-1, I\}$, is of dimension $(2I+1) \times (2I+1)$.
2) The diagonal elements of $\hat{H}_Q$ is $\hat{H}_{Q,diag} = \frac{eV_{zz}Q}{4I(2I-1)\hbar^2}\left[3\hat{I}_z^2 - \hat{I}^2\right]$.
3) For the off-diagonal terms, the only non-zero elements of $\hat{H}_Q$ are the terms connecting $|I,m\rangle$ to $|I,m\pm2\rangle$ for fixed values of m. This feature means that only the $(m, m\pm2)$ terms for $m, m\pm2 \in \{-I, -I+1, \dots, I-1, I\}$ will be non-zero, and the rest of the off-diagonal terms is zero. The relevant Hamiltonian for the plus term is $\hat{H}_{Q,+} = -\frac{eV_{zz}Q}{4I(2I-1)\hbar^2}\left(\frac{\eta}{2}\hat{I}_+^2\right)$ and the minus term $\hat{H}_{Q,-} = -\frac{eV_{zz}Q}{4I(2I-1)\hbar^2}\left(\frac{\eta}{2}\hat{I}_-^2\right)$.

Recalling our quantum mechanics formalism for angular momentum (equation $(2.2a$ & $2.2b)$), along with the ladder operators acting on the state $|I,m\rangle$ (See [19], Section 5.3):

$$\hat{I}_\pm|I,m\rangle = \hbar\sqrt{(I \mp m)(I \pm m + 1)}|I, m \pm 1\rangle, \quad (2.48a)$$

$$\hat{I}_{\pm}^{2}|I,m\rangle = \hbar^{2}\sqrt{\big(I \mp (m \pm 1)\big)(I \pm (m \pm 1) + 1)(I \mp m)(I \pm m + 1)}|I,m \pm 2\rangle,$$

$$\hat{I}_{\pm}^{2}|I,m\rangle = \hbar^{2}\sqrt{(I \mp m - 1)(I \pm m + 2)(I \mp m)(I \pm m + 1)}|I,m \pm 2\rangle. \qquad (2.48b)$$

We obtain the matrix elements for $\widehat{H}_Q$. Dropping the subscript "Q" for brevity, we have:

$$H_{m,m} = \frac{eV_{zz}Q}{4I(2I-1)}\big(3m^{2} - I(I+1)\big), \qquad (2.49a)$$

$$H_{m,m\pm2} = -\frac{eV_{zz}Q}{4I(2I-1)}\frac{\eta}{2}\sqrt{(I \mp m - 1)(I \pm m + 2)(I \mp m)(I \pm m + 1)}. \qquad (2.49b)$$

We define our quadrupole frequency ω_Q:

$$\omega_Q = \frac{eV_{zz}Q}{4I(2I-1)\hbar}. \qquad (2.50)$$

As a reminder: Q is the quadrupole moment of our nuclear probe and is defined via equation (2.18).

We can write equation $(2.49a\ \&\ 2.49b)$ in a compact notation:

$$H_{m,m} = \hbar\omega_Q\big(3m^{2} - I(I+1)\big), \qquad (2.51a)$$

$$H_{m,m\pm2} = -\hbar\omega_Q\frac{\eta}{2}\sqrt{(I \mp m - 1)(I \pm m + 2)(I \mp m)(I \pm m + 1)}. \qquad (2.51b)$$

The rest of the matrix elements are 0, following our discussion in pointer 3) on the previous page.

2.3.2) Special case for which $\eta = 0$ and $I = 5/2$

In the case in which $\eta = 0$, equation $(2.51a\ \&\ 2.51b)$ simplifies to a Hamiltonian with only non-zero diagonal elements.

As the "m" terms exist as a square in $H_{m,m}$ as per equation (2.49), we will expect $|I,m\rangle$ and $|I,-m\rangle$ to be degenerate for all $m \in \{-I, -I+1, \dots, I-1, I\}$. Therefore, we will expect our energy spectrum to be twofold degenerate, with $(2I+1)/2$ unique eigenvalues for $\vec{\vec{H}}$.

Since we are dealing with ^{181}Ta as an intermediate state, for which it has a total angular momentum of $I = 5/2$, let's fix the value of $I = 5/2$ for the remainder of the script. We should expect three unique eigenvalues:

$E_{\pm\frac{1}{2}} = -8\hbar\omega_Q$, with eigenstates

$$\left\{\left|\tfrac{5}{2}, \pm\tfrac{1}{2}\right\rangle\right\}, \qquad (2.52a)$$

$E_{\pm\frac{3}{2}} = -2\hbar\omega_Q$, with eigenstates

$$\left\{\left|\tfrac{5}{2}, \pm\tfrac{3}{2}\right\rangle\right\}, \qquad (2.52b)$$

$E_{\pm\frac{5}{2}} = 10\hbar\omega_Q$, with eigenstates

$$\left\{\left|\frac{5}{2}, \pm\frac{5}{2}\right\rangle\right\}. \tag{2.52c}$$

We would refer to equations $(2.51a \ \& \ 2.51b)$ and $(2.52a - \ 2.52c)$ later in section 2.3.3.

2.3.3) General case for η, with $I = 5/2$

In the general case of η not necessarily being 0, we would expect a mixing of the $\{|I, m\rangle\}$ states; this would mean that our eigenbasis of $\widehat{H}_Q$ would be a linear combination of some states of $\{|I, m\rangle\}$, which must be determined by the diagonalisation of H.

We would refer to Butz's paper [23] for this section, which he had additionally treated for other values of I. We would, of course, focus on the particular case of $I = 5/2$ (Reproduced with permission; copyright retained under Springer Nature).

We first recognise two essential properties of $\overleftrightarrow{H}$. Let's take a general matrix $\overleftrightarrow{A}$ of dimension $(2I + 1) \times (2I + 1)$. $\overleftrightarrow{A}$ is said to be (With $m, m' \in \{-I, -I + 1, \dots, I - 1, I\}$):

1) Symmetric under even permutations of the cycle notation $\prod_{m\in\left\{\frac{1}{2},\frac{3}{2},\dots,I-1,I\right\}}\{m\ (-m)\}$ if:
$$A_{m,m'} = A_{-m,-m'}, \tag{2.53a}$$
2) Symmetric if:
$$A_{m,m'} = A_{m',m}. \tag{2.53b}$$

We claim that $\overleftrightarrow{H}$ obeys both properties $(2.53a, 2.53b)$:

Proof for equation $(2.53a)$:

For the diagonal entry $H_{m,m}$ as shown in section 2.3.2, we only have the m^2 term dependence. So $H_{m,m} = H_{-m,-m}$. For the off-diagonal entries, we start with the expression for $H_{m,m\pm2}$ (Equation $(2.51b)$) and show:

$$\begin{aligned} H_{m,m\pm2} =\ & \hbar\omega_Q \frac{\eta}{2} \sqrt{(I \mp m - 1)(I \pm m + 2)(I \mp m)(I \pm m + 1)} \\ &= \hbar\omega_Q \frac{\eta}{2} \sqrt{(I \pm (-m) - 1)(I \mp (-m) + 2)\big(I \pm (-m)\big)(I \mp (-m) + 1)} \\ &= H_{-m,-m\mp2} = H_{-m,-(m\pm2)}. \end{aligned}$$

Proof for $(2.53b)$:

We first prove the off-diagonal terms: That is, $H_{m,m\pm2} = H_{-(m\pm2),-m}$. Subbing m with $-m' \mp 2$ gives:

$$H_{-m'\mp2,-m'\mp2\pm2} = H_{-(m'\pm2),-m'} = \hbar\omega_Q \frac{\eta}{2} \times$$

$$\sqrt{(I \mp (-m' \mp 2) - 1)(I \pm (-m' \mp 2) + 2)\big(I \mp (-m' \mp 2)\big)(I \pm (-m' \mp 2) + 1)}$$

$$= \hbar\omega_Q \frac{\eta}{2} \sqrt{(I \pm m' + 1)(I \mp m')(I \pm m' + 2)(I \mp m' - 1)} = H_{m',m'\pm2}.$$

We then use property $(2.53a)$ to achieve $H_{m,m\pm2} = H_{m\pm2,m}$. Property $(2.53b)$ is trivial for the diagonal terms $H_{m,m}$.

Property $(2.53a \ \& \ 2.53b)$ has a consequence for $\overleftrightarrow{H}$: For a half-integer I, we can find a unitary matrix $\overleftrightarrow{U}$ such that if:

$$\overleftrightarrow{H}' = \overleftrightarrow{U}^{-1}\overleftrightarrow{H}\overleftrightarrow{U}, \tag{2.54a}$$

$$\overleftrightarrow{H}' = \begin{pmatrix} \overleftrightarrow{H}_1 & 0_{\left(I+\frac{1}{2}\right)\times\left(I+\frac{1}{2}\right)} \\ 0_{\left(I+\frac{1}{2}\right)\times\left(I+\frac{1}{2}\right)} & \overleftrightarrow{H}_2 \end{pmatrix}, \tag{2.54b}$$

where $\overleftrightarrow{H}_1$ and $\overleftrightarrow{H}_2$ are of dimension $\left(I+\frac{1}{2}\right)\times\left(I+\frac{1}{2}\right)$. Furthermore, by property $(2.53a \ \& \ 2.53b)$, we must have:

$$\overleftrightarrow{H}_1 = \overleftrightarrow{H}_2. \tag{2.55}$$

Like the case in which $\eta = 0$ (Section 2.3.2), this implies that all eigenvalues are doubly degenerate. Also, for the off-diagonal terms, we only have $H_{m,m\pm2}$ as the non-zero terms, implying that we only have a mixing between the $|I,m\rangle$ and the $|I,m\pm2\rangle$ states only.

For $I = 5/2$, we have $\overleftrightarrow{H}$ of the form:

$$\overleftrightarrow{H} = \begin{pmatrix} 10 & 0 & -\eta\sqrt{10} & 0 & 0 & 0 \\ 0 & -2 & 0 & -\eta\sqrt{18} & 0 & 0 \\ -\eta\sqrt{10} & 0 & -8 & 0 & -\eta\sqrt{18} & 0 \\ 0 & -\eta\sqrt{18} & 0 & -8 & 0 & -\eta\sqrt{10} \\ 0 & 0 & -\eta\sqrt{18} & 0 & -2 & 0 \\ 0 & 0 & 0 & -\eta\sqrt{10} & 0 & 10 \end{pmatrix}\hbar\omega_Q. \tag{2.56a}$$

Applying equation $(2.54a \ \& \ 2.54b)$, with:

$$\overleftrightarrow{U} = \begin{pmatrix} 1 & 0 & 0 & 0 & 0 & 0 \\ 0 & 0 & 0 & 0 & 0 & 1 \\ 0 & 1 & 0 & 0 & 0 & 0 \\ 0 & 0 & 0 & 0 & 1 & 0 \\ 0 & 0 & 1 & 0 & 0 & 0 \\ 0 & 0 & 0 & 1 & 0 & 0 \end{pmatrix}, \tag{2.56b}$$

gives $H_1 = H_2$ with:

$$\overleftrightarrow{H}_1 = \overleftrightarrow{H}_2 = \begin{pmatrix} 10 & -\eta\sqrt{10} & 0 \\ -\eta\sqrt{10} & -8 & -\eta\sqrt{18} \\ 0 & -\eta\sqrt{18} & -2 \end{pmatrix}\hbar\omega_Q. \tag{2.56c}$$

The eigenvalues of $\overleftrightarrow{H}_1 = \overleftrightarrow{H}_2$ is such that we solve the 3rd-order polynomial characteristic equation over real coefficients. By the fundamental theorem of Algebra, we should have three roots, and since $\overleftrightarrow{H}_1 = \overleftrightarrow{H}_2$ is Hermitian, we should expect three real roots:

$$(10-E)(-8-E)(-2-E) - 18\eta^2(10-E) - 10\eta^2(-2-E) = 0. \tag{2.57}$$

Butz [23] provides an analytical solution to equation (2.57). It is independently derived and verified in Appendix A. We have:

$$E_1 = -2r\cos\left(\frac{\varphi}{3}\right)\hbar\omega_Q, \tag{2.58a}$$

$$E_2 = \left(r\cos\left(\frac{\varphi}{3}\right) - \sqrt{3}r\sin\left(\frac{\varphi}{3}\right)\right)\hbar\omega_Q, \tag{2.58b}$$

$$E_3 = \left(r\cos\left(\frac{\varphi}{3}\right) + \sqrt{3}r\sin\left(\frac{\varphi}{3}\right)\right)\hbar\omega_Q, \tag{2.58c}$$

with

$$\cos(\varphi) = \frac{q}{r^3}, \tag{2.58d}$$

$$r = \mathrm{sgn}(q) * \sqrt{|p|} = -\sqrt{|p|}, \tag{2.58e}$$

$$p = -28\left(1 + \frac{\eta^2}{3}\right), \tag{2.58f}$$

$$q = -80(1 - \eta^2), \tag{2.58g}$$

$$\eta \in [0,1], \tag{2.58h}$$

and all three energy eigenvalues are doubly degenerate.

Equivalently, E.Geradu et al. [25] provide an alternate, but the equivalent form of E_1, E_2, E_3:

$$E_1 = 2\alpha\hbar\omega_Q\cos\left(\frac{1}{3}\cos^{-1}\beta\right), \tag{2.59a}$$

$$E_2 = -2\alpha\hbar\omega_Q\cos\left(\frac{1}{3}(\pi + \cos^{-1}\beta)\right), \tag{2.59b}$$

$$E_3 = -2\alpha\hbar\omega_Q\cos\left(\frac{1}{3}(\pi - \cos^{-1}\beta)\right), \tag{2.59c}$$

with

$$\alpha = \sqrt{\left(\frac{28}{3}\right)(3 + \eta^2)}, \tag{2.59d}$$

$$\beta = \frac{80(1 - \eta^2)}{\alpha^3}, \tag{2.59e}$$

$$\eta \in [0,1]. \tag{2.59f}$$

By setting $\eta = 0$ in the limiting case and concerning equation $(2.52a - 2.52c)$, we can see that:

$$E_1(\eta = 0) = -2r\cos\left(\frac{\varphi}{3}\right)\hbar\omega_Q\Big|_{\eta=0} = 10\hbar\omega_Q = E_{\pm\frac{5}{2}}, \tag{2.59a}$$

$$E_2(\eta = 0) = \left(r\cos\left(\frac{\varphi}{3}\right) - \sqrt{3}r\sin\left(\frac{\varphi}{3}\right)\right)\hbar\omega_Q\Big|_{\eta=0} = -2\hbar\omega_Q = E_{\pm\frac{3}{2}}, \tag{2.59b}$$

$$E_3(\eta = 0) = \left(r\cos\left(\frac{\varphi}{3}\right) + \sqrt{3}r\sin\left(\frac{\varphi}{3}\right)\right)\hbar\omega_Q\Big|_{\eta=0} = -8\hbar\omega_Q = E_{\pm\frac{1}{2}}. \qquad (2.59c)$$

Hence, we will denote the eigenenergies of $\overleftrightarrow{H}$, which are the solutions of equation (2.56), with reference to their eigenvectors when $\eta = 0$ (equations $(2.52a - 2.52c)$), i.e., with no mixing terms. This style means that we conveniently denote:

$$E_{\pm\frac{5}{2}} = -2r\cos\left(\frac{\varphi}{3}\right)\hbar\omega_Q, \qquad (2.60a)$$

$$E_{\pm\frac{3}{2}} = \left(r\cos\left(\frac{\varphi}{3}\right) - \sqrt{3}r\sin\left(\frac{\varphi}{3}\right)\right)\hbar\omega_Q, \qquad (2.60b)$$

$$E_{\pm\frac{1}{2}} = \left(r\cos\left(\frac{\varphi}{3}\right) + \sqrt{3}r\sin\left(\frac{\varphi}{3}\right)\right)\hbar\omega_Q, \qquad (2.60c)$$

with φ following the same convention as equation $(2.58d - 2.58h)$.

The last thing we should consider: Does any form of level-crossing exist for energies $E_{\pm\frac{5}{2}}, E_{\pm\frac{3}{2}}$ and $E_{\pm\frac{1}{2}}$? Equivalently, do any value of $\eta \in [0,1]$ exist in which 2 of the eigenvalues of the E's are the same. If there is such an $\eta \in [0,1]$ such that it introduces any level crossings, there will be a mixture of eigenstates of the E's that have the same value at that particular η. Such an existence of η would further complicate our analysis.

Fortunately, a graphical plot of the eigenenergies against η shows no such level crossings (See Figure 6), i.e., there exist no such $\eta \in [0,1]$ such those level crossings are induced.

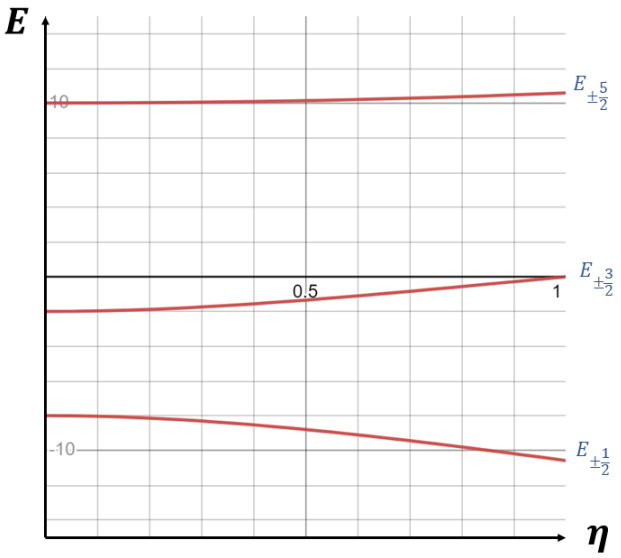


Figure 6: The graphical solution to the eigenvalue problem (2.56), using Wolfram Alpha. We plot the independent variable E (in units of $\hbar\omega$), and the asymmetry parameter η (between 0 to 1) as the dependent variable.

The non-existence of such level crossings means that the linear combination of the eigenvectors of $|I, \pm m\rangle$ will only be mixed with those of $|I, \pm(m \pm 2)\rangle$ for all $\eta \in [0,1]$.

We will not attempt to derive the explicit values of the eigenvectors as a function of η, as we do not need them for the general understanding of the TDPAC. Instead, we would refer to [23] for further reference.

3) Principles of Time-Dependent Perturbed Angular Correlation (TDPAC)

The basic idea of Time-Dependent Perturbed Angular Correlation (TDPAC) is the emission of two consecutive (within the order of nanoseconds) γ-γ rays (or e^--γ particle-ray) from the internal de-excitation of a probe nucleus. Due to the conservation of angular momentum, there is a correlation between the emission directions of the γ-γ rays (or e^--γ particle-ray). This way, TDPAC spectroscopy measures the precession of the angular correlation of the γ-γ rays (or e^--γ particle-ray).

We would start from the principle of γ-decay of the nucleus, followed by the introduction of the simple case of TDPAC, then the general case as outlined in Schatz's textbook [3] (Reproduced with permission; copyright retained under Wiley). We would rely mainly on the exposition of Butz's [23] in the general formalism for the general case of TDPAC, in which he had referred to Steffen et al. [26] for certain fundamental equations, for which we would refer to as well in this script (Reproduced with permission; copyright retained under Springer Nature). In addition, we would refer to the papers by Butz [23] and Steffen et al. [26] for a more thorough treatment not found in Schatz's textbook.

3.1) Nuclear γ-decay

We note that the content in this section is adapted from chapter 2.3 of Schatz's textbook [3], repurposed with permission and with copyright is retained under Wiley.

The heart of TDPAC lies in the γ-γ (or e^--γ) cascade of the decay of an excited probe nucleus. In this section, we will analyse and characterise such γ-rays.

We first state: From the field of nuclear physics, the quantum levels of nuclei are distinguished by a well-defined total angular momentum I and parity Π, for which we have exploited once for equation (2.32).

A γ-ray (quantum) is emitted when a nucleus undergoes a transition from a higher energy level to a lower energy level (This process is commonly termed "de-excitation"). By the conservation of energy, angular momentum, and parity, we have three fundamental relations:

Energy:

$$E_i = E_f + \hbar\omega, \tag{3.1a}$$

Angular momentum:

$$I_i = I_f + l, M_i = M_f + m, \tag{3.1b}$$

Parity:

$$\Pi_i = \Pi_f * \pi. \tag{3.1c}$$

That is, equation $(3.1a - 3.1c)$ states that when a nucleus undergoes a shift from an initial (higher energy) state (I_i, M_i, Π_i) to a final (lower energy) state (I_f, M_f, Π_f), a photon of energy $\hbar\omega$ with the quantum numbers (l, m, π) is emitted.

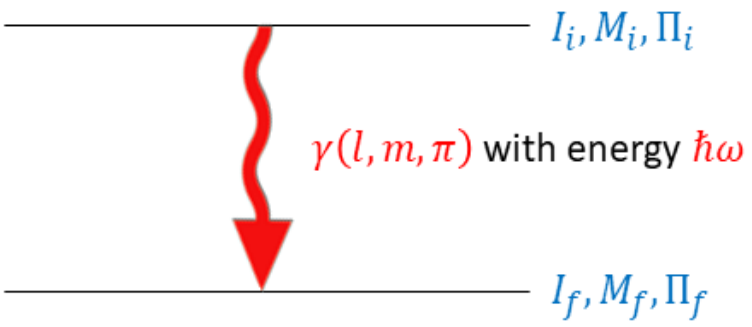


Figure 7: Schematic of a γ-decay from a higher to lower nucleus energy level. The figure is adapted from [3] as figure 2.5). Copyright retained under Wiley.

In classical electrodynamics, this photon emission (in a quantum mechanical sense) is analogous to creating an electromagnetic wave with energy $\hbar\omega$. The conservation of angular momentum and parity implies that the released electromagnetic wave must have a definite angular momentum m and parity π, similar to the case for the nuclear states.

Thus, we naturally will search for solutions to Maxwell's equations (in free space) written in the multipole radiation formalism, in which the angular momentum m and parity π are utilized as explicit terms.

In free space, the Maxwell equations, expressed in differential form, are (See Chapter 9.2 of [21]):

$$\nabla \times \vec{E} = -\frac{\partial \vec{B}}{\partial t}, \tag{3.2a}$$

$$\nabla \times \vec{B} = \frac{1}{c^2}\frac{\partial \vec{E}}{\partial t}, \tag{3.2b}$$

$$\nabla . \vec{E} = 0, \tag{3.2c}$$

$$\nabla . \vec{B} = 0. \tag{3.2d}$$

We note that $\vec{E}$ is the electric field, $\vec{B}$ is the magnetic field and c is the speed of light in a vacuum.

From either Chapter 9.2.2 of Griffith's textbook [21] or Chapter 9 of Jackson's textbook [27], we have the solution of a monochromatic plane wave:

$$\vec{E}(\vec{r}, t) = \widetilde{E_0} \exp\left(i\vec{k}.\vec{r} - i\omega t\right) \hat{n}, \tag{3.3a}$$

$$\vec{B}(\vec{r}, t) = \widetilde{B_0} \exp\left(i\vec{k}.\vec{r} - i\omega t\right) \left(\vec{k} \times \hat{n}\right). \tag{3.3b}$$

We note that $\widetilde{E_0}$ and $\widetilde{B_0}$ are fixed 3-component (possibly with complex entries) initial vectors of the $\vec{E}$ and $\vec{B}$ fields respectively, $\hat{n}$ is the polarisation unit vector and is parallel to $\vec{E}$, $\vec{k}$ is the propagation vector perpendicular to both $\vec{E}$ and $\vec{B}$ and $\omega = ck$.

Applying equation $(3.3a\ \&\ 3.3b)$ to equation $(3.2a - 3.2d)$:

$$\nabla \times \vec{E} = i\omega\vec{B} = ikc\vec{B}, \tag{3.4a}$$

$$\nabla \times \vec{B} = -\frac{i\omega}{c^2}\vec{E} = -\frac{ik}{c}\vec{B}. \tag{3.4b}$$

We recall a vector identity for an arbitrary vector $\vec{A}$:

$$\nabla \times \left(\nabla \times \vec{A}\right) = \nabla\left(\nabla . \vec{A}\right) - \nabla^2\vec{A}. \tag{3.5}$$

We note that ∇^2 is the Laplacian operator.

Applying equation (3.5) to equation $(3.2a - 3.2d)$ with the help of equation $(3.4a\ \&\ 3.4b)$, we have:

$$(\nabla^2 + k^2)\vec{E} = 0, \tag{3.6a}$$

$$(\nabla^2 + k^2)\vec{B} = 0. \tag{3.6b}$$

Equations $(3.6a\ \&\ 3.6b)$ are called the Helmholtz equations for $\vec{E}$ and $\vec{B}$. We note that our TDPAC setup exhibits spherical symmetry. Solving the Helmholtz equation in Spherical coordinates (Using methods as written in Peter Young's script [28]):

$$(\nabla^2 + k^2)\phi(r,\theta,\varphi) = 0 \Rightarrow \phi(r,\theta,\varphi) = \sum\nolimits_{l,m} f_l(kr)Y_{l,m}(\theta,\varphi)\,. \tag{3.7}$$

$f_l(kr)$ is the radial part of $\phi(r,\theta,\varphi)$ that is only dependent on r. Often called the spherical Bessel or Neumann functions, they are the solutions to the spherical Bessel's equation of order $(l + 1/2)$. We will not derive $f_l(kr)$ further, as it does not contribute to the angular dependence.

$Y_{l,m}(\theta,\varphi)$ are the spherical harmonics, which gives the Legendre polynomials in the case of $m = 0$.

We should also note that the solutions for $(3.6a\ \&\ 3.6b)$ are constrained by equations $(3.2c)$ and $(3.2d)$, respectively.

Jackson (Page 427 of [27]) has provided a neat solution for multipole fields, for which the electromagnetic wave (field) is expressed as a multipole of order (l, m). We introduce the spatial angular momentum vector:

$$\vec{L} = -ih(\vec{r} \times \nabla). \tag{3.8}$$

For an electric multipole of order (l, m), we have:

$$B_{l,m}^{(E)} = f_l(kr)\vec{L}Y_{l,m}(\theta,\varphi), \tag{3.9a}$$

$$E_{l,m}^{(E)} = \frac{ic}{k}\left(\nabla \times B_{l,m}^{(M)}\right). \tag{3.9b}$$

For a magnetic multipole of order (l, m), we have:

$$E_{l,m}^{(M)} = f_l(kr)\vec{L}Y_{l,m}(\theta, \varphi), \tag{3.10a}$$

$$B_{l,m}^{(M)} = -\frac{i}{ck}\left(\nabla \times E_{l,m}^{(E)}\right). \tag{3.10b}$$

We note that equations $(3.9a \,\&\, 3.9b)$ & $(3.10a \,\&\, 3.10b)$ are the radiation fields of oscillating 2^l-poles. We also note that the superscript "(E)" and "(M)" are used to distinguish the electric and magnetic multipoles from each other.

Bohr's correspondence will assert that the classical electrodynamics of electromagnetic radiation will have a quantum electrodynamics analogue, in which the quantum of γ-ray corresponding to a multipole radiation l will have an angular momentum of $\sqrt{l(l+1)}\hbar$ and a z-compoment $m\hbar$.

In particular, the quantum mechanics of multipole radiation obeys the general angular momentum algebra and hence, the addition of angular momenta.

Furthermore, these multipole fields have a well-defined parity:

For (E)-radiation:

$$\Pi = (-1)^l. \tag{3.11a}$$

For (M)-radiation:

$$\Pi = (-1)^{l+1}. \tag{3.11b}$$

Even more, the multipole transition must obey the angular momentum selection rules:

$$l = I_i + I_f, I_i + I_f - 1, \dots, \left|I_i - I_f\right| + 1, \left|I_i - I_f\right|. \tag{3.12}$$

We hence obtain the multipole transitions that are allowed under the selection rules, in which the transitions of the lower order(s) are shown in Table 1:

Angular Momentum Change ΔI		0 (No $0 \to 0$)	1	2	3
Parity Change	Yes	$E1$ $(M2)$	$E1$ $(M2)$	$M2$ $E3$	$E3$ $(M4)$
	No	$M1$ $E2$	$M1$ $E2$	$E2$ $(M3)$	$M3$ $E4$

Table 1: Allowed multipole transition for a given angular momentum and parity change. It was reproduced with permission from [3] as table 2.1. Copyright retained under Wiley.

Given specific radiation of a particular multipole order, the magnetic transition is usually much smaller as compared to the electric transitions, so $M(l+1)$ can be neglected as compared to $E(l)$, but often wise, $M(l)$ often has the same order of magnitude as $E(l+1)$.

3.2) Radial Angular Distribution

With the solutions of Maxwell's equations in the multipole from (See equations $(3.9a - 3.10b)$, we can calculate the angular distribution of the γ-rays.

We utilise the concept of Poynting's Theorem (Chapter 8.2 from ref [21]) and state the Poynting vector $\vec{S}$, which is defined to be the energy flux density of an electromagnetic wave:

$$\vec{S} = \frac{1}{\mu_0}(\vec{E} \times \vec{B}). \tag{3.13}$$

Since the distance between the detectors and the source is of a much higher magnitude as compared to the dimensions of the source (i.e., nuclear transitions on a nuclear scale), we can use the far-fetched solutions of $\vec{E}$ and $\vec{B}$:

$$\varepsilon_0 |\vec{E}|^2 = \frac{1}{\mu_0} |\vec{B}|^2. \tag{3.14}$$

As the speed of light, c is defined to be such that:

$$c^2 = \frac{1}{\mu_0 \varepsilon_0}, \tag{3.15}$$

we thus have:

$$|\vec{E}| = c|\vec{B}|, \tag{3.16}$$

and hence:

$$|\vec{S}| = \frac{c}{\mu_0} |\vec{B}|^2 = c\varepsilon_0 |\vec{E}|^2. \tag{3.17}$$

From Equation $(3.9a \ \& \ 3.9b)$ & $(3.10a \ \& \ 3.10b)$, we obtain:

$$|\vec{S}| = c\varepsilon_0 |\vec{E}|^2 \propto |\hat{L} Y_{l,m}(\theta, \varphi)|^2, \tag{3.18a}$$

$$|\vec{S}| = \frac{c}{\mu_0} |\vec{B}|^2 \propto |\hat{L} Y_{l,m}(\theta, \varphi)|^2. \tag{3.18b}$$

One observes that the electric and magnetic radiations of the same multipole order have the same angular pattern and are only distinguishable by polarisation measurement of such multipoles.

$|\hat{L} Y_{l,m}(\theta, \varphi)|$ is hence, of particular interest to us for TDPAC measurements. We will analyse it further.

The algebra for orbital angular momentum follows the Casimir algebra of general angular momentum, in which we have the equations $(2.2a \ \& \ 2.2b)$ in section 2.1. Furthermore, we want to use the ladder operators, which are equations $(2.45a \ \& \ 2.45b)$ and $(2.46a - 2.46c)$ in section 2.3.1. We would write them down here again in the case of $\hat{L}$:

$$\hat{L}_+ = \hat{L}_x + i\hat{L}_y, \tag{3.19a}$$

$$\hat{L}_- = \hat{L}_x - i\hat{L}_y. \tag{3.19b}$$

Again, we use equation $(2.48a \,\&\, 2.48b)$ in the eigenvector basis spanned by $\{|l,m\rangle\}$, with $m \in \{-l, -l+1, \dots, l-1, l\}$:

$$\hat{L}_\pm |l,m\rangle = \hbar\sqrt{l(l+1) - m(m\pm 1)}\,|l, m\pm 1\rangle, \tag{3.20a}$$

$$\hat{L}_z |l,m\rangle = m\hbar |l,m\rangle. \tag{3.20b}$$

Noting that $\hat{L}^2 = \hat{L}_x + \hat{L}_y + \hat{L}_z$:

$$\begin{aligned}
\left|\hat{L}Y_{l,m}(\theta,\varphi)\right|^2 &= \left|\hat{L}_x Y_{l,m}(\theta,\varphi)\right|^2 + \left|\hat{L}_y Y_{l,m}(\theta,\varphi)\right|^2 + \left|\hat{L}_z Y_{l,m}(\theta,\varphi)\right|^2 \\
&= \left|\frac{1}{2}\left(\hat{L}_+ + \hat{L}_-\right)Y_{l,m}(\theta,\varphi)\right|^2 + \left|\frac{1}{2i}\left(\hat{L}_+ - \hat{L}_-\right)Y_{l,m}(\theta,\varphi)\right|^2 + \left|\hat{L}_z Y_{l,m}(\theta,\varphi)\right|^2 \\
&= \frac{1}{2}\left|\hat{L}_+ Y_{l,m}(\theta,\varphi)\right|^2 + \frac{1}{2}\left|\hat{L}_- Y_{l,m}(\theta,\varphi)\right|^2 + \left|\hat{L}_z Y_{l,m}(\theta,\varphi)\right|^2 \\
&= \frac{1}{2}\left|\hat{L}_+ Y_{l,m}(\theta,\varphi)\right|\left|\hat{L}_+ Y_{l,m}(\theta,\varphi)\right|^* + \frac{1}{2}\left|\hat{L}_- Y_{l,m}(\theta,\varphi)\right|\left|\hat{L}_- Y_{l,m}(\theta,\varphi)\right|^* \\
&\quad + \left|\hat{L}_z Y_{l,m}(\theta,\varphi)\right|\left|\hat{L}_z Y_{l,m}(\theta,\varphi)\right|^*,
\end{aligned}$$

$$\begin{aligned}
\left|\hat{L}Y_{l,m}(\theta,\varphi)\right|^2 = \frac{1}{2}\Big(\hbar^2\big(l(l+1) - m(m+1)\big)\Big)\left|Y_{l,m+1}(\theta,\varphi)\right|^2 + \frac{1}{2}\Big(\hbar^2\big(l(l+1) - m(m-1)\big)\Big)\left|Y_{l,m-1}(\theta,\varphi)\right|^2 \\
+ m^2\hbar^2\left|Y_{l,m}(\theta,\varphi)\right|^2.
\end{aligned} \tag{3.21}$$

In the following equation, we refer to Chapter 7.3.5 of [19] and state the expansion of the product of spherical harmonics:

$$Y_{l_1,m_1}(\theta,\varphi)Y_{l_2,m_2}(\theta,\varphi) = \sum_{l'=|l_1-l_2|}^{l_1+l_2}\sum_{m'=|m_1-m_2|}^{|m_1-m_2|}\sqrt{\frac{(2l_1+1)(2l_2+1)}{4\pi(2l'+1)}}\langle l_1, l_2, 0,0|l',0\rangle\langle l_1, l_2, m_1, m_2|l', m'\rangle Y_{l',m'}(\theta,\varphi), \tag{3.22}$$

and note that the expansion coefficients $\langle l_1, l_2, m_1, m_2|l', m'\rangle$ are often called the Clebsch-Gordan coefficients, with the order of the indices following reference [19].

Since $\left|Y_{l,m}(\theta,\varphi)\right|^2 = Y^*_{l,m}(\theta,\varphi)Y_{l,m}(\theta,\varphi)$, and $Y^*_{l,m}(\theta,\varphi) = (-1)^m Y_{l,-m}(\theta,\varphi)$, we will replace the variables l_1, l_2, m_1, m_2:

$l_1 = l_2 \to l$,

$m_1 \to m, m_2 \to -m$.

Hence, we note that the summation indices m' trivially goes through 0:

$m' \to 0$,

and for conciseness, we relabel l':

$l' \to k$, with $k_{\max} = 2l$.

Thus, with the above considerations, equation (3.22) is reduced to:

$$\left|Y_{l,m}(\theta,\varphi)\right|^2 = \sum_k \frac{(2l+1)}{\sqrt{4\pi(2k+1)}}\langle l, l, 0,0|k,0\rangle\langle l, l, m, -m|k, 0\rangle Y_{k,0}(\theta,\varphi). \tag{3.23}$$

We note that:

$$Y_{k,0}(\theta,\varphi)=\sqrt{\frac{2k+1}{4\pi}}P_k(\cos\theta), \tag{3.24}$$

where $P_k(x)$ are the Legendre polynomials, with $k\in\mathbb{N}$. It is consistent with our definition of l' in equation (3.22), where $l'\in\mathbb{N}$.

We use the Wigner $3j$-symbols in place of the Clebsch-Gordan coefficients:

$$\begin{pmatrix} j_1 & j_2 & j_3 \\ m_1 & m_2 & m_3 \end{pmatrix}=\frac{(-1)^{j_1-j_2-m_3}}{\sqrt{2j_3+1}}\langle j_1,j_2,m_1,m_2|j_3,-m_3\rangle, \tag{3.25a}$$

$$\langle j_1,j_2,m_1,m_2|j_3,m_3\rangle=(-1)^{-j_1+j_2+m_3}\sqrt{2j_3+1}\begin{pmatrix} j_1 & j_2 & j_3 \\ m_1 & m_2 & m_3 \end{pmatrix}. \tag{3.25b}$$

We thus have:

$$\left|Y_{l,m}(\theta,\varphi)\right|^2$$

$$=\sum_k\frac{(2l+1)}{\sqrt{4\pi(2k+1)}}(-1)^0\sqrt{2k+1}\begin{pmatrix} l & l & k \\ 0 & 0 & 0 \end{pmatrix}(-1)^0\sqrt{2k+1}\begin{pmatrix} l & l & k \\ m & -m & 0 \end{pmatrix}\sqrt{\frac{2k+1}{4\pi}}P_k(\cos\theta),$$

$$\left|Y_{l,m}(\theta,\varphi)\right|^2=\sum_k\frac{(2l+1)}{4\pi}(2k+1)\begin{pmatrix} l & l & k \\ 0 & 0 & 0 \end{pmatrix}\begin{pmatrix} l & l & k \\ m & -m & 0 \end{pmatrix}P_k(\cos\theta). \tag{3.26}$$

We note in advance that the 4π term in equation (3.26) is related to the solid angle of a unit sphere, in which we have integrated φ from 0 to 2π. Hence, there is no φ dependence on the right-hand side of the equation (3.26).

Equation (3.26) allows us to define the normalised angular distributions:

$$F_{l,m}(\theta)=\frac{\left|\hat{L}Y_{l,m}(\theta,\varphi)\right|^2}{\sum_m\left|\hat{L}Y_{l,m}(\theta,\varphi)\right|^2}. \tag{3.27}$$

Equation (3.27) is also the result of the integration over the whole of $\varphi\in[0,2\pi]$, and consequently, there is no dependence on φ.

Furthermore, from the properties of the $3j$- symbols, the following constraints are applied to k:

$$k\le 2l, k\in 2\mathbb{Z}. \tag{3.28}$$

Equation (3.28) stems from equation (3.22), where it is explicitly stated that $k_{\max}=2l$, alongside the fact that $\begin{pmatrix} l & l & k \\ 0 & 0 & 0 \end{pmatrix}=0$ if $k\in 2\mathbb{Z}+1$.

As $\left|\vec{S}\right|\propto\left|\hat{L}Y_{l,m}(\theta,\varphi)\right|^2$ from equation ($3.18a$ & $3.18b$), we can immediately observe that $F_{l,m}(\theta)$ follows the probability distribution of the photon γ in the direction of θ. Table 2 and

Figure 8 below show a graphical plot of $F_{l,m}(\theta)$ (Equation 3.28) for dipoles and quadrupoles, along with their distribution functions with respect to θ:

	$m = 0$	$m = \pm 1$	$m = \pm 2$
$l = 1$ (dipole)	$\frac{1}{2}\sin^2\theta$	$\frac{1}{4}(1 + \cos^2\theta)$	–
$l = 2$ (quadrupole)	$\frac{3}{2}\sin^2\theta\cos^2\theta$	$\frac{1}{4}(1 - 3\cos^2\theta + 4\cos^4\theta)$	$\frac{1}{4}(1 - \cos^4\theta)$

Table 2: This table shows the Angular distribution functions $F_{l,m}(\theta)$ for dipole and quadrupole transition. It was reproduced with permission from [3] as Table 2.2. Copyright retained under Wiley.

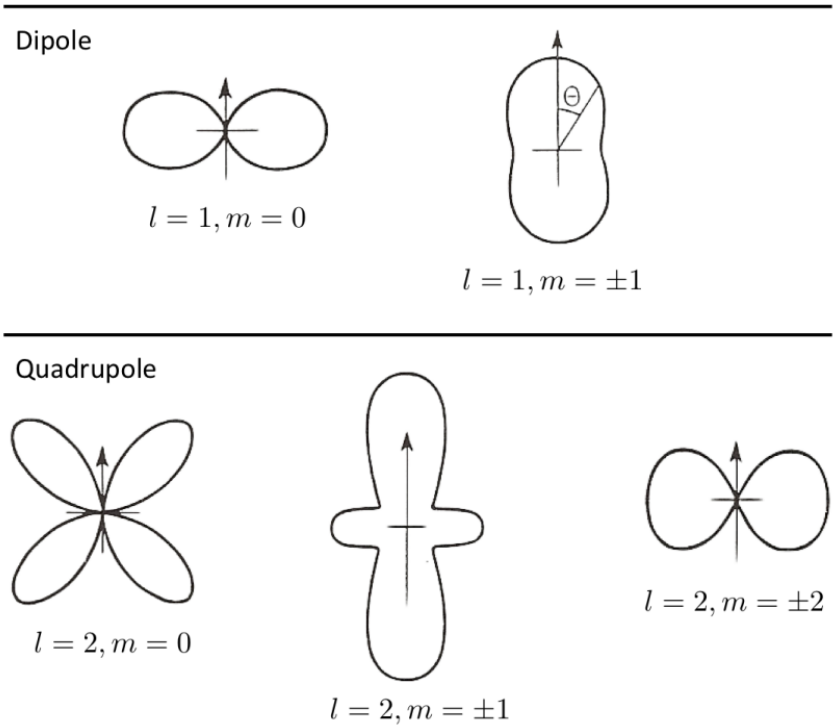


Figure 8: This figure shows the graphical emission patterns of pure dipole and quadrupole transitions. The horizontal line represents the x-y plane, while the vertical line represents the z-axis. They were reproduced with permission from [3] as figure 2.6). Copyright retained under Wiley.

To conclude this section, we also note that $F_{l,m}(\theta)$ has certain symmetries and properties [3]:

1) $\sum_m F_{l,m}(\theta) = 1$, i.e., $F_{l,m}(\theta)$ is isotropic over the sum of all m.
2) $F_{l,m}(\theta) = F_{l,-m}(\theta)$, i.e. $F_{l,m}(\theta)$ is symmetric in m.
3) $F_{l,m}(\theta) = F_{l,m}(\pi - \theta)$, i.e. $F_{l,m}(\theta)$ exhibits mirror symmetry in the x-y plane.
4) $F_{l,m}(\theta = 0°) = 0$ for $m \neq \pm 1$.

3.3) Theory for Unperturbed $\gamma - \gamma$ Angular Correlation

Now that we have introduced equations (3.26) and (3.27), developing the angular correlation and the probabilistic distribution of the emission direction of a photon, we can start to develop the fundamental concepts of TDPAC.

We would refer to Chapter 5.1 of Schatz's textbook [3] (Reproduced with permission; copyright retained under Wiley, respectively).

The fundamental essence of a $\gamma-\gamma$ TDPAC is the angular correlation measurement of the consecutive γ emission from the same source (Usually on the time order of ns). Consider a scenario (See Figure 9), in which we have a nuclear state $|I_i, M_i\rangle$ that undergoes the first γ decay into the intermediate state $|I, M\rangle$ and then into the final state $|I_f, M_f\rangle$ by the second γ decay. We call these two emissions γ_1 and γ_2.

Photon γ_1, having the properties of multipolarity l_1 and projection m_1, is detected in a fixed direction and photon γ_2, having multipolarity l_2 and m_2, is detected in a polar (θ)-free detector (in the direction of $\hat{\theta}$). Since θ is the only free parameter, we have the coincidence count rate as the function of θ, which would ultimately lead to the angular correlation between γ_1 and γ_2.

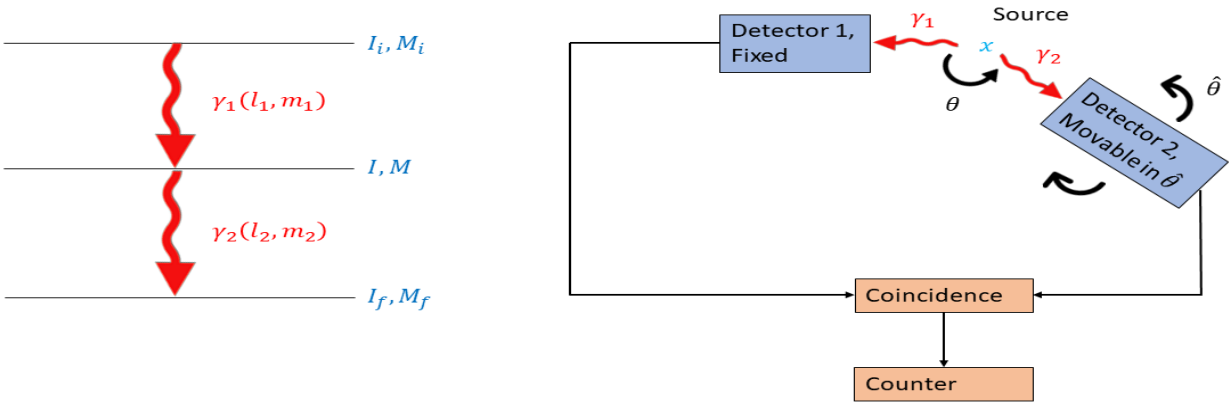


Figure 9: Schematic diagram of the $\gamma-\gamma$ decay and the basic PAC principle with apparatus. It was adapted from [3] as Figure 5.1). Copyright retained under Wiley.

3.3.1) Special case in which the z-axis is aligned with detector 1 and with only a single multipole transition

We note that the content in this section is adapted from chapter 5.1.1 of Schatz's textbook [3], repurposed with permission and with copyright is retained under Wiley.

We assume an equal M-state occupation in the initial nuclear state $|I_i, M_i\rangle$. The population $P(M)$ of the M substate in the intermediate state $|I, M\rangle$ is given by:

$$P(M) = \sum_{M_i} G(M_i \to M) F_{l_1, m_1}(\theta_1)\,. \tag{3.29}$$

$F_{l,m}(\theta)$ gives the angular distribution probabilistic function as defined in equation (3.27). For a quantum of γ-ray having multipolarity l_1 and $m_1 = M_i - M$, $F_{l_1, m_1}(\theta_1)$ measures the probability that γ_1 would be emitted at an angle θ_1 with respect to the z-axis.

$G(M_i \to M)$, as the integrated rate for the transition between $|I_i, M_i\rangle$ to $|I, M\rangle$, could be written in the angular momentum coupling formalism. With the help of Wigner-Eckart's Theorem (See Appendix 3 of [3]), we can write:

$$G(M_i \to M) = \left|\langle I, M | \mathcal{M}_{l_1, m_1} | I_i, M_i \rangle\right|^2 = \left|\langle I_i, M_i | \mathcal{M}_{l_1, m_1} | I, M \rangle\right|^2,$$

$$G(M_i \to M) = \begin{pmatrix} I_i & l_1 & I \\ -M_i & m_1 & M \end{pmatrix}^2 \langle I || \mathcal{M}_{l_1} || I_i \rangle^2, \tag{3.30}$$

where $\mathcal{M}_{l_1,m_1}$ is the multipole operator for the multipole γ-ray with orders l_1 and m_1, as reflected in equations $(3.9a\ \&\ 3.9b)$ & $(3.10a\ \&\ 3.10b)$. As mentioned in section 2.2, $\langle I||\mathcal{M}_{l_1}||I_i\rangle^2$ is the dynamical (reduced) matrix element that is not dependent on the geometry of the system, i.e., it is an intrinsic element that is only dependent on I. It will be of the same value for all transitions between $|I_i, M_i\rangle$ to $|I, M\rangle$.

Therefore, we can reduce equation (3.30) to:

$$G(M_i \to M) \propto \begin{pmatrix} I_i & l_1 & I \\ -M_i & m_1 & M \end{pmatrix}^2 . \tag{3.31}$$

For this special case, we align the z-axis with the emission direction of γ_1, such that $\theta_1 = 0$. Then $m_1 = \pm 1$, since $\forall m \neq \pm 1, F_{l,m}(0°) = 0$. Thus, we have reduced the equation (3.29) to:

$$P(M) \propto \sum_{M_i} \begin{pmatrix} I_i & l_1 & I \\ -M_i & \pm 1 & M \end{pmatrix}^2 F_{l,\pm 1}(0°) . \tag{3.32}$$

The above equation implies that the substates of the intermediate state $|I, M\rangle$ are not equally populated since the transition for $m_1 \neq \pm 1$ is prohibited. Hence, $P(M) \neq P(M')$ in general and $|I, M\rangle$ can be aligned. However, we note that overall, the intermediate state is not polarised, as $P(M) = P(-M)$.

Alignment of the intermediate state $|I, M\rangle$ further implies that the emission pattern of γ_2 is not isotropic, and it has a θ dependence. Since the detection of γ_1 determines the alignment of the intermediate nuclear state $|I, M\rangle$, γ_1 and γ_2 must be measured in coincidence (consecutively).

The emission with γ_2 (in coincidence with γ_1) has the following angular dependence:

$$W(\theta) \propto \sum_{M,M_f} P(M) G\big(M \to M_f\big) F_{l_2,m_2}(\theta) . \tag{3.33}$$

θ, as found in equation (3.33), is the angle that the emission direction of γ_2 makes with that of γ_1 (and hence $\hat{z}$).

For the second γ ray emission, as mentioned in the above two paragraphs, we have no equal values of $P(M)$ for all values of M. Hence, by substituting equation (3.32) alongside the $\big(M \to M_f\big)$ analogue of equation (3.31) into equation (3.33), we finally have:

$$W(\theta) \propto \sum_{M_i,M,M_f} \begin{pmatrix} I_i & l_1 & I \\ -M_i & \pm 1 & M \end{pmatrix}^2 F_{l,\pm 1}(0°) \begin{pmatrix} I & l_2 & I_f \\ -M & m_2 & M_f \end{pmatrix}^2 F_{l_2,m_2}(\theta) . \tag{3.34}$$

We note that the angular dependence $W(\theta)$ as reflected in equation (3.34), only has an explicit dependence on θ.

In essence, we can sweep detector 2 through $\theta \in [0, 2\pi]$ and determine the angular dependence $W(\theta)$. In practice, though, we need to further refine the theory as:

1) In experiments, we do often see transitions that involve more than a single multipole (i.e. more than just a single l_1 value). Therefore, there will be interferences in the γ-ray emissions, and we must include in the amplitudes (arising from the reduced matrix element $\langle I||\mathcal{M}_{l_1}||I_i\rangle^2$) in our calculation of $W(\theta)$.
2) The unique choice of the alignment of the z-axis to the emission direction of γ_1 makes it challenging to introduce a perturbation in the form of an external magnetic or electric field. We would ideally want to free up the z-axis.
3) Even in the case of pure multipole transitions (i.e., only a single l_1 value), perturbations from the environment induce interferences in the transitions. Therefore, transition amplitudes need to be adequately accounted for in our theory of PAC.

Even though there are severe limitations in this particular case of PAC, it illustrates that, in principle, the angular correlation between two successive γ-rays is an observable quantity, and we can understand the basic gist of angular correlation with a pure multipole transition and with a unique choice of axis. The following section will free up this choice of particular axis and allow for multiple multipole transitions, which will serve as the backbone of our current TDPAC setups.

3.3.2) General case of PAC

In this section, we will follow the exposition by Butz [23] and from section 5.1.2 of Schatz [3] (Reproduced with permission; copyright retained under Springer Nature and Wiley, respectively).

We free up the choice of coordinate system as compared to section 3.3.1. Thus, the emissions of γ_1 and γ_2 are treated in an arbitrary choice of spherical coordinates θ_1, φ_1 and θ_2, φ_2 respectively (See Figure 10).

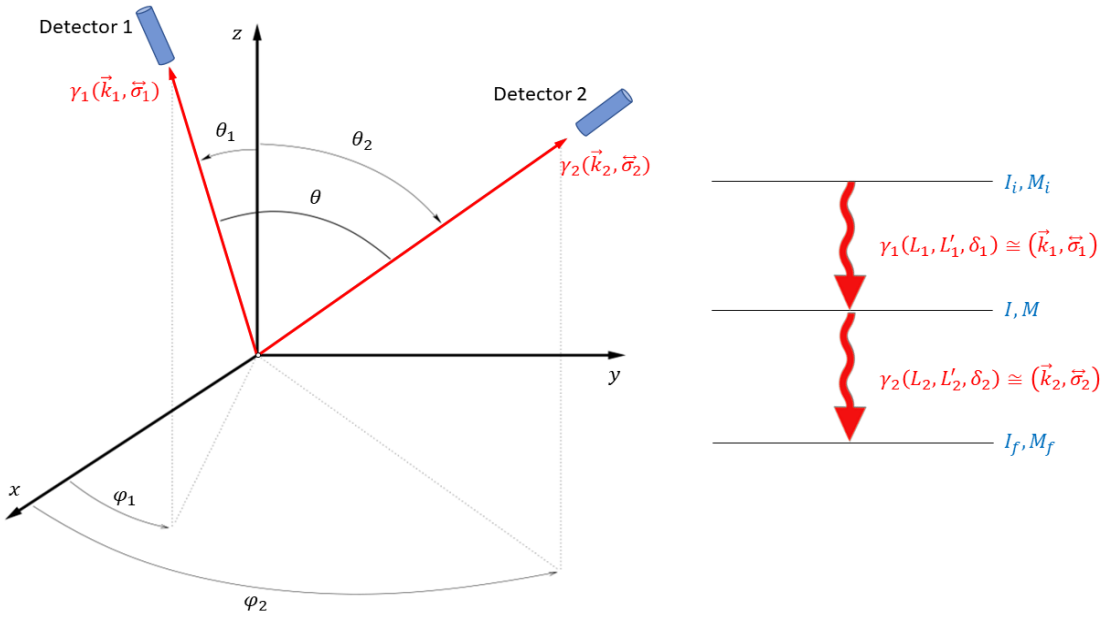


Figure 10: Schematic representation of the γ-γ cascade in the generalised coordinate system. We note that θ is the angle between the two γ-quanta. $\vec{k}_1, \vec{\sigma}_1$ and $\vec{k}_2, \vec{\sigma}_2$, are the wave vectors and polarisation of γ_1 and γ_2 respectively. $(\vec{k}_1, \vec{\sigma}_1)$ is analogous to (L_1, L_1', σ_1), which are the multipolarities (L, L'), with a mixing ratio σ_1. Likewise, $(\vec{k}_2, \vec{\sigma}_2)$ is analogous to (L_2, L_2', σ_2). Adopted from [3] as figure 5.5 (left) and 5.6 (right). Copyright is retained under Wiley.

The transitional amplitudes for the γ-quanta from the initial state to the intermediate state and for the intermediate state to the final state are determined respectively by:

$$\langle I, M, \vec{k}_1, \vec{\sigma}_1 | \mathcal{H}_1 | I_i, M_i \rangle \tag{3.35a}$$

$$\langle I_f, M_f, \vec{k}_2, \vec{\sigma}_2 | \mathcal{H}_2 | I, M \rangle \tag{3.35b}$$

$\vec{k}_1, \vec{\sigma}_1$ are the wave vector and polarisation of γ_1 and $\vec{k}_2, \vec{\sigma}_2$ are the wave vector and polarisation of γ_2. $\mathcal{H}_1$ and $\mathcal{H}_2$ are the Hamiltonian interaction operators for the emission of γ_1 and γ_2 respectively.

The angular correlation for a specific set of transition $(\vec{k}_1, \vec{\sigma}_1)$ and $(\vec{k}_2, \vec{\sigma}_2)$ from $|I_i, M_i\rangle$ to $|I_f, M_f\rangle$ follows from equation $(3.35a \ \& \ 3.35b)$:

$$W(M_i \to M_f) = \left| \sum_M \langle I_f, M_f, \vec{k}_2, \vec{\sigma}_2 | \mathcal{H}_2 | I, M \rangle \langle I, M, \vec{k}_1, \vec{\sigma}_1 | \mathcal{H}_1 | I_i, M_i \rangle \right|^2 \tag{3.36}$$

Since the intermediate state $|I, M\rangle$ is not observed directly, we need to sum the transitional amplitudes all over the possible substates $M \in \{-I, -I+1, \dots, I-1, I\}$, which was glossed over for the particular case in section 3.3.1 due to our special choice of axis.

Note that we also sum the probabilities over M_i and M_f instead of the amplitudes, as the polarisations of γ_1 with $|I_i, M_i\rangle$ and of γ_2 with $|I_f, M_f\rangle$, are observables. With that in mind, we can sum up over the initial set of values $M_i \in \{-I_i, -I_i+1, \dots, I_i-1, I_i\}$ and $M_f \in \{-I_f, -I_f+1, \dots, I_f-1, I_f\}$, with all possible values of $(\vec{k}_1, \vec{\sigma}_1)$ and $(\vec{k}_2, \vec{\sigma}_2)$, giving us the angular correlation:

$$W(\vec{k}_1, \vec{k}_2) = \sum_{M_i, M_f, \vec{\sigma}_1, \vec{\sigma}_2} \left| \sum_M \langle I_f, M_f, \vec{k}_2, \vec{\sigma}_2 | \mathcal{H}_2 | I, M \rangle \langle I, M, \vec{k}_1, \vec{\sigma}_1 | \mathcal{H}_1 | I_i, M_i \rangle \right|^2 . \tag{3.37}$$

Frauenfelder and Steffen [29,30] calculated the matrix elements and summed them to obtain a simplified form of $W(\vec{k}_1, \vec{k}_2)$ with a θ dependence:

$$W(\vec{k}_1, \vec{k}_2) = W(\theta) = \sum_{k, k \ even}^{k_{max}} A_k(\gamma_1) A_k(\gamma_2) P_k(\cos\theta) . \tag{3.38}$$

We note that the wave vector and polarisation $\vec{k}_i, \vec{\sigma}_i$ are hidden in the $A_k(\gamma_i)$ parameter. For more accessible literature that elaborates on the nature of $A_k(\gamma_i)$, the reader is encouraged to look at the master's thesis by Barbosa [31].

θ is the angle that the emission direction of γ_1 makes with the emission direction of γ_2. We note that the quantum numbers of $\vec{k}_1$ and $\vec{k}_2$, denoted k_1 and k_2, only accepts even numbers as a consequence of the parity conservation of the electromagnetic interaction responsible for the γ emission [23]. We have seen the flavour of this statement in section 3.2, under equation (3.28). $P_k(x)$ is the Legendre Polynomial of order k.

Hence, we have the summation of k over even values and that:

$$0 \leq k \leq \min(2I, L_1 + L_1', L_2 + L_2') = k_{\max}. \tag{3.39}$$

We note that I is the spin of the intermediate state, (L_1, L_1', δ_1) are the analogous quantum numbers, which are their multipole quantum number (L_1, L_1'), along with their mixing ratio δ_1, to the emission of the first γ-ray with $\left(\vec{k}_1, \vec{\sigma}_1\right)$. (L_2, L_2', δ_2) are the analogous quantum numbers, which are their multipole quantum number (L_2, L_2'), along with their mixing ratio δ_2, to the emission of the second γ-ray with $\left(\vec{k}_2, \vec{\sigma}_2\right)$.

The orientation coefficient $A_{k_1}(\gamma_1)$, which depends on the first γ-ray transition, is given by [23]:

$$A_{k_1}(\gamma_1) = \frac{\left\{F_{k_1}(L_1, L_1; I_i, I) + (-1)^{L_1 - L_1'} 2\delta_1 F_{k_1}(L_1, L_1'; I_i, I) + \delta_1^2 F_{k_1}(L_1', L_1'; I_i, I)\right\}}{1 + \delta_1^2}. \quad (3.40)$$

The correlation coefficients $A_{k_2}(\gamma_2)$, which depends only on the second γ-ray transition, is given by [23]:

$$A_{k_2}(\gamma_2) = \frac{\left\{F_{k_2}\left(L_2, L_2; I_f, I\right) + 2\delta_2 F_{k_2}\left(L_2, L_2'; I_f, I\right) + \delta_2^2 F_{k_2}\left(L_2', L_2'; I_f, I\right)\right\}}{1 + \delta_2^2}. \quad (3.41)$$

The monstrous F_k coefficients are defined by:

$$F_k(L, L'; I', I) = (-1)^{I + I' - 1}\sqrt{(2L+1)(2L'+1)(2k+1)(2I+1)} \times \begin{pmatrix} L & L' & k \\ 1 & -1 & 0 \end{pmatrix} \begin{Bmatrix} I & I & k \\ L' & L & I' \end{Bmatrix}. \quad (3.42)$$

$\begin{pmatrix} j_1 & j_2 & j_3 \\ m_1 & m_2 & m_3 \end{pmatrix}$ is the Wigner $3j$-symbol and is defined in their Clebsch-Gordan coefficient form as seen in Section 3.2, equation $(3.25a)$.

$\begin{Bmatrix} j_1 & j_2 & j_3 \\ j_4 & j_5 & j_6 \end{Bmatrix}$ is the Wigner $6j$-symbol, and is defined as the sum over products of four $3j$-symbols:

$$\begin{Bmatrix} j_1 & j_2 & j_3 \\ j_4 & j_5 & j_6 \end{Bmatrix} = \sum\nolimits_{m_1, \ldots, m_6} (-1)^{\sum_{k=1}^{6}(j_k - m_k)} \begin{pmatrix} j_1 & j_2 & j_3 \\ -m_1 & -m_2 & -m_3 \end{pmatrix} \begin{pmatrix} j_1 & j_5 & j_6 \\ m_1 & -m_5 & m_6 \end{pmatrix} \times \begin{pmatrix} j_4 & j_2 & j_6 \\ m_4 & m_2 & -m_6 \end{pmatrix} \begin{pmatrix} j_4 & j_5 & j_3 \\ -m_4 & m_5 & m_3 \end{pmatrix}. \quad (3.43)$$

The summation over all six m_i's is regulated by the selection rules of the $3j$-symbols.

As this script is not a theoretical thesis, we would stop our analysis here and refer to the tabulated form by either Yamazaki [32] or Ferguson [33].

A side remark: To this point, we have only considered the case that the unequal population of the substates $|I, M\rangle$ purely arises from the detection of the γ_1-ray. This phenomenon might not be the only possibility/source [3]. For example, the temperature of the environment might affect the population of the substates for instance.

In the general case, we might want to take the density matrix approach, with our angular correlation $W\left(\vec{k}_1, \vec{k}_2\right)$ being written as [3]:

$$W(\vec{k}_1, \vec{k}_2) = W(\theta) = \sum_{k,k\ even}^{k_{max}} \rho_k(I) A_k(\gamma_2) P_k(\cos\theta)\,, \tag{3.44}$$

with the statistical tensor:

$$\rho_k(I) = \sqrt{(2k+1)(2I+1)} \sum_M (-1)^{I-M} \begin{pmatrix} I & I & k \\ M & -M & 0 \end{pmatrix} P(M) \tag{3.45}$$

The $P(M)$'s are the probabilities that are first introduced in section 3.3.1, under equation (3.29). If $P(M)$ is entirely determined by the detection of the first γ ray, then $\rho_k(I) = A_k(\gamma_1)$.

3.4) Theory of Time-Dependent Perturbed Angular Correlation (TDPAC)

Finally, we introduce either an external electric/magnetic interaction and assume that the initial population of the substates $|I, M\rangle$ purely arises from the emission of the γ_1 ray. Within the time t that elapsed between the emission of the γ_1 ray and the subsequent γ_2 ray (related to the lifetime τ_N of the intermediate state), there will be a repopulation of the intermediate substates or a phase change of $|I, M\rangle$. The experimental measurement of such a correlation between the two successive γ-emissions probes precisely the effects of the external interaction on $|I, M\rangle$ and subsequently allows us to study the local electric/magnetic environment of the host lattice that surrounds the probe atom.

3.4.1) TDPAC Angular Correlation $W(\vec{k}_1, \vec{k}_2, t)$

We note that the content in this section is adapted from chapter 5.2 of Schatz's textbook [3], repurposed with permission and with copyright is retained under Wiley.

To distinguish the intermediate states $|I, M\rangle$ in which the external interaction, $\Lambda(t)$ will act on, we denote $|I, M_a\rangle$ as the intermediate state right after the emission of the γ_1 ray, and $|I, M_b\rangle$ to be the intermediate state right before the emission of the γ_2 ray (Refer to Figure 11).

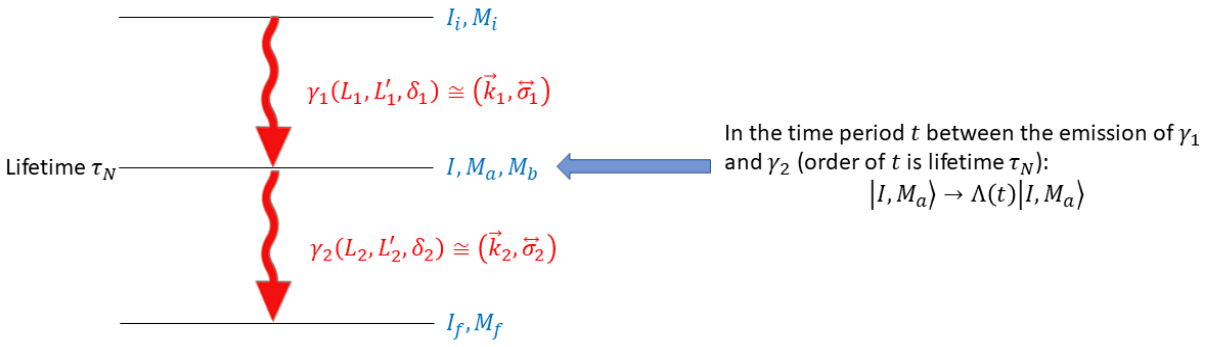


Figure 11: The γ-cascade with a mean lifetime τ_N in the intermediate state. During the lifetime of the intermediate state, the external hyperfine interaction operator, $\Lambda(t)$, will induce a repopulation or the phase change of $|I, M_a\rangle$. Adapted from [3] as figure 5.7. Copyright is retained under Wiley.

The influence of the time-development operator induced by the external magnetic or electrical interaction, $\Lambda(t)$ is given by:

$$|I, M_a\rangle \rightarrow \Lambda(t)|I, M_a\rangle = \sum_{M_b} |I, M_b\rangle\langle I, M_b|\Lambda(t)|I, M_a\rangle\,. \tag{3.46}$$

$|I, M_a\rangle$ is the initial intermediate substate and $|I, M_b\rangle$'s are the sublevels that arise from the interaction of $\Lambda(t)$ on $|I, M_a\rangle$. From basic quantum mechanics, $\sum_{M_b}|I, M_b\rangle\langle I, M_b| = \overleftrightarrow{Id}$. We also note that $\Lambda(0) = \overleftrightarrow{Id}$.

We want to construct the time-dependent interaction analogue of equation (3.36), which describes the angular correlation for a vanishing perturbation. We would need to consider the effects of $\Lambda(t)$, which changes the population of the intermediate substates in the time t between the emission of the two γ-rays (Replacing $|I, M\rangle$ in equation (3.36) with $\Lambda(t)|I, M\rangle$ essentially):

$$W(\vec{k}_1, \vec{k}_2, t) = \sum_{\substack{M_i, M_f, \\ \overleftrightarrow{\sigma}_1, \overleftrightarrow{\sigma}_2}} \left| \sum_{M_a} \langle I_f, M_f, \vec{k}_2, \overleftrightarrow{\sigma}_2 | \mathcal{H}_2 \Lambda(t) | I, M_a \rangle \langle I, M, \vec{k}_1, \overleftrightarrow{\sigma}_1 | \mathcal{H}_1 | I_i, M_i \rangle \right|^2 . \quad (3.47)$$

Applying equation (3.46) into equation (3.47) and expanding the square terms with M, M' gives:

$$W(\vec{k}_1, \vec{k}_2, t) \quad (3.48)$$
$$= \sum_{\substack{M_i, M_f, \overleftrightarrow{\sigma}_1, \overleftrightarrow{\sigma}_2 \\ M_a, M_a', M_b, M_b'}} \begin{pmatrix} \langle I_f, M_f, \vec{k}_2, \overleftrightarrow{\sigma}_2 | \mathcal{H}_2 | I, M_b \rangle \langle I, M_b | \Lambda(t) | I, M_a \rangle \langle I, M_a, \vec{k}_1, \overleftrightarrow{\sigma}_1 | \mathcal{H}_1 | I_i, M_i \rangle \\ \times \langle I_f, M_f, \vec{k}_2, \overleftrightarrow{\sigma}_2 | \mathcal{H}_2 | I, M_b' \rangle^* \langle I, M_b' | \Lambda(t) | I, M_a' \rangle^* \langle I, M_a', \vec{k}_1, \overleftrightarrow{\sigma}_1 | \mathcal{H}_1 | I_i, M_i \rangle^* \end{pmatrix}.$$

A tedious evaluation of the individual matrix elements will return the final form of the time-dependent perturbed angular correlation of the γ-γ cascade:

$$W(\vec{k}_1, \vec{k}_2, t) = N \sum_{k_1, k_2 \, even} \begin{pmatrix} A_{k_1}(\gamma_1) A_{k_2}(\gamma_2) \dfrac{1}{\sqrt{(2k_1+1)(2k_2+1)}} \\ \times \sum_{N_1, N_2} G_{k_1, k_2}^{N_1, N_2}(t) Y_{k_1, N_1}^*(\theta_1, \varphi_1) Y_{k_2, N_2}(\theta_2, \varphi_2) \end{pmatrix}. \quad (3.49)$$

N is the normalisation coefficient, $A_{k_1}(\gamma_1)$ and $A_{k_2}(\gamma_2)$ are the orientation and correlation coefficients as defined via equations (3.40) and (3.41), and $Y_{k,N}(\theta, \varphi)$ are the spherical harmonics and are related to the multipoles of order (k, N) (See section 3.1).

As usual, we have the summation of k_i over even values and that the accepted values of k_i are such that $0 \leq k_i \leq \min(2I, L_i + L_i')$. Furthermore, the summation of N_i is such that N_i takes in the values of $\{0,2, \ldots, k_i\}$.

The influence of the perturbation factor $\Lambda(t)$ on the intermediate nuclear state is captured in the expression $G_{k_1, k_2}^{N_1, N_2}(t)$, called the single crystal perturbation factor and is defined as:

$$G_{k_1, k_2}^{N_1, N_2}(t) = \sum_{M_a, M_b} \begin{pmatrix} (-1)^{2I + M_a + M_b} \sqrt{(2k_1+1)(2k_2+1)} \begin{pmatrix} I & I & k_1 \\ M_a' & -M_a & N_1 \end{pmatrix} \\ \times \begin{pmatrix} I & I & k_2 \\ M_b' & -M_b & N_2 \end{pmatrix} \langle I, M_b | \Lambda(t) | I, M_a \rangle \langle I, M_b' | \Lambda(t) | I, M_a' \rangle^* \end{pmatrix} \quad (3.50)$$

The sum in equation (3.50) is run over $-I \leq M_a, M_b \leq I$. The $3j$-symbols are zero unless $M_a' - M_a + N_1 = 0$ and $M_b' - M_b + N_2 = 0$, which then uniquely defines M_a' and M_b'. Hence, we can drop M_a' and M_b' [23].

For accessible literature that derives equations $(3.49\ \&\ 3.50)$ from first principles, the reader is referred to the master's thesis by Barbosa [31] again.

In the polycrystalline sample, we can obtain a simple expression based on θ, where θ is the angle between the emission direction of γ_1 and γ_2 [29,30]:

$$W(\theta, t) = N \sum_{k\ even} A_k(\gamma_1) A_k(\gamma_2) G_{kk}(t)\,. \tag{3.51}$$

$P_k(x)$ are the Legendre polynomials of order k.

$G_{kk}(t)$, termed as the powder perturbation function, is being defined as [23]:

$$G_{kk}(t) = (2k+1)^{-1} \sum_{N=-k\,,k\ even}^{k} G_{kk}^{NN}(t)\,. \tag{3.52}$$

Equation (3.52) is obtained by averaging equation (3.49) over all $\theta_1, \theta_2, \varphi_1, \varphi_2$ [29,30], and it is often called "statistical distribution of electric field gradient orientations" [23].

3.4.2) Analysis of the interaction Hamiltonian $\widehat{H}_I$

We note that the content in this section is adapted from the paper from Butz, T. [23], adapted with permission and with copyright is retained under Springer Nature.

Given a time-independent Hamiltonian $\widehat{H}_I$, the time evolution operator is written as:

$$\Lambda(t) = \exp\left(\frac{-i\widehat{H}_I t}{\hbar}\right). \tag{3.53}$$

We note that $\widehat{H}_I$ is the Hamiltonian describing the coupling of the intermediate nuclear state with the external magnetic/electric field arising from its environment via its nuclear dipole or quadrupole moment. We have explored this phenomenon in chapter 2.

Under the assumption that we have either magnetic interactions or axially symmetric quadrupole interactions: $\widehat{H}_I$ is diagonal, and we have our time evolution matrix elements can be written as:

$$\langle I, M_b | \Lambda(t) | I, M_a \rangle = \exp\left(\frac{-iE_M t}{\hbar}\right) \delta_{M,M_a} \delta_{M,M_b}, \tag{3.54a}$$

$$\langle I, M_b' | \Lambda(t) | I, M_a' \rangle = \exp\left(\frac{-iE_{M'} t}{\hbar}\right) \delta_{M',M_a'} \delta_{M',M_b'}. \tag{3.54b}$$

E_M are the eigenvalues of $\widehat{H}_I$ (Read $(M,M)^{th}$ element of the diagonal matrix $\overleftrightarrow{H}_I$).

Thus, with the assumption mentioned above, equation (3.50) is reduced to:

$$G_{k_1,k_2}^{N_1,N_2}(t) \tag{3.55}$$
$$= \sum_M \sqrt{(2k_1+1)(2k_2+1)} \begin{pmatrix} I & I & k_1 \\ M' & -M & N \end{pmatrix} \begin{pmatrix} I & I & k_2 \\ M' & -M & N \end{pmatrix} \exp\left(\frac{-i(E_M - E_{M'})t}{\hbar}\right).$$

We note that the Axial symmetry of such a system assures $N_1 = N_2 = N$, but does not guarantee that $k_1 = k_2$.

Unfortunately, our TDPAC experiment does not assume an axial symmetry, and hence we have a non-diagonal $\widehat{H}_I$. Following standard procedures in Linear Algebra: as the null space of $\widehat{H}_I = \{0\}$, and $\widehat{H}_I$ is Hermitian, we assert that there is a unitary matrix $\vec{\vec{U}}$ that diagonalises $\vec{\vec{H}}_I$:

$$\vec{\vec{U}}^{-1}\vec{\vec{H}}_I\vec{\vec{U}} = \vec{\vec{U}}^{T}\vec{\vec{H}}_I\vec{\vec{U}} = \vec{\vec{E}}_I. \tag{3.56}$$

$\vec{\vec{E}}_I$ is a diagonal matrix of eigenvalues E_M's in the $(M,M)^{th}$ entry.

Thus, we can represent the matrix elements of the time-evolution operator $\Lambda(t)$ as:

$$\langle I, M_b|\Lambda(t)|I, M_a\rangle = \sum\nolimits_N \langle N|I, M_b\rangle^* \exp\left(\frac{-iE_N t}{\hbar}\right)\langle N|I, M_a\rangle\,. \tag{3.57}$$

We note that $|N\rangle$ is the eigenvector basis of the unitary matrix $\vec{\vec{U}}$, and $\langle N|I, M\rangle$ are the matrix elements of $\vec{\vec{U}}$. N is summed over all eigenvector basis (and hence eigenvalues) of $\vec{\vec{H}}_I$.

We can see the proof of equation (3.57) as follows:

Note that $\vec{\vec{U}}^{-1}\vec{\vec{H}}_I\vec{\vec{U}} = \vec{\vec{E}}_I \Rightarrow \vec{\vec{H}}_I = \vec{\vec{U}}\vec{\vec{E}}_I\vec{\vec{U}}^{-1} \Rightarrow \vec{\vec{H}}_I^n = \underbrace{\vec{\vec{U}}\vec{\vec{E}}_I\vec{\vec{U}}^{-1}\vec{\vec{U}}\vec{\vec{E}}_I\vec{\vec{U}}^{-1}\ldots\vec{\vec{U}}\vec{\vec{E}}_I\vec{\vec{U}}^{-1}\vec{\vec{U}}\vec{\vec{E}}_I\vec{\vec{U}}^{-1}}_{n\ times}$

$$\Rightarrow \vec{\vec{H}}_I^n = \vec{\vec{U}}\vec{\vec{E}}_I^n\vec{\vec{U}}^{-1}$$

Recalling our definition of our matrix exponential: If $\vec{\vec{A}}$ is a $n \times n$ matrix:

$$\exp\vec{\vec{A}} = \sum\nolimits_{n\in\mathbb{N}\cup\{0\}} \frac{1}{n!}\vec{\vec{A}}^n$$

Therefore:

$$\exp\left(\frac{-i\vec{\vec{H}}_I t}{\hbar}\right) = \sum\nolimits_{n\in\mathbb{N}\cup\{0\}} \frac{1}{n!}\left(\frac{-it}{\hbar}\right)^n \vec{\vec{H}}_I^n = \sum\nolimits_{n\in\mathbb{N}\cup\{0\}} \frac{1}{n!}\left(\frac{-it}{\hbar}\right)^n \vec{\vec{U}}\vec{\vec{E}}_I^n\vec{\vec{U}}^{-1}$$

$$= \vec{\vec{U}}\left(\sum\nolimits_{n\in\mathbb{N}\cup\{0\}} \frac{1}{n!}\left(\frac{-it}{\hbar}\right)^n \vec{\vec{E}}_I^n\right)\vec{\vec{U}}^{-1} = \vec{\vec{U}}\exp\left(\frac{-i\vec{\vec{E}}_I^n t}{\hbar}\right)\vec{\vec{U}}^{-1}$$

Also:

$$\left\langle I, M_b\middle|\vec{\vec{H}}_I\middle|I, M_a\right\rangle = \left\langle I, M_b\middle|\left(\sum\nolimits_N |N\rangle\langle N|\right)\vec{\vec{H}}_I\middle|I, M_a\right\rangle$$

As $\vec{\vec{H}}_I|N\rangle = E_N|N\rangle$:

$$\left\langle I, M_b\middle|\vec{\vec{H}}_I\middle|I, M_a\right\rangle = \langle I, M_b|\sum\nolimits_N |N\rangle\, E_N\langle N|I, M_a\rangle = \sum\nolimits_N \langle N|I, M_b\rangle^* E_N\langle N|I, M_a\rangle$$

This result completes the proof (E_N are the eigenvalues extracted from $\vec{\vec{E}}_I$).

After all this work, we have the final form of the perturbation function (Compare the following equation to equation (3.50)):

$$G_{k_1,k_2}^{N_1,N_2}(t) = \sum\nolimits_{\substack{M_a,\\ M_b}} \left(\begin{matrix} (-1)^{2I+M_a+M_b}\sqrt{(2k_1+1)(2k_2+1)}\begin{pmatrix} I & I & k_1 \\ M_a' & -M_a & N_1\end{pmatrix}\begin{pmatrix} I & I & k_2 \\ M_b' & -M_b & N_2\end{pmatrix} \\ \times \sum\nolimits_{N,N'} \langle N|I, M_b\rangle^*\langle N|I, M_a\rangle\,\langle N'|I, M_b'\rangle\langle N'|I, M_a'\rangle^* \exp\left(\frac{-i(E_N - E_{N'})t}{\hbar}\right) \end{matrix} \right). \tag{3.58}$$

The above equation is the working form of $G_{k_1,k_2}^{N_1,N_2}(t)$ that is widely used and cited in literature such as Gerdau et al. [25]. We also note that for non-axially symmetric quadrupole interactions, the matrix elements of U are real. This restriction implies that the matrix elements of $\langle N|I,M_b\rangle$ and $\langle N|I,M_a\rangle$ are real and:

$$\langle N|I,M_a\rangle^* = \langle N|I,M_a\rangle, \tag{3.59a}$$

$$\langle N|I,M_b\rangle^* = \langle N|I,M_b\rangle. \tag{3.59b}$$

We note that $\Lambda(t)$ for the static electric quadrupole interaction satisfies equations $(2.53a \,\&\, 2.53b)$:

$$\Lambda(t)_{m,m'} = \Lambda(t)_{-m,-m'}, \tag{3.60a}$$

$$\Lambda(t)_{m,m'} = \Lambda(t)_{m',m}. \tag{3.60b}$$

Proof for equation $(3.60a)$:

We note that $\exp\left(\frac{-i\overleftrightarrow{H}_I t}{\hbar}\right) = \sum_{n\in\mathbb{N}\cup\{0\}} \frac{1}{n!}\left(\frac{-it}{\hbar}\right)^n \overleftrightarrow{H}_I^n$. Then we show that if the three matrices $\overleftrightarrow{A},\overleftrightarrow{B},\overleftrightarrow{C}$ is such that $A_{m,m'} = A_{-m,-m'}$ and $B_{m,m'} = B_{-m,-m'}$ and $\overleftrightarrow{C} = \overleftrightarrow{A}\overleftrightarrow{B}$, then:

$$C_{-m,-m'} = \sum\nolimits_j A_{-m',j}B_{j,-m} = \sum\nolimits_{-j} A_{m',-j}B_{-j,m} = C_{m,m'}$$

This result completes the proof.

Proof for equation $(3.60b)$:

We note here (too) that $\exp\left(\frac{-i\overleftrightarrow{H}_I t}{\hbar}\right) = \sum_{n\in\mathbb{N}\cup\{0\}} \frac{1}{n!}\left(\frac{-it}{\hbar}\right)^n \overleftrightarrow{H}_I^n$. Then we show that if the three matrices $\overleftrightarrow{A},\overleftrightarrow{B},\overleftrightarrow{C}$ is such that $A_{m,m'} = A_{m',m}$ and $B_{m,m'} = B_{m',m}$ and $\overleftrightarrow{C} = \overleftrightarrow{A}\overleftrightarrow{B}$, then:

$$C_{m',m} = \sum\nolimits_j A_{m',j}B_{j,m} = \sum\nolimits_j B_{m,j}A_{j,m'} = (B^T A^T)_{m,m'} = C^T_{m,m'}$$

We also note that $\overleftrightarrow{H}_I$ obeys property (2.53), i.e., $H_{I\,m,m'} = H_{I\,m',m}$. This identity means that $\overleftrightarrow{H}_I = \overleftrightarrow{H}_I^T$ and thus, complete the proof.

Just as a sanity check, we want to see if equation (3.49), along with equation (3.50), reduces to equation (3.38) in the limit of vanishing perturbation. We check: If $\Lambda(t) \to \Lambda(0) = \overleftrightarrow{Id}$ for all t, then [3]:

$$\langle I,M_b|\Lambda(t)|I,M_a\rangle = \delta_{M_a,M_b}, \tag{3.61a}$$

$$\langle I,M_b'|\Lambda(t)|I,M_a'\rangle = \delta_{M_a',M_b'}. \tag{3.61b}$$

Similar to equations $(3.54a \,\&\, 3.54b)$, in the limit of a vanishing perturbation, our system displays axial symmetry. Hence $N_1 = N_2 = N$. Furthermore, from equation $(3.61a \,\&\, 3.61b)$, $M_a = M_b = M$ and $M_a' = M_b' = M'$. Hence, equation (3.50) is reduced to this form:

$$G_{k_1,k_2}^{N_1,N_2}(t) = \sum\nolimits_M \sqrt{(2k_1+1)(2k_2+1)} \begin{pmatrix} I & I & k_1 \\ M' & -M & N \end{pmatrix} \begin{pmatrix} I & I & k_2 \\ M' & -M & N \end{pmatrix}. \tag{3.62}$$

We use the orthogonal relation [34]:

$$(2j_3+1)\sum_{m_1,m_2}\begin{pmatrix} j_1 & j_2 & j_3 \\ m_1 & m_2 & m_3 \end{pmatrix}\begin{pmatrix} j_1 & j_2 & j_3' \\ m_1 & m_2 & m_3' \end{pmatrix} = \delta_{j_3,j_3'}\delta_{m_3,m_3'}, \tag{3.63}$$

and note: Since N is fixed, we can reduce the sum over M, M' to just the sum over M due to the selection rule that $M' - M + N = 0$ in equation (3.62). Hence:

$$G_{k_1,k_2}^{N_1,N_2}(t) = \delta_{k_1,k_2}\delta_{N_1,N_2}. \tag{3.64}$$

We compare equation (3.64) to equation (3.55) and note that the orthogonality of the $3j$ symbol in equation (3.64) forces $k_1 = k_2$, in which equation (3.55) lacks that additional requirement of orthogonality.

Subbing equation (3.64) back into equation (3.49) gives (Recall that $t = 0$ is fixed):

$$W(\vec{k}_1, \vec{k}_2) = N\sum_{k,k\ even}\left(A_k(\gamma_1)A_k(\gamma_2)\frac{1}{2k+1}\sum_N Y_{k,N}^*(\theta_1,\varphi_1)Y_{k,N}(\theta_2,\varphi_2)\right). \tag{3.65}$$

Using the addition theorem for spherical harmonics [35]:

$$P_k(\cos\theta) = \frac{4\pi}{2k+1}\sum_{N\in\{-k,\dots,k\}} Y_{k,N}^*(\theta_1,\varphi_1)Y_{k,N}(\theta_2,\varphi_2)\,. \tag{3.66}$$

We note that $P_k(x)$ are the Legendre polynomials, and θ is the angle between the direction of the two emitted γ rays and is defined as:

$$\cos\theta = \cos\theta_1\cos\theta_2 + \sin\theta_1\sin\theta_2\cos(\varphi_1 - \varphi_2) \tag{3.67}$$

Finally, we got back the expression for the angular correlation without an external perturbation (With the normalisation factor baked in):

$$W(\vec{k}_1, \vec{k}_2) = W(\theta) = \sum_{k,k\ even}^{k_{max}} A_k(\gamma_1)A_k(\gamma_2)P_k(\cos\theta) \tag{3.68}$$

That is equation (3.38) in section 3.3.2.

3.4.3) Properties of the Unitary Matrix U and the Perturbation $G_{k_1,k_2}^{N_1,N_2}(t)$ under the influence of the static electric quadrupole interactions (Summary)

Since we are going to use software to numerically fit our perturbation function, an analytical understanding of the unitary matrix $\overleftrightarrow{U}$ and the perturbation function $G_{k_1,k_2}^{N_1,N_2}(t)$ is of lesser importance.

Therefore, we would only present the summary of the properties of U and $G_{k_1,k_2}^{N_1,N_2}(t)$ from Butz's paper [23] without proof here. The proof is found in Butz's article [23] and is reproduced in Appendix B (Reproduced with permission; copyright retained under Springer Nature, respectively).

Properties of $\overleftrightarrow{U}$:

1) $\overleftrightarrow{U}$ must be a checkerboard matrix. This property is inherited from H_I being a chessboard matrix (See equation $(2.51a\ \&\ 2.51b)$). Physically, it means that for a

given state $|I, M\rangle$, it could only be coupled to $|I, M \pm 2\rangle$. Equivalently, for $m, m' \in \{-I, -I+1, \dots, I-1, I\}$:

$$U_{m,m'} = 0 \; if \; m' \neq m \pm 2. \tag{3.69}$$

Mathematically, to the best of the author's knowledge as of this writing, he has not found nor constructed a proof for general I.

2) $\overleftrightarrow{U}$ is a real matrix. This restriction stems from the fact that $\overleftrightarrow{H}_I$ is a real matrix and has real eigenvalues.

3) The condition for the matrix elements of $\overleftrightarrow{U}$ must be satisfied:

$$\langle N|I, M_b\rangle\langle N|I, M_a\rangle = \langle N|I, -M_b\rangle\langle N|I, -M_a\rangle \tag{3.70}$$

This condition stems from both the symmetry argument (Equation $(3.60b)$) of $\Lambda(t)$ and using the fact that $\overleftrightarrow{H}_I$ and $\overleftrightarrow{U}$ are both real, such that $\langle N|I, M\rangle^* = \langle I, M|N\rangle$ as applied to equation (3.57):

$$\langle I, M_b|\Lambda(t)|I, M_a\rangle = \sum\nolimits_N \langle N|I, M_b\rangle \exp\left(\frac{-iE_N t}{\hbar}\right)\langle N|I, M_a\rangle \tag{3.71a}$$

$$\langle I, M_b|\Lambda(t)|I, M_a\rangle = \sum\nolimits_N \langle N|I, -M_b\rangle \exp\left(\frac{-iE_N t}{\hbar}\right)\langle N|I, -M_a\rangle \tag{3.71b}$$

4) For half-integer spins I, as noted from equation (2.55), we have the symmetric pairing of the eigen-energies $E_n = -E_n$. Therefore:

$$\langle N|I, M_b\rangle\langle N|I, M_a\rangle = \langle -N|I, -M_b\rangle\langle -N|I, -M_a\rangle$$
$$\Rightarrow \langle N|I, M\rangle = \langle -N|I, M\rangle \tag{3.72}$$

That is the consequence of the symmetry of equation $(3.60a)$.

We cannot say the same for integer spins I. At most, we can only say that: Due to the equal mixing of a state $|I, M\rangle$ and a state $|I, -M\rangle$, we have:

$$\langle N|I, M\rangle = \pm\langle N|I, -M\rangle \tag{3.73}$$

We include the minus sign, as equal mixing is unique to $|I, M\rangle$ up to the sign of M.

5) Although $\Lambda(t)$ is a symmetric matrix based on equation $(3.60b)$, $\overleftrightarrow{U}$ in general, is not a symmetric matrix. The only symmetry of the equation that is forced on $\overleftrightarrow{U}$ is such that (Based on equations (3.57) and $(3.71a \;\&\; 3.71b)$):

$$\langle N|I, M_b\rangle\langle N|I, M_a\rangle = \langle I, M_b|N\rangle\langle I, M_a|N\rangle \tag{3.74}$$

I.e., $\overleftrightarrow{U}$ is pairwise symmetric.

Properties of $G_{k_1 k_2}^{N_1 N_2}(t)$:

1) $$G_{0,0}^{0,0}(t) = 1 \tag{3.75}$$

2) $$N_1 + N_2 \in 2\mathbb{Z} \tag{3.76}$$

3) $$G_{k_1,k_2}^{N_1,N_2}(t) = G_{k_2,k_1}^{N_2,N_1}(t) \tag{3.77}$$

4) $$G_{k_1,k_2}^{N_1,N_2}(t) = G_{k_1,k_2}^{-N_1,-N_2}(t) \tag{3.78}$$

The above identity is an essential property as it ensures that $W\left(\vec{k}_1, \vec{k}_2, t\right)$ is real-valued and is thus observable.

5) $$G_{k_1,k_2}^{N_1,N_2}(t) = \left(G_{k_1,k_2}^{N_1,N_2}(t)\right)^* \tag{3.79}$$

This identity means that the perturbation function is real-valued and that the sign of the quadrupole frequency cannot be determined in a γ-γ TDPAC. Classically, the spin undergoes a precession simultaneously in the clockwise and anticlockwise directions.

6) $$G_{0,k_2}^{0,N_2}(t) = 0 \; if \; k_2 = 0 \tag{3.80}$$

7) $$G_{k_1,k_2}^{N_1,N_2}(t=0) = \delta_{k_1,k_2}\delta_{N_1,N_2} \tag{3.81}$$

We have treated this case in the limit of vanishing perturbations in section 3.4.2, with equation (3.64). The cross-terms with $k_1 \neq k_2$ will only be relevant for non-axial symmetry, which implies a mixing of the eigenstates of $\overleftrightarrow{H}_I$.

4) Working Principles of TDPAC: The Relevance of $R(t)$.

After we have demonstrated the principles of TDPAC, we will next focus on the experimental observables of TDPAC, including the discussion of the well-known counting ratio $R(t)$.

In essence, $R(t)$ is the TDPAC observable containing all the extracted hyperfine information of the TDPAC nuclear probe interacting with its host environment. It is beneficial because $R(t)$ is formulated after a series of intelligent approximations and reasonable cut-offs and can be expressed as the sum of cosines modulated with a Lorentzian/Gaussian parameter and the time-resolution function, alongside a constant called the "hardcore" value in literature.

The $R(t)$ for polycrystalline sources is well-developed, following the assumption of the statistical distribution of the EFG orientations. On the other hand, the $R(t)$ for single crystals is less understood, but surprisingly, its final form follows that of the polycrystals, but with a different coefficient on each of its cosines.

This chapter is developed after a discourse on Butz's work [23] (Reproduced with permission; copyright retained under Springer Nature, respectively). Valuable insights are also obtained from Wegner's paper [36]. In particular, we will use Butz's [23] for the overview of calculating $G_{k_1,k_2}^{N_1,N_2}(t)$ and $G_{kk}(t)$, and then refer to the other papers for a more palatable expression. We then calculate the $R(t)$ for both single crystal and polycrystalline sources and consider the effect of a statistical ensemble of TDPAC probe nuclei embedded in the host material with a Lorentzian/Gaussian distribution.

4.1) Expressions of $G_{k_1,k_2}^{N_1,N_2}(t)$ and $G_{kk}(t)$

In [23], Butz calculated the unitary matrix $\overleftrightarrow{U}$ associated with the static electric quadrupole moment $\vec{H}_I$ (See equation $(2.56a - 2.56c)$ in section 2.3.3). This expression of $\overleftrightarrow{U}$ is pretty ugly, and we would relegate the expression of $\overleftrightarrow{U}$ to either Butz's paper [23], or over at Appendix C of this paper (for ease of reference).

This expression of $\overleftrightarrow{U}$ is then used to derive the $G_{k_1,k_2}^{N_1,N_2}(t)$ for the expression of single crystals, and $G_{kk}(t)$ for the case of polycrystals. We note that for polycrystalline TDPAC spectroscopy, the $G_{22}(t)$ is the most critical and dominant term, and hence we can neglect higher order k-terms.

An excellent example of the use of such expressions for $G_{k_1,k_2}^{N_1,N_2}(t)$ is covered in [37], even though the TDPAC probe used is such that $I = 9/2$ and is consequently more complicated than our case for $I = 5/2$.

We first start by recalling the eigenvalues of $\vec{H}_I$ from section 2.3.3, under equation $(2.58a - 2.58h, 2.60a - 2.60c)$, alongside equation (2.50):

$$E_{\pm\frac{5}{2}} = -2r\cos\left(\frac{\varphi}{3}\right)\hbar\omega_Q, \qquad (2.58a, 2.60a)$$

$$E_{\pm\frac{3}{2}} = \left(r\cos\left(\frac{\varphi}{3}\right) - \sqrt{3}r\sin\left(\frac{\varphi}{3}\right)\right)\hbar\omega_Q, \qquad (2.58b, 2.60b)$$

$$E_{\pm\frac{1}{2}} = \left(r\cos\left(\frac{\varphi}{3}\right) + \sqrt{3}r\sin\left(\frac{\varphi}{3}\right)\right)\hbar\omega_Q, \qquad (2.58c, 2.60c)$$

with

$$\cos(\varphi) = \frac{q}{r^3}, \qquad (2.58d)$$

$$r = \mathrm{sgn}(q) * \sqrt{|p|} = -\sqrt{|p|}, \qquad (2.58e)$$

$$p = -28\left(1 + \frac{\eta^2}{3}\right), \qquad (2.58f)$$

$$q = -80(1 - \eta^2), \qquad (2.58g)$$

$$\eta \in [0,1], \qquad (2.58h)$$

$$\omega_Q = \frac{eV_{zz}Q}{4I(2I-1)\hbar}. \qquad (2.50)$$

All single crystal perturbation functions could be written in the form [23]:

$$G_{k_1,k_2}^{N_1,N_2}(t) = \sum\nolimits_{i=0}^{3} \xi_i \cos(\omega_i t)\,, \qquad (4.1a)$$

with:

$$\omega_0 = 0, \qquad (4.1b)$$

$$\omega_1 = \frac{1}{\hbar}\left(E_{\pm\frac{3}{2}} - E_{\pm\frac{1}{2}}\right), \qquad (4.1c)$$

$$\omega_2 = \frac{1}{\hbar}\left(E_{\pm\frac{5}{2}} - E_{\pm\frac{3}{2}}\right), \qquad (4.1d)$$

$$\omega_3 = \frac{1}{\hbar}\left(E_{\pm\frac{5}{2}} - E_{\pm\frac{1}{2}}\right), \qquad (4.1e)$$

and:

$$\xi_0 = \frac{1}{2}\sum\nolimits_{m=\frac{1}{2},\frac{3}{2},\frac{5}{2}} S(m,m) = \delta_{k_1,k_2}\delta_{N_1,N_2} - \xi_1 - \xi_2 - \xi_3, \qquad (4.1f)$$

$$\xi_1 = S\left(\frac{1}{2},\frac{3}{2}\right), \qquad (4.1g)$$

$$\xi_2 = S\left(\frac{3}{2},\frac{5}{2}\right), \qquad (4.1h)$$

$$\xi_3 = S\left(\frac{1}{2},\frac{5}{2}\right). \qquad (4.1i)$$

The $S(m,m')$, with $m,m' \in \left\{\frac{1}{2},\frac{3}{2},\frac{5}{2}\right\}$ are dependent on k_1,k_2,N_1,N_2 and shows up as a complicated list of cases, and one needs to use: Equation 79, alongside table 2 from Butz's

paper [23], to determine the value of $S(m,m')$. The same table and equation will be mentioned in Appendix C for ease of reference.

One technical note: In the derivation of $R(t)$, we would ideally want $W(\theta,t)$, be it for the single crystal or the polycrystalline case, to be ultimately expressed as a product of $P_k(\cos\theta)$.

We remark: We can indeed extract $P_2(\cos\theta)$ out of equation (3.50) since [23]:

1) We set $k_{\max}=2$ as an approximation.
2) We assume that our sample is placed in a transverse geometry, with the direction of the largest EFG axis V_{zz} making the angle with the detector plane such that $\theta_1=\theta_2=90°$.
    a. The above statement implies by equations 81 & 82 of [23], that $N_1,N_2\in 2\mathbb{Z}$, i.e., even.
3) Furthermore, if the sample is rotated about the direction of V_{zz}, terms with $N_1\neq N_2$ will be extinguished, leaving the terms with $N_1=N_2$ inside.
4) From the selection rules, we can rule out both cases: $(k_1,k_2)=(0,2)$ and $(2,0)$.
5) The surviving single crystal perturbation terms $G_{k_1,k_2}^{N_1,N_2}(t)$ include $G_{00}^{00}(t)=1, G_{22}^{00}(t), G_{22}^{-2-2}(t), G_{22}^{22}(t)$, of which they are associated with $(k_1,k_2)=(0,0)$ & $(2,2)$.
    a. The case for $(k_1,k_2)=(0,0)$ will ultimately lead to the corresponding term being independent of θ and the value of the coefficient is 1.
    b. The case $(k_1,k_2)=(2,2)$ will include the complimentary spherical harmonics $Y_{2,N}(\theta_1,\varphi_1)$ & $Y_{2,N}^*(\theta_2,\varphi_2)$. Using the addition theorem for spherical harmonics [35] implies that the associated term must contain the expression $P_2(\cos\theta)$.

In principle, the expression for $R(t)$ for both single crystal and the polycrystalline case must be similar, with the only difference being the value of the coefficients ξ_i's for each cosine wave component associated with ω_i.

To determine $G_{22}(t)$, we refer to equation (3.52).

We make some further remarks: Wegner [36] had put another set of closed empirical formulas for the single crystal TDPAC angular correlation $W(\vec{k}_1,\vec{k}_2,t)$, which allows for the measure of the V_{zz} direction with respect to the crystal axes. In particular, ξ_i for the polycrystalline case depends only on the asymmetry parameter η, while ξ_i for the single crystal case depends on both η and the orientation of the V_{zz} with respect to the axes of the detector plane.

To end this section, we would like to refer to Mendoza-Zelis et al. [38] for their calculation of $G_{22}(t)$, i.e., for the polycrystalline case. In some sense, their calculations are less convoluted as compared to Butz's equations: The $S(m,m')$ in equation $(4.1f-4.1i)$, and with $m,m'\in\left\{\frac{1}{2},\frac{3}{2},\frac{5}{2}\right\}$, can alternatively be written as:

$$S(m,m')$$

$$= \frac{1}{35} a_m^2 a_{m'}^2 \begin{Bmatrix} \frac{1}{3}[5b_m b_{m'} - c_m c_{m'} - 4]^2 + 10[b_m c_{m'} - b_{m'} c_m]^2 + 4[c_m - c_{m'}]^2 \\ +\left[\sqrt{5} b_m + 3c_{m'}\right]^2 + \left[\sqrt{5} b_{m'} + 3c_m\right]^2 \end{Bmatrix} \quad (4.2a)$$

$$a_m = \frac{1}{\sqrt{1 + b_m^2 + c_m^2}} \quad (4.2b)$$

$$b_m = \frac{\sqrt{10}\eta}{\left(\frac{E_m}{\hbar\omega_Q} - 10\right)} \quad (4.2c)$$

$$c_m = \frac{\sqrt{18}\eta}{\left(\frac{E_m}{\hbar\omega_Q} + 2\right)} \quad (4.2d)$$

With the expression of $G_{k_1,k_2}^{N_1,N_2}(t)$, as well as $G_{kk}(t)$, we could proceed to formulate the count rate ratio $R(t)$ in the next section.

4.2) The count rate ratio $R(t)$ and the polycrystalline experimental observable $A_2(\gamma_1)A_2(\gamma_2)G_{22}(t)$ in data acquisition and computation.

In the TDPAC experiment, we could observe the angular correlation function $W(\vec{k}_1, \vec{k}_2, t)$ (See equations $(3.49 \,\&\, 3.51)$ from section 3.4.1), which is naturally tied to the lifetime of the intermediate state of the TDPAC probe. In this section, we will derive the count rate ratio $R(t)$ for the case of the polycrystalline explicitly. For the case of single crystals, the derivation is analogous; refer to Wegner [36] for further details.

In the case of a polycrystalline sample, which assumes a statistical distribution of the EFG orientations, we can use equation (3.51), which we will write here for convenience:

$$W(\theta, t) = N \sum_{k\ even} A_k(\gamma_1) A_k(\gamma_2) G_{kk}(t) P_k(\cos\theta)\,, \quad (3.51)$$

with $P_k(x)$ being the Legendre polynomial and θ being the angle between the emission direction of γ_1 and γ_2.

In a typical γ-γ TDPAC setup, we use the four/six-detector setup with planar geometry, which implies that each detector forms a $90°$ angle to its adjacent neighbours. Hence, the only values of observable θ are $90°$ and $180°$.

We hence utilise the coincidence spectrum to construct our first observable, the coincidence count rate $N(\theta, t)$:

$$N(\theta, t) = N_0 \exp\left(-\frac{t}{\tau_N}\right) W(\theta, t) + C, \quad (4.3)$$

noting that $\tau_N = \ln 2 \,/ t_{1/2}$ is the lifetime of the intermediate state, N_0 is the coincidence count rate at time $t = 0$, and C describes the background count rate arising from random coincidences and hence, subtracted.

Typically, in a TDPAC spectroscopy, we ought to include the solid angle of the detectors Ω. However, as it turns out, it will have no impact on the construction of $R(t)$, as they will cancel each other out. Hence, we will leave Ω out for readability.

We perform the expansion of equation (3.51), noting that $A_0(\gamma_1) = A_0(\gamma_2) = 1$ and $G_{00}(t) = 1$:

$$W(\theta, t)$$
$$= 1 + A_2(\gamma_1)A_2(\gamma_2)G_{22}(t)P_2(\cos\theta) + A_4(\gamma_1)A_4(\gamma_2)G_{44}(t)P_4(\cos\theta) + O\big(P_6(\cos\theta)\big). \quad (4.4)$$

We note that the probability of the higher multipole transition is of an order of magnitudes lower than the lower multipole transition (See Chapter 9 of [27]), which implies that the lower order k terms contribute much more than the higher order k terms. Thus, we set the cut-off at $k_{\max} = 2$, and approximate $W(\theta, t)$ to the second Legendre order.

Also, as $P_2(x) = \frac{1}{2}(3x^2 - 1)$, we thus have:

$$W(\theta, t) \approx 1 + \frac{1}{2}A_2(\gamma_1)A_2(\gamma_2)G_{22}(t)(3\cos^2\theta - 1), \quad (4.5)$$

At certain angles of $\theta = 90°, 180°$:

$$W(90°, t) \approx 1 - \frac{1}{2}A_2(\gamma_1)A_2(\gamma_2)G_{22}(t), \quad (4.6a)$$

$$W(180°, t) \approx 1 + A_2(\gamma_1)A_2(\gamma_2)G_{22}(t). \quad (4.6b)$$

Thus:

$$N(90°, t) \approx N_0 \exp\left(-\frac{t}{\tau_N}\right)\left(1 - \frac{1}{2}A_2(\gamma_1)A_2(\gamma_2)G_{22}(t)\right), \quad (4.7a)$$

$$N(180°, t) \approx N_0 \exp\left(-\frac{t}{\tau_N}\right)\big(1 + A_2(\gamma_1)A_2(\gamma_2)G_{22}(t)\big). \quad (4.7b)$$

And:

$$2\big(N(180°, t) - N(90°, t)\big) \approx 3A_2(\gamma_1)A_2(\gamma_2)G_{22}(t), \quad (4.8a)$$

$$N(180°, t) + 2N(90°, t) \approx 3. \quad (4.8b)$$

We finally arrive at the expression of $R(t)$ using equation $(4.8a \;\&\; 4.8b)$:

$$R(t) = \frac{2N(180°, t) - 2N(90°, t)}{N(180°, t) + 2N(90°, t)} \approx A_2(\gamma_1)A_2(\gamma_2)G_{22}(t) \quad (4.9)$$

We note that the common factor $N_0 \exp\left(-\frac{t}{\tau_N}\right)$ and the solid angle Ω (Not included for readability) were expressed and factored out both in the numerator and denominator of $R(t)$ and hence, cancelled out.

Also, one implicit assumption in equation (4.9) is that the $N(90°, t)$ and $N(180°, t)$ terms are the arithmetic mean of all the possible start-stop coincidences from the different possible

combinations of the entire four-/six-detector setup. For example, one can count 24 unique $90°$ start-stop coincidences and six unique $180°$ start-stop coincidences for the six-detector configuration. In the four-detector configuration, one counts eight unique $90°$ start-stop coincidences and four unique $180°$ start-stop coincidences.

On the left-hand side of equation (4.9), we have an expression of the observables consisting of $N(90°, t)$ and $N(180°, t)$, in which they were obtained experimentally from our TDPAC experiments. On the right-hand side, we have an expression consisting of the orientation $A_2(\gamma_1)$ and correlation anisotropy $A_2(\gamma_2)$ coefficients, as well as our powder perturbation function $G_{22}(t)$.

Following the discussion in section 4.1, $G_{22}(t)$ can be written as:

$$G_{22}(t) = \sum_{i=0}^{3} \xi_i \cos(\omega_i t)\,. \tag{4.10}$$

The value of ξ_i's are obtained from equations $(4.2a - 4.2d)$, and ω_i's are obtained from equations $(4.1b - 4.1e)$.

In theory, $A_2(\gamma_1)$ and $A_2(\gamma_2)$ can be calculated via equations (3.40) and (3.41), but with the assumption that the detectors are point-like. However, in practice, the detectors are not point-like and occupy a finite volume space. We would want to calculate the effective anisotropy coefficients, considering the geometry of our detectors in our TDPAC system.

A simple estimation of our effective anisotropy coefficients, which we will call $A_{2,\text{eff}}(\gamma_1)$ and $A_{2,\text{eff}}(\gamma_2)$, is by including our approximation in what we call the attenuation coefficients $Q_2(\gamma_1)$ and $Q_2(\gamma_2)$ respectively:

$$A_{2,\text{eff}}(\gamma_1) = A_2(\gamma_1)Q_2(\gamma_1) \tag{4.11}$$

$$A_{2,\text{eff}}(\gamma_2) = A_2(\gamma_2)Q_2(\gamma_2) \tag{4.12}$$

We note that $Q_2(\gamma_1), Q_2(\gamma_2) \in (0,1]$ and can be analytically estimated by integrating over a normalised Legendre polynomial $P_k(x)$ along the geometrical solid angle Ω of the scintillator in our γ-detectors. The expression is further modulated by the efficiency of the creation of the photon peak, which depends on the energy of our γ-ray and the material of our scintillator [39]. It is given in a closed form [40-42] as ($i \in \{1,2\}$):

$$Q_k(\gamma_i) = \frac{\int_0^{\alpha} P_k(\cos\beta)\varepsilon(\beta)\sin\beta \; d\beta}{\int_0^{\alpha} \varepsilon(\beta)\sin\beta \; d\beta}. \tag{4.13}$$

β describes the angle between the direction of the emission of the γ_i-ray and the axis of the detector (scintillator), α is described as the maximum possible angle as allowed by our solid angle Ω. $\varepsilon(\beta)$ is the probability that for a given angle β, the scintillator detects γ_i-ray.

However, in our estimation, $A_{2,\text{eff}}(\gamma_1)$ and $A_{2,\text{eff}}(\gamma_2)$ are calculated using the software that employs a Monte Carlo method to obtain $Q_2(\gamma_1)$ and $Q_2(\gamma_2)$ [39,43-45]. The calculations are valid for BaF_2 scintillation crystals, but could be used for $CeBr_3$ scintillators without a deviation

of more than 5%. Furthermore, we include in our fitting, a multiplicative constant to detect any further deviation from our expected effective anisotropy coefficients.

Hence, our (incomplete) fitting function takes the form of:

$$R(t) = \frac{2N(180°, t) - 2N(90°, t)}{N(180°, t) + 2N(90°, t)} \approx A_{2,\text{eff}}(\gamma_1) A_{2,\text{eff}}(\gamma_2) \sum_{i=0}^{3} \xi_i \cos(\omega_i t)\,. \qquad (4.14)$$

4.3) Experimental imperfections and the implementation of the time resolution function and the Lorentzian/Gaussian function.

In general, after fitting the $R(t)$ function, we would perform a cosine fast Fourier transformation (referred to as FFT afterwards) to obtain the frequency spectrum. However, in a realistic experimental setup, the peak of the frequency distribution (around ω_1, ω_2 and ω_3) is not a Dirac-delta distribution but rather a Gaussian/Lorentzian distribution with a common full width at half maximum (FWHM) [25].

This is caused by:

1) Imperfections in the lattice dynamics of the host material, and thus, the local environment (and the EFGs) may slightly but statistically differ for an ensemble of implanted TDPAC probes,
2) The finite time-resolution of the detector (in the order of a tenth of a nanosecond).

We start with our incomplete fitting function, described by equation (4.14).

For point 1), we convolute $G_{22}(t)$ with either the Gaussian or Lorentzian distribution for each peak ω_i. This is mathematically described as:

$$G_{\text{eff},22}(t) = \sum_{i=0}^{3} \xi_i \int_{\mathbb{R}} \cos(\omega_i t)\, f_D(\omega - \omega_i)\, d\omega\,. \qquad (4.15)$$

The subscript "D" is used to denote either a Gaussian "G" or a Lorentzian "L" distribution.

The Gaussian/Lorentzian distribution in frequency space is:

$$f_G(\omega - \omega_i) = \frac{1}{2\pi\sqrt{\sigma}} \exp\left(-\frac{(\omega - \omega_i)^2}{2\sigma^2}\right), \qquad (4.16a)$$

$$f_L(\omega - \omega_i) = \frac{1}{\pi} \frac{\Gamma/2}{((\Gamma/2)^2 + (\omega - \omega_i)^2)}\,. \qquad (4.16b)$$

σ in $f_G(\omega - \omega_i)$ is the parameter relating to the standard deviation of the Gaussian distribution and is the same for all ω_i's. Γ in $f_L(\omega - \omega_i)$ is the equivalent parameter relating to the FWHM of the Lorentzian distribution and is the same for all ω_i's.

An inverse FFT on equation (4.15), described with $(4.16a\ \&\ 4.16b)$ reveals:

$$G_{\text{eff},22,\text{G}}(t) = \xi_0 + \sum_{i=1}^{3} \xi_i \cos(\omega_i t) \exp\left(-\frac{(\delta_G \omega_i t)^2}{2}\right), \qquad (4.17a)$$

$$G_{\text{eff,22,L}}(t) = \xi_0 + \sum_{i=1}^{3} \xi_i \cos(\omega_i t) \exp(-\delta_L \omega_i t)\,. \qquad (4.17b)$$

δ_G (δ_L) is the damping term associated with the Gaussian (Lorentzian) distribution and is defined as:

$$\delta_G = \sigma/\omega_Q, \qquad (4.18a)$$

$$\delta_L = \Gamma/2\omega_Q, \qquad (4.18b)$$

with ω_Q is the quadrupole frequency as defined via equation (2.50). Typically, δ_G and δ_L are typically expressed in percentage $(\%)$. In our fittings, we used the Lorentzian distribution and hence, used the expression relating to equation $(4.17b\ \&\ 4.18b)$.

Hence, our $R(t)$ takes this current form:

$$R(t) \approx A_{2,\text{eff}}(\gamma_1) A_{2,\text{eff}}(\gamma_2) \left(\xi_0 + \sum_{i=1}^{3} \xi_i \cos(\omega_i t) \exp(-\delta_L \omega_i t)\right). \qquad (4.19)$$

For point 2, we incorporate the time resolution function $\rho(t - t_v)$ to account for the finite time resolution of the detector. Hence, the final equation of our experimental $R(t)$ fit for the ^{181}Ta(TiO_2) γ-γ TDPAC spectroscopy is:

$$R(t) \approx A_{2,\text{eff}}(\gamma_1) A_{2,\text{eff}}(\gamma_2) \sum_v \rho(t - t_v) \left(\xi_0 + \sum_{i=1}^{3} \xi_i \cos(\omega_i t) \exp(-\delta_L \omega_i t)\right) \qquad (4.20)$$

4.4) Miscellaneous section on experimental TDPAC spectroscopy.

While the final experimental $R(t)$ fit for ^{181}Ta(TiO_2) γ-γ TDPAC spectroscopy was derived in the last section; experimentalists often use some quantities and relations.

4.4.1) Fundamental frequency

In practice, the fundamental frequency ω_0 frequently appears in the fitting parameters, and thus we define it as:

$$\omega_0 = 6\omega_Q. \qquad (4.21)$$

4.4.2) Geometry

In the standard six-detector setup, assuming perfect geometry considerations of the three planes as per the four-detector setup, we note that:

$$|\theta_{x-y}| + |\theta_{x-z}| = |\theta_{x-y}| + |\theta_{y-z}| = 90°, \qquad (4.22a)$$

$$|\varphi_{x-y}| + |\varphi_{x-z}| = |\varphi_{x-y}| + |\varphi_{y-z}| = 90°. \qquad (4.22b)$$

$\theta_{x-y}, \theta_{x-z}, \theta_{y-z}$ is the polar angle of the $x-y$, $x-z$ and $y-z$ planes, and for a specific plane, the vector corresponding to $\theta = 0°$ implies that this vector must be perpendicular to the said plane.

$\varphi_{x-y}, \varphi_{x-z}, \varphi_{y-z}$ is the azimuthal angle of the $x-y$, $x-z$ and $y-z$ planes and for a specific plane, for all vectors corresponding to an arbitrary φ, with $\theta = 90°$, implies that this vector must lie in the said plane.

Derivation of relations $(4.22a \ \& \ 4.22b)$ could be found in Appendix B of [2]. Subsequently, they are republished in this thesis under Appendix D, for which copyright is retained under the authors' ownership.

5) Working Principles of TDPAC: The γ-γ and e-γ TDPAC setup

Having developed the $R(t)$ as an experimental observable that contains all the information of the hyperfine parameters, we turn to the details of our γ-γ and e-γ TDPAC setup. But first, we need to highlight the subtle between the γ-γ and e-γ TDPAC setup.

5.1) From γ-γ to e-γ correlations

In chapters 2 to 4, we have explicitly dealt with γ-γ correlations. In this section, instead of measuring the correlation direction between two consecutive γ-rays, we can replace the detection of the first γ-ray with the conversion electron instead.

As mentioned in chapter 2, the emitted γ-rays are due to the direct de-excitation of the nucleus of the TDPAC probe (See Figure 12). However, in the case of the conversion electron, the excited nucleus interacts with the inner-shell electron(s), resulting in the ejection of the said electron from the TDPAC probe. This process is termed "internal conversion" in the literature, and the ejected electron is called the "conversion electron" (See left side of Figure 13). The conversion electron can be from the K, L or M shell, and we typically choose the electron shell with the highest probability of occurrence (and hence, the strongest signal).

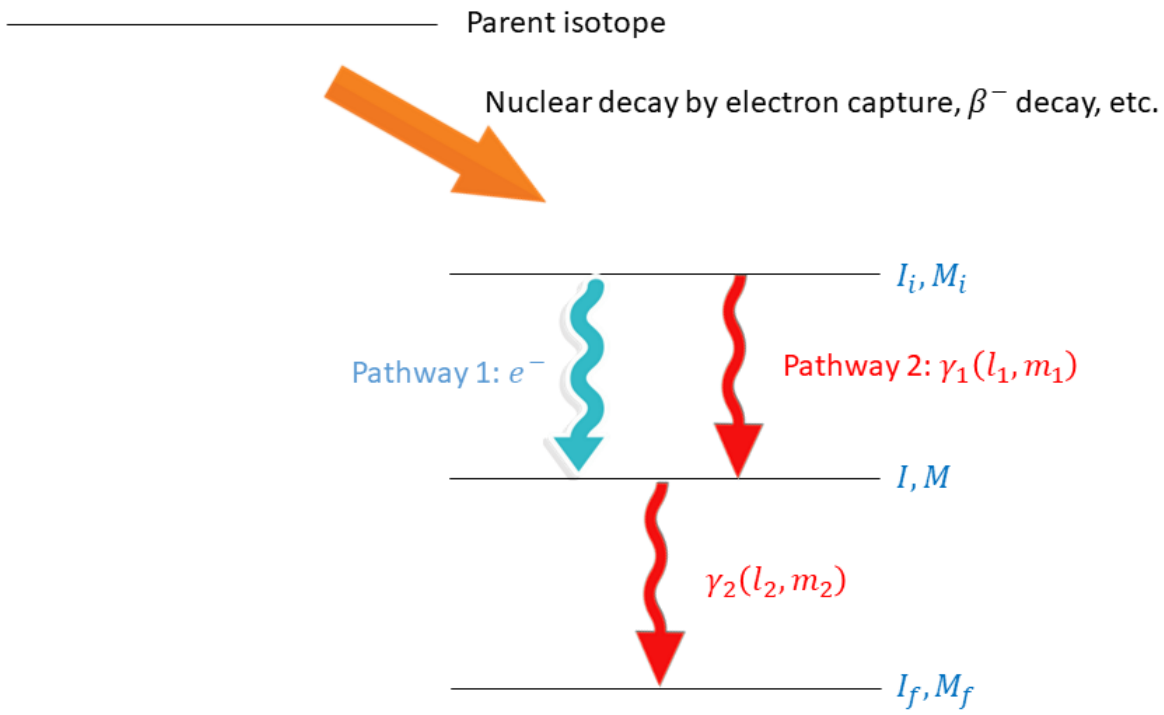


Figure 12: A simple sketch of the different pathways of the de-excitation of the nucleus of the TDPAC probe. Pathway 1, which forms the basis of the e-γ TDPAC setup, involves the internal conversion of the excited TDPAC probe nucleus, resulting in the ejection of the conversion electron. Pathway 2, which forms the basis of the γ -γ TDPAC setup, involves the direct de-excitation of the excited TDPAC probe nucleus, resulting in the emission of the γ-quanta.

In response to the vacancy (hole) left in the inner electron shell of the TDPAC probe following internal conversion, an electron cascade (or recombination process) then occurs, where electrons from the higher-energy shell fill the lower energy shell, emitting a series of x-rays and/or Auger electrons. The process of the electron cascade terminates when the vacancy

reaches the valence shell of the TDPAC probe and is filled up by the recombination process provided by the host material (See right side of Figure 13).

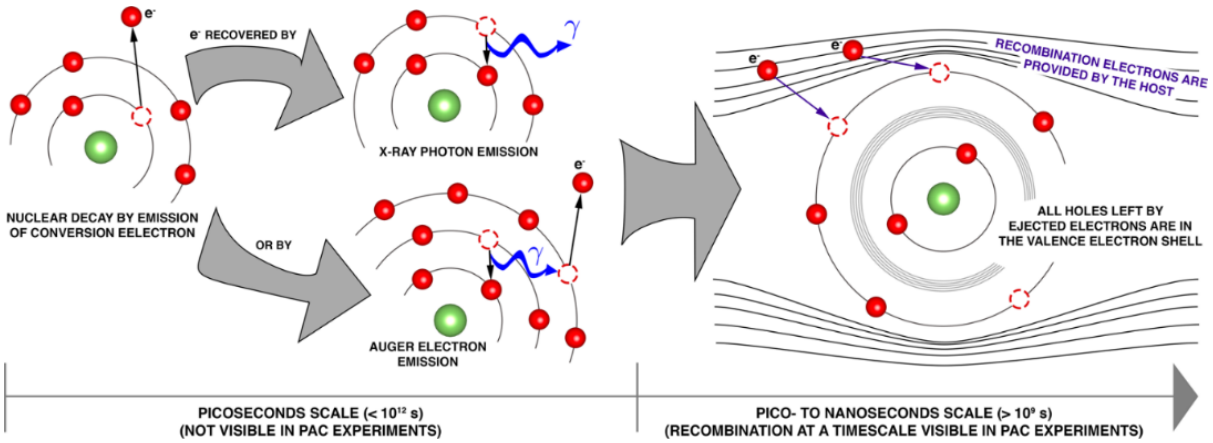


Figure 13: Schematic representation of electron cascade after ejection of conversion electron from nuclear decay. Electrons from higher shells de-excite to fill the vacant lower-energy shells, emitting either characteristic x-rays, Auger electrons, or both. This process occurs on a time scale on the order of picoseconds, which is three orders of magnitude faster than the nanosecond time resolution of a typical TDPAC spectroscopy. The electron cascade ends once the vacancy induced by the ejection of the conversion electron reaches the valence shell and is filled by recombination electrons provided by the host material. If the electron recombination process occurs on a timescale greater than nanoseconds, then the dynamic e−γ TDPAC signal differs from the γ−γ TDPAC signal. It is reprinted with permission from Ref. [18] under the Creative Commons Attribution 4.0 International License. Copyright 2019, Barbosa, M.B. et al..

In the more traditional γ-γ TDPAC setup, we have discussed the orientation $A_{k_1}(\gamma_1)$ and correlation coefficients $A_{k_2}(\gamma_2)$, as reflected in equation (3.40 & 3.41). For the e-γ TDPAC setup, while the correlation coefficients remain the same, $A_{k_1}(\gamma_1)$ is modified with the particle parameters b_k to produce its conversion electron equivalent $A'_{k_1}(e^-)$ [31]:

$$A'_{k_1}(e^-) = \frac{\{b_k(L_1,L_1)F_{k_1}(L_1,L_1;I_i,I) + (-1)^{L_1-L'_1}2\delta'_1 b_k(L_1,L'_1)F_{k_1}(L_1,L'_1;I_i,I) + (\delta'_1)^2 b_k(L'_1,L'_1)F_{k_1}(L'_1,L'_1;I_i,I)\}}{1+(\delta'_1)^2} \quad (5.1a)$$

δ'_1, the conversion electron equivalent of the mixing term δ_1, is defined as:

$$\delta'_1 = \delta_1 \sqrt{\frac{c(L'_1,\pi)}{c(L_1,\pi)}}, \quad (5.1b)$$

with π being the parity of the γ_1-ray (See Section 3.1). $c(L_1,\pi)$ is called the conversion coefficient of a multipole and is defined as:

$$c(L_1,\pi) = \frac{N(e^-)}{N(L_1,\pi,\gamma_1)}, \quad (5.1c)$$

with $N(e^-)$ & $N(\gamma_1)$ being the probabilities of the emission of the conversion electron or the γ_1-ray with multipolarity L_1 and parity π.

The particle parameters b_k, δ'_1 and $c(L_1,\pi)$ are collected and referenced in [39,43-45].

Typically, to condense the notation, we collect all effective contributions of b_k's on $A_{k_1}(\gamma_1)$, into one single parameter b'_k. Hence, our fitting function for the $R(t)$ relating to the e-γ TDPAC setup takes on the following form:

$$R(t) \approx b'_2 A_{2,\text{eff}}(\gamma_1) A_{2,\text{eff}}(\gamma_2) \sum_v \rho(t - t_v) \left(\xi_0 + \sum_{i=1}^{3} \xi_i \cos(\omega_i t) \exp(-\delta_L \omega_i t) \right) \quad (5.2)$$

The coupling of the excited nucleus to the inner-shell electron(s) is a subtle but important factor in distinguishing the e-γ TDPAC setup from its γ-γ counterpart. If the electron recombination process is at least on the order of the half-life $t_{1/2}$ of the intermediate state of the TDPAC probe, or above, we can observe for e-γ TDPAC setup, a characteristic dynamic signal that differs from that of the corresponding γ-γ setup. Conversely, if the recombination process is much less than the half-life $t_{1/2}$ of the intermediate state of the TDPAC probe, we could not distinguish the hyperfine parameters of both the e-γ and γ-γ TDPAC setup. One example of the former case is the study of ^{181}Ta(GaN) [18,31], and the example of the latter case, as we will soon see, will be our study of ^{181}Ta(TiO_2).

5.2) The γ-γ and e-γ TDPAC setup

For our γ-γ TDPAC setup, we used a setup that was called DIGIPAC (See Figure 14, with reference [46]). DIGIPAC is a digital TDPAC spectrometer that, compared to conventional analogue TDPAC spectrometers, is more user-friendly and flexible.

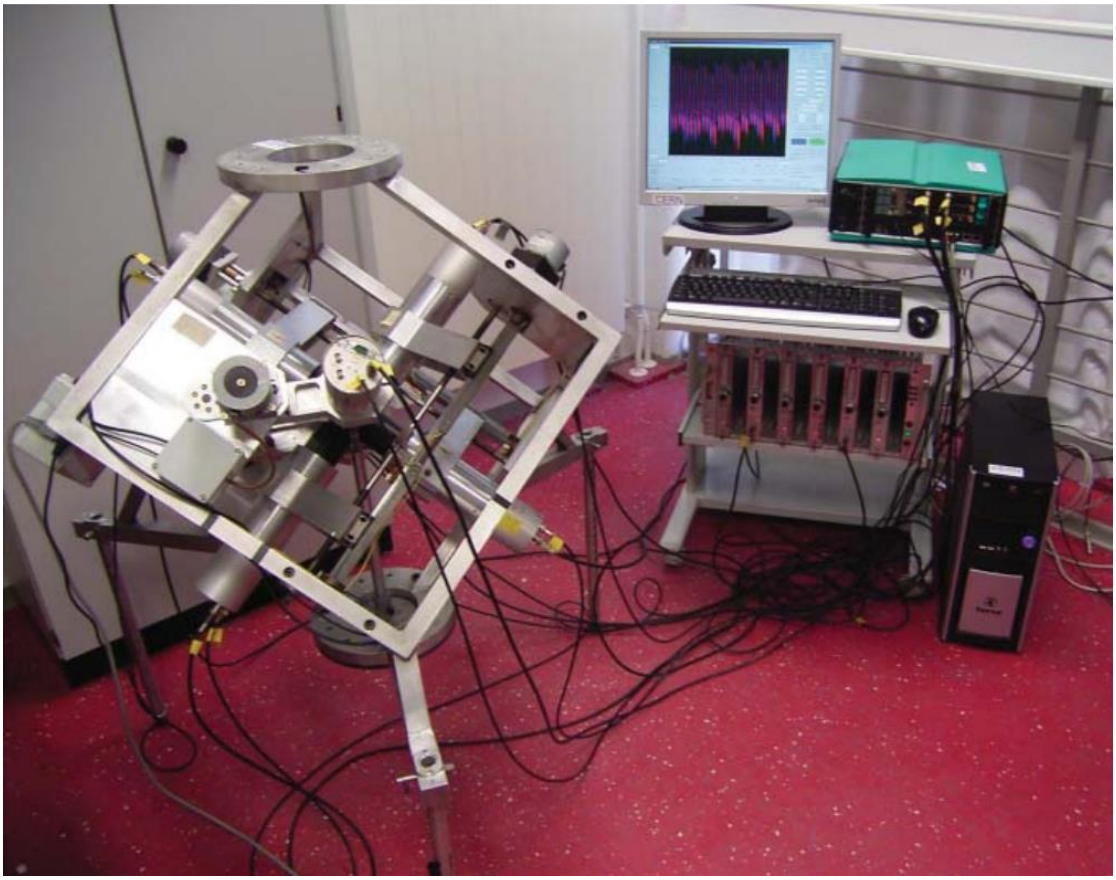


Figure 14: DIGIPAC is a digitalised TDPAC setup that uses digitisers with field programmable gate arrays (FPGA) support to overcome the limitations set by the fast-slow-coincidence circuit, in which traditional analogue TDPAC setup uses. It was reproduced as figure 1 from [46] with permission from AIP Publishing. Copyright retained under AIP Publishing.

For historical reasons, we will discuss the traditional analogue TDPAC spectrometer. DIGIPAC is part of the next-generation digital spectrometer and does not employ techniques in the analogue setup.

In the older analogue TDPAC spectrometer (See Figure 15), to obtain $N(90°, t)$ and $N(180°, t)$ (See equation (4.3)), we first note that the energies γ_1-ray (defining the start) and the γ_2-ray (defining the stop), must differ significantly for accurate coincidence. For example, for ^{181}Ta TDPAC probe, the energy of the γ_1-ray is $137\ keV$, which can be discriminated from the energy of the γ_2-ray, which is $482\ keV$. The TDPAC probe is assumed to rest with an equidistance between detector A, which, for illustration, collects the γ_1-ray, and detector B, which collects the γ_2-ray.

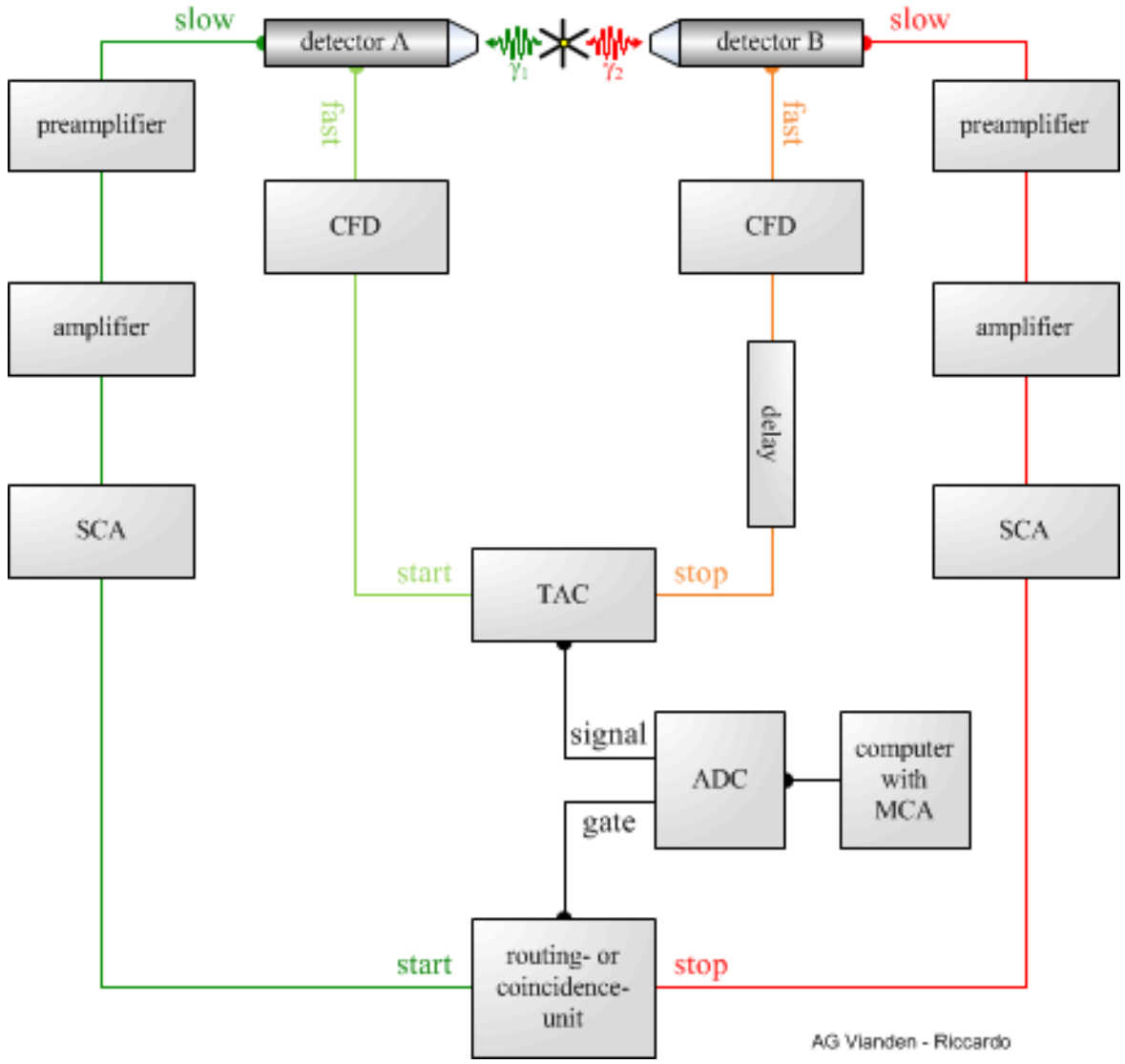


Figure 15: A schematic of the traditional analogue TDPAC setup using the fast-slow-coincidence circuit. It was widely used in the 1970s before advances in computational and electronic capabilities led to the increased adaptation of digitised TDPAC setups such as DIGIPAC [8]. Adapted from [47].

The two detectors are connected to a fast-slow coincidence circuit, such that two signals are acquired from each detector: the fast-timing signal and the slow energy pulse. The fast-timing signals are fed into the constant fraction discriminators (CFD), which mimics the mathematical

operation of finding the maximum height of the pulse by finding the zero of the slopes [48]. They are then fed into the common time-to-amplitude converter (TAC). The TAC is an electronic clock which measures the time t in which the TDPAC probe stays in the intermediate state and operates, with the start time being the acquisition of the fast-timing signal of the γ_1-ray and the stop time being the acquisition of the fast-timing signal of the γ_2-ray. The output amplitude of the TAC is proportional to the length of the time t between the two γ-γ pulses.

The slow energy pulses serve as a check to ensure that the energies of the γ_1-ray and γ_2-ray is statistically correct/acceptable. The slow energy pulses from the scintillator are first amplified using the pre-amplifiers and amplifiers, then passed through the single channel analysers (SCA), which filter out energies of the wrong values. The resulting signals are sent as a start-stop coincidence into the routing- (coincidence-) unit, which gates the signal from the TAC. The processed slow-fast signals were then sent to the analogue-to-digital (ADC) converter, which will then be stored as data in a computer with a multi-channel analyser (MCA), which sorts the incoming signals by their amplitudes into channels.

Details on the traditional TDPAC setup can be found in [3,47].

On the other hand, DIGIPAC extensively uses digitisers with field programmable gate arrays (FPGA) support to eliminate the fast-slow coincidence circuit. The FPGA is designed to handle the ADC part from the traditional TDPAC setup, allowing the data stream to be processed in real time and the TDPAC spectrometer to be fully digitalised. More details on DIGIPAC can be found in [46].

In DIGIPAC, six $LaBr_3$ scintillators in the standard geometry were used. They are selected specifically for their high light yields and ultra-fast response time. The time resolution of the $LaBr_3$ detectors is in the sub-ns, with only the BaF_2 detectors slightly edging it out [8,49,50]. The typical energy resolution for a specific energy of 551/662 keV is about 4% FWHM, which is the current state of the art.

For our e-γ TDPAC setup (See Figure 16), we used the same coincidence setup as the traditional analogue TDPAC setup, but with the setup consisting of two-electron detectors and two γ-ray detectors. As of this writing, no currently working e-γ TDPAC setup exists other than our own, housed in SSP ISOLDE.

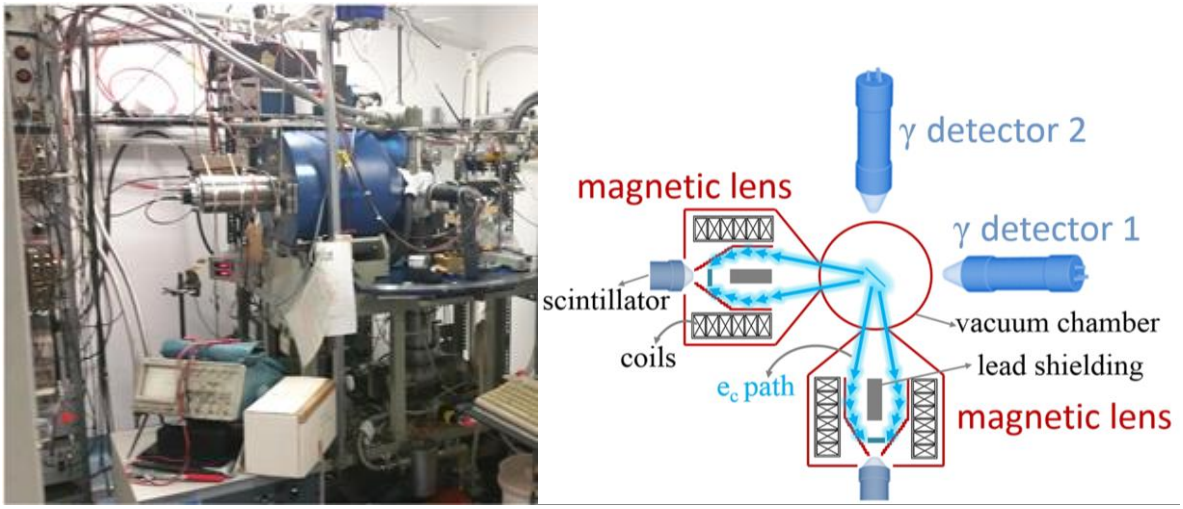


Figure 16: Left photo: The e-γ TDPAC setup in question. It is currently the only working setup in this world. It is reproduced from [8] under the Creative Commons Attribution 3.0 International License. Copyright 2019 under Johnston, K. et al. Right figure: The schematics of the e-γ TDPAC setup. It includes a vacuum chamber that encloses the sample, 2 BaF_2 scintillators that act as γ-ray detectors, and two magnetic lenses of the Siegbahn type [51] coupled to the scintillators and the photomultiplier tube. It is reproduced from [15] under the Creative Commons Attribution 3.0 (CC BY) license. Copyright 2017 under Schell, J. et al.

The conversion electron detectors consist of magnetic lenses of the Siegbahn type [51] that focuses on the conversion electrons that are ejected out of the TDPAC probe following internal conversion (See section 5.1) onto fast plastic scintillators. The conversion electron serves as the start signal as well. In contrast, the corresponding γ-ray detectors consist of BaF_2 scintillators that detect the γ_2-ray, which corresponds to the stop signal.

Due to the magnetic dispersive elements, the conversion electron detectors have better energy resolution than the γ-ray detectors [51,52]. We also note that compared to the γ-γ setup, the e-γ spectroscopy's statistics are reduced. This is because, for the γ-γ setup, the γ-detectors can detect both γ_1 (start) and γ_2 (stop) rays. However, for the e-γ setup, the electron detectors only detect conversion electrons (start), and the γ-detectors only detect γ-rays (start). This means that the 4-detector e-γ setup could only count two unique $90°$ and $180°$ start-stop coincidences each, as compared to eight and four $90°$ and $180°$ start-stop coincidences for its γ-γ counterpart.

More details on the e-γ setup can be found in [15,51,52].

6) Properties of rutile TiO_2 and $^{181}Hf(^{181}Ta)$ as a TDPAC probe nucleus and experimental details

In the previous chapters, in sufficient detail, we have described the γ-γ and e-γ TDPAC spectroscopies, including the experimental setup. In this chapter, we turn to the properties of rutile TiO_2 as the host material, the properties of $^{181}Hf(^{181}Ta)$ radioactive nuclei that make it a good candidate for both γ-γ and e-γ TDPAC spectroscopies, as well as the experimental conditions and data acquisition, which includes the method of implantation of $^{181}Hf(^{181}Ta)$ into rutile TiO_2. We will also mention a state-of-the-art summary for $^{181}Ta(TiO_2)$ γ−γ TDPAC Spectroscopy.

While parts of the content in the previous chapters are paraphrased and adopted from relevant parts of this paper [2], in this chapter, the following contents are explicitly reproduced ab verbatim from and previously published in [2]:

Section of this thesis	Reproduced from [2] under section
6.1) Literature on TiO_2 and $^{181}Ta(TiO_2)$ γ−γ TDPAC Spectroscopy	1) Introduction
6.1.1) State of the Art ($^{181}Ta(TiO_2)$ γ−γ TDPAC Spectroscopy)	1.1) State of the Art ($^{181}Ta(TiO_2)$ γ−γ TDPAC Spectroscopy)
6.1.2) Properties of Rutile TiO_2	1.2) Physics and Properties of Rutile TiO_2
6.1.3) Motivation for applying the e−γ TDPAC Spectroscopy to the TiO_2 Material	1.3) Motivation for Applying the e−γ TDPAC Spectroscopy to the TiO_2 Material
6.2) $^{181}Hf(^{181}Ta)$ as a TDPAC probe	Parts of the section from 2) Time Differential Perturbed Agular Correlations
6.3.1) $^{181}Hf(^{181}Ta)$ implantation process into rutile TiO_2	3.1) Implantation of ^{181}Hf isotope at the Bonn Radioisotope Separator
6.3.2) Data Acquisition of $^{181}Ta(TiO_2)$ γ−γ and e−γ TDPAC Spectroscopy	3.2) Data Acquisition of $^{181}Ta(TiO_2)$ γ−γ and e−γ TDPAC Spectroscopy
6.3.3) X-ray Diffraction of the $^{181}Ta(TiO_2)$ Sample after the γ−γ and e−γ TDPAC Spectroscopy	3.3) X-ray Diffraction of the $^{181}Ta(TiO_2)$ Sample after the γ−γ and e−γ TDPAC Spectroscopy

Copyright is retained by the authors of the mentioned paper (to which I am one of them) and licensed under the Creative Commons CC BY 4.0 license.

6.1) Literature on TiO_2 and $^{181}Ta(TiO_2)$ γ−γ TDPAC Spectroscopy

TiO_2, also known as titanium dioxide in the literature, is a solid inorganic compound with wide technological applications in the industry. Pure TiO_2 crystal is available in three phases: rutile, anatase, and brookite [53]. Anatase and brookite are metastable states and thus convert irreversibly into rutile TiO_2 upon heating to $600-800\ ^{\circ}C$ and beyond in air [54]. Typical uses of TiO_2 include but are not limited to (1) photocatalytic applications [55,56], (2) as an ultraviolet-light blocker in sunscreen materials [57], and (3) as a white pigment or whitening material in various everyday commodities such as paints, papers, foods, medicinal pills, tablets, and toothpaste [58].

6.1.1) State of the Art ($^{181}Ta(TiO_2)$ γ−γ TDPAC Spectroscopy)

The first $^{181}Ta(TiO_2)$ γ−γ TDPAC spectroscopy was done by Adams & Catchen [59]. They measured the hyperfine parameters of a ^{181}Ta probe in bulk polycrystalline rutile TiO_2 over a wide range of temperatures, acquiring signals corresponding to the presence of the single-site electric-field gradients (EFGs), but no local magnetic ordering in $^{181}Ta(TiO_2)$. This result was confirmed by Darriba et al. in their corresponding temperature-dependent study of bulk single crystal rutile $^{181}Ta(TiO_2)$, accompanied by their ab initio density-functional theory simulations to explain the effect of the background temperature on the EFG of rutile $^{181}Ta(TiO_2)$ [60].

A side note: Darrida et al., in their γ-γ single crystal rutile $^{181}Ta(TiO_2)$ study [60], made use of Wegner's empirical formula as found in [36] and determined that the V_{zz} direction coincides with the [001] axis of rutile TiO_2.

Further studies of $^{181}Ta(TiO_2)$ γ−γ TDPAC spectroscopy at room temperature were conducted by a group in the Bhabha Atomic Research Centre. They measured the EFGs of the bulk $^{181}Ta(TiO_2)$ system in both the rutile and anatase crystalline phases [61] and probed the EFGs of the ^{181}Ta probe in the TiO_2 nanocrystal environment [62]. The room-temperature TDPAC signature(s) of the ^{181}Ta probe located at both the surface and the bulk of the TiO_2 nanocrystal (anatase and rutile) were obtained. They simultaneously implanted both $^{111}In \rightarrow ^{111}Cd$ and $^{181}Hf \rightarrow ^{181}Ta$ probe nuclei into a bulk rutile TiO_2 sample and detected signals corresponding to the EFGs of ^{111}Cd and ^{181}Ta, located at the substitutional sites of the TiO_2 sample [63]. Their research applications involved the study of the γ-radiation and the leaching behaviour on the $^{181}Ta(TiO_2)$ crystal matrix [64].

Schell et al. conducted $^{181}Ta(TiO_2)$ γ−γ TDPAC spectroscopy over a range of temperatures, the host TiO_2 material being a thin film instead of the usual bulk phase [65,66]. They collected TDPAC signals corresponding to the presence of the EFGs of the ^{181}Ta probe at two unique sites of the thin film TiO_2. The magnitude of the EFGs at one such location suggests that the local environment of the ^{181}Ta probe nucleus is like that of anatase TiO_2, implying that the implantation of the ^{181}Hf nucleus modifies the local structure of the TiO_2 thin film.

Finally, at the 2011 International Nuclear Atlantic Conference held in Belo Horizonte (Brazil), Martucci et al. presented their $^{181}Ta(TiO_2)$ TDPAC and their corresponding X-ray diffraction (XRD) results on the effects of thermal annealing on polycrystalline samples produced using the sol-gel Pechini method [67]. A literature review of the sol-gel Pechini process [68] on the precipitation of TiO_2 powder reveals the formation of anatase and rutile phases, with their ratio determined by the molar ratio of citric acid/metallic Ti cations as reagents [69]. They have shown that if their TiO_2 powder is subjected to a $10h$ thermal annealing of $1273\ K$ in the nitrogenic atmosphere, then their XRD and $^{181}Hf \rightarrow ^{181}Ta$ γ−γ TDPAC spectroscopies demonstrate a complete phase transformation from the anatase phase to the rutile phase, consistent with reference [54].

Further literature on TDPAC spectroscopy applied to TiO_2 is available in reference [70], which gives room-temperature results from various TDPAC probes.

6.1.2) Properties of rutile TiO_2

Bulk rutile TiO_2 is spatiality related to the tetragonal space group $P4_2/mnm$ [71]. The lattice parameters of the unit cell are such that it has lattice translational vectors $\vec{R} = \sum_{i\in\{1,2,3\}} n_i \vec{a}_i$, where $\forall i \in \{1,2,3\},\ n_i \in \mathbb{Z}$, alongside $\vec{a}_1 = a\hat{x},\ \vec{a}_2 = a\hat{y}, \vec{a}_3 = c\hat{z}$, with the lattice parameters $a = 4.65922$ Å and $c = 2.9574$ Å [72]. The unit cell comprises two titanium ions, located at both $[0,0,0]$ and $[0.5a, 0.5a, 0.5c]$, and four oxygen ions, located at $[\pm xa, \pm xa, 0]$ and $[(0.5 \mp x)a, (0.5 \pm x)a, 0.5c]$, where x is defined as the internal parameter, is dimensionless and is experimentally verified as 0.30496 [72].

Under this perfect lattice configuration, both titanium ions in the unit cell are site-equivalent, forming bonds with its six nearest neighbour oxygen ions under the distorted octahedral geometry. It is more precisely understood as having a D_{2h} site symmetry. Each of the oxygen atoms in the unit cell is site-equivalent as well, forming a 3-fold coordinated bond with its three nearest neighbour titanium ions in a trigonal planar form, their site symmetry being C_{2v}.

In practice, high-quality single crystal rutile TiO_2 could be commercially manufactured using, for example, the Verneuil method [73]. However, it is known that even for such a refined method, there exists a non-trivial number density of oxygen vacancies (site defects where the supposing oxygen atoms are missing) for freshly fabricated single crystal rutile TiO_2. Numerous experiments have verified this phenomenon, including a recent 2018 experiment using the Femtosecond Time-Resolved Spectroscopy on bulk rutile TiO_2 to determine its charge carrier dynamics. This result revealed that the presence of innate oxygen vacancies as a trap site contributes to a fast recombination/annihilation lifetime (<1 ns) of the electrons (as a charge carrier) [74].

The oxygen vacancies (if numerous enough) create a large density of localised states in the band gap of rutile TiO_2. As the name implies, electrons in these localised states are not mobile (compared to the delocalised states at the valence and conduction bands). However, quantum tunnelling between localised states is possible. With that principle, an electron can travel from one localised state to another, a phenomenon is known as “hopping transport”, “variable range hopping”, or “hopping conduction” [75,76].

At the surface and interfaces, the phenomenon of hopping transport becomes a lot more critical due to the existence of surface states (another set of localised electronic states) caused by the sharp transition (surface reconstructions) between atoms of both materials located near the interface (air and vacuum can be understood as material in this sense) [75].

Numerous experimental studies have been conducted on the nature of the electronic surface states of rutile TiO_2, which (1) includes the longer vacuum decay length of the Ti(3d) surface electronic states over the O(2p) surface electronic states (discovered using Scanning Tunnel Microscopy) [77], (2) the nature of the oxygen adatoms at the surface (using sensitive Fast Atomic Force Microscopy), which could exist as single quantum dots [78], and (3) a paper that explores on the electronic structures of rutile (110), anatase (101) and anatase (001) single crystal surfaces using Resonant Photoemission and X-ray Absorption Spectroscopy [79]. They

have discovered that the rutile single crystal surfaces, prepared under cycles of bombarding and annealing in a vacuum, show a higher concentration of oxygen vacancies over the anatase variant, which is consistent with the findings of [74]. Moreover, they have shown that the method of surface preparation, and thus, the concentration of the oxygen vacancies, is proportional to the σ-antibonding hybridisation between the Ti(3d-e_g) and the O(2p) states (using X-ray Absorption Spectroscopy) and that the π-bonds between the Ti(3d-t_{2g}) and the O(2p) states are increasingly disrupted as the amount of surface defects increases (using Resonant Photoemission).

Theoretically, Density Functional Theory (DFT) techniques have been used to study the electronic structure of bulk rutile TiO_2 with various point defects (including oxygen vacancies) [80], alongside the electronic structure of surface rutile TiO_2 in various surface orientations [81].

To encapsulate the discussion in this section, semiconductor oxides like TiO_2 present exciting electronic properties in the hopping transport (a form of quantum-mechanical tunnelling), which, once well-understood, can increase the number of high technology applications of the material, including the enhancement of its photocatalysis capability [76,82].

6.1.3) Motivation of applying the e−γ TDPAC Spectroscopy to the TiO_2 Material

The e−γ TDPAC spectroscopy could probe physics typically inaccessible from its more experimentally established γ−γ TDPAC counterpart. The degree to which the e−γ and γ−γ TDPAC signals differ from each other depends on the timescale (and hence speed) of the host material to provide its recombination electrons to the TDPAC nuclear probe following internal conversion of the excited ^{181}Ta to ground state ^{181}Ta as a TDPAC probe (Further details are contained in Section 2).

This phenomenon is wonderfully demonstrated in the recent ^{181}Ta(GaN) TDPAC experiment by Barbosa et al. [18], where they performed a temperature- and "Si- and Zn- dopant" concentration-dependent study. In Figure 3 of the corresponding paper, they had shown that their e−γ signals differ from those of the corresponding γ−γ signals. Furthermore, with the help of their in-house dynamic fitting program PACme^{TM} and DFT, they can assign electronic charges to the metastable states related to their e−γ signals. These metastable states represent the various stages (around the nanosecond scale) in which the recombination electrons will fill the holes following the internal conversion process of the excited ^{181}Ta to ground state ^{181}Ta as a TDPAC probe (Further details are contained in Section 5.1).

On a related note on the topic of electronic recombination, Schell et al. have conducted and compared the signals acquired from both single crystals (^{111}In→^{111}Cd)TiO_2 and (^{111m}Cd→^{111}Cd)TiO_2 TDPAC spectroscopies [83]. While both TDPAC spectroscopies exhibit a common set of hyperfine parameters (largest EFG and asymmetry parameter, see Chapters 2 and 3) relating to the Ti-substitutional site, an additional set of hyperfine parameters (with a high asymmetry parameter) is manifested in the (^{111m}Cd→^{111}Cd)TiO_2 TDPAC spectroscopy (colloquially referred to as the second site). DFT simulations accompanying this study also revealed that the individual EFGs (the largest EFG and the asymmetry parameter) of a single

charge-deficient Cd atom resting in the Ti-substitutional site are consistent with the second site. Noting that the valence number of ^{111}In and ^{111m}Cd in TiO_2 are +3 and +2, respectively, (Ti has a valence number of +4), and the fact that the half-life of the intermediate ^{111}Cd state is 85ns, ^{111}In$\rightarrow^{111}$Cd requires only one recombination electron from the host TiO_2 material, whereas ^{111m}Cd$\rightarrow^{111}$Cd needs two. This result implies that, at least qualitatively, the time required to fill up two holes in a single ^{111}Cd atom sitting in the Ti-substitutional site is around the order of tens of nanoseconds.

Thus, e−γ TDPAC spectroscopy, complementing γ−γ TDPAC spectroscopy, can probe even further into the electronic structure in TiO_2, both in bulk and on the surface. For bulk rutile TiO_2, we can compare the degree to which their e−γ and γ−γ ^{181}Ta(TiO_2) TDPAC signals differ to verify that the recombination lifetime of the electrons is indeed on the sub-ns scale according to [74]. Further possible applications of e−γ TDPAC on TiO_2 could be made on its surfaces and interfaces, where we can further probe the local electronic characters of the Ti and O ions around our TDPAC probe in a more precise manner as compared to other typical experimental methods.

6.2) ^{181}Hf(^{181}Ta) as a TDPAC probe

For a radioactive source to be a good candidate as a TDPAC probe, it must have several properties [3]:

1) The parent isotope is such that it is easy to produce, with a good half-life. If the half-life of the parent isotope is short, the TDPAC experiment must be conducted “on-line”, i.e., on-site in the ISOLDE hall.
2) The half-life $t_{1/2}$ of the intermediate state of the TDPAC probe must lie within the order of $10\ ns$ to $1\ \mu s$. The lower limit is due to the time-resolution detector (which could improve with technological advances), while the upper limit is due to the signal-to-noise ratio, in which the rate of the real coincidence to accidental coincidence count decreases with $t_{1/2}$.
3) For EFG characterisation, the quadrupole moment Q must be significant, i.e., $Q \geq 0.1b$.
4) The effective orientation $A_{2,eff}(\gamma_1)/A'_{2,eff}(\gamma_1)$ and correlation $A_{2,eff}(\gamma_2)$ anisotropy coefficients must be sufficiently large as well, and the energy of the γ_1-ray must be distinguishable from the energy of the γ_2-ray.
5) The probability of the daughter isotope reaching the desired intermediate state must be moderately high, such that the signal arising from the detection of γ_1-ray or the conversion electron is sufficiently high and above the signal-to-noise ratio.

^{181}Hf$\rightarrow^{181}$Ta is considered a suitable TDPAC probe for both EFG studies related to e−γ and γ−γ TDPAC spectroscopy, as it fits all five criteria (See Figure 17). We note that for the e−γ TDPAC spectroscopy, we detect the conversion electrons arising from <L> shell, as they have the highest signal-to-noise ratio. Also, the emission spectrum of the <L> shell electrons peaks at $122\ keV$, as we would need to consider the binding energy of the <L> shell ($\sim 11\ keV$).

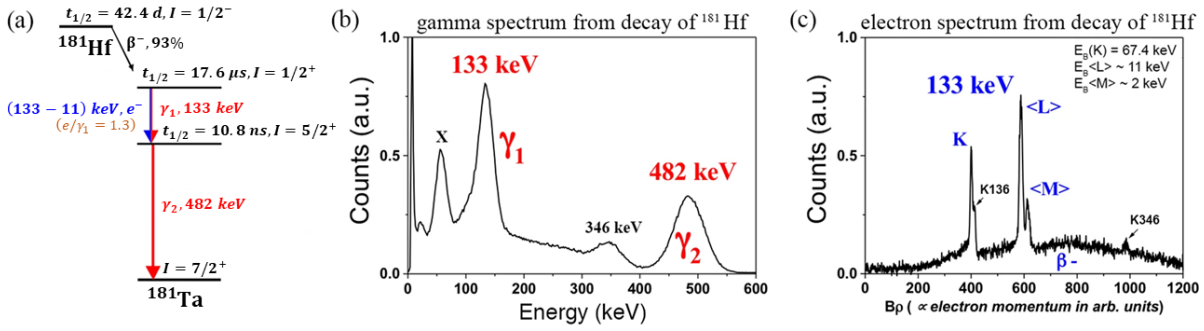


*Figure 47: (**a**) The relevant decay paths of ^{181}Hf(^{181}Ta), with the fractions representing the quantum number of the total angular momentum I of the particular state. More details can be found in reference [84]. (**b**) The emission spectrum of γ rays, with γ_1 at 133 keV and γ_2 at 482 keV. (**c**) The emission spectrum of electrons, in which we take the <L> shell with an average energy of 122 keV (133 keV–11 keV) for e−γ TDPAC spectroscopy. Adapted with permission from Ref. [18] and reproduced from [2] under the Creative Commons Attribution 4.0 International License. Copyright 2019, Barbosa, M.B. et al.*

We especially note that the desired ^{181}Hf radioactive isotope is produced by the irradiation of the hafnium oxide (HfO_2) source with neutrons, which causes the neutron capture [^{180}Hf(*n*,γ)] process in the ^{180}Hf isotope in HfO_2 to produce the desired ^{181}Hf isotope, which will be mass separated from other by-products at BONIS.

We emphasise again that for the first-stage process of an isomer probe in γ-γ TDPAC spectroscopy, the TDPAC probe nucleus is de-excited, releasing γ rays of a specific energy that thus do not interact with the electron shells of the TDPAC probe. This issue will not be the case with parent isotopes decaying via electron capture (EC), such as ^{111}In(^{111}Cd) [85]. However, ^{181}Hf decays via the beta-minus emission to the $1/2^+$ excited nuclear level in ^{181}Ta. This level has a half-life of $17.6\ \mu s$ [85], which is long enough for electronic rearrangements. Thus, no after-effects [86] from the primary ^{181}Hf decay are expected in the subsequent TDPAC cascades proceeding via the $5/2^+$ state with a $10.8\ ns$ half-life (See Figure 1a for the ^{181}Hf→^{181}Ta decay path).

6.3) Experimental procedure for ^{181}Ta(TiO_2) γ−γ and e−γ TDPAC spectroscopy

With the completion of the literature review on the ^{181}Ta(TiO_2) γ−γ spectroscopy, as well as the physics of the study of the EFGs using the ^{181}Hf(^{181}Ta) TDPAC probe nucleus, we are ready to describe the experimental procedure and our experimental conditions of our ^{181}Ta(TiO_2) γ−γ and e−γ TDPAC spectroscopy.

6.3.1) ^{181}Hf(^{181}Ta) implantation process into rutile TiO_2

The radioactive isotope ^{181}Hf (half-life of 42.4 days) was produced by irradiating $1.5\ mg$ of hafnium oxide (HfO_2) powder for six days in a thermal-neutron flux of $10^{15}\ n\ \mathrm{cm}^{-2}\ \mathrm{s}^{-1}$ in the V4 beam tube of the high-flux reactor of Institut Laue-Langevin (ILL) in Grenoble, France. The ^{180}Hf isotope in the hafnium oxide undergoes neutron capture [^{180}Hf(*n*,γ)] to produce the desired ^{181}Hf isotope.

Single crystal rutile TiO_2 substrates measuring $10 \times 10 \times 1.0\ mm^3$ were commercially purchased from Crystal GmbH in Germany [87] (See Figure 18 for a photograph of the crystal(s)). The samples were then brought to BONIS, where a long side of the sample was ion-implanted with ^{181}Hf isotopes at $80\ keV$ and an incidence angle of $10°$ with respect to the

normal of the sample. The beam-sweeping technique was employed, ensuring that the implanted face of the sample was homogeneously covered with the implanted ^{181}Hf isotope.

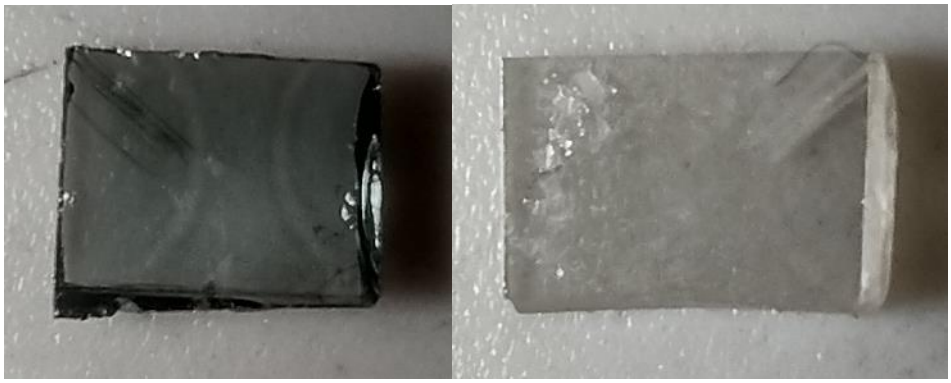


Figure 18: A photograph of both TiO_2 samples after completion of the TDPAC spectroscopies, commercially fabricated and purchased by Crystal GmbH [87]. Both samples are ion-implanted with ^{181}Hf isotope at 80 keV and were sufficiently annealed at a temperature of 873K in a vacuum for 5.25 h. The photographs are adapted from [2] under the Creative Commons Attribution 4.0 International License.

Some technical details of the implantation process and the Bonn Radioisotope Separator are already available in section 1.2, with the complete information in references [9,65].

A quick and naive calculation of the stopping and range of ions in matter (SRIM, [88]) for the implantation of ^{181}Hf in rutile TiO_2 using the stoichiometric composition and with a density of $4.25\ g/cm^3$ [89] reveals a peak of 233 Å with a standard deviation of 60 Å (Figure 19). This calculation implies that the ^{181}Hf isotope is deeply embedded in the bulk region of the rutile TiO_2 substrate. Thus, short of thermal diffusion at sufficiently high temperatures, we expect our resulting TDPAC signals of ^{181}Ta to probe the bulk region of TiO_2.

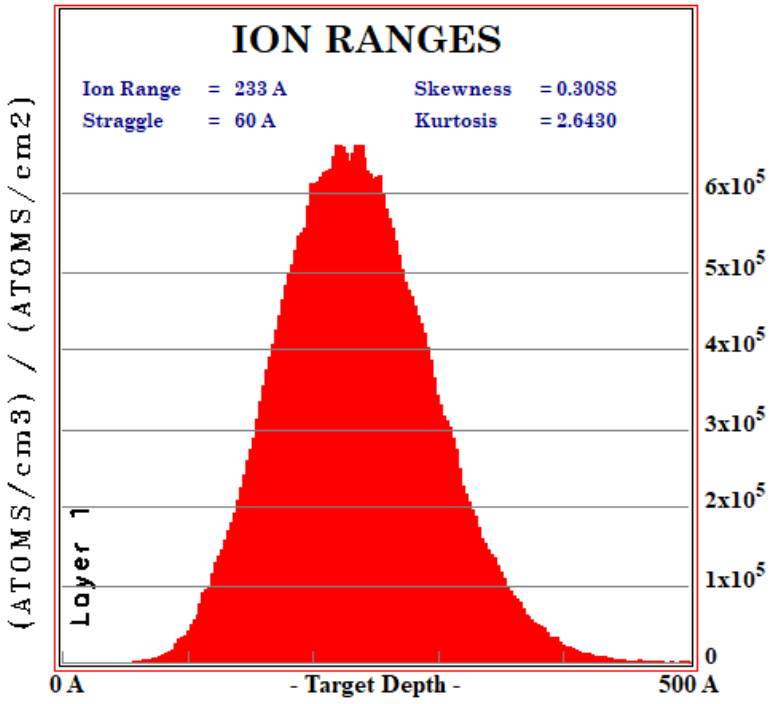


Figure 19: Simulation of distribution of stopping range of implanted 181Hf isotope in rutile TiO2 using SRIM 2013 [88]. We assume that rutile TiO2 has a density of 4.25 g/cm3 [89]. It is adapted from [2] under the Creative Commons Attribution 4.0 International License.

6.3.2) Data Acquisition of $^{181}Ta(TiO_2)$ γ−γ and e−γ TDPAC Spectroscopy

The resulting samples were then safely transported to the SSP lab at ISOLDE, CERN, where they were sufficiently annealed at a temperature of $873\ K$ in a vacuum for $5.25\ h$ to repair the damage and the distortion to the TiO_2 lattice caused by ^{181}Hf-ion implantation and to allow ^{181}Hf to diffuse to a preferable site.

The samples were then analysed by both γ-γ and e-γ TDPAC spectroscopies. As mentioned in section 5.2, six $LaBr_3$ scintillators in the standard geometry [46] were used in a coincidence setup of the $133 - 482\ keV$ γ-cascade of the ^{181}Ta isotope (Figure 17a,b) for the γ-γ TDPAC spectroscopy.

For the e-γ TDPAC spectroscopy, the coincidence setup consists of two electron detectors and two γ-ray detectors, as mentioned in section 5.2. The electron detectors consist of magnetic lenses of the Siegbahn type [51] that focus the $122\ keV$ conversion electrons arising from the internal conversion onto fast plastic scintillator detectors (Figure 17a,c). In contrast, the corresponding γ-ray detectors consist of BaF_2 scintillators that detect the $482\ keV$ γ-rays arising from the decay of the $5/2^+$ level (Figure 17a,b).

For e−γ TDPAC spectroscopy, we placed one such sample in the preferred Raghavan geometry configuration [90], where the long side of the $^{181}Ta(TiO_2)$ sample (the $10 \times 10\ mm^2$ side) makes a $45°$ angle with the detectors in the $x - y$ plane of the detector setup. Another such sample was used for the γ−γ TDPAC spectroscopy. However, the sample could not be mounted in the Raghavan geometry due to vertical constraints. Hence the sample was additionally tilted at an angle with respect to the z-axis.

The corresponding raw TDPAC signals were then processed, first through Interlude™ [91] to extract out $R(t)$ and then through Gfit19™, which is a modified version of the NNfit™ software package [92–94]. For the six-detector γ−γ TDPAC spectroscopy setup, we produce four $R(t)$ graphs, three of which correspond to the four-detector configuration in the $x - y$, $x - z$, and $y - z$ plane, while the last $R(t)$ graph corresponds to the full six-detector setup. With the four-detector e−γ TDPAC spectroscopy setup at each temperature point, we produce only a single $R(t)$ graph. Given that the concept of angles is ill-defined for $R(t)$ corresponding to the six-detector setup, we use the polycrystalline fit instead of the single crystal fit, unlike the other $R(t)$ graphs. In addition, we verified with Nightmare™ that $R(t)$ fits independently [95].

Based on private communication with Correia [39,43-45,96,97] and alongside the geometry of both our TDPAC setups, we use the following parameters for the effective $A_{kk} = A_{2,\text{eff}}(\gamma_1)A_{2,\text{eff}}(\gamma_2)$ for the γ−γ TDPAC spectroscopy:

$$A_{22} = -0.2213, A_{24} = -0.0276, A_{42} = -0.1491, A_{44} = -0.0186.$$

For our e−γ TPDAC spectroscopy ($A_{kk} = b_2 A_{2,\text{eff}}(\gamma_1)A_{2,\text{eff}}(\gamma_2)$), we use

$$A_{22} = -0.3077, A_{24} = -0.0494, A_{42} = -0.0803, A_{44} = -0.0129.$$

Finally, our time calibration is 0.101 ns/channel for our γ-γ TDPAC spectroscopy and 0.195 ns/channel for our e-γ TDPAC spectroscopy.

6.3.3) X-ray Diffraction of the $^{181}Ta(TiO_2)$ Sample after the γ−γ and e−γ TDPAC Spectroscopy

After the completion of both $^{181}Ta(TiO_2)$ γ-γ and e-γ TDPAC spectroscopies, both samples, as well as another fresh and commercially manufactured rutile TiO_2 sample bought from Crystals GmbH [87] (for reference), were sent to the University of São Paulo, Brazil. X-ray diffraction (XRD) using the Empyrean diffractometer (Malvern Panalytical, [98]) was conducted on the samples to determine their global crystalline structure unambiguously. We have also compared our diffractogram(s) to the corresponding results produced in the paper of Guo et al. [99], in which the mentioned researchers fabricated their own single crystal rutile TiO_2 from powdered anatase TiO_2 using the floating zone method (See [100] for a detailed explanation of the floating zone method).

In the Empyrean diffractometer, the crystal is, with its long side, placed face up in the goniometer and was subjected to a beam of X-rays (K_α, K_β lines) produced by the deceleration of the electrons in the copper plate target. The voltage and current of the electrons are $45\ kV$ and $40\ mA$. The sample is then rotated through an angle of 5 to 80 degrees, with a step size of 0.013 degrees and a step time of $2\ s$. The detectors capture X-rays (both background and crystal-reflected) in the angle direction in the Empyrean diffractometer. To generate the diffractogram, we subtract the background intensity (measurements with the absence of the crystal) from the observed intensity, which is succinctly referred to as “Icalc” in the outputs of the Empyrean diffractometer. Considering the kinetic energy of the electrons and that we are analysing a commercially manufactured single crystal rutile TiO_2, we expect our diffractogram to mainly reflect a single dominant peak in a specified crystalline direction.

The peaks of the diffractogram are fitted with the corresponding analysis software graciously provided onboard the Empyrean diffractometer, giving various information such as the full width at half maximum (FWHM), crystalline size, and microstrain. With this XRD analysis, we could investigate, in more detail, the effects of the implantation of the ^{181}Hf isotopes and the subsequent annealing with respect to our single crystal rutile TiO_2 sample.

6.3.4) Expectations from $^{181}Ta(TiO_2)$ γ-γ and e-γ TDPAC Spectroscopies

From the literature, the hyperfine parameters extracted from the TDPAC observable for bulk $^{181}Ta(TiO_2)$ γ-γ TDPAC spectroscopy reveal only the presence of electric quadrupole interactions but not magnetic dipole interactions [59,60]. Furthermore, with extensive annealing, the γ-γ $R(t)$ signal corresponds to the EFGs of just a single site.

The EFGs detected by the $^{181}Ta(TiO_2)$ e−γ TDPAC spectroscopy may differ from the corresponding γ-γ TDPAC spectroscopy if the recombination time is on the half-life order $t_{1/2}$ of the intermediate stage of ^{181}Ta (See section 5.1). Otherwise, both $R(t)$ signals correspond to the same EFG magnitudes.

7) γ-γ and e-γ TDPAC results

This chapter will report our $^{181}Ta(TiO_2)$ γ-γ and e-γ TDPAC spectroscopies.

For the $^{181}Ta(TiO_2)$ γ-γ spectroscopy, seven individual signals, measured under room temperature, are acquired, two of which are signals right after implantation, i.e., unannealed. The following four signals are taken after a 30-minute anneal, i.e., a heat treatment in an oven (vacuum) for 600℃ for 30-minutes, then removed and quenched with wet paper to reduce the temperature drastically. The last signal corresponds to a 315-minute anneal, to which we will compare its (obtained) hyperfine parameters to the relevant literature in the next chapter.

For the $^{181}Ta(TiO_2)$ e-γ spectroscopy, we would measure three signals relating to the unannealed case and five signals with a 30-minute anneal. These signals are measured under room conditions. After that, the remaining 67 signals are taken under various temperatures, but the implanted samples are processed under a 315-minute anneal. We will compare the obtained hyperfine parameters to the relevant literature and its γ-γ kin under room temperature conditions and then explore the temperature dependence of V_{zz} and η of ^{181}Ta in TiO_2 in the next chapter.

Results on the room temperature bulk rutile $^{181}Ta(TiO_2)$ e-γ TDPAC spectroscopy have been communicated and published in [2], which we are augmenting with the temperature-dependent results. The X-ray diffraction results conducted after the conclusion of the TDPAC spectroscopies were previously published in [2] and re-communicated in this thesis. In case of any discrepancies in the numeric of the data, the reader should consult this chapter of this thesis, as it is the later publication in which non-trivial errors are corrected.

7.1) γ-γ TDPAC spectroscopy setup

Table 3 shows the value of the hyperfine parameters and the relevant experimental parameters for the room temperature (and 6-detectors) bulk rutile $^{181}Ta(TiO_2)$ γ-γ TDPAC spectroscopy under various annealing conditions. Note that we have acquired seven independent signals. Signals 1 and 2 correspond to the unannealed case, signals 3-6 correspond to the 30-mins annealed case, while signal 7 corresponds to the 315-mins annealed case. Also, we fixed a unique set of additive and multiplicative constants for each set of signals corresponding to the same degree of annealing. From the geometry of the 6-detector setup, we can have the three 4-detector $R(t)$ signals (termed the x-y, x-z, and y-z detector planes for convenience) and a single 6-detector $R(t)$ signal.

The in-house Gfit19™ program does the $R(t)$ fits. For the individual values of V_{zz}, the fit uncertainty is separated into (a) the statistical uncertainty caused by our instruments and (b) the (dominant) systematic uncertainty of the quadrupole moment (±2.1%) as quoted in reference [23]. (c) We write the value of θ in this way as its uncertainty greatly exceeds its value. Note (1) the large χ^2 value of the six-detector measurement and (2) the large multiplicative constant of the four-detector in the *x-y* plane TDPAC measurement vis-à-vis the two other four-detector TDPAC measurements.

Signal and detector plane	Sample condition	Fundamental frequency ω_0 (Mrad/s)	Asymmetry parameter η	V_{zz} (10^{20} V/m^2)*	Delta Lorentzian δ (%)	Chi Squared χ^2	Theta θ (deg)	Phi ϕ (deg)	Additive constant	Multiplicative constant
1 (x-y)	As Implanted.	763(1)	0.520(6)	141.9 $\pm$ 0.2[a] $\pm$ 3.0[b]	3.2(2)	0.78	-0.02 $\pm$ 9.54[c]	41.5(3)	-0.0169	0.876
1 (x-z)		762(2)	0.527(5)	141.7 $\pm$ 0.3[a] $\pm$ 3.0[b]	3.4(2)	0.73	31.1(6)	43.9(7)	-0.0574	0.703
1 (y-z)		760(1)	0.529(3)	141.4 $\pm$ 0.2[a] $\pm$ 3.0[b]	4.1(2)	0.98	37.8(8)	44.6(6)	-0.0478	0.781
1 (Full)		764(1)	0.526(3)	142.0 $\pm$ 0.2[a] $\pm$ 3.0[b]	3.2(2)	1.0	N.A	N.A	0.00548	0.902
2 (x-y)	As Implanted.	764.4(6)	0.525(3)	142.1 $\pm$ 0.1[a] $\pm$ 3.0[b]	3.31(8)	0.94	0.00 $\pm$ 5.89[c]	41.7(2)	-0.0169	0.876
2 (x-z)		763.4(9)	0.532(2)	141.9 $\pm$ 0.2[a] $\pm$ 3.0[b]	3.5(1)	1.0	32.0(4)	44.1(3)	-0.0574	0.703
2 (y-z)		761.7(7)	0.529(2)	141.6 $\pm$ 0.1[a] $\pm$ 3.0[b]	3.93(9)	1.3	38.1(4)	44.7(2)	-0.0478	0.781
2 (Full)		765.0(6)	0.529(2)	142.2 $\pm$ 0.1[a] $\pm$ 3.0[b]	3.25(8)	1.8	N.A	N.A	0.00548	0.902
3 (x-y)	TA=600C, 30m, vacuum.	762.1(7)	0.541(1)	141.7 $\pm$ 0.1[a] $\pm$ 3.0[b]	0.24(9)	0.71	70(1)	43(2)	-0.0955	0.764
3 (x-z)		761(2)	0.547(5)	141.5 $\pm$ 0.4[a] $\pm$ 3.0[b]	0.7(3)	0.63	35(3)	45(1)	-0.195	0.356
3 (y-z)		760(2)	0.548(5)	141.2 $\pm$ 0.3[a] $\pm$ 3.0[b]	0.3(2)	0.81	30(3)	46(1)	-0.190	0.308
3 (Full)		762(1)	0.540(3)	141.6 $\pm$ 0.2[a] $\pm$ 3.0[b]	1.1(1)	1.1	N.A	N.A	-0.119	0.763
4 (x-y)	TA=600C, 30m, vacuum.	763.1(7)	0.540(1)	141.9 $\pm$ 0.1[a] $\pm$ 3.0[b]	0.30(9)	0.69	70(1)	44(1)	-0.0955	0.764
4 (x-z)		761(2)	0.546(3)	141.6 $\pm$ 0.3[a] $\pm$ 3.0[b]	0.9(1)	0.64	34(3)	45.3(9)	-0.195	0.356
4 (y-z)		759(2)	0.549(5)	141.2 $\pm$ 0.3[a] $\pm$ 3.0[b]	0.36(5)	0.82	31(2)	46(1)	-0.190	0.308
4 (Full)		763(1)	0.538(2)	141.9 $\pm$ 0.2[a] $\pm$ 3.0[b]	1.2(1)	1.2	N.A	N.A	-0.119	0.763

Signal and detector plane	Sample condition	Fundamental frequency ω_0 (Mrad/s)	Asymmetry parameter η	V_{zz} (10^{20} V/m^2)*	Delta Lorentzian δ (%)	Chi Squared χ^2	Theta θ (deg)	Phi ϕ (deg)	Additive constant	Multiplicative constant
5 (x-y)	TA=600C, 30m, vacuum.	763.3(6)	0.540(1)	141.9 $\pm$ 0.1[a] $\pm$ 3.0[b]	0.36(8)	0.66	70(1)	43(1)	−0.0955	0.764
5 (x-z)		762(2)	0.544(3)	141.6 $\pm$ 0.4[a] $\pm$ 3.0[b]	1.09(9)	0.62	34(3)	45.3(9)	−0.195	0.356
5 (y-z)		759(2)	0.552(4)	141.2 $\pm$ 0.3[a] $\pm$ 3.0[b]	0.6(2)	0.83	34(2)	45.4(8)	−0.190	0.308
5 (Full)		764(1)	0.537(2)	142.0 $\pm$ 0.2[a] $\pm$ 3.0[b]	1.3(1)	1.2	N.A	N.A	−0.119	0.763
6 (x-y)	TA=600C, 30m, vacuum.	762.6(3)	0.541(1)	141.79 $\pm$ 0.05[a] $\pm$ 3.00[b]	0.36(3)	0.76	70.3(5)	42.7(6)	−0.0955	0.764
6 (x-z)		760.2(8)	0.548(2)	141.4 $\pm$ 0.2[a] $\pm$ 3.0[b]	1.0(1)	0.82	36(1)	45.8(4)	−0.195	0.356
6 (y-z)		761.6(7)	0.545(2)	141.6 $\pm$ 0.1[a] $\pm$ 3.0[b]	0.60(8)	0.98	33.7(9)	45.4(5)	−0.190	0.308
6 (Full)		762.8(4)	0.539(1)	141.83 $\pm$ 0.07[a] $\pm$ 3.00[b]	1.27(6)	4.1	N.A	N.A	−0.119	0.763
7 (x-y)	TA=600C, 315m, vacuum.	761.8(2)	0.542(1)	141.64 $\pm$ 0.04[a] $\pm$ 3.00[b]	0.17(3)	0.77	64.3(5)	47.1(3)	−0.0817(5)	0.719(5)
7 (x-z)		761.9(7)	0.545(2)	141.7 $\pm$ 0.1[a] $\pm$ 3.0[b]	0.49(9)	0.79	28.6(8)	45.8(3)	−0.1795(5)	0.314(7)
7 (y-z)		761.5(6)	0.544(2)	141.6 $\pm$ 0.1[a] $\pm$ 3.0[b]	0.46(8)	0.96	29.5(7)	46.3(5)	−0.1843(4)	0.300(6)
7 (Full)		762.0(4)	0.540(1)	141.68 $\pm$ 0.07[a] $\pm$ 3.00[b]	0.94(5)	3.5	N.A	N.A	−0.1111(4)	0.692(5)

Table 3: The table of fitted hyperfine and experimental parameters for the seven independent signals of γ-γ TDPAC measurement of $^{181}Ta(TiO_2)$ with four possible geometries, as returned by the Gfit19™ program. For the individual values of V_{zz}, the fit uncertainty is separated into (a) the statistical uncertainty caused by our instruments and (b) the (dominant) systematic uncertainty of the quadrupole moment (±2.1%) as quoted in reference [23]. (c) We write the value of θ in this way as its uncertainty greatly exceeds its value. Note (1) the large χ^2 value of the six-detector measurement and (2) the large multiplicative constant of the four-detector in the x-y plane TDPAC measurement vis-à-vis the two other four-detector TDPAC measurements. Signal 7 is reproduced in [2].

The left half of figures 20.1 - 20.7 (TOSC0x in figure 20.x corresponding with Signal x in Table 3, where "x" represents the number 1-7) in the following two pages show the $R(t)$ (blue data points) in different geometries after the corresponding raw TDPAC signal was processed with Interlude. The right half shows the corresponding cosine FFT, which displays the frequencies $\omega_i, i \in \{1,2,3\}$ that drive $R(t)$ (Equation (20)), the peak amplitudes $[A_{22}s_i(\eta), i \in \{1,2,3\}]$, and their spread (delta Lorentzian δ).

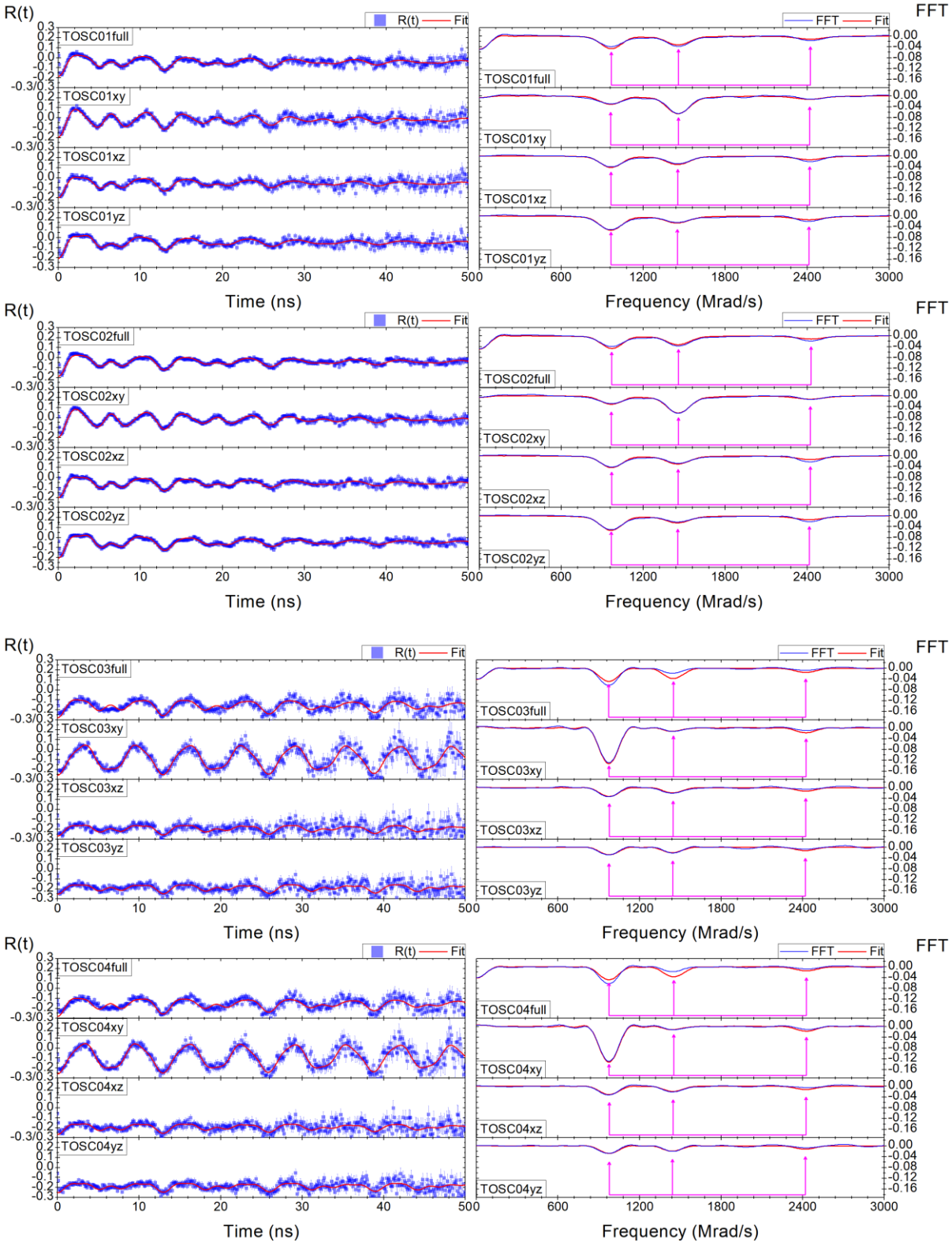


*Figure 20.1 – 20.4: (**left**) $R(t)$ graph and (**right**) corresponding FFT spectrum of the single γ−γ TDPAC measurement of $^{181}Ta(TiO_2)$ with four possible geometries for each signal TOSC0x corresponding to signal x in table 3. The TDPAC probe used is $^{181}Hf \rightarrow ^{181}Ta$, with the raw TDPAC spectrum (from the coincidence searches on the detectors) processed and converted into R(t) observables (see blue curves in $R(t)$ and corresponding FFT graphs) by Interlude™. The $R(t)$ signals are then fit using the Gfit19™ program (see red curves in $R(t)$ and the corresponding FFT graphs). For clarity, we show only the first 50 ns on the $R(t)$ graph because shorter coincidence searches of γ−γ rays are less noisy and thus more statistically significant than longer coincidence searches.*

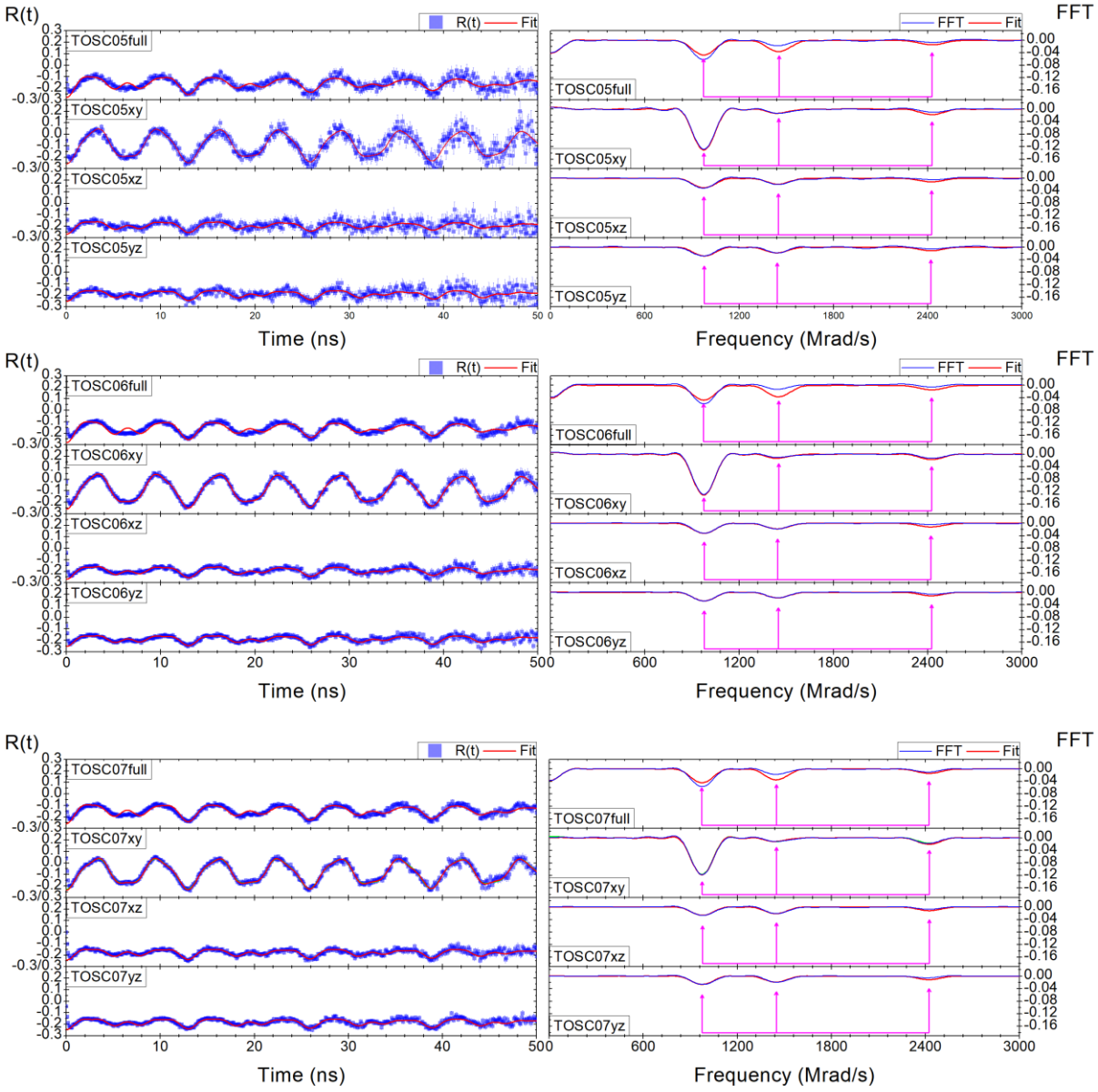


*Figure 20.5 – 20.7: (**left**) $R(t)$ graph and (**right**) corresponding FFT spectrum of the single γ−γ TDPAC measurement of $^{181}Ta(TiO_2)$ with four possible geometries for each signal TOSC0x corresponding to signal x in table 3. The TDPAC probe used is $^{181}Hf \rightarrow ^{181}Ta$, with the raw TDPAC spectrum (from the coincidence searches on the detectors) processed and converted into R(t) observables (see blue curves in $R(t)$ and corresponding FFT graphs) by Interlude™. The $R(t)$ signals are then fit using the Gfit19™ program (see red curves in $R(t)$ and the corresponding FFT graphs). For clarity, we show only the first 50 ns on the $R(t)$ graph because shorter coincidence searches of γ−γ rays are less noisy and thus more statistically significant than longer coincidence searches. Figure 20.7 is reproduced in [2].*

7.2) e-γ TDPAC spectroscopy setup

Table 4 shows the value of the hyperfine parameters and the relevant experimental parameters for the temperature-dependent 4-detector bulk rutile $^{181}Ta(TiO_2)$ e-γ TDPAC spectroscopy under various annealing conditions. Signals 1 to 3 described the signal under no annealing and were measured in room temperature conditions. Signals 4 to 8 described the signal under 30-minute annealing and were measured in room temperature conditions. Signals 9 to 49b described the signal under 315-minute annealing and were measured with

the surrounding temperature varying from $39.3 - 474.15\ K$ (Refer to table 4 for the exact temperature).

We note for all signals corresponding to either no annealing or annealing under 315-minutes (i.e., all signals except signals 4-8), the sample is placed such that the direction of V_{zz} (the largest EFG component of ^{181}Ta embedded in the TiO_2 matrix) is perpendicular to the plane where the four detectors reside. In other words, the polar angle θ is $0°$, and our sample lies flat with respect to the detector plane. For signals 4-8, our ^{181}Ta(TiO_2) sample is tilted at a $45°$ angle with respect to the detector plane, i.e., $\theta = 45°$. This change will be reflected in the column denoting the angle φ in table 4, with the inclusion of the additional angle θ on top of angle φ for signals 4-8.

In fitting the $R(t)$ spectrum from our e-γ TDPAC experiment, we realized that the multiplicative constant does not deviate significantly from unity and hence was fixed to 1. Furthermore, we note that we have taken the TDPAC signals in several settings, and between each set, the ^{181}Ta(TiO_2) sample was taken out, to be put back in after an annealing operation or transferred to a new sample holder between the furnace and the cryostat:

1) Signals 1-3 under no annealing (Additive constant is taken to be varied)
2) Signals 4-8 under 30-mins annealing (Additive constant is fixed at -0.0398)
3) Signals 9-23b under 315-mins annealing, with the sample placed in the furnace (Additive constant is fixed at 0.0187).
4) Signals 24-49b under 315-mins annealing, with the sample placed in the cryostat (Additive constant is fixed at 0.00851).

$R(t)$ signals are generated from the same sample in a unique sample holder and are expected to have the same additive constant if the experimental setup is not altered or disturbed in any form.

Note also that the angle θ is robust against fitting and does not deviate significantly from zero (with the error included). Thus, for all $R(t)$ signals (excluding signals 4-8), we fixed $\theta = 0°$. For signals 4-8, we allow for the varying of θ.

$R(t)$ signal	Sample condition	Measurement Temperature (Kelvins)	Fundamental frequency ω_0 (Mrad/s)	Asymmetry parameter η	V_{zz} $(10^{20}$ V/m$^2)^*$	Delta Lorentzian δ (%)	Chi Squared χ^2	Phi ϕ (deg)	Additive constant
1	As Implanted.	Room	764(4)	0.54(1)	142.0 $\pm$ 0.7^a $\pm$ 3.0^b	6.6(7)	0.98	41.3(6)	$-0.0181(3)$
2	As Implanted.	Room	766.31(7)	0.525(7)	142.48 $\pm$ 0.01^a $\pm$ 3.02^b	6.0(2)	1.2	38.5(2)	$-0.005(1)$
3	As Implanted.	Room	759.70(1)	0.519(4)	141.255 $\pm$ 0.002^a $\pm$ 2.993^b	6.1(2)	1.4	38.8(2)	$-0.00(1)$
4	TA=600C, 30m, vacuum.	Room	762(2)	0.548(4)	141.6 $\pm$ 0.4^a $\pm$ 3.0^b	1.1(3)	0.83	45(3)^c 58.8(7)	-0.0398
5	TA=600C, 30m, vacuum.	Room	760(2)	0.548(4)	141.3 $\pm$ 0.3^a $\pm$ 3.0^b	1.0(2)	0.83	44(3)^c 57.9(6)	-0.0398
6	TA=600C, 30m, vacuum.	Room	763.0(8)	0.543(2)	141.9 $\pm$ 0.2^a $\pm$ 3.0^b	0.9(1)	0.94	45(1)^c 58.5(3)	-0.0398
7	TA=600C, 30m, vacuum.	Room	762.9(5)	0.543(1)	141.85 $\pm$ 0.09^a $\pm$ 3.01^b	0.95(7)	1.3	45.7(8)^c 58.5(2)	-0.0398
8	TA=600C, 30m, vacuum.	Room	762.4(5)	0.543(1)	141.75 $\pm$ 0.09^a $\pm$ 3.00^b	1.04(7)	1.4	45.9(8)^c 58.4(2)	-0.0398
9	TA=600C, 315m, vacuum.	296.15	765.0(5)	0.549(3)	142.23 $\pm$ 0.09^a $\pm$ 3.01^b	0.03(6)	0.72	37.8(4)	0.0187
10	TA=600C, 315m, vacuum.	296.15	765.6(3)	0.546(2)	142.35 $\pm$ 0.06^a $\pm$ 3.02^b	0.04(6)	0.99	37.9(2)	0.0187
10B	TA=600C, 315m, vacuum.	296.15	765.6(3)	0.546(2)	142.35 $\pm$ 0.06^a $\pm$ 3.02^b	0.04(6)	0.99	37.9(2)	0.0187
11	TA=600C, 315m, vacuum.	348.45	767.9(5)	0.548(3)	142.8 $\pm$ 0.1^a $\pm$ 3.0^b	0.04(6)	0.71	37.1(3)	0.0187
12	TA=600C, 315m, vacuum.	348.45	768.0(4)	0.549(2)	142.79 $\pm$ 0.07^a $\pm$ 3.03^b	0.03(4)	0.89	37.5(3)	0.0187
13	TA=600C, 315m, vacuum.	395.75	768.8(4)	0.545(2)	142.96 $\pm$ 0.07^a $\pm$ 3.03^b	0.03 $\pm$ 0.12^d	0.97	37.7(3)	0.0187
14	TA=600C, 315m, vacuum.	426.85	770.5(7)	0.552(3)	143.3 $\pm$ 0.1^a $\pm$ 3.0^b	0.039 $\pm$ 0.099^d	0.82	36.7(4)	0.0187
15	TA=600C, 315m, vacuum.	426.95	769.3(6)	0.549(3)	143.0 $\pm$ 0.1^a $\pm$ 3.0^b	0.03 $\pm$ 0.177^d	0.68	37.5(4)	0.0187

$R(t)$ signal	Sample condition	Measurement Temperature (Kelvins)	Fundamental frequency ω_0 (Mrad/s)	Asymmetry parameter η	V_{zz} $\left(10^{20}\ \mathrm{V/m^2}\right)^*$	Delta Lorentzian δ (%)	Chi Squared χ^2	Phi ϕ (deg)	Additive constant (fixed)
15B	TA=600C, 315m, vacuum.	426.95	765.2(6)	0.549(3)	142.3 $\pm$ 0.1[a] $\pm$ 3.0[b]	0.031 $\pm$ 0.199[d]	0.97	37.2(4)	0.0187
16	TA=600C, 315m, vacuum.	474.15	771.8(4)	0.550(2)	143.51 $\pm$ 0.07[a] $\pm$ 3.04[b]	0.03(5)	0.88	37.7(3)	0.0187
16B	TA=600C, 315m, vacuum.	474.15	771.8(4)	0.550(2)	143.51 $\pm$ 0.07[a] $\pm$ 3.04[b]	0.03(5)	0.88	37.7(3)	0.0187
17	TA=600C, 315m, vacuum.	430.95	770.5(5)	0.552(3)	143.26 $\pm$ 0.09[a] $\pm$ 3.04[b]	0.09(6)	0.60	37.5(3)	0.0187
18	TA=600C, 315m, vacuum.	428.45	770.5(5)	0.551(2)	143.27 $\pm$ 0.09[a] $\pm$ 3.04[b]	0.10(6)	0.66	37.6(3)	0.0187
18B	TA=600C, 315m, vacuum.	428.45	770.5(5)	0.551(2)	143.27 $\pm$ 0.09[a] $\pm$ 3.04[b]	0.10(6)	0.66	37.6(3)	0.0187
19	TA=600C, 315m, vacuum.	396.65	769.4(3)	0.550(2)	143.07 $\pm$ 0.06[a] $\pm$ 3.03[b]	0.033 $\pm$ 0.108[d]	0.80	37.7(2)	0.0187
19B	TA=600C, 315m, vacuum.	396.65	769.4(3)	0.550(2)	143.06 $\pm$ 0.06[a] $\pm$ 3.03[b]	0.033 $\pm$ 0.109[d]	0.80	37.6(2)	0.0187
20	TA=600C, 315m, vacuum.	343.05	767.7(8)	0.552(4)	142.7 $\pm$ 0.2[a] $\pm$ 3.0[b]	0.03(9)	0.70	37.9(6)	0.0187
21	TA=600C, 315m, vacuum.	343.55	766.8(4)	0.547(2)	142.57 $\pm$ 0.08[a] $\pm$ 3.02[b]	0.027 $\pm$ 0.124[d]	0.80	37.9(3)	0.0187
21B	TA=600C, 315m, vacuum.	343.55	766.8(4)	0.547(2)	142.57 $\pm$ 0.08[a] $\pm$ 3.02[b]	0.027 $\pm$ 0.123[d]	0.80	37.9(3)	0.0187
22	TA=600C, 315m, vacuum.	292.55	764.4(3)	0.543(2)	142.12 $\pm$ 0.06[a] $\pm$ 3.01[b]	0.02(2)	0.89	37.5(2)	0.0187
23	TA=600C, 315m, vacuum.	296.35	764.4(3)	0.543(2)	142.12 $\pm$ 0.06[a] $\pm$ 3.01[b]	0.02(2)	0.89	37.5(2)	0.0187
23B	TA=600C, 315m, vacuum.	296.35	764.4(3)	0.543(2)	142.12 $\pm$ 0.06[a] $\pm$ 3.01[b]	0.02(2)	0.89	37.5(2)	0.0187
24	TA=600C, 315m, vacuum.	294.65	763.8(7)	0.536(4)	142.0 $\pm$ 0.1[a] $\pm$ 3.0[b]	0.04(9)	0.73	38.6(5)	0.00851
25	TA=600C, 315m, vacuum.	294	764.6(5)	0.539(2)	142.17 $\pm$ 0.08[a] $\pm$ 3.01[b]	0.09(6)	0.85	38.8(3)	0.00851

$R(t)$ signal	Sample condition	Measurement Temperature (Kelvins)	Fundamental frequency ω_0 (Mrad/s)	Asymmetry parameter η	V_{zz} $(10^{20}$ V/m$^2)^*$	Delta Lorentzian δ (%)	Chi Squared χ^2	Phi ϕ (deg)	Additive constant (fixed)
25B	TA=600C, 315m, vacuum.	294	764.6(5)	0.539(2)	142.17 $\pm$ 0.08^a $\pm$ 3.01^b	0.09(6)	0.85	38.8(3)	0.00851
26	TA=600C, 315m, vacuum.	260.1	762.5(6)	0.543(3)	141.8 $\pm$ 0.1^a $\pm$ 3.0^b	0.1(1)	0.72	37.6(4)	0.00851
27	TA=600C, 315m, vacuum.	260	762.5(5)	0.542(3)	141.78 $\pm$ 0.09^a $\pm$ 3.00^b	0.04(6)	0.78	38.0(4)	0.00851
27B	TA=600C, 315m, vacuum.	260	762.5(5)	0.542(3)	141.78 $\pm$ 0.09^a $\pm$ 3.00^b	0.04(6)	0.78	38.0(4)	0.00851
28	TA=600C, 315m, vacuum.	220	760.3(9)	0.547(5)	141.4 $\pm$ 0.2^a $\pm$ 3.0^b	0.1(1)	0.88	37.4(6)	0.00851
29	TA=600C, 315m, vacuum.	219.6	760.2(6)	0.545(3)	141.3 $\pm$ 0.1^a $\pm$ 3.0^b	0.1(1)	0.84	37.5(2)	0.00851
29B	TA=600C, 315m, vacuum.	219.6	760.2(6)	0.545(3)	141.3 $\pm$ 0.1^a $\pm$ 3.0^b	0.1(1)	0.83	37.5(2)	0.00851
30	TA=600C, 315m, vacuum.	180.21	756(1)	0.547(5)	140.6 $\pm$ 0.2^a $\pm$ 3.0^b	0.1(2)	0.75	37.9(7)	0.00851
31	TA=600C, 315m, vacuum.	179.65	757.2(7)	0.547(4)	140.8 $\pm$ 0.1^a $\pm$ 3.0^b	0.1(1)	0.76	38.3(5)	0.00851
32	TA=600C, 315m, vacuum.	179.89	757.1(5)	0.547(3)	140.8 $\pm$ 0.1^a $\pm$ 3.0^b	0.07(8)	0.82	37.9(4)	0.00851
32B	TA=600C, 315m, vacuum.	179.89	757.1(5)	0.547(3)	140.8 $\pm$ 0.1^a $\pm$ 3.0^b	0.07(8)	0.82	37.9(4)	0.00851
33	TA=600C, 315m, vacuum.	138.74	754.4(4)	0.544(2)	140.28 $\pm$ 0.08^a $\pm$ 2.97^b	0.1(1)	0.89	38.7(3)	0.00851
33B	TA=600C, 315m, vacuum.	138.74	754.4(4)	0.544(2)	140.27 $\pm$ 0.08^a $\pm$ 2.97^b	0.1(1)	0.89	38.7(3)	0.00851
34	TA=600C, 315m, vacuum.	99.1	750.6(9)	0.547(5)	139.6 $\pm$ 0.2^a $\pm$ 3.0^b	0.1(1)	0.65	37.7(6)	0.00851
35	TA=600C, 315m, vacuum.	101.6	750.7(7)	0.548(4)	139.6 $\pm$ 0.1^a $\pm$ 3.0^b	0.1(2)	0.68	37.9(5)	0.00851
36	TA=600C, 315m, vacuum.	100	750.4(6)	0.550(3)	139.5 $\pm$ 0.1^a $\pm$ 3.0^b	0.046 $\pm$ 0.179^d	0.79	37.8(4)	0.00851

$R(t)$ signal	Sample condition	Measurement Temperature (Kelvins)	Fundamental frequency ω_0 (Mrad/s)	Asymmetry parameter η	V_{zz} $(10^{20}$ V/m$^2)^*$	Delta Lorentzian δ (%)	Chi Squared χ^2	Phi ϕ (deg)	Additive constant (fixed)
37	TA=600C, 315m, vacuum.	100	750.2(3)	0.545(2)	139.49 $\pm$ 0.06^a $\pm$ 2.96^b	0.09(4)	0.94	38.4(2)	0.00851
37B	TA=600C, 315m, vacuum.	100	750.2(3)	0.545(2)	139.49 $\pm$ 0.06^a $\pm$ 2.96^b	0.09(4)	0.94	38.4(2)	0.00851
38	TA=600C, 315m, vacuum.	69.99	749(1)	0.558(8)	139.2 $\pm$ 0.2^a $\pm$ 2.9^b	0.045 $\pm$ 0.29^d	1.1	36.0(8)	0.00851
39	TA=600C, 315m, vacuum.	71	747(1)	0.545(7)	138.8 $\pm$ 0.2^a $\pm$ 2.9^b	0.1(3)	1.0	36.4(7)	0.00851
40	TA=600C, 315m, vacuum.	70	746.0(7)	0.545(4)	138.7 $\pm$ 0.1^a $\pm$ 2.9^b	0.14(9)	0.90	37.7(5)	0.00851
41	TA=600C, 315m, vacuum.	70	745.4(6)	0.547(4)	138.6 $\pm$ 0.1^a $\pm$ 2.9^b	0.11(8)	0.92	38.0(4)	0.00851
42	TA=600C, 315m, vacuum.	70	746.9(4)	0.543(2)	138.88 $\pm$ 0.07^a $\pm$ 2.94^b	0.1(1)	0.96	38.5(2)	0.00851
42B	TA=600C, 315m, vacuum.	70	746.9(4)	0.543(2)	138.88 $\pm$ 0.07^a $\pm$ 2.94^b	0.1(1)	0.96	38.5(2)	0.00851
43	TA=600C, 315m, vacuum.	39.3	744(2)	0.537(4)	138.3 $\pm$ 0.3^a $\pm$ 2.9^b	0.3(1)	0.71	37.3(9)	0.00851
44	TA=600C, 315m, vacuum.	296.4	765(1)	0.552(5)	142.2 $\pm$ 0.2^a $\pm$ 3.0^b	0.1(1)	0.60	37.2(7)	0.00851
44B	TA=600C, 315m, vacuum.	296.4	765(1)	0.552(5)	142.2 $\pm$ 0.2^a $\pm$ 3.0^b	0.1(1)	0.60	37.2(7)	0.00851
45	TA=600C, 315m, vacuum.	296.8	765.1(5)	0.544(3)	142.3 $\pm$ 0.1^a $\pm$ 3.0^b	0.06(7)	0.71	36.3(3)	0.00851
45B	TA=600C, 315m, vacuum.	296.8	765.1(5)	0.544(3)	142.3 $\pm$ 0.1^a $\pm$ 3.0^b	0.06(7)	0.71	36.3(3)	0.00851
46	TA=600C, 315m, vacuum.	50.13	747.1(6)	0.544(3)	138.9 $\pm$ 0.1^a $\pm$ 2.9^b	0.07(8)	0.63	35.6(4)	0.00851
47	TA=600C, 315m, vacuum.	49.97	747.1(6)	0.544(3)	138.9 $\pm$ 0.1^a $\pm$ 2.9^b	0.03(4)	0.66	35.5(3)	0.00851
47B	TA=600C, 315m, vacuum.	49.97	747.1(6)	0.544(3)	138.9 $\pm$ 0.1^a $\pm$ 2.9^b	0.03(4)	0.66	35.5(3)	0.00851

$R(t)$ signal	Sample condition	Measurement Temperature (Kelvins)	Fundamental frequency ω_0 (Mrad/s)	Asymmetry parameter η	V_{zz} $(10^{20}$ V/m$^2)^*$	Delta Lorentzian δ (%)	Chi Squared χ^2	Phi ϕ (deg)	Additive constant (fixed)
48	TA=600C, 315m, vacuum.	59.9	747(1)	0.544(5)	$138.9 \pm 0.2^a \pm 2.9^b$	0.1(1)	0.67	35.6(6)	0.00851
49	TA=600C, 315m, vacuum.	59.97	745.9(5)	0.548(3)	$138.7 \pm 0.1^a \pm 2.9^b$	0.1(1)	0.75	35.7(3)	0.00851
49B	TA=600C, 315m, vacuum.	59.97	745.9(5)	0.547(3)	$138.7 \pm 0.1^a \pm 2.9^b$	0.1(1)	0.74	35.6(3)	0.00851

Table 4: The table of fitted hyperfine and experimental parameters for the set of 67 different e-γ TDPAC measurements of $^{181}Ta(TiO_2)$ as returned by the Gfit19™ program. For the individual values of V_{zz}, the fit uncertainty is separated into (a) the statistical uncertainty caused by our instruments and (b) the (dominant) systematic uncertainty of the quadrupole moment (±2.1%) as quoted in reference [23]. (c) For signals 4-8, the $^{181}Ta(TiO_2)$ sample is additionally tilted at a 45° angle with respect to the detector plane, and hence we have an additional free parameter θ. For the rest of the signals, θ is fixed at 0°. (d) The averaged δ is written in this form, as its uncertainty greatly exceeds its value. Room temperature results are reproduced in [2].

The left half of figures 21.1 and 21.2 (TOSC0x contained in figure 20.y corresponds to Signal x in Table 4, where "x" represents the number 1-49, and if applicable, with prefix "B") in the following three pages show the $R(t)$ (blue data points) after the corresponding raw TDPAC signal was processed with Interlude. The right half shows the corresponding cosine FFT, which displays the frequencies $\omega_i, i \in \{1,2,3\}$ that drive $R(t)$ (Equation (20)), the peak amplitudes $[A_{22}s_i(\eta), i \in \{1,2,3\}]$, and their spread (delta Lorentzian δ).

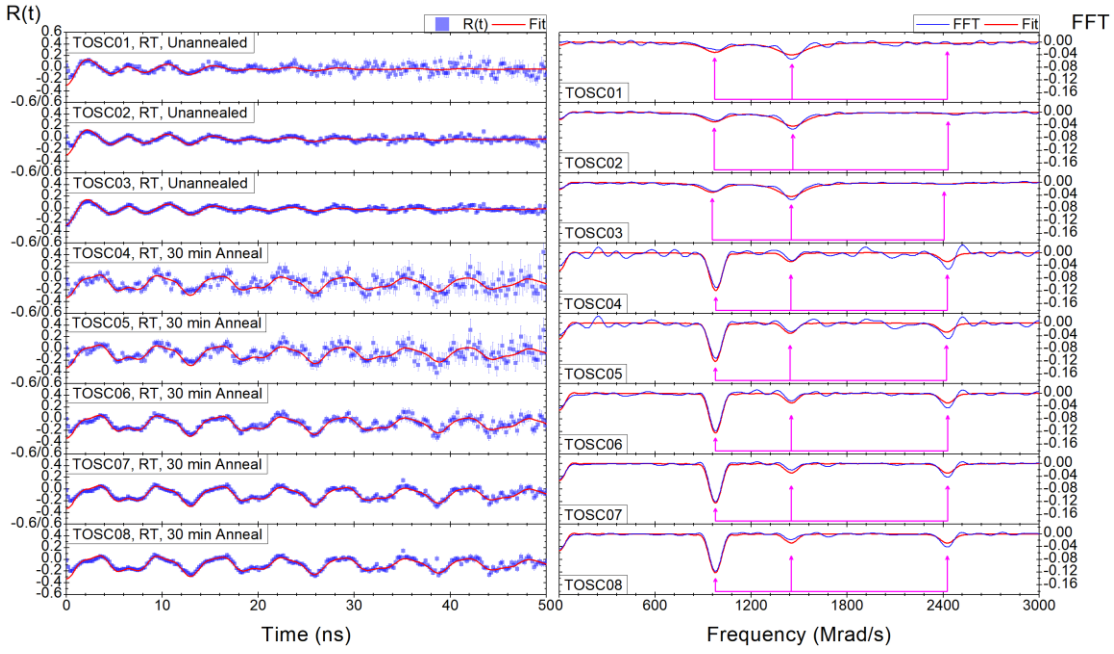
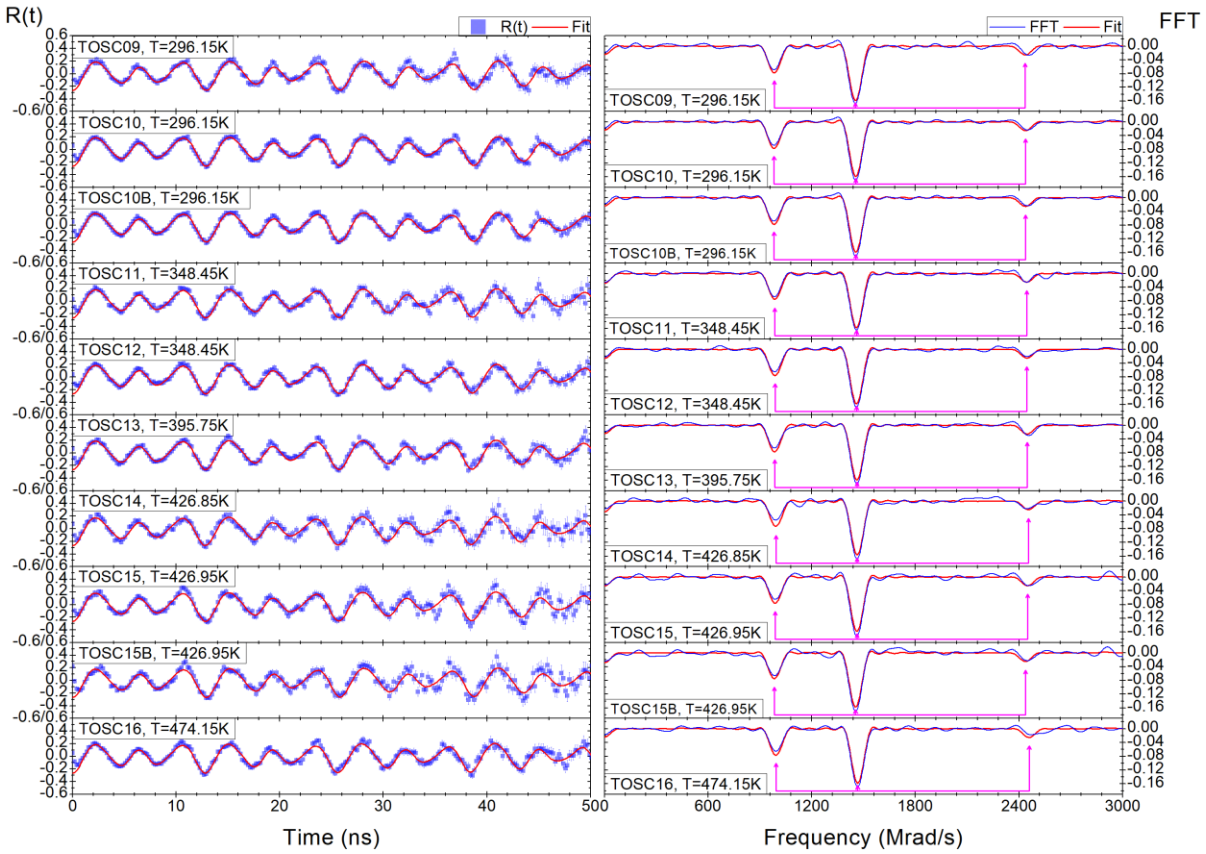
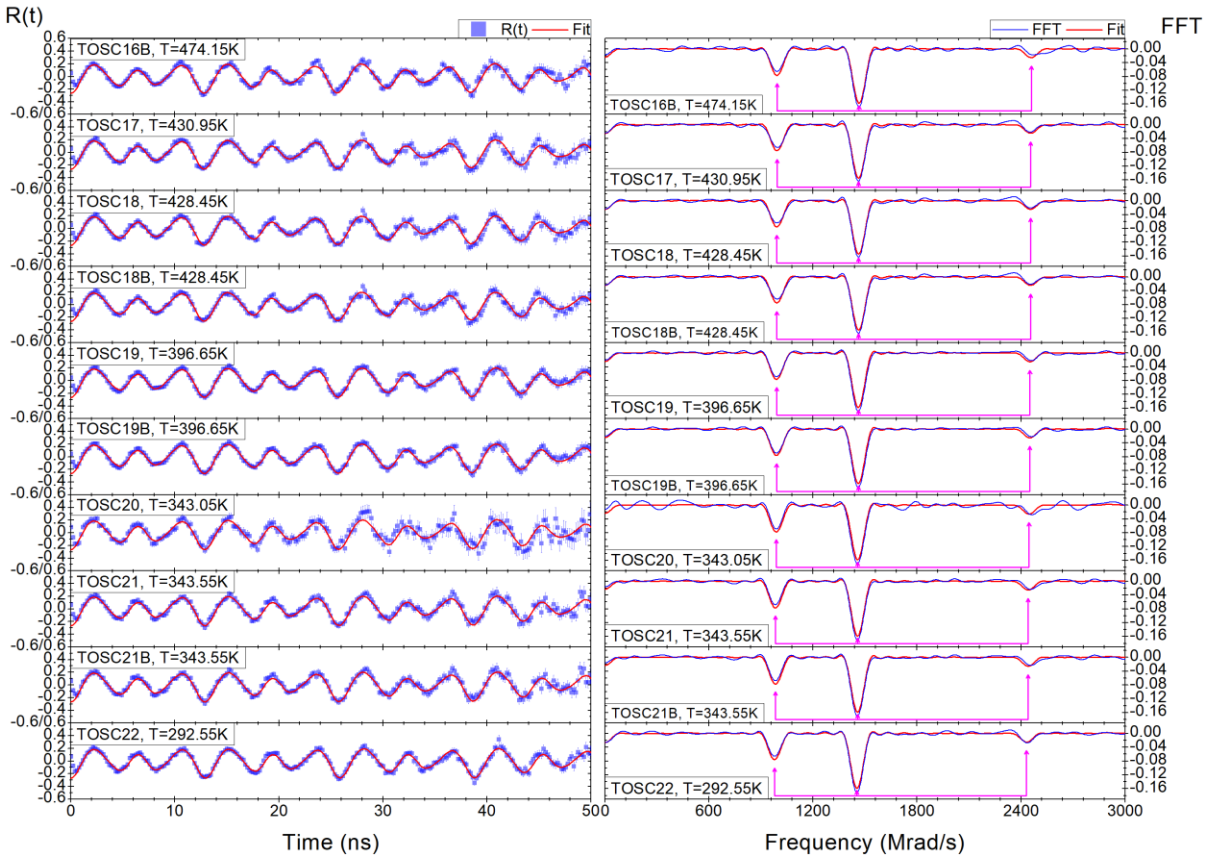
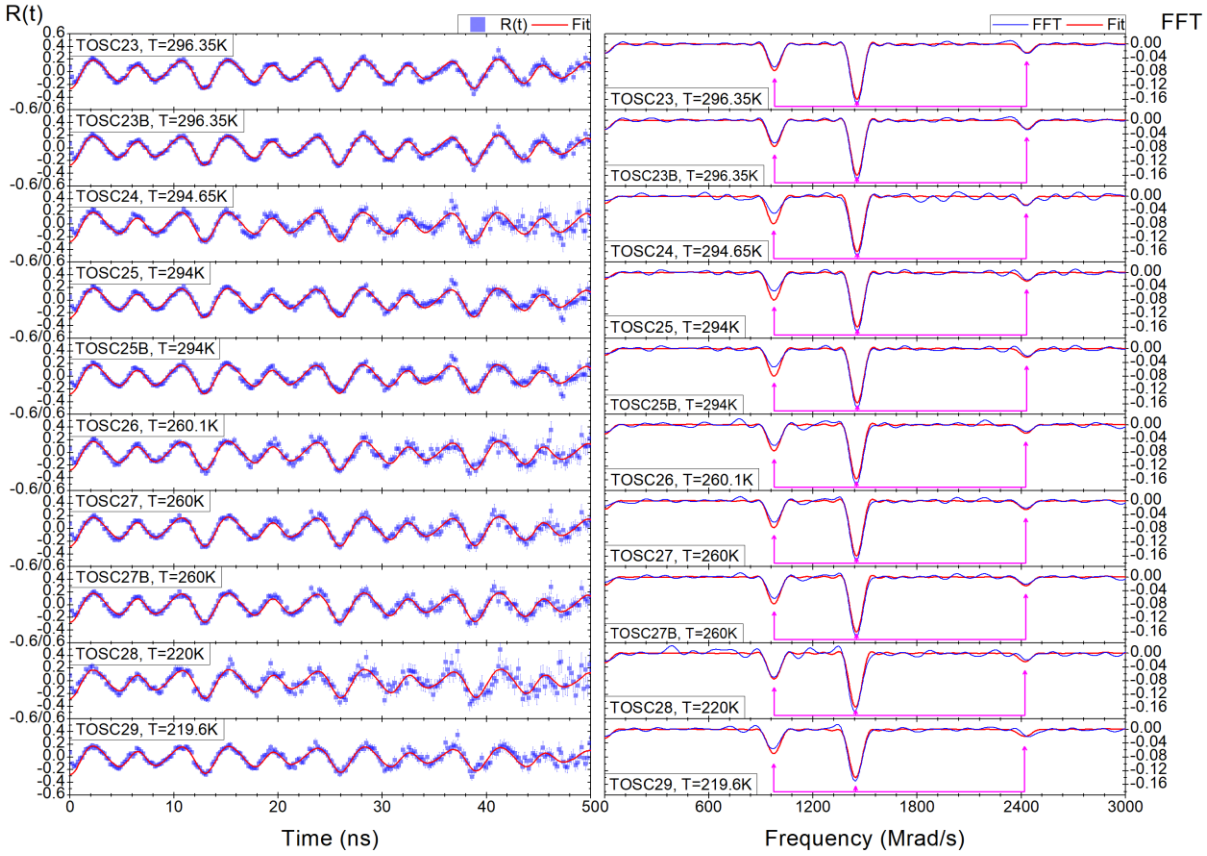
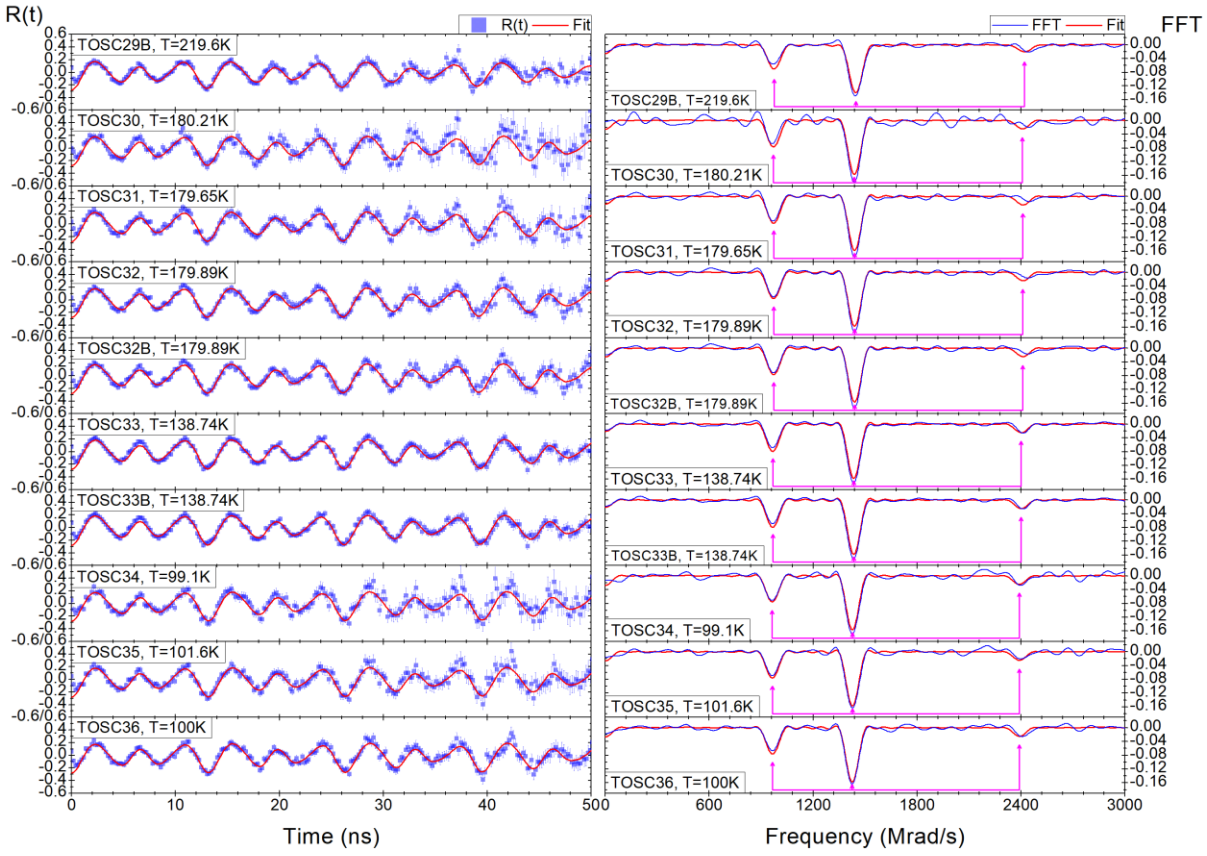


*Figure 21.1: (**left**) R(t) graph and (**right**) corresponding FFT spectrum of the e−γ TDPAC measurements of $^{181}Ta(TiO_2)$ related to the unannealed case and the 30-mins annealed case (TOSC01-TOSC08, corresponding to signals 1-8 respectively). The TDPAC probe used is $^{181}Hf \rightarrow ^{181}Ta$, with the raw TDPAC spectrum (from the coincidence searches on the detectors) processed and converted into $R(t)$ observables [blue curves in the R(t) and the corresponding FFT graphs] by Interlude™. The $R(t)$ signals are then fit by using the Gfit19™ program [see red curves in R(t) and the corresponding FFT graphs]. For clarity, we show only the first 50 ns on the $R(t)$ graph because shorter coincidence searches of e−γ rays are less noisy and thus more statistically significant than longer coincidence searches. Reproduced in [2].*


R(t)
R(t)
Fit
FFT
Fit
FFT
TOSC09, T=296.15K
TOSC10, T=296.15K
TOSC10B, T=296.15K
TOSC11, T=348.45K
TOSC12, T=348.45K
TOSC13, T=395.75K
TOSC14, T=426.85K
TOSC15, T=426.95K
TOSC15B, T=426.95K
TOSC16, T=474.15K
Time (ns)
Frequency (Mrad/s)


R(t)
R(t)
Fit
FFT
Fit
FFT
TOSC16B, T=474.15K
TOSC17, T=430.95K
TOSC18, T=428.45K
TOSC18B, T=428.45K
TOSC19, T=396.65K
TOSC19B, T=396.65K
TOSC20, T=343.05K
TOSC21, T=343.55K
TOSC21B, T=343.55K
TOSC22, T=292.55K
Time (ns)
Frequency (Mrad/s)


R(t)
R(t)
Fit
FFT
Fit
FFT
TOSC23, T=296.35K
TOSC23B, T=296.35K
TOSC24, T=294.65K
TOSC25, T=294K
TOSC25B, T=294K
TOSC26, T=260.1K
TOSC27, T=260K
TOSC27B, T=260K
TOSC28, T=220K
TOSC29, T=219.6K
Time (ns)
Frequency (Mrad/s)


R(t)
R(t)
Fit
FFT
Fit
FFT
TOSC29B, T=219.6K
TOSC30, T=180.21K
TOSC31, T=179.65K
TOSC32, T=179.89K
TOSC32B, T=179.89K
TOSC33, T=138.74K
TOSC33B, T=138.74K
TOSC34, T=99.1K
TOSC35, T=101.6K
TOSC36, T=100K
Time (ns)
Frequency (Mrad/s)

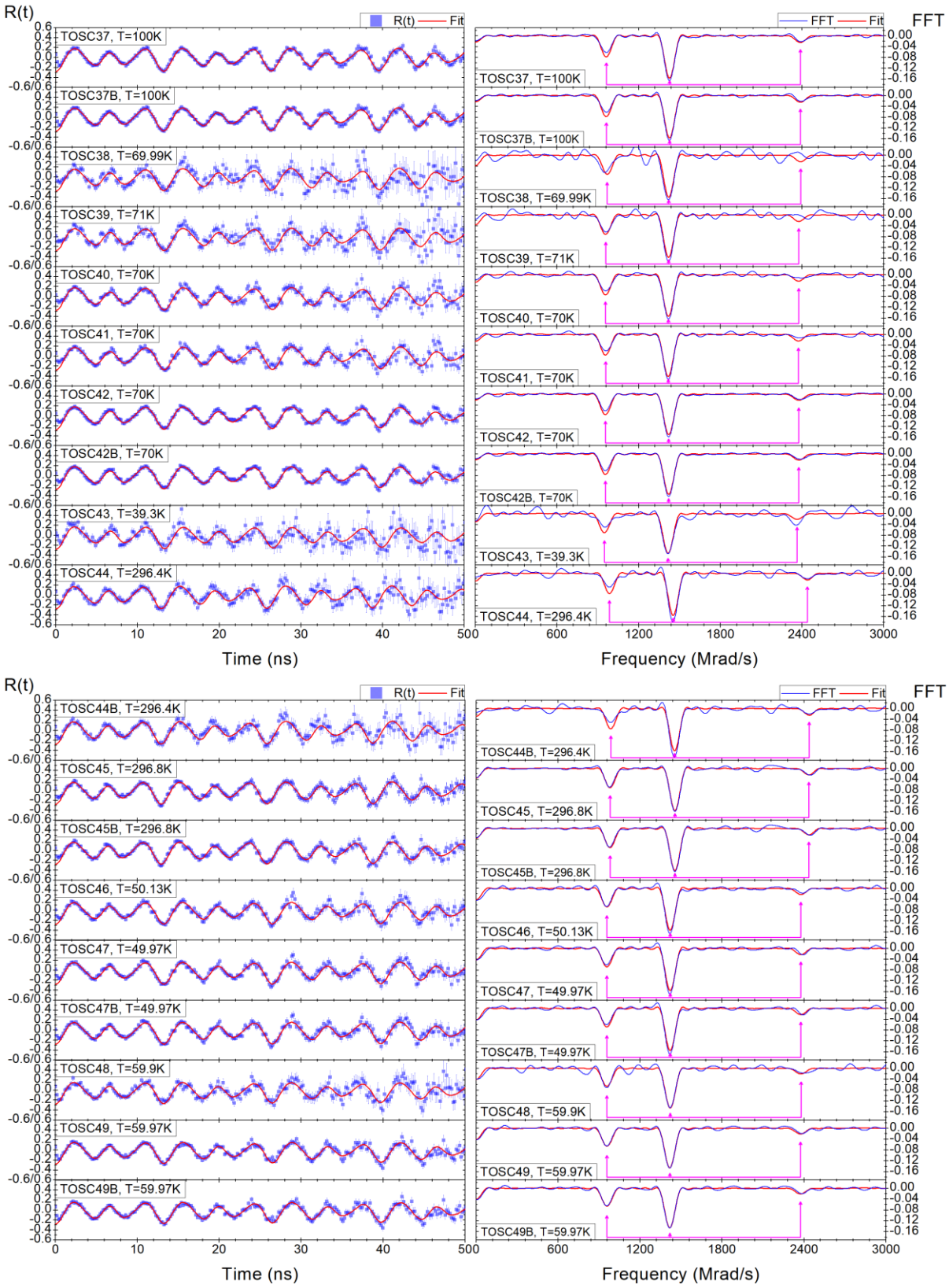


*Figure 21.2: (**left**) R(t) graph and (**right**) corresponding FFT spectrum of the e−γ TDPAC measurements of $^{181}Ta(TiO_2)$ related to the 315-mins annealed case (TOSC09 and onwards, corresponding to signals nine and onwards, respectively). The TDPAC probe used is $^{181}Hf \rightarrow ^{181}Ta$, with the raw TDPAC spectrum (from the coincidence searches on the detectors) processed and converted into $R(t)$ observables [blue curves in the R(t) and the corresponding FFT graphs] by Interlude™. The $R(t)$ signals are then fit by using the Gfit19™ program [see red curves in R(t) and the corresponding FFT graphs]. For clarity, we show only*

the first 50 ns on the $R(t)$ graph because shorter coincidence searches of $e-\gamma$ rays are less noisy and thus more statistically significant than longer coincidence searches.

7.3) X-ray Diffraction of the $^{181}Ta(TiO_2)$ Sample after the $\gamma-\gamma$ and $e-\gamma$ TDPAC Spectroscopy

Note: The following contents in this subchapter are explicitly reproduced ab verbatim from and previously published in [2] under section 4.3: "X-ray Diffraction of the 181Ta(TiO2) Sample after the γ−γ and e−γ TDPAC Spectroscopy". Copyright is retained with the authors.

Figure 22 shows the XRD diffractogram of both our ($80\ keV$ ion-implanted ^{181}Hf complimented with $5.25\ h$ of thermal annealing) TiO_2 samples alongside a corresponding reference sample (fresh sample from Crystals GmbH [87]) for comparison. Note that on the left side of the graphs, we show a log-10 plot of the intensity ("Icalc") between $0-80°$, and on the right-hand side, we show a linear plot of the intensity between $38-40°$. We present the graphs in this way as (1) the peaks in the domain of $39-40°$ dominate all other peaks and (2) to allow for the visualization of the successful resolution of the two most dominant peaks as shown in the right-sided graphs contained in Figure 22.

For ease of comparison, at the bottom of Figure 22, we present two corresponding graphs in which all three diffractograms are normalized (with respect to the highest recorded intensity for each diffractogram) and plotted in the same window(s).

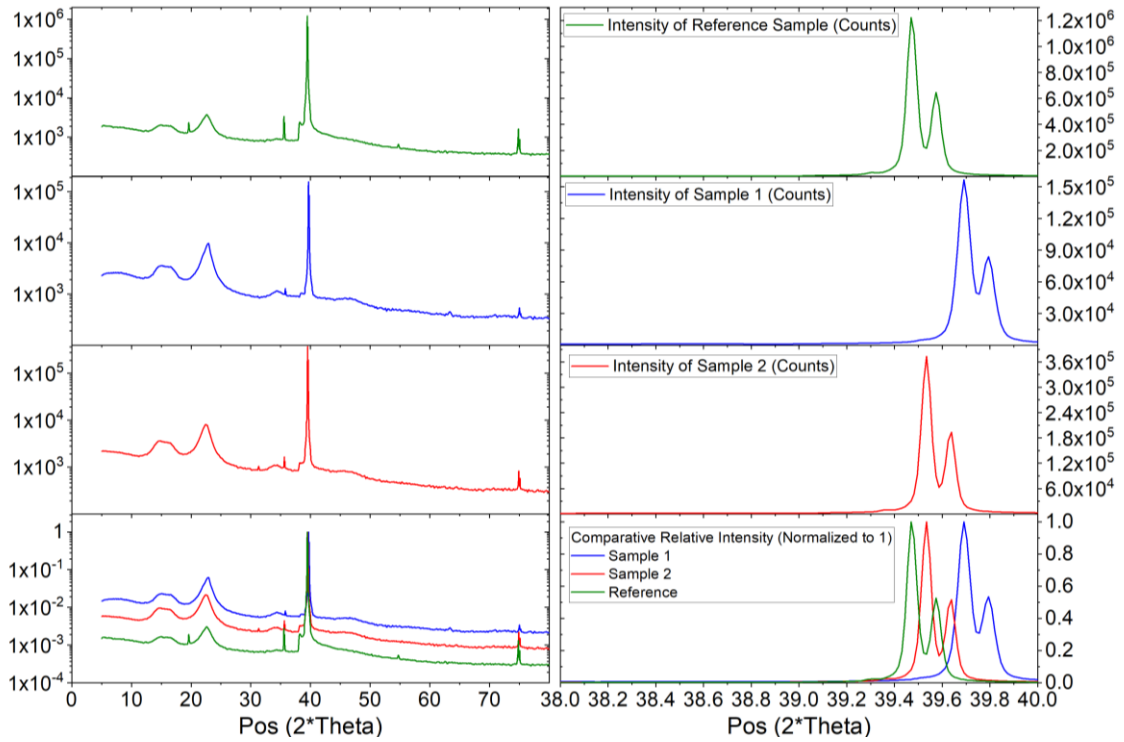


Figure 22: Top graph: The XRD diffractogram of a freshly fabricated TiO_2 sample from Crystal GmbH [87]. The following two graphs: The XRD diffractogram of our (80 keV ion-implanted ^{181}Hf complemented with sufficient thermal annealing) TiO_2 sample, measured after our TDPAC measurements. Bottom graph: the combined XRD diffractogram of the three abovementioned samples, with each corresponding intensity normalized concerning their individual highest recorded intensity. The left side of the graphs is presented as the log-10 plot of the measured intensity (counts) against the diffraction angle from 0–80°. For the top 3 graphs on the left side, the intensity starts from 1×10^{-2}, while for the bottom graph (on the left side), it starts from 1×10^{-4}. The right side of the graphs is presented as the linear plot of the measured intensity (counts) against the restricted domain of the diffraction angle from 38–40°. In all the right-sided graphs, the intensity starts from 0. We present the results of our XRD diffractions in this manner: (a) the peaks in the domain of 39–40° dominate all other peaks, and (b) to allow for the visualization of the successful resolution of the two most dominant peaks. Reproduced in [2].

Table 5 shows the two most dominant peaks (right side of Figure 22) produced by the analysis software (that comes complimentary to the Empyrean diffractometer), alongside the corresponding information (d-spacing, full width at half maximum [FWHM], crystalline size, and micro-strain).

Sample and Peak Number	Angle 2θ ($2 \times$ Deg)	d-Spacing (Angstrom)	Observed Intensity (Counts)	$FWHM$ ($2 \times$ Deg)	Background Intensity (Counts)	Crystallite Size (Angstrom)	Micro-Strain (%)
Reference Sample, Peak 1	39.4731	2.28104	1,264,663	0.0468	4616.40	29,652	0.003846
Reference Sample, Peak 2	39.5760	2.28100	612,150	0.0468	4647.93	29,735	0.003846
Sample 1, Peak 1	39.6912	2.26901	152,133	0.0624	1421.86	29,672	0.003823
Sample 1, Peak 2	39.7943	2.26900	76,443	0.0468	1427.01	29,756	0.003813
Sample 2, Peak 1	39.5332	2.27771	378,807	0.0468	2202.72	29,658	0.003840
Sample 2, Peak 2	39.6359	2.27769	182,428	0.0468	2227.21	29,741	0.003829

Table 5: The relevant parameters of the fit produced by Empyrean diffractometer's complimentary analysis software. We note here that the splitting between the two peaks in the same sample is on the order of 0.1°, and there is a systematic shift of the two most dominant peaks across all three samples, within a small range of 0.22°. This shift could be attributed to the individual micro-stress of each sample. Reproduced in [2].

We note that up to a systematic shift of 0.22°, all three samples exhibit the same double peaks, and within the same sample, the split between the two peaks is in the order of 0.1°. The ratio of the intensity between the left peak and the right peak is 2.07 for the reference sample, 1.99 for our first sample, and 2.08 for our second sample.

8) Interpretation of γ-γ and e-γ TDPAC results.

In this chapter, following the presentation of the results for our γ-γ and e-γ TDPAC results in the previous chapter, we will interpret and discuss the results. As outlined in chapter 7, we would first discuss the room temperature results and then the temperature-dependent results.

The methodology is as follows:

1) First, we would report on the 6-detector bulk rutile $^{181}Ta(TiO_2)$ γ-γ TDPAC spectroscopy and verify that our results correspond to the literature in section 6.1.1.
2) We would then communicate the temperature-dependent bulk rutile $^{181}Ta(TiO_2)$ e-γ TDPAC spectroscopy, to which we would first compare the e-γ room temperature results to the corresponding γ-γ results.
3) Finally, we would look at the temperature-dependent bulk rutile $^{181}Ta(TiO_2)$ e-γ TDPAC spectroscopy as a whole and derive any trends on the experimental and relevant hyperfine parameters with respect to temperature.

As such, for our e-γ TDPAC spectroscopy results, we would extract the room temperature results from the collective whole (Chapter 7) for easier reference. Also, we select a representative from each corresponding temperature range to visualise the change in the FFT spectrum alongside the $R(t)$ results with respect to temperature.

Discussion on the room temperature bulk rutile $^{181}Ta(TiO_2)$ e-γ TDPAC spectroscopy and X-ray diffraction results have been communicated and published in [2]. They are re-communicated, some ab-verbatim, in this thesis:

Section of this thesis	Reproduced from [2] under section
8.1.1) γ-γ TDPAC spectroscopy setup	5.1) γ−γ TDPAC Spectroscopy Setup
8.1.2) e-γ TDPAC spectroscopy setup	5.2) e−γ TDPAC Spectroscopy Setup Compared with γ−γ TDPAC Spectroscopy Setup
8.3) X-ray Diffraction of the 181Ta(TiO2) Sample after the γ−γ and e−γ TDPAC Spectroscopy	5.3) X-ray Diffraction of the 181Ta(TiO2) Sample after the γ−γ and e−γ TDPAC Spectroscopy

Copyright is retained by the authors of the mentioned paper (to which I am one of them) and licensed under the Creative Commons CC BY 4.0 license.

8.1) Room Temperature results

This section will discuss the room temperature results and the physical implications for the $^{181}Ta(TiO_2)$ γ-γ and e-γ TDPAC spectroscopy.

8.1.1) γ-γ TDPAC spectroscopy setup

For all the signals shown in Table 3, the multiplicative constant for the $y-z$ and $x-z$ plane measurements of the four-detector γ-γ TDPAC spectroscopy is less than half of the multiplicative constant of the $x-y$ plane. This observation suggests that the effective anisotropy constant $A_{kk}=A_{2,eff}(\gamma_1)A_{2,eff}(\gamma_2)$ of the $y-z$ and $x-z$ plane geometry is much less than that of the $x-y$ plane. This discrepancy may be attributed to the reduced solid angle of the detectors lying on the z-axis, which in turn is because the distance between the sample and the z-axis detectors is greater than the distances between the sample and the x- and y-axis detectors. Another plausible reason is due to the presence of the shielding material that blocks the γ-rays from reaching the detectors on the z-axis.

This result implies that, in the analysis of the full six-detector $R(t)$ spectra, the signal from the *x-y* plane is more pronounced than that of the $x-z$ or $y-z$ plane, which would invalidate the assumption of random distribution of the size and direction of the individual crystallites as per the definition of a polycrystalline solid. Thus, the high χ^2 of the six-detector is expected from the relative ill-fitting.

We next highlight the Lorentzian delta δ concerning the degree of annealing. We note that the annealing time corresponds to a drastic decrease in the magnitude of δ of the $R(t)$ signals across all geometries. For example, if we consider the $R(t)$ signals from the $x-y$ plane, $\delta=3\%$ for the unannealed case, which decreases to $\delta=0.4\%$ for the case of a 30-minutes anneal, which further decreases to $\delta=0.2\%$ for the case of a 315-minutes anneal. We would explore the reduction of the Lorentzian delta δ for the e-γ TDPAC results room temperature measurement in section 8.1.2.

We also note that for signals corresponding to the unannealed case (Signals 1 & 2), $|\theta_1|+|\theta_{2,3}|$ does not add up to be near $90°$, while $|\varphi_1|+|\varphi_{2,3}|$ is close to $90°$ (See equation $(4.22a\ \&\ 4.22b)$). It is conjectured that there exist active ^{181}Ta probes that do not sit in the Ti-substitutional sites of rutile TiO_2 and may sit in the intrastitial areas (i.e., at points where the native ions of TiO_2 do not sit at). Furthermore, even if the existence of a secondary site (and hence fraction) is not the case, the relatively high value of the delta Lorentzian δ suggest that the high statistical distribution and degree of the imperfect lattice structure of TiO_2 surrounding the ensemble of the active ^{181}Ta probes.

We also note that for signals 3 to 6, $|\theta_1|+|\theta_{2,3}|\approx 100°$ to $110°$ and $|\varphi_1|+|\varphi_{2,3}|\approx 90°$ to $95°$. We cannot achieve the perfect condition of $90°$, possibly due to the defects not resolved from the short annealing time.

For signal seven which is of our main interest, we have the relevant experimental parameters:

$$|\theta_{x-y}|+|\theta_{x-z}|=93.0(9)°,$$

$$|\theta_{x-y}|+|\theta_{x-z}|=93.9(9)°,$$

$$|\varphi_{x-y}|+|\varphi_{x-z}|=92.9(4)°,$$

$$|\varphi_{x-y}|+|\varphi_{y-z}|=93.4(5)°.$$

In our derivation based on geometric considerations, we assume that the crystal is an infinitely thin sheet centred in the middle of the detector setup. The slight offset of the angles from the expected values may be attributed to (1) the sample not being a perfect single crystal; (2) the crystal not being infinitesimally thin, so the average depth of the implantation may vary statistically; and (3) the ^{181}Ta implantation being done only on one long side of the sample, as discussed in the experimental setup section of the paper.

To compare with the e-γ TDPAC spectroscopy setup, we use averaged values for the fundamental frequency ω_0, the asymmetry parameter η, and the largest component of the electric-field gradient V_{zz} arising from a set of single γ−γ TDPAC measurements in all four geometries. The quoted uncertainty for the averaged hyperfine parameters is the square root of the sum of squares of each measurement's statistical uncertainty. Table 6 reflects this averaged quantity for signal 7, our main interest. This table is reproduced from Table 1 of this paper [2], in which the authors retain the copyright.

Geometry	Fundamental Frequency ω_0 (Mrad/s)	Asymmetry Parameter η	V_{zz} (10^{20} V/ m^2)	Delta Lorentzian δ (%)	Chi Squared χ^2	Theta θ (Deg)	Phi ϕ (Deg)	Multiplicative Constant	Additive Constant
Six-detectors	762.0(4)	0.540(1)	141.68 ± 0.07 [a] ± 3.00 [b]	0.94(5)	3.5	N.A.	N.A.	0.692(5)	−0.1111(4)
Four-detector x-y plane	761.8(2)	0.542(1)	141.64 ± 0.04 [a] ± 3.00 [b]	0.17(3)	0.77	64.4(5)	47.1(3)	0.719(5)	−0.0817(5)
Four-detector x-z plane	761.9(7)	0.545(2)	141.7 ± 0.1 [a] ± 3.0 [b]	0.49(9)	0.79	28.6(8)	45.8(3)	0.314(7)	−0.1795(5)
Four-detector y-z plane	761.5(6)	0.544(2)	141.6 ± 0.1 [a] ± 3.0 [b]	0.46(8)	0.96	29.5(7)	46.3(4)	0.300(6)	−0.1843(4)
Average	762(1)	0.543(3)	141.6 ± 0.2 [c]	N.A.	N.A.	N.A.	N.A.	N.A.	N.A.

Table 6: This table was copied from signal 7 of Table 3. For the individual values of V_{zz}, the fit uncertainty is separated into (a) the statistical uncertainty caused by our instruments and (b) the (dominant) systematic uncertainty of the quadrupole moment (±2.1%) as quoted in reference [23]. The averaged values of ω_0, η, and V_{zz} from the four different geometries were calculated, with (in the case of V_{zz}, (c)) the uncertainty assigned the square root of the sum of squares of their statistical uncertainty (in the case of V_{zz}, (a)). Reproduced from [2].

8.1.2) e-γ TDPAC spectroscopy setup

From section 7.2, we extract:

1) Concerning the time length of the anneal, we extract signals TOSC01 to TOSC08. We will rename them in the following tables (7 & 8) for easier reading.
2) Concerning the room temperature $R(t)$ measurement under significant (315-mins) anneal**,** we extract TOSC09, TOSC10, TOSC10B, TOSC22, TOSC23, TOSC23B, TOSC24, TOSC25, TOSC25B, TOSC44, TOSC44B, TOSC45, TOSC45B.

Recall that for our e-γ TDPAC spectroscopy setup; we fixed our multiplicative constant at 1.

The literature review on the ion implantation damage to our TiO_2 sample that affects the value of our Delta Lorentzian δ is discussed in Appendix A.1 of this paper [2] and is subsequently reproduced in this thesis as Appendix E.

Table 7 and 8 depicts the value of the hyperfine parameters and the relevant experimental parameters for the room temperature $^{181}Ta(TiO_2)$ e-γ TDPAC spectroscopy under no annealing and 30-min annealing, respectively. The corresponding $R(t)$ and FFT graphs are visualised in figure 23. They are reproduced from Appendix A.2 of this paper [2], in which the authors retain the copyright.

$R(t)$ Signal	Fundamental Frequency ω_0 (Mrad/s)	Asymmetry Parameter η	V_{zz} $(10^{20}\ \mathrm{V/m^2})$	Delta Lorentzian δ (%)	Chi Squared χ^2	Theta θ (deg)	Phi ϕ (deg)	Additive Constant
U_1 (TOSC01)	763(4)	0.54(1)	142.0 ± 0.7 [a] ± 3.0 [b]	6.6(7)	0.98	0(6)	37.8(4)	−0.0181(3)
U_2 (TOSC02)	766.31(7)	0.525(7)	142.48 ± 0.01 [a] ± 3.02 [b]	6.0(2)	1.20	0.0(4)	37.9(2)	−0.005(1)
U_3 (TOSC03)	759.7(1)	0.519(4)	141.255 ± 0.002 [a] ± 2.993 [b]	6.0(2)	1.40	0(2)	37.9(2)	−0.00(1)
Average	763(4)	0.53(1)	141.9 ± 0.7 [c]	6.2(8)	N.A.	N.A.	N.A.	N.A.

Table 7: Table of fitted hyperfine and experimental parameters for this set of 3 different e−γ TDPAC measurements of $^{181}Ta(TiO_2)$, returned by the Gfit19™ program. It is noted that this set contains e−γ TDPAC signals corresponding to the unannealed case (Termed "U_" and equals to the relevant TOSC signals reflected in Table 3). For the individual values of V_{zz}, the fit uncertainty is separated into (a) the statistical uncertainty caused by our instruments and (b) the (dominant) systematic uncertainty of the quadrupole moment (±2.1%) as quoted in reference [23]. The multiplicative constant of this set of e−γ TDPAC measurements is fixed at 1. The averaged values of ω_0, η, and V_{zz} from this set of e−γ TDPAC measurements were calculated, with (in the case of V_{zz}, (c)) the uncertainty assigned the square root of the sum of squares of their statistical uncertainty (in the case of V_{zz}, (a)). Reproduced from [2].

$R(t)$ Signal	Fundamental Frequency ω_0 (Mrad/s)	Asymmetry Parameter η	V_{zz} $(10^{20}\ \mathrm{V/m^2})$	Delta Lorentzian δ (%)	Chi Squared χ^2	Theta θ (Deg)	Phi ϕ (Deg)	Additive Constant (Fixed)
A_1 (TOSC04)	762(2)	0.548(4)	141.6 ± 0.4 [a] ± 3.0 [b]	1.1(3)	0.83	45(3)	58.8(7)	−0.0398
A_2 (TOSC05)	760(2)	0.548(4)	141.3 ± 0.3 [a] ± 3.0 [b]	1.0(2)	0.83	44(3)	57.9(6)	−0.0398
A_3 (TOSC06)	763.0(8)	0.543(2)	141.9 ± 0.2 [a] ± 3.0 [b]	0.9(1)	0.94	45(1)	58.5(3)	−0.0398
A_4 (TOSC07)	762.9(5)	0.543(1)	141.85 ± 0.09 [a] ± 3.01 [b]	0.95(7)	1.3	45.7(8)	58.5(2)	−0.0398
A_5 (TOSC08)	762.4(5)	0.543(1)	141.75 ± 0.09 [a] ± 3.00 [b]	1.04(7)	1.4	45.9(8)	58.4(2)	−0.0398
Average	762(3)	0.545(6)	141.07 ± 0.5 [c]	1.0(4)	N.A.	N.A.	N.A.	N.A.

Table 8: Table of fitted hyperfine and experimental parameters for this set of 5 different e−γ TDPAC measurements of $^{181}Ta(TiO_2)$, returned by the Gfit19™ program. It is noted that this set contains e−γ TDPAC signals corresponding to the case where our ^{181}Hf-implanted single crystal TiO_2 was subjected to 30-minute annealing at a temperature of 873 K in a vacuum (Termed "A_" and corresponds to the relevant TOSC signals reflected from Table 3). For the individual values of V_{zz}, the fit uncertainty is separated into (a) the statistical uncertainty caused by our instruments and (b) the (dominant) systematic uncertainty of the quadrupole moment (±2.1%) as quoted in reference [23]. The multiplicative constant and additive constant of this set of e−γ TDPAC measurements is fixed at 1 and −0.0398, respectively. The averaged values of ω_0, η, and V_{zz} from this set of e−γ TDPAC measurements were calculated, with (in the case of V_{zz}, (c)) the uncertainty assigned the square root of the sum of squares of their statistical uncertainty (in the case of V_{zz}, (a)). Reproduced from [2].

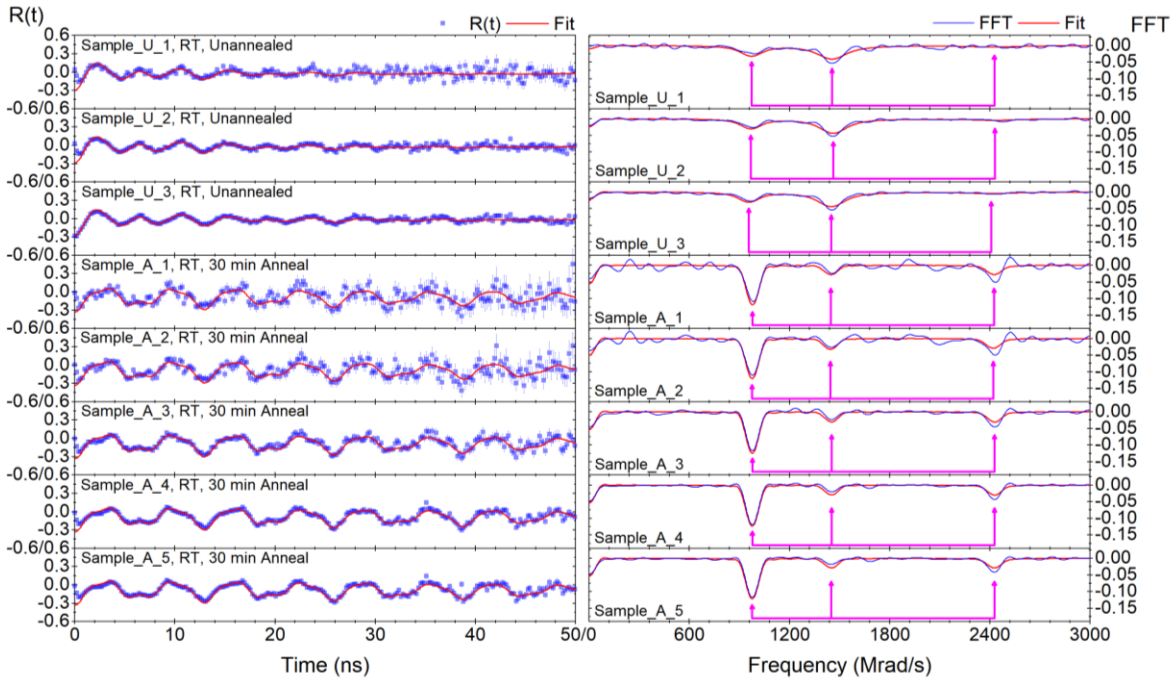


*Figure 23: (**left**) R(t) graph and (**right**) corresponding FFT spectrum of 2 sets totalling 8 different e−γ TDPAC measurements of $^{181}Ta(TiO_2)$. The additive constant for set "U_" (Unannealed) varies for all three members. The additive constant for set "A_" (30 min annealing at 873K) is −0.0398. The TDPAC probe used is $^{181}Hf \rightarrow ^{181}Ta$, with the raw TDPAC spectrum (from the coincidence searches on the detectors) processed and converted into R(t) observables [see blue curves in the R(t) and their corresponding FFT graphs] by Interlude™. The R(t) signals are then fit by using the Gfit19™ program [see red curves in R(t) and the corresponding FFT graphs]. For clarity, we show only the first 50 ns on the R(t) graph because shorter coincidence searches of e−γ rays are less noisy and thus more statistically significant than longer coincidence searches.*

Table 9 depicts the value of the hyperfine parameters and the relevant experimental parameters for the room temperature $^{181}Ta(TiO_2)$ e-γ TDPAC spectroscopy under 315-mins annealing. The corresponding $R(t)$ and FFT graphs are visualised in figures 24 & 25. They are reproduced in table 2 and figures 7 & 8 from this paper [2], in which the authors retain the copyright.

$R(t)$ Signal	Fundamental Frequency ω_0 (Mrad/s)	Asymmetry Parameter η	V_{zz} $(10^{20}\ \mathrm{V/m^2})$	Delta Lorentzian δ (%)	Chi Squared χ^2	Phi ϕ (Deg)	Additive Constant (Fixed)
9 (TOSC09)	765.0(5)	0.549(3)	142.23 ± 0.09 [a] ± 3.01 [b]	0.03(6)	0.72	37.8(4)	0.0187
10 (TOSC10)	765.6(3)	0.546(2)	142.35 ± 0.06 [a] ± 3.02 [b]	0.04(6)	0.99	37.9(2)	0.0187
10B (TOSC10B)	765.6(3)	0.546(2)	142.35 ± 0.06 [a] ± 3.02 [b]	0.04(6)	0.99	37.9(2)	0.0187
22 (TOSC22)	764.4(3)	0.543(2)	142.12 ± 0.06 [a] ± 3.01 [b]	0.02(2)	0.89	37.5(2)	0.0187
23 (TOSC23)	764.4(3)	0.543(2)	142.12 ± 0.06 [a] ± 3.01 [b]	0.02(2)	0.89	37.5(2)	0.0187
23B (TOSC23B)	764.4(3)	0.543(2)	142.12 ± 0.06 [a] ± 3.01 [b]	0.02(2)	0.89	37.5(2)	0.0187
24 (TOSC24)	763.8(7)	0.536(4)	142.0 ± 0.1 [a] ± 3.0 [b]	0.04(9)	0.73	38.6(5)	0.0085

$R(t)$ Signal	Fundamental Frequency ω_0 (Mrad/s)	Asymmetry Parameter η	V_{zz} $(10^{20}\ \mathrm{V/m^2})$	Delta Lorentzian δ (%)	Chi Squared χ^2	Phi ϕ (Deg)	Additive Constant (Fixed)
25 (TOSC25)	764.6(4)	0.539(2)	142.17 ± 0.08 [a] ± 3.01 [b]	0.09(6)	0.85	38.8(3)	0.0085
25B (TOSC25B)	764.6(4)	0.539(2)	142.17 ± 0.08 [a] ± 3.01 [b]	0.09(6)	0.85	38.8(3)	0.0085
44 (TOSC44)	765(1)	0.552(5)	142.2 ± 0.2 [a] ± 3.0 [b]	0.07(1)	0.60	37.2(7)	0.0085
44B (TOSC44B)	765(1)	0.552(5)	142.2 ± 0.2 [a] ± 3.0 [b]	0.07(1)	0.60	37.2(7)	0.0085
45 (TOSC45)	765.1(5)	0.544(3)	142.3 ± 0.1 [a] ± 3.0 [b]	0.06(7)	0.71	36.3(3)	0.0085
45B (TOSC45B)	765.1(5)	0.544(3)	142.3 ± 0.1 [a] ± 3.0 [b]	0.06(7)	0.71	36.3(3)	0.0085
Average	765(2)	0.54(1)	142.2 ± 0.4 [c]	0.05 ± 0.19 [d]	N.A.	38(1)	0.0085

Table 9: Table of fitted hyperfine and experimental parameters for the set of 13 different $e-\gamma$ TDPAC measurements of $^{181}Ta(TiO_2)$, returned by the Gfit19™ program. It is noted that this set contains $e-\gamma$ TDPAC signals corresponding to the case where our ^{181}Hf-implanted single crystal TiO_2 was subjected to 315-min annealing at a temperature of 873 K in a vacuum (corresponds to the relevant TOSC signals reflected from Table 3). For the individual values of V_{zz}, the fit uncertainty is separated into (a) the statistical uncertainty caused by our instruments and (b) the (dominant) systematic uncertainty of the quadrupole moment (±2.1%) as quoted in reference [23]. The multiplicative constant and additive constant of this set of $e-\gamma$ TDPAC measurements is fixed at 1 and 0.0187 or 0.0085, respectively. The averaged values of ω_0, η, and V_{zz} from this set of $e-\gamma$ TDPAC measurements were calculated, with (in the case of V_{zz}, (c)) the uncertainty assigned the square root of the sum of squares of their statistical uncertainty (in the case of V_{zz}, (a)). (d) The averaged δ is written in this form, as its uncertainty exceeds its value. Reproduced from [2].

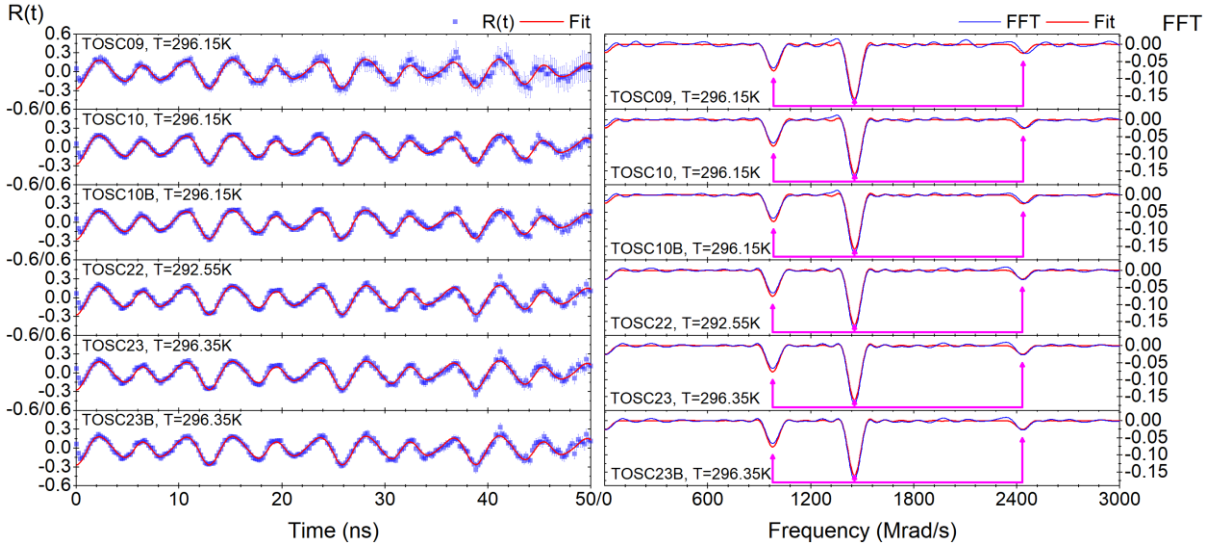


*Figure 24: **(left)** R(t) graph and **(right)** corresponding FFT spectrum of the first six of the 13 different $e-\gamma$ TDPAC measurements of $^{181}Ta(TiO_2)$ from Table 8. The additive constant is 0.0187. The TDPAC probe used is $^{181}Hf \rightarrow {}^{181}Ta$, with the raw TDPAC spectrum (from the coincidence searches on the detectors) processed and converted into R(t) observables [blue curves in the R(t) and the corresponding FFT graphs] by Interlude™. The R(t) signals are then fit by using the Gfit19™ program [see red curves in R(t) and the corresponding FFT graphs]. For clarity, we show only the first 50 ns on the R(t) graph because shorter coincidence searches of $e-\gamma$ rays are less noisy and thus more statistically significant than longer coincidence searches. Reproduced from [2].*

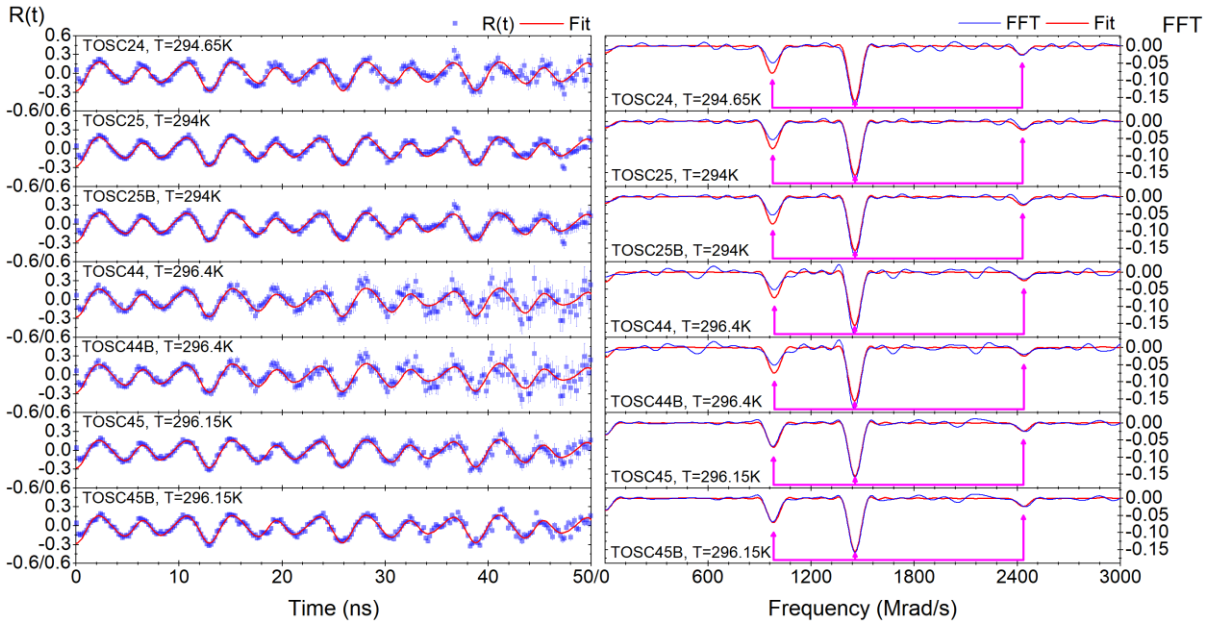


*Figure 25: (**left**) R(t) graph and (**right**) corresponding FFT spectrum of the latter seven of the set of 13 different e−γ TDPAC measurements of $^{181}Ta(TiO_2)$ from Table 8. The additive constant is 0.0085. The TDPAC probe used is $^{181}Hf \rightarrow ^{181}Ta$, with the raw TDPAC spectrum (from the coincidence searches on the detectors) processed and converted into R(t) observables [see blue curves in the R(t) and their corresponding FFT graphs] by Interlude™. The R(t) signals are then fit by using the Gfit19™ program [see red curves in R(t) and the corresponding FFT graphs]. For clarity, we show only the first 50 ns on the R(t) graph because shorter coincidence searches of e−γ rays are less noisy and thus more statistically significant than longer coincidence searches. Reproduced from [2].*

Table 10 portrays the collection of all the averaged results of the experimental and hyperfine parameters relating to the time-length of the annealing process (temperature of $873K$ in vacuum). It is reproduced in table A3 from this paper [2]:

Annealing Time (mins)	**Fundamental Frequency ω_0 (Mrad/s)**	**Asymmetry Parameter η**	**V_{zz} (10^{20} V/m^2)**	**Delta Lorentzian δ (%)**
0 (3 samples)	763(4)	0.53(1)	141.9(7)	6.2(8)
30 (5 samples)	762(3)	0.545(6)	141.7(5)	1.0(4)
315 (13 samples)	765(2)	0.54(1)	142.2(4)	0.05 ± 0.19 [a]

Table 10: The collection of the averaged results of the experimental and hyperfine parameters tailored to the time length of the annealing process (temperature of 873 K in vacuum). We principally want to point out the rapidly decreasing Delta Lorentzian δ, as a measure of the restoration of the lattice structure (at least around the ^{181}Ta probes located at the Ti-substitutional site with a D_{2h} site symmetry) that was caused by the 80 keV ^{181}Hf implanted ions. (a) The averaged δ is written in this form, as its uncertainty greatly exceeds its value. Reproduced from [2].

The results suggest that under thermal annealing at a temperature of $873\ K$ in a vacuum, the damage caused to the lattice structure (at least locally around the vicinity of the substitutional ^{181}Ta probe with D_{2h} site symmetry) is rapidly repaired, causing a decrease of the Delta Lorentzian spread from $6.2(8)\%$ to $1.0(4)\%$ within 30 mins. More impressively, after $5.25\ h$, the Delta Lorentzian drops by several orders of magnitude to $(0.05 \pm 0.19)\%$, even more than what we have observed for the γ-γ counterpart. It is suspected that further prior measurements from room temperature to $428.45K$ over a considerable period further annealed the $^{181}Ta(TiO_2)$ sample.

The delta Lorentzian δ is the measure of the statistical distribution of the sites (interstitial/substitutional) of our implanted ^{181}Hf probes, along with the degree of damage to the local environment (caused by the implantation) around the different substitutional ^{181}Hf probes. We note that our dose of implanted ions is low (part per billion number density), and our implanted ion is heavy. Hence, we expect to see some damaged clusters that behave like polycrystalline solid with moderate Frankel defects. Coupled with the literature review in Appendix E of this thesis, it suggests that 5.25-h thermal annealing at a temperature of $873\ K$ in a vacuum applied to our single crystal TiO_2 that was ^{181}Hf ion-implanted at $80\ keV$ repairs almost all implantation damage, and in particular, possibly the Frankel defects, the heavily disordered damage clusters that behave like a polycrystalline, and the dislocation loops and lines.

Comparing the $R(t)$ acquired by the γ-γ TDPAC spectroscopy setup (see Figure 20.7) with room-temperature $R(t)$ acquired by the e-γ TDPAC spectroscopy setup (Figures 24 & 25) reveals that the periodicity of the γ-γ $R(t)$ signals are roughly twice that of the e-γ $R(t)$ signals. This effect is qualitatively shown in Figure 26, which compares $R(t)$ between the $x-y$ plane of signal 7 of the γ-γ TDPAC spectroscopy setup with $R(t)$ from signal 25 (TOSC25) of the e-γ TDPAC spectroscopy setup.

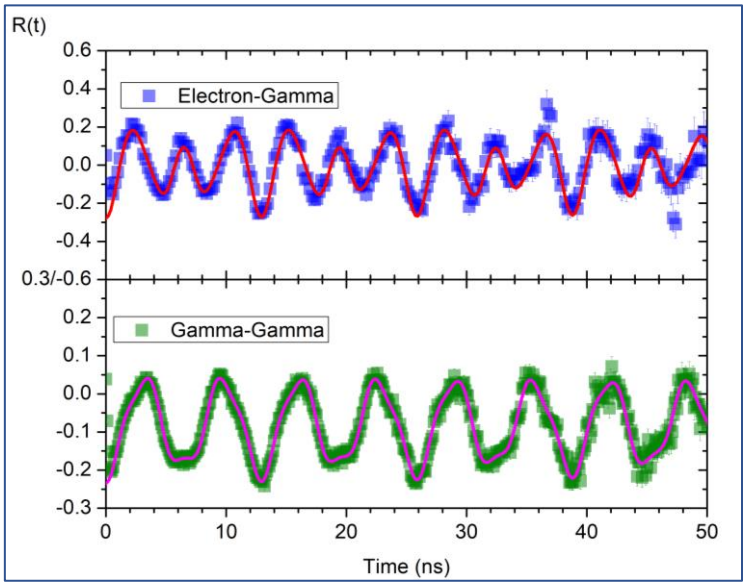


Figure 26: $R(t)$ (with the same scale) between the signal 8, the x-y plane of γ-γ TDPAC spectroscopy setup (lower panel, data points are green dots, and the fit is the magenta line) compared with $R(t)$ from signal 25 (TOSC25) of e-γ TDPAC spectroscopy setup (upper panel, data points are blue dots and fit is red line). Due to the difference in time calibration (0.101 ns/channel for γ-γ TDPAC spectroscopy and 0.195 ns/channel for e−γ TDPAC spectroscopy), the periodicity of the γ-γ $R(t)$ is roughly twice that of the e-γ $R(t)$. Nevertheless, from the Gfit19™ fitting process, the average fundamental frequencies and the asymmetry parameters for the γ−γ TDPAC spectroscopy setup [762(1) Mrad/s, 0.543(3)] are close to those of the e-γ TDPAC spectroscopy setup [765(2) Mrad/s, 0.54(1)]. Reproduced from [2].

This discrepancy is attributed to the difference in the time calibration (0.101 ns/channel for the γ−γ TDPAC spectroscopy and 0.195 ns/channel for the e−γ TDPAC spectroscopy; See equation (4.20)). Given that the Gfit19™ fitting process considers the time calibration for each TDPAC spectroscopy setup as a parameter, we note that the average fundamental frequencies and the asymmetry parameters for the γ−γ TDPAC spectroscopy setup $(762(1)$

Mrad/s, $0.543(3)$, [Table 6]) lie very close to those of the e−γ TDPAC spectroscopy setup ($765(2)$ Mrad/s, $0.54(1)$, [Table 9]).

After correcting for the quadrupole moment of ^{181}Ta according to reference [23], V_{zz} (and ω_0 in extension) obtained from both our γ-γ and e-γ ^{181}Ta(TiO_2) TDPAC spectroscopies are consistent with published values up to an order of magnitude, and our asymmetry parameter η is consistent with the quoted values up to 0.05. This claim is shown in Table 11 in numerical details of the relevant hyperfine parameters and Figures 27 and 28 for the corresponding graphical outputs for the values of V_{zz} and η, respectively.

Paper	V_{zz} $(10^{20}\ \mathrm{V/m^2})$	Asymmetry Parameter η	Delta Lorentzian δ (%)	Crystal Type	Sample Preparation	Reference
James 1994	141.6(7)	0.57(1)	≈0.01	Polycrystal	Thermal Annealing at 1570 K for several hrs	[59]
Darriba 2011	143.2(7)	0.555(8)	0.4(2)	Single Crystal	Thermal Annealing at 1073 K for 6 h	[60]
Banerjee 2016	141.9(2)	0.56(1)	0.6(1)	Polycrystal	Thermal Annealing at 1273 K for 10 h	[63]
Satyendra 2009	145(1)	0.56(1)	Unknown	Polycrystal	Thermal Annealing at 1273 K for 10 h	[61]
Banerjee 2010 {S4}	149.5(8)	0.51(1)	5.2(5)	Polycrystal	Thermal Annealing at 1123 K for 4 h	[62]
Banerjee 2010 {S7}	145.6(1)	0.55(1)	1.0(1)	Polycrystal	Thermal Annealing Anatase TiO_2 at 1223 K for 8 h (Convert to Rutile TiO_2)	[62]
Martucci 2011 {3}	142.06 [a]	0.55 [a,b]	Unknown	Polycrystal	Thermal Annealing Anatase TiO_2 at 973 K for 10 h under Nitrogen (Convert to Rutile TiO_2)	[67]
Martucci 2011 {4}	139.00 [c]	0.55 [a,b]	Unknown	Polycrystal	Thermal Annealing Anatase TiO_2 at 1223 K for 10 h under Nitrogen (Convert to Rutile TiO_2)	[67]
This study ($\gamma-\gamma$)	141.6(2)	0.543(3)	N.A.	Single Crystal	Thermal Annealing at 873 K for 5.25 h	N.A.
This study ($e-\gamma$)	142.2(4)	0.54(1)	0.05 ± 0.19 [d]	Single Crystal	Thermal Annealing at 873 K for 5.25 h	N.A.

Table 11: Published literature values (after correcting for the quadrupole moment of ^{181}Ta according to reference [23]) of the relevant hyperfine parameters for the room temperature ^{181}Ta(TiO_2) γ−γ TDPAC spectroscopy compared with the hyperfine parameters obtained from our room temperature γ−γ and e−γ experiments. All the papers mentioned in this table did not consider the dominant systematic uncertainty of the quadrupole moment, as quoted in reference [23]. Hence, for our values, we only consider the statistical uncertainty caused by our instruments. Note that (a) Martucci et al. [67] did not include the uncertainty in their report, (b) they mentioned that their asymmetry parameters agree with the reference [62], and (c) they also mentioned that discrepancy of V_{zz} of their sample 4 concerning the literature values are due to the presence of the fluorine atoms (A byproduct caused by their preparation method) near the ^{181}Ta probe, and (d) the averaged δ is written in this form, as its uncertainty exceeds its value. Republished from [2].

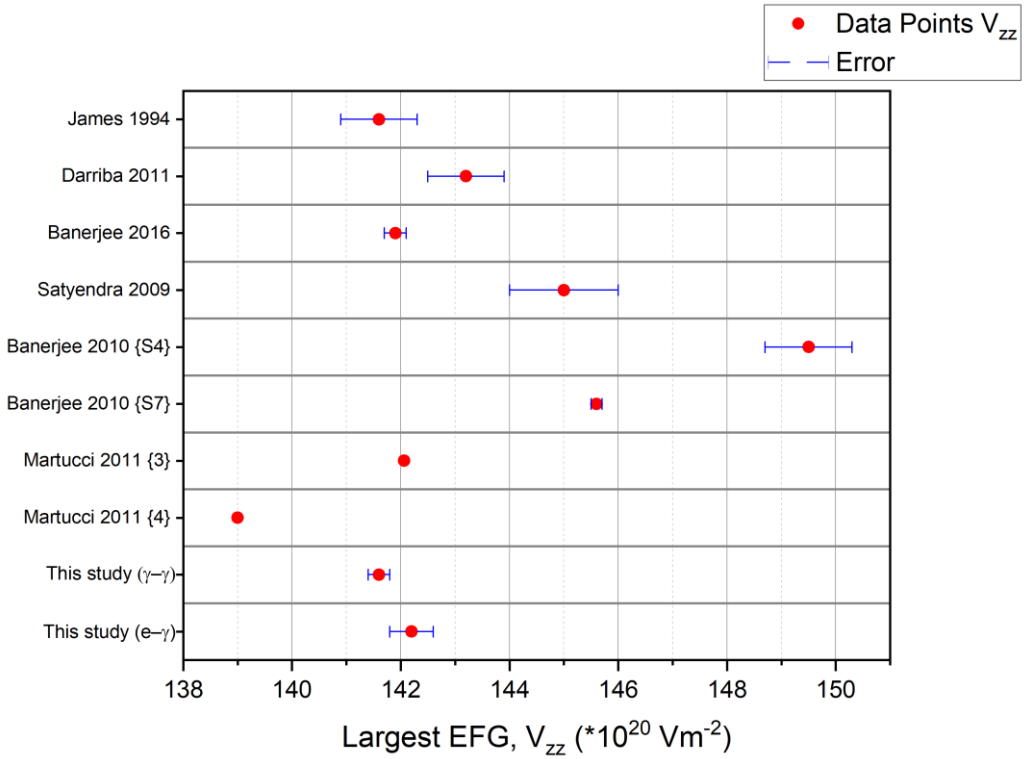


Figure 27: The values of V_{zz} obtained from our room temperature γ−γ and e−γ experiments are visually compared with accepted literature values from Table 11. Republished from [2].

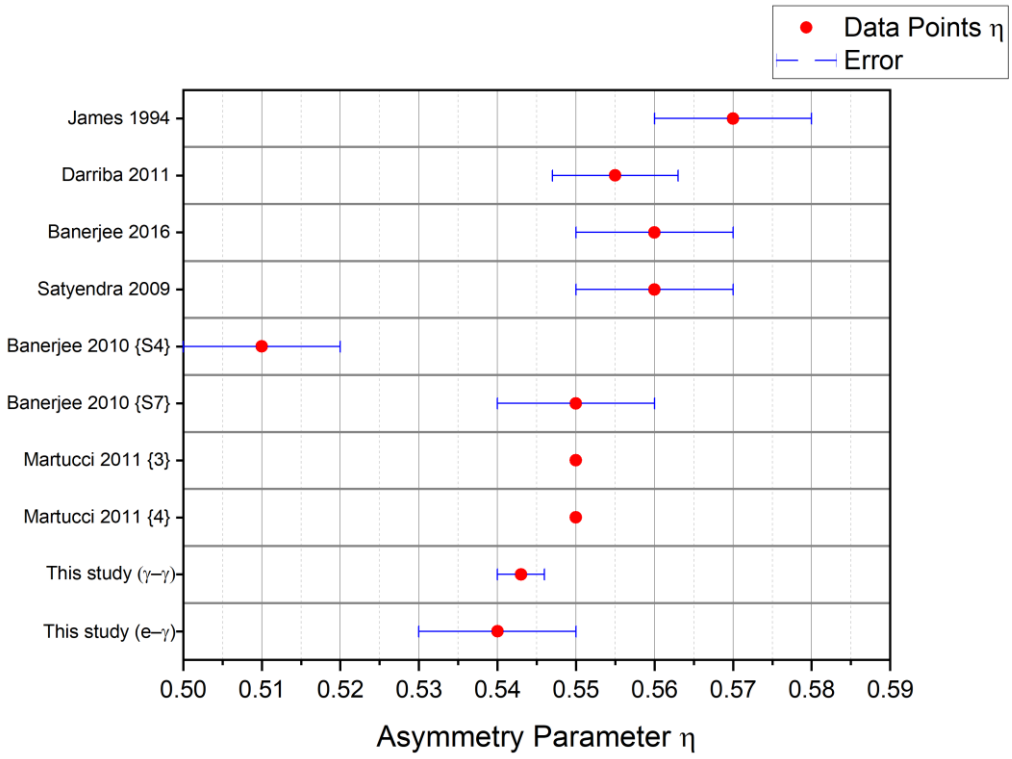


Figure 28: The values of η obtained from our room temperature γ−γ and e−γ experiments are visually compared with accepted literature values from Table 11. Republished from [2].

These results show that the room temperature hyperfine parameters determined from the ^{181}Ta(TiO_2) γ−γ and e−γ TDPAC experiments are consistent with the literature values for the corresponding ^{181}Ta(TiO_2) γ−γ TDPAC results.

Following the understanding of the electron-recombination process (see Figure 13 and Section 5.1), we conclude that the timescale of the electron-recombination process is at least one order of magnitude faster than nanoseconds, which is the timescale of the half-life of the second-stage decay (10.8 ns) of the ^{181}Hf→^{181}Ta probe nucleus. This conclusion also implies that we cannot detect the recombination process with our present setup for ^{181}Ta(TiO_2) e−γ TDPAC spectroscopy.

This conclusion is consistent with the implications of the findings concerning the Femtosecond Time-Resolved Spectroscopy conducted by a group from the KAUST Solar Centre, in which an induced hole (as an electron trap) in the bulk rutile TiO_2 will capture an electron in the order of picoseconds [74].

8.2) Temperature-dependent e−γ TDPAC results

In the previous section, we determined that the hyperfine parameters extracted from the $R(t)$ for both room temperature γ−γ & e−γ TDPAC spectroscopy are similar due to the short timescale of the electron-recombination process relative to the half-life of the decay of the intermediate ^{181}Ta state. We can, thus, directly compare our temperature-dependent set of ^{181}Ta(TiO_2) e−γ TDPAC spectroscopy to existing γ−γ literature, mainly [59] and [60].

Note here that the ^{181}Ta(TiO_2) e−γ TDPAC spectroscopy analysis only includes samples that have undergone 315-mins of thermal annealing. There is an implicit assumption that we will refer to signals TOSC09 to TOSC49B and will not involve TOSC01 to TOSC08.

We extract several samples as representatives of each temperature point to have a physical intuition of the temperature dependence of our hyperfine parameters in our e−γ TDPAC spectroscopy. They are collated in Table 12:

$R(t)$ signal	Sample condition	Measurement Temperature (Kelvins)	Fundamental frequency ω_0 (Mrad/s)	Asymmetry parameter η	V_{zz} $(10^{20}$ V/m$^2)^*$	Delta Lorentzian δ (%)	Chi Squared χ^2	Phi ϕ (deg)	Additive constant
43	TA=600C, 315m, vacuum.	39.3	744(2)	0.537(4)	138.3 $\pm 0.3^a$ $\pm 2.9^b$	0.3(1)	0.71	37.3(9)	0.00851
49	TA=600C, 315m, vacuum.	59.97	745.9(5)	0.548(3)	138.7 $\pm 0.1^a$ $\pm 2.9^b$	0.1(1)	0.75	35.7(3)	0.00851
42	TA=600C, 315m, vacuum.	70	746.9(4)	0.543(2)	138.88 $\pm 0.07^a$ $\pm 2.94^b$	0.1(1)	0.96	38.5(2)	0.00851
35	TA=600C, 315m, vacuum.	101.6	750.7(7)	0.548(4)	139.6 $\pm 0.1^a$ $\pm 3.0^b$	0.1(2)	0.68	37.9(5)	0.00851

$R(t)$ signal	Sample condition	Measurement Temperature (Kelvins)	Fundamental frequency ω_0 (Mrad/s)	Asymmetry parameter η	V_{zz} $(10^{20}$ V/m$^2)^*$	Delta Lorentzian δ (%)	Chi Squared χ^2	Phi ϕ (deg)	Additive constant
33B	TA=600C, 315m, vacuum.	138.74	754.4(4)	0.544(2)	$140.27 \pm 0.08^a \pm 2.97^b$	0.1(1)	0.89	38.7(3)	0.00851
32	TA=600C, 315m, vacuum.	179.89	757.1(5)	0.547(3)	$140.8 \pm 0.1^a \pm 3.0^b$	0.07(8)	0.82	37.9(4)	0.00851
29	TA=600C, 315m, vacuum.	219.6	760.2(6)	0.545(3)	$141.3 \pm 0.1^a \pm 3.0^b$	0.1(1)	0.84	37.5(2)	0.00851
27B	TA=600C, 315m, vacuum.	260	762.5(5)	0.542(3)	$141.78 \pm 0.09^a \pm 3.00^b$	0.04(6)	0.78	38.0(4)	0.00851
44	TA=600C, 315m, vacuum.	296.4	765(1)	0.552(5)	$142.2 \pm 0.2^a \pm 3.0^b$	0.1(1)	0.60	37.2(7)	0.00851
23	TA=600C, 315m, vacuum.	296.35	764.4(3)	0.543(2)	$142.12 \pm 0.06^a \pm 3.01^b$	0.02(2)	0.89	37.5(2)	0.0187
12	TA=600C, 315m, vacuum.	348.45	768.0(4)	0.549(2)	$142.79 \pm 0.07^a \pm 3.03^b$	0.03(4)	0.89	37.5(3)	0.0187
19	TA=600C, 315m, vacuum.	396.65	769.4(3)	0.550(2)	$143.07 \pm 0.06^a \pm 3.03^b$	0.033 ± 0.108^d	0.80	37.7(2)	0.0187
18	TA=600C, 315m, vacuum.	428.45	770.5(5)	0.551(2)	$143.27 \pm 0.09^a \pm 3.04^b$	0.10(6)	0.66	37.6(3)	0.0187
16	TA=600C, 315m, vacuum.	474.15	771.8(4)	0.550(2)	$143.51 \pm 0.07^a \pm 3.04^b$	0.03(5)	0.88	37.7(3)	0.0187

Table 12: Table of fitted hyperfine and experimental parameters for the set of 14 specially selected $e-\gamma$ TDPAC measurements of $^{181}Ta(TiO_2)$, arranged by measurement temperature and returned by the Gfit19™ program. It is noted that this set contains $e-\gamma$ TDPAC signals corresponding to the case where our ^{181}Hf-implanted single crystal TiO_2 was subjected to 315-min annealing at a temperature of 873 K in a vacuum. For the individual values of V_{zz}, the fit uncertainty is separated into (a) the statistical uncertainty caused by our instruments and (b) the (dominant) systematic uncertainty of the quadrupole moment (±2.1%) as quoted in reference [23]. The multiplicative constant and additive constant of this set of $e-\gamma$ TDPAC measurements is fixed at 1 and 0.0187 or 0.0085, respectively. The averaged values of ω_0, η, and V_{zz} from this set of $e-\gamma$ TDPAC measurements were calculated, with (in the case of V_{zz}, (c)) the uncertainty assigned the square root of the sum of squares of their statistical uncertainty (in the case of V_{zz}, (a)). (d) The averaged δ is written in this form, as its uncertainty exceeds its value.

Note that we could already qualitatively sense an increase in both the fundamental frequency ω_0 (and hence V_{zz}), with an increase in temperature.

The corresponding $R(t)$ and FFT spectra are plotted in figure 29 for visual comparison. We would note that the orange line serves as a guideline concerning the three peaks of the room temperature FFT (TOSC23) as depicted by $\omega_1, \omega_2, \omega_3$ from equation $(4.1c - 4.1e)$.

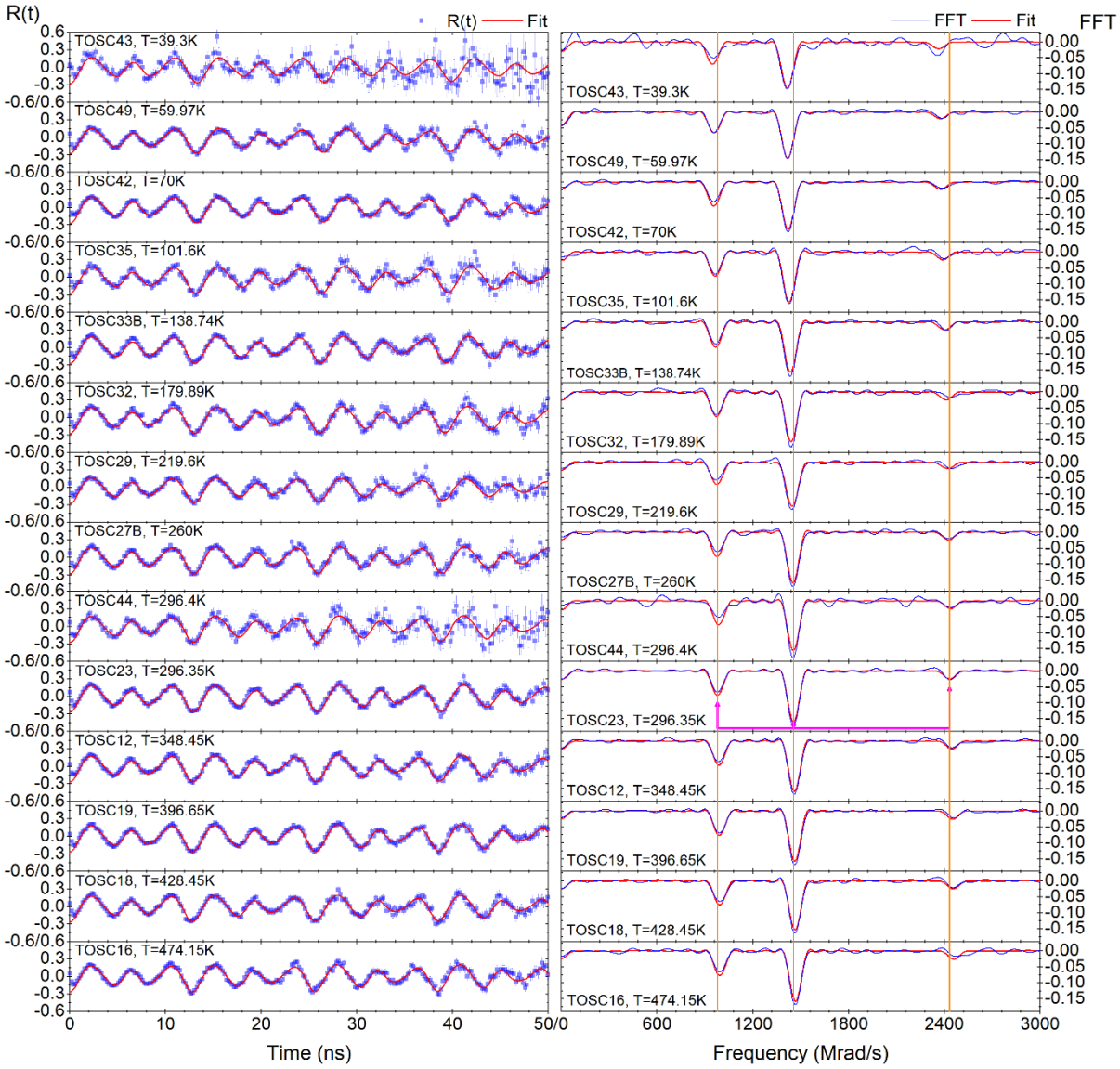


*Figure 29: (**left**) R(t) graph and (**right**) corresponding FFT spectrum of 14 specially selected $e-\gamma$ TDPAC measurements ofs $^{181}Ta(TiO_2)$ as reflected in Table 8. They are also arranged from top to bottom in the order of increasing temperature. It is noted that this set contains $e-\gamma$ TDPAC signals corresponding to the case where our ^{181}Hf-implanted single crystal TiO_2 was subjected to 315-min annealing at a temperature of 873 K in a vacuum. The TDPAC probe used is $^{181}Hf \rightarrow ^{181}Ta$, with the raw TDPAC spectrum (from the coincidence searches on the detectors) processed and converted into R(t) observables [blue curves in the R(t) and the corresponding FFT graphs] by Interlude™. The R(t) signals are then fit by using the Gfit19™ program [see red curves in R(t) and the corresponding FFT graphs]. The orange lines serve as a guideline concerning the three peaks of the room temperature FFT (TOSC23) as depicted by ω_1, ω_2, ω_3 from equation $(4.1c - 4.1e)$. For clarity, we show only the first 50 ns on the R(t) graph because shorter coincidence searches of $e-\gamma$ rays are less noisy and thus more statistically significant than longer coincidence searches.*

We can already see a systematic rightwards shift in the peaks with the increase of the temperature, which corresponds to the rise in both ω_0 and V_{zz}. Also, such a systematic increase implies that a particular physical order exists, encapsulating the temperature-dependent distortion of the external electrical fields provided by the (supposing shifting) arrangement of the ions of the host material.

This insight leads us to fit the curve of the fundamental frequency ω_0 (and hence V_{zz}), against temperature quantitatively. For this, we take the experimental and hyperfine parameters of

our $^{181}Ta(TiO_2)$ e−γ TDPAC spectroscopy in Table 4 and plot the parameters against temperature, as shown in figures 30 and 31.

At this point, we note that following additional internal analysis, TOSC15B is an artefact and is probably mixed with the room temperature measurements. As such, we would discard TOSC15B when we plot the trendline.

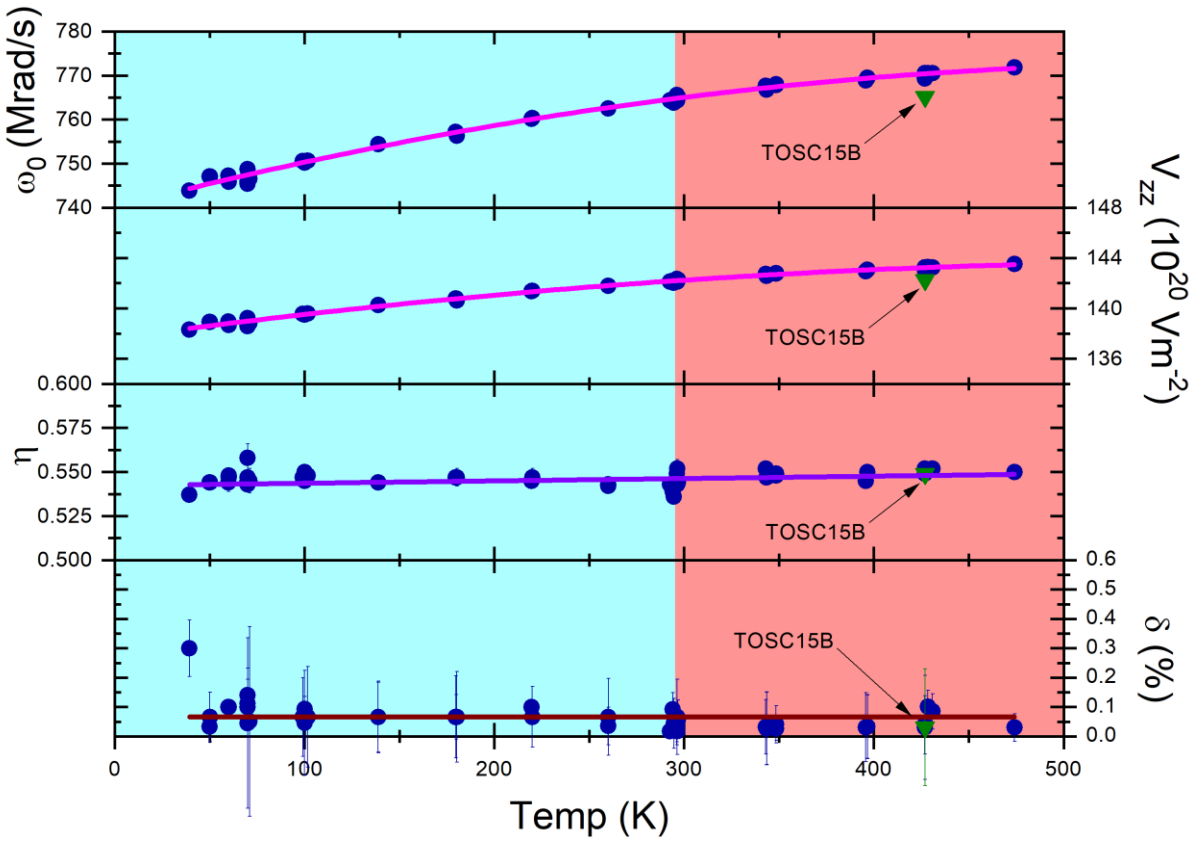


Figure 30: The following graphs of hyperfine parameters are arranged from top to bottom: 1) Fundamental frequency ω_0, 2) Largest electric field gradient V_{zz}, 3) Asymmetry parameter η and 4) Delta Lorentzian δ, as a function of temperature. The following graphs are plotted with a standard temperature axis and scale. We note that for temperatures above room temperature, the e−γ TDPAC measurements are done in the hot furnace, as depicted by the red region. For temperatures below room temperature, the e−γ TDPAC measurements are done in the cold cryostat, as represented by the blue area. Note that for the uncertainties of ω_0 and V_{zz}, we only take their statistical uncertainties (See Table 4). The magenta line represents the parabolic best fit for ω_0 and V_{zz}, with the equation of best fit for ω_0 being $[740.1(3) + 0.112(3) * T - 0.000096(5) * T^2]$ Mrad/s and the equation of best fit for V_{zz} is $[137.63(6) + 0.0207(5) * T - 0.000017(1) * T^2] * 10^{20}$ V/m² (Units of T is in K). The violet line portrays the linear best fit for η and is $0.5423(9) + 0.000013(3) * T$. The wine line shows the averaged value of $\delta = 0.66\%$ for the whole e−γ TDPAC set.

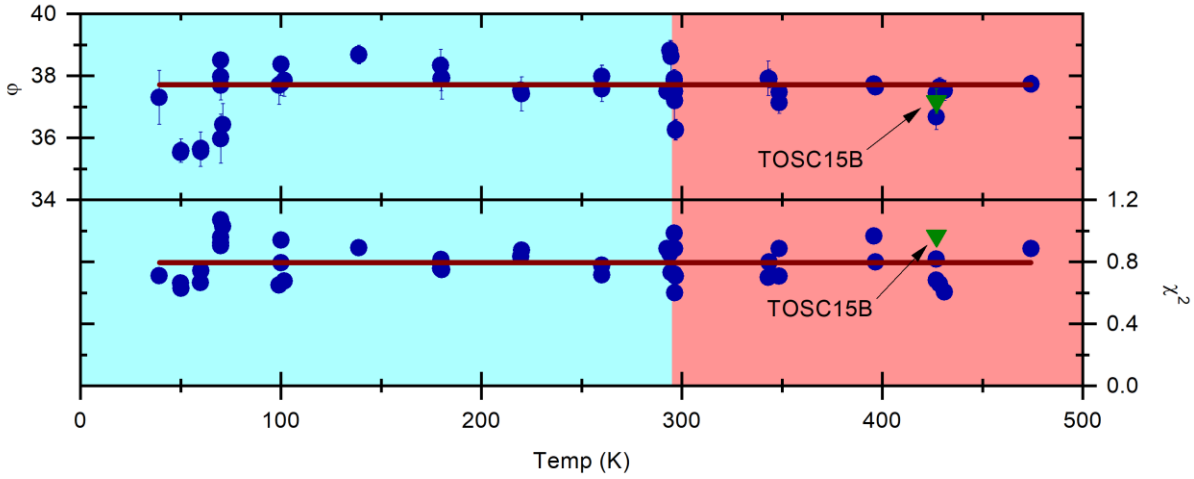


Figure 31: The following graphs of experimental parameters are arranged from top to bottom: 1) Azimuth angle φ, 2) Chi-square χ^2. The following graphs are plotted with a standard temperature axis and scale. We note that for temperatures above room temperature, the e−γ TDPAC measurements are done in the hot furnace, as depicted by the red region. For temperatures below room temperature, the e−γ TDPAC measurements are done in the cold cryostat, as represented by the blue area. We note that the polar angle θ is fixed at 0. Two wine lines are drawn to help in the visuals, and they represent the averaged values of the set for both φ (37.715°) and χ^2 (0.79).

We report the best fit of ω_0, V_{zz} and η for our ^{181}Ta(TiO$_2$) e−γ TDPAC dataset:

$$\omega_0 = 740.1(3) + 0.112(3) * \mathrm{T} - 0.000096(5) * \mathrm{T}^2\ Mrad/s,$$

$$V_{zz} = [137.63(6) + 0.0207(5) * \mathrm{T} - 0.000017(1) * \mathrm{T}^2] * 10^{20}\ Vm^{-2},$$

$$\eta = 0.5423(9) + 0.000013(3) * \mathrm{T}.$$

From the entire literature on bulk rutile ^{181}Ta(TiO$_2$) γ−γ TDPAC spectroscopy, we found that only Adams, J.M. and Catchen, G.L. has the temperature-dependent results that we could directly compare against [59], in which Darriba, G.N. et al. has confirmed [60]. A close look at their dataset reveals that they have mainly done a temperature-dependent analysis mainly from $T \approx 600K$ to $1300K$, alongside their room temperature measurement of $T = 297.15\ K$. Their dataset and research show a weak linear dependence for their V_{zz} and η. Furthermore, after correcting for the quadrupole moment, the following parameters were reported [59]:

$$V_{zz} = [0.000038(6) * T + 141.2(6)] * 10^{20}\ Vm^{-2},$$

$$\eta = 0.57(1) + 0.000011(5) * T.$$

It is noted that their Lorentzian delta value δ shows a maximum of 0.01%, which suggests that, like our ^{181}Ta(TiO$_2$) e−γ TDPAC spectroscopy, their ^{181}Ta sits in a well-defined substitutional site of Ti in TiO$_2$, which make sense as their annealing process is much more severe than ours (See Table 11).

Figure 32 compares the hyperfine parameters obtained from our temperature-dependent ^{181}Ta(TiO$_2$) e−γ TDPAC spectroscopy against the corresponding temperature-dependent ^{181}Ta(TiO$_2$) γ−γ TDPAC spectroscopy obtained from Adams, J.M. and Catchen, G.L. [59].

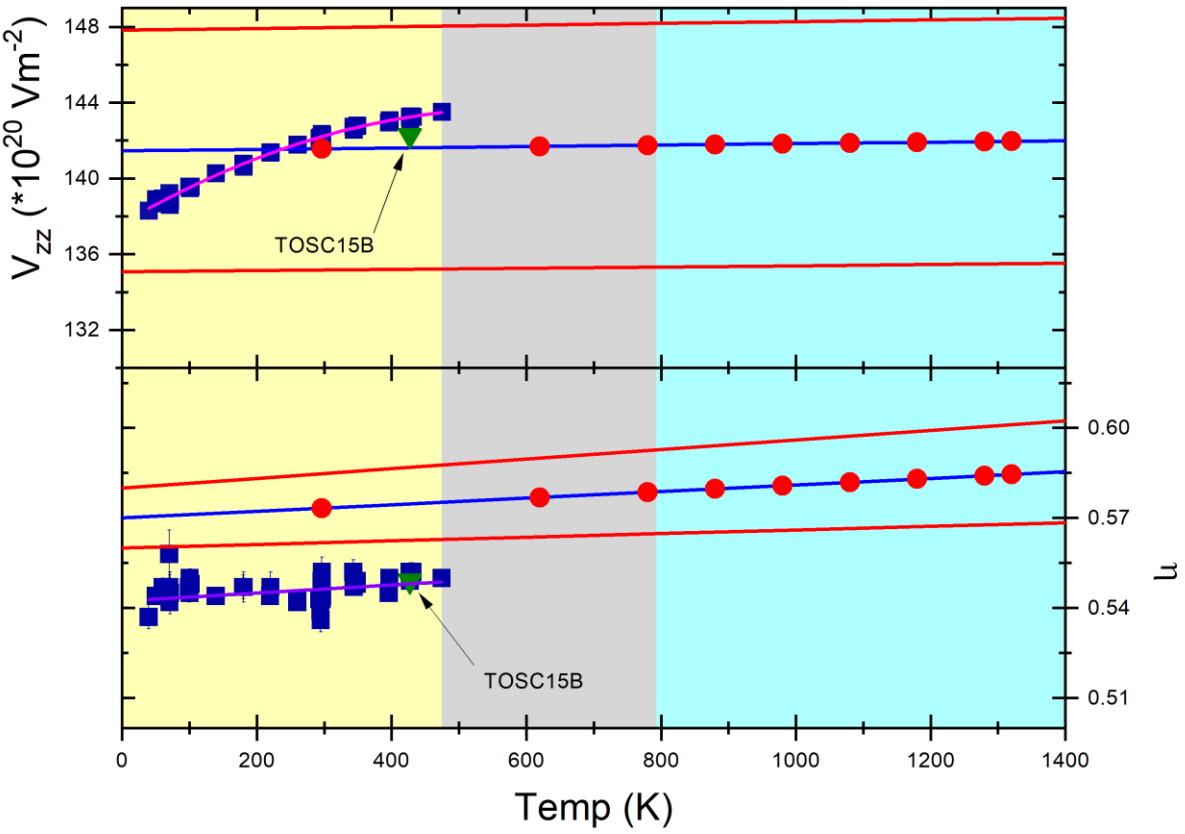


Figure 32: A comparison of our V_{zz} and η (for bulk rutile $^{181}Ta(TiO_2)$ e−γ TDPAC spectroscopy) with that of Adams, J.M. and Catchen, G.L. [59]. The navy-blue points represent our experimental values, while the blue line represents the least sum of squares fit that Adams and Catchen have obtained. The red lines represent the lower and upper threshold for their least fit values. The magenta line shows the parabolic best fit curve of V_{zz} for our data set. The red points show the temperature at which Adams and Catchen conducted their corresponding bulk rutile $^{181}Ta(TiO_2)$ γ−γ TDPAC spectroscopy. It is highlighted that Adams and Catchen have concluded in their paper [59] that within their temperature range (blue region) and projected to the low-temperature region (yellow region), a weak linear dependence of V_{zz} and η with respect to temperature is expected/predicted. However, our data shows otherwise, with V_{zz} showing a distinct parabolic trend, at least in the yellow region. Currently, there is no experimental data in the grey area nor any theoretical models predicting the grey region's trendline. It is hence suggested that research efforts should be expanded to determine 1) the experimental/theoretical trendline of V_{zz} and η with respect to the temperature in the grey region, and 2) theoretically construct a model to sufficiently explain this unusual and (possibly) concave trend [65] as shown in the graph.

It should be noted that contrary to what Adams, J.M. and Catchen, G.L. [59] and in extension, Darriba, G.N. et al. [60] have predicted: In the low-temperature region (See the yellow part in Figure 32), our trendline shows a moderate parabolic behaviour for V_{zz}, while showing a similar weak linear temperature dependence for η.

Hence, with the augmentation of our data, we can split the temperature region into three parts (See Figure 32):

1) $0\,K - 428\,K$, yellow region: V_{zz} is parabolic w.r.t temperature based on our $^{181}Ta(TiO_2)$ e−γ TDPAC spectroscopy.
2) $428\,K - 800\,K$, grey region: There are no experimental data to sufficiently determine the trendline for V_{zz}.
3) $800\,K - 1300\,K$, blue region: V_{zz} is weakly linear w.r.t temperature based on $^{181}Ta(TiO_2)$ γ−γ TDPAC spectroscopy by Adams, J.M. and Catchen, G.L. [59].

We have a solid reason to believe that the temperature dependence of V_{zz} is parabolic concave. Schell, J. et al. have pointed out that similar behaviour is observed in one of the ^{181}Ta sites of thin-film TiO_2 that shows an anatase behaviour [65]. In particular, there exists a non-linear (and possibly parabolic) increase in fundamental frequency ω_0 within the $300K - 473K$ region, in which our single crystal ^{181}Ta(TiO_2) also exhibits (See Figure 33). More interestingly, above the $523K$ region, there is a linear increase of the ω_0, similar to the trendlines discovered by Adams, J.M. and Catchen, G.L. [59] and Darriba, G.N. et al. [60]. Most interestingly, there is a (possibly parabolic) decrease of the fundamental frequency within the $473K - 523K$, and the curvature is steeper than the $300K - 473K$ region.

Hence, augmented with the thin film ^{181}Ta(TiO_2) research by Schell, J. et al. [65], we have a prior belief that our hyperfine parameters (V_{zz} & ω_0) for bulk rutile ^{181}Ta(TiO_2), TDPAC spectroscopy would follow the trendline as seen in Figure 33 presented by Schell, J. et al. [65]. In particular, we conjecture that local maxima exist in both ω_0 & V_{zz} in the temperature range of $400 - 600K$ for bulk rutile ^{181}Ta(TiO_2) TDPAC spectroscopy.

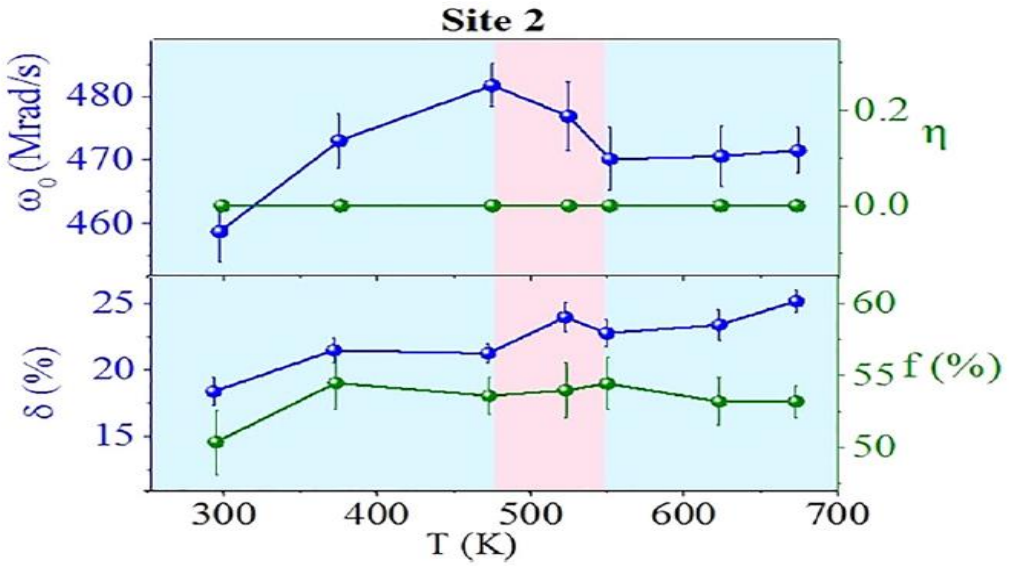


FIG. 4. Hyperfine parameters and their respective errors in the TiO_2 thin film using ^{181}Hf(^{181}Ta) as the test nucleus. Some error bars cannot be seen, because their uncertainties are smaller than the data points.

Figure 33: A graph of the fundamental frequency ω_0 and delta Lorentzian δ in thin film ^{181}Ta(TiO_2) γ−γ TDPAC spectroscopy, in which two sites are identified. We would want to point out this unusual trend of ω_0 in one of the sites, shown as the blue line, in which the hyperfine parameters ω_0 & V_{zz} of bulk rutile ^{181}Ta(TiO_2) TDPAC spectroscopy may follow. It is reprinted from [65] with permission from AIP Publishing. Copyright is retained by AIP Publishing and to the authors of [65].

Currently, no theoretical model can sufficiently explain the abovementioned unusual trend. Previous theoretical models that include the point charge model [101] have insufficient predictive power, and it was evident that the V_{zz} trend for bulk rutile ^{181}Ta(TiO_2) TDPAC spectroscopy does not follow the empirical $T^{3/2}$ law, which several non-cubic metals are shown to follow [102] and debunked following the very recent (2022) efforts by Heinz Hass, which incorporates his method of DFT methodology and analysis [103,104], showing that even simple metals exhibit complex behaviour that the $T^{3/2}$ law could not sufficiently capture.

In addition, temperature-dependent DFT studies by Darriba, G.N. et al. [60] do not predict the unique parabolic trend in the low-temperature region (Yellow region in Figure 32). This discrepancy is expected because they mainly focused on high-temperature regions (Blue region in Figure 32).

In the related temperature-dependent bulk rutile ^{44}Sc(TiO_2) TDPAC experiment [105], Butz, T. and Vianden, R. have reported a convex parabolic-like increase of ω_Q (and hence V_{zz}), and an almost constant η of ^{44}Sc in the TiO_2 matrix from the temperature of $300K - 945K$. Like the case of the ^{181}Ta(TiO_2) TDPAC experiment, there exist no theoretical models that explain the temperature trend of ω_Q in the bulk rutile ^{44}Sc(TiO_2) TDPAC experiment.

Both Butz, T. and Vianden, R. have conjectured that the origins of such a temperature dependence could be attributed to [105]:

1) Lattice expansion/phonon modes,
2) Lattice relaxation around the impurity ion,
3) Localised electron orbitals,
4) Thermal repopulation of electron states.

In their conclusion of this paper [105], Butz, T. and Vianden, R. mentioned that theoreticians must develop a model that can predict the EFG components of the impurity ion in the TiO_2 matrix. Our temperature-dependent e−γ ^{181}Ta(TiO_2) TDPAC experiment adds urgency to their call. We suspect a wealth of physics is waiting to be discovered following the development of the mentioned sufficient model.

Hence, following the conclusion of part 1 of this duo/trio-logy, current efforts are being made towards developing such a theoretical model. In particular, we have secured the assistance of Peter Blöchl, the developer of the CP-PAW program [4,106], and based on the earlier work by him, Peter Blaha and Helena Petrilli [107], we are employing DFT methods alongside the (1) frozen phonon method and (2) local lattice relaxation around the impurity ion, in the hopes of theoretically replicating the temperature dependence of the EFG components for Ti in pure TiO_2 [108] and Ta in doped ^{181}Ta(TiO_2).

8.3) X-ray Diffraction of the 181Ta(TiO_2) Sample after the γ−γ and e−γ TDPAC Spectroscopy

From the results in Table 5, we can see that up to a systematic shift of $0.22°$, the corresponding peaks of our ($80\ keV$ ^{181}Hf ion-implanted and complimented with sufficient thermal annealing) TiO_2, as well as the reference sample, agree with each other. The cause of such a systematic shift could be due to the individual micro-stress of each sample. We also note that the X-rays produced from the Empyrean diffractometer are not monochromatic, which explains the double peaks observed on the right side of Figure 22. We especially note that the micro-strain of our samples, along with the reference, is about 0.0038%, which is very low. The micro-strain is a measure of the amorphisation of a solid sample, and thus, both our TiO_2 samples and the reference could be said to exhibit single crystal-like properties.

As seen on the left side of Figure 22, the other small peaks could be attributed to the oxygen vacancies (see Section 6.1.2). We make no further attempts to characterise these peaks at

the time of dissemination, as our main result is on the TDPAC study of (^{181}Ta)TiO_2. Our ^{181}Ta probe (which sits on a well-defined Ti-substitutional site) does not detect such oxygen deficiencies explicitly.

The dominant peaks in our result correspond to the (200) Miller index direction of the rutile TiO_2 (regarding the polycrystalline rutile TiO_2 sample taken from the RRUFF™ Project website [109,110]).

In addition to our reference sample, we refer to a paper by Guo et al. [99], in which they fabricated their own single crystal rutile TiO_2, and their corresponding X-ray diffractograms have revealed a similar (single peak-like) behaviour. The position of their peaks and sample preparation are elaborated in Table 13 below.

Sample and Peak Number	**Angle 2θ (2 × Deg)**	**Peak Identity (Miller Indices)** [a]	**Sample Preparation**
Sample from [99], cut along an arbitrary direction.	62.6	(002)	The sample is produced in the laboratory setting via the floating zone method. The resulting sample is cut into 5 × 2 mm^2 thin slices alongside an arbitrary direction and the crystal growth direction, respectively.
Sample from [99], cut perpendicular to the c-axis.	27.5	(110)	
Reference Sample, Peak 1.	39.5	(200)	The sample (10 × 10 × 1.0 mm^3) is commercially manufactured by Crystal GmbH [55]. XRD measurement is conducted face-(10 × 1.0 mm^2) side up.
Reference Sample, Peak 2.	39.6		
Sample 1, Peak 1, This study.	39.7	(200)	The sample (10 × 10 × 1.0 mm^3) is commercially manufactured by Crystal GmbH [55], then 80 keV ^{181}Hf ion-implanted and thermally annealed at 873 K for 5.25 h. XRD measurement is conducted face-(10 × 1.0 mm^2) side up.
Sample 1, Peak 2, This study.	39.8		
Sample 2, Peak 1, This study.	39.5		
Sample 2, Peak 2, This study.	39.6		

Figure 13: An XRD comparison of the two dominant peaks of our single crystal rutile TiO_2 samples to the (1) reference sample produced by Crystal GmbH [87] and (2) the samples produced via the floating zone method as described in the paper of Guo et al. [99]. We note that in their corresponding XRD diffractogram (Figure 2 of [99]), regardless of the direction of the cut, we could see multiple small peaks that are too fine to be distinguished with their domain of 20–50°, like our case as seen in Figure 22, in which we must restrict our domain from 0–80° to 38–40° to allow for sufficient resolution. (a) The peak identification of the Miller indices for our samples (and the reference sample) concerns reference [109]. For samples from paper [99], the peaks are already identified in the corresponding paper and cross-verified with reference [109].

From the information obtained in the XRD diffraction of our TiO_2 sample, we can conclude that the treatment of our parts per billion ^{181}Hf ion-implanted TiO_2 samples, complimented with 5hr 15 min of thermal annealing at $873\ K$, does not significantly alter its global structure, as the low value of the micro-strain shows in all 3 of our XRD diffractograms.

9) Conclusion

In this thesis, the physics of the $^{181}Ta(TiO_2)$ e−γ TDPAC spectroscopy was investigated in depth over a wide temperature range.

Chapter 1 introduces ISOLDE and BONIS as premier ion-implantation facilities where today's TDPAC experiments are primarily conducted. ISOLDE is particularly singled out due to its ability to produce short-lived isotopes, whose TDPAC-related experiments must be performed onsite for signal acquisition.

In chapter 2, we reveal the origin of EFGs as a hyperfine parameter caused by the hyperfine interaction between the nucleus and its electron cloud in the TDPAC probe. The electron cloud could be distorted by the local lattice environment of the host material, which contributes to temperature dependence.

In chapter 3, we explore the theoretical principles of TPDAC spectrascopy needed to understand the TDPAC experiment. We introduce the angular correlation between two consecutive emissions of γ-rays by the direct de-excitation of the relevant nucleus, which is caused by the host material as an external influence covered in chapter 2.

In chapter 4, we then work on the experimental subtleties. We develop the concept of count rate ratio $R(t)$ and discussed the statistical distribution of an ensemble of implanted TDPAC probes, which is said to follow either a Lorentzian or Gaussian distribution.

In chapter 5, we focus on the angular correlation between 1) two consecutive emissions of γ-rays to 2) the angular correlation between the emission of a conversion electron (utilising a mechanism called the internal conversion), followed by a γ-ray. We also discussed the schematics and setup of the γ-γ and e-γ TDPAC spectroscopy experiments.

In chapter 6, having discussed the TDPAC setup and theory in sufficient detail, we then discuss the specifics of the bulk rutile $^{181}Ta(TiO_2)$ e-γ and γ-γ TDPAC spectroscopy. In this chapter, the energies of the orientation and correlation γ-rays, as well as the conversion electron for ^{181}Ta, were stated. The physics and properties of TiO_2, particularly the fast recombination of the electrons as a charge carrier, are discussed. The details of the ion-implantation of ^{181}Ta into single crystal rutile TiO_2 and the thermal treatment were discussed sufficiently in detail. Last, the experimental procedure for the XRD diffraction of our TiO_2 sample used to determine the degree of the ion-implantation damage (and the subsequent thermal treatment) to our TiO_2 was also briefly sketched out.

In chapter 7, we have analysed and collected the room temperature TDPAC bulk rutile $^{181}Ta(TiO_2)$ γ-γ signal and the temperature-dependent bulk rutile $^{181}Ta(TiO_2)$ e-γ signal. We have also provided the XRD diffractogram of the reference TiO_2 sample and both our $^{181}Ta(TiO_2)$ sample in the aftermath of the TDPAC spectroscopy.

In chapter 8, we analyse the TDPAC data collected in chapter 7. At room temperature, the hyperfine parameters obtained from $^{181}Ta(TiO_2)$ γ-γ and e-γ TDPAC spectroscopy agree. This result suggests that the recombination process is an order of magnitude faster than the $10\ ns$

of the half-life of the intermediate state of the ^{181}Ta TDPAC probe and, thus, could not be recorded by our e-γ TDPAC setup. The mentioned phenomenon is in line with the recent experiment by a team from the KAUST Solar Centre [74], in which an induced hole in bulk rutile will capture an electron in the order of picoseconds.

If we include the effects of temperature, Adams, J.M. and Catchen, G.L. [59] and Darriba, G.N. et al. [60] have predicted an extension of the weak linear temperature dependence of the fundamental frequency ω_0 (and hence V_{zz}) to the low-temperature regime, for which we have tested with our e-γ TDPAC setup, which shows a concave, parabolic curve. A similar experiment on thin film ^{181}Ta(TiO_2) research by Schell, J. et al. [65] revealed the same shape, both in the low-temperature regime $(0 - 440K)$ as per our e-γ TDPAC experiments and high-temperature regime $(550 - 1300K)$, shown by the work of Adams, J.M. and Catchen, G.L. [59]. In addition, in the mid-temperature region $(440 - 550K)$, the curvature of the seemingly parabolic trendline on the ω_0 (and hence V_{zz}) of the thin film ^{181}Ta(TiO_2) is higher in magnitude compared to the low-temperature regime.

We have also verified, via the XRD diffractogram, that sufficient thermal treatment of the ion-implanted ^{181}Ta(TiO_2) recovers the global single crystal-like properties of the whole rutile and single-crystal fabricated TiO_2.

To end this thesis, I would like to reiterate that we have a prior belief that the physics behind the unusual temperature dependence of ^{181}Ta that is Ti-substitutionally embedded in bulk TiO_2 will be significant. Hence, as of this writing, efforts are underway to theoretically simulate the V_{zz} temperature dependence of ^{181}Ta(TiO_2) using the frozen phonon method and DFT. We could uncover profound insights into the nature of TiO_2.

This point concludes part 1 of my thesis, submitted as a requirement for my master's degree. I hope that with time, I can report on part 2 of this chronology, hopefully with surprising insights beyond our imagination.

Fin,

Ian Yap Chang Jie

This thesis was written in August 2022 in the peaceful and quiet city of Gottingen, Germany.

"From yesterday´s me to tomorrow's you."

Appendix A: Analytical solution to the eigenvalue equation (2.57).

We refer to equation (2.57) and have the characteristic equation written as:

$$E^3 - 28(\eta^2 + 3)E - 160(1 - \eta^2) = 0 \qquad (2.57a)$$

We note that the equation $(2.57a)$ is already in the depressed cubic form. This expression means that we can use the method of Scipione (outlined in [111]) to obtain an analytical solution of E.

We also note that the general solution to a cubic equation was discovered by Girolamo Cardano in the 14th century (as recorded in his book, Ars Magma [112]) by converting a general cubic equation $Ax^3 + Bx^2 + Cx + D = 0$, with $A, B, C, D \in \mathbb{R}$ into the depressed cubic form.

We first define a general cubic equation of a depressed form: Let y be a free variable and $A, B \in \mathbb{R}$. Then a general depressed cubic form is written as:

$$y^3 + Ay = B. \qquad (A1.1)$$

Scipione then asserts that $\exists s, t \in \mathbb{R}$ such that

$$3st = A, \qquad (A1.2a)$$
$$s^3 - t^3 = B, \qquad (A1.2b)$$

and

$$y = s - t \qquad (A1.3)$$

is the solution to the depressed cubic equation $(A1.1)$. We check:

$$y^3 + Ay = (s - t)^3 - 3st(s - t) = s^3 - t^3 = B$$

From equation $(A1.2a \ \& \ A1.2b)$,

$$\left(\frac{A}{3t}\right)^3 - t^3 = B \Rightarrow t^6 + Bt^3 - \frac{A^3}{27} = 0 \qquad (A1.4)$$

Thus, by solving for t^3 in the polynomial equation $(A1.4)$, we have:

$$t^3 = \frac{-B \pm \sqrt{B^2 + \frac{4A^3}{27}}}{2} \qquad (A1.5)$$

From equation $(2.57a)$, we have:

$$A = -28(\eta^2 + 3), B = 160(1 - \eta^2) \qquad (A1.6)$$

In anticipation of less cluttering and retrospect, we define:

$$p = \frac{A}{3} = -28\left(1 + \frac{\eta^2}{3}\right), \qquad (A1.7a)$$
$$q = -\frac{B}{2} = -80(1 - \eta^2). \qquad (A1.7b)$$

Thus, equation $(2.57a)$ is reduced to

$$E^3 + 3pE + 2q = 0 \qquad (A1.8)$$

And from equation $(A1.5)$, we have:

$$t^3 = \frac{2q \pm \sqrt{4q^2 - 4p^3}}{2} = q \pm \sqrt{q^2 - p^3} \qquad (A1.9)$$

We note that if $\eta \in [0,1]$, then $p \in \left[-28\left(\frac{4}{3}\right), -28\right] \Rightarrow p \in \left[-\left(28\left(\frac{4}{3}\right)\right)^3, -(28)^3\right]$ and $q \in [-80,0] \Rightarrow q^2 \in [0,80^2]$. These intervals mean that $\forall \eta \in [0,1]$, $q^2 - p^3 < 0$. Thus,

$$t^3 = q \pm i\sqrt{|p|^3 - |q|^2}. \qquad (A1.10)$$

Both roots lead to the same solution by a mathematical symmetry. To illustrate the meaning of this mathematical symmetry, I will keep both solutions for now.

In a general setting, all complex numbers of the form $A' + B'i$, with $A' \,\&\, B' \in \mathbb{R}$ can be written in the form of:

$$A' + B'i = \sqrt{A'^2 + B'^2}\exp(i\theta), \qquad (A1.11a)$$

$$\theta = \cot^{-1}(B'/A'). \qquad (A1.11b)$$

From equation $(A1.11a)$, we have:

$$\left|q \pm i\sqrt{|p|^3 - |q|^2}\right| = \sqrt{|q|^2 + |p|^3 - |q|^2} = \sqrt{|p|^3} = |p|^{\frac{3}{2}} \qquad (A1.12)$$

We have a look at the representation of the complex number $q \pm i\sqrt{|p|^3 - |q|^2}$ in the complex plane below:

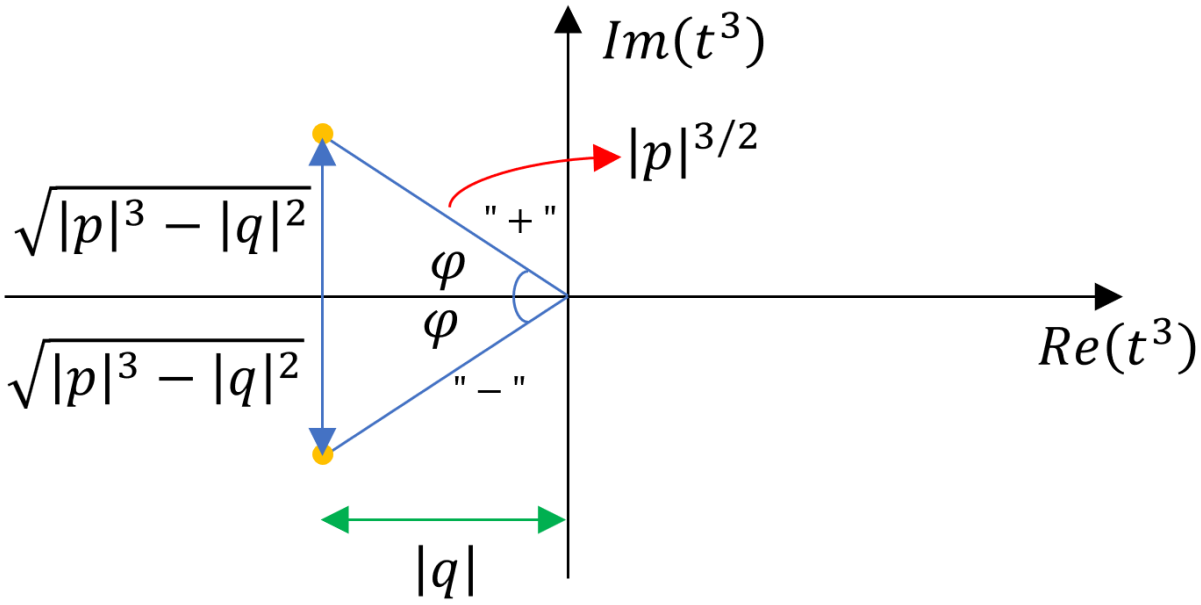


Figure A1: The representation of the complex number $q \pm i\sqrt{|p|^3 - |q|^2}$ to extract the geometrical features shown in the equation $(A1.14)$.

In anticipation of the roots of unity, we define (Remember that $p < 0$):

$$r = |p|^{\frac{1}{2}} = (-p)^{\frac{1}{2}} \qquad (A1.13a)$$

$$\varphi = \cos^{-1}\frac{|q|}{r^3} \in \left[0, \frac{\pi}{2}\right] \qquad (A1.13b)$$

Thus,

$$t^3 = r^3 \exp\big(i(\pi \mp \varphi)\big) = \exp(i\pi)\, r^3 \exp(\mp i\varphi)\,. \qquad (A1.14)$$

De Moiré's formula allows us to write:

$$t = \exp\left(\frac{i\pi}{3}\right) r \exp\left(\mp\frac{i\varphi}{3} + \frac{2k\pi i}{3}\right), k \in \{-1,0,1\} \qquad (A1.15)$$

And hence, we have three solutions of t:

$$k = 1\colon t_1 = r\exp\left(\frac{i\pi}{3}\right)\exp\left(\mp\frac{i\varphi}{3} + \frac{2\pi i}{3}\right) = r\exp(i\pi)\exp\left(\mp\frac{i\varphi}{3}\right) = -r\exp\left(\mp\frac{i\varphi}{3}\right) \qquad (A1.16a)$$

$$k = 0\colon t_2 = r\exp\left(\frac{i\pi}{3}\right)\exp\left(\mp\frac{i\varphi}{3}\right) = r\exp\left(\frac{i\pi}{3}\right)\exp\left(\mp\frac{i\varphi}{3}\right) = \frac{r}{2}\left(1 + i\sqrt{3}\right)\exp\left(\mp\frac{i\varphi}{3}\right) \qquad (A1.16b)$$

$$k = -1\colon t_3 = r\exp\left(\frac{i\pi}{3}\right)\exp\left(\mp\frac{i\varphi}{3} - \frac{2\pi i}{3}\right) = r\exp\left(-\frac{i\pi}{3}\right)\exp\left(\mp\frac{i\varphi}{3}\right) = \frac{r}{2}\left(1 - i\sqrt{3}\right)\exp\left(\mp\frac{i\varphi}{3}\right) \qquad (A1.16c)$$

We are left to calculate s as shown in equation $(A1.2a \;\&\; A1.2b)$. Using $s = A/3t$, using the expression of A from equation $(A1.7a)$:

$$s_1 = \frac{3p}{3t_1} = \frac{-(-p)}{-\sqrt{-p}}\exp\left(\pm\frac{i\varphi}{3}\right) = \sqrt{-p}\exp\left(\pm\frac{i\varphi}{3}\right) = r\exp\left(\pm\frac{i\varphi}{3}\right) \qquad (A1.17a)$$

$$s_2 = \frac{3p}{3t_2} = \frac{-(-p)}{\sqrt{-p}}\exp\left(\pm\frac{i\varphi}{3}\right)\exp\left(-\frac{i\pi}{3}\right) = -\sqrt{-p}\exp\left(\pm\frac{i\varphi}{3}\right)\exp\left(-\frac{i\pi}{3}\right)$$
$$= -r\exp\left(\pm\frac{i\varphi}{3}\right)\exp\left(-\frac{i\pi}{3}\right) = -\frac{r}{2}\left(1 - i\sqrt{3}\right)\exp\left(\pm\frac{i\varphi}{3}\right) \qquad (A1.17b)$$

$$s_3 = \frac{3p}{3t_3} = \frac{-(-p)}{\sqrt{-p}}\exp\left(\pm\frac{i\varphi}{3}\right)\exp\left(\frac{i\pi}{3}\right) = -\sqrt{-p}\exp\left(\pm\frac{i\varphi}{3}\right)\exp\left(\frac{i\pi}{3}\right)$$
$$= -r\exp\left(\pm\frac{i\varphi}{3}\right)\exp\left(\frac{i\pi}{3}\right) = -\frac{r}{2}\left(1 + i\sqrt{3}\right)\exp\left(\pm\frac{i\varphi}{3}\right) \qquad (A1.17c)$$

And hence from equation $(A1.3)$, with $E = s - t$,

$$E_1 = s_1 - t_1 = r\left(\exp\left(\pm\frac{i\varphi}{3}\right) + \exp\left(\mp\frac{i\varphi}{3}\right)\right)$$
$$= r\left(\cos\left(\frac{\varphi}{3}\right) \pm i\sin\left(\frac{\varphi}{3}\right) + \cos\left(\frac{\varphi}{3}\right) \mp i\sin\left(\frac{\varphi}{3}\right)\right) = 2r\cos\left(\frac{\varphi}{3}\right) \qquad (A1.18a)$$

$$E_2 = s_2 - t_2 = -r\left(\exp\left(\pm\frac{i\varphi}{3}\right)\exp\left(-\frac{i\pi}{3}\right) + \exp\left(\mp\frac{i\varphi}{3}\right)\exp\left(\frac{i\pi}{3}\right)\right)$$
$$= -\frac{r}{2}\left(\left(1 - i\sqrt{3}\right)\exp\left(\pm\frac{i\varphi}{3}\right) + \left(1 + i\sqrt{3}\right)\exp\left(\mp\frac{i\varphi}{3}\right)\right)$$
$$= -\frac{r}{2}\left(\exp\left(\pm\frac{i\varphi}{3}\right) - i\sqrt{3}\exp\left(\pm\frac{i\varphi}{3}\right) + \exp\left(\mp\frac{i\varphi}{3}\right) + i\sqrt{3}\exp\left(\mp\frac{i\varphi}{3}\right)\right)$$
$$= -\frac{r}{2}\left(2\cos\left(\frac{\varphi}{3}\right) - i\sqrt{3}\exp\left(\pm\frac{i\varphi}{3}\right) + i\sqrt{3}\exp\left(\mp\frac{i\varphi}{3}\right)\right)$$
$$= -\frac{r}{2}\left(2\cos\left(\frac{\varphi}{3}\right) + i\sqrt{3}\left(-\cos\left(\frac{\varphi}{3}\right) \mp i\sin\left(\frac{\varphi}{3}\right) + \cos\frac{\varphi}{3} \mp i\sin\left(\frac{\varphi}{3}\right)\right)\right)$$
$$= -\frac{r}{2}\left(2\cos\left(\frac{\varphi}{3}\right) + i\sqrt{3}\left(\mp i\sin\left(\frac{\varphi}{3}\right) \mp i\sin\left(\frac{\varphi}{3}\right)\right)\right)$$
$$= -\frac{r}{2}\left(2\cos\left(\frac{\varphi}{3}\right) \pm 2\sqrt{3}\sin\left(\frac{\varphi}{3}\right)\right) = -r\left(\cos\left(\frac{\varphi}{3}\right) \pm \sqrt{3}\sin\left(\frac{\varphi}{3}\right)\right) \qquad (A1.18b)$$

$$E_3 = s_3 - t_3 = -r\left(\exp\left(\pm\frac{i\varphi}{3}\right)\exp\left(\frac{i\pi}{3}\right) + \exp\left(\mp\frac{i\varphi}{3}\right)\exp\left(-\frac{i\pi}{3}\right)\right)$$
$$= -\frac{r}{2}\left(\left(1 + i\sqrt{3}\right)\exp\left(\pm\frac{i\varphi}{3}\right) + \left(1 - i\sqrt{3}\right)\exp\left(\mp\frac{i\varphi}{3}\right)\right)$$
$$= -\frac{r}{2}\left(\exp\left(\pm\frac{i\varphi}{3}\right) + i\sqrt{3}\exp\left(\pm\frac{i\varphi}{3}\right) + \exp\left(\mp\frac{i\varphi}{3}\right) - i\sqrt{3}\exp\left(\mp\frac{i\varphi}{3}\right)\right)$$
$$= -\frac{r}{2}\left(2\cos\left(\frac{\varphi}{3}\right) + i\sqrt{3}\left(\cos\left(\frac{\varphi}{3}\right) \pm i\sin\left(\frac{\varphi}{3}\right) - \cos\frac{\varphi}{3} \pm i\sin\left(\frac{\varphi}{3}\right)\right)\right)$$
$$= -\frac{r}{2}\left(2\cos\left(\frac{\varphi}{3}\right) \mp 2\sqrt{3}\sin\left(\frac{\varphi}{3}\right)\right) = -r\left(\cos\left(\frac{\varphi}{3}\right) \mp \sqrt{3}\sin\left(\frac{\varphi}{3}\right)\right) \qquad (A1.18c)$$

Under the change of the roots of t^3 as seen in equation A1.10, the eigenvalues remain the same, with E_2 exchanging its eigenvalue with E_3. Since we are using the numerical method for our TDPAC experiment fitting (Gfit19), we would just leave the analysis up till the exact determination of the eigenvalues of the Hamiltonian equation 2.49 with $I = 5/2$.

We note that in our derivation, we define our $r = (-p)^{1/2}$. However, Butz's definition of $r = -(-p)^{1/2}$. Consequently, the signs of our E_1, E_2 and E_3 are reversed as compared to Butz.

To see the equivalency of Geradu's expression (Equation $(2.59a - 2.59f)$) to that of Butz (Equation $(2.58a - 2.58h)$), we note that:

$$\alpha = \sqrt{28\left(1 + \frac{\eta^2}{3}\right)} = \sqrt{|p|} = r, \qquad (A1.19a)$$

$$\beta = \frac{80(1-\eta^2)}{\alpha^3} = -\frac{80(1-\eta^2)}{r^3} = \frac{q}{r^3}, \qquad (A1.19b)$$

Then:

$$\cos^{-1}\beta = \cos^{-1}\left(\frac{q}{r^3}\right) = \varphi\,. \qquad (A1.19c)$$

By using the identity $\cos(x \pm y) = \cos x \cos y \mp \sin x \sin y$, we have (in units of $\hbar\omega_Q$):

$$E_1 = 2\alpha \cos\left(\frac{1}{3}\cos^{-1}\beta\right) = 2r\cos\left(\frac{\varphi}{3}\right), \qquad (A1.19d)$$

$$E_2 = -2\alpha \cos\left(\frac{1}{3}(\pi + \cos^{-1}\beta)\right) = 2r\left[\cos\left(\frac{\pi}{3}\right)\cos\left(\frac{\varphi}{3}\right) - \sin\left(\frac{\pi}{3}\right)\sin\left(\frac{\varphi}{3}\right)\right]$$

$$= -r\left(\cos\left(\frac{\varphi}{3}\right) - \sqrt{3}\sin\left(\frac{\varphi}{3}\right)\right), \qquad (A1.19e)$$

$$E_3 = -2\alpha \cos\left(\frac{1}{3}(\pi - \cos^{-1}\beta)\right) = 2r\left[\cos\left(\frac{\pi}{3}\right)\cos\left(\frac{\varphi}{3}\right) + \sin\left(\frac{\pi}{3}\right)\sin\left(\frac{\varphi}{3}\right)\right]$$

$$= -r\hbar\omega_Q\left(\cos\left(\frac{\varphi}{3}\right) + \sqrt{3}\sin\left(\frac{\varphi}{3}\right)\right), \qquad (A1.19f)$$

which are precisely the solutions $(A1.18a - A1.18c)$.

Appendix B: Butz's derivation of the properties of $G_{k_1,k_2}^{N_1,N_2}(t)$ (And some comments on the unitary matrix $\overleftrightarrow{U}$).

In this appendix, we will mainly look at Butz's proof [23] on the properties of $G_{k_1,k_2}^{N_1,N_2}(t)$. It is reproduced here (with permission) for ease of reference. Copyright is retained under Springer Nature.

We start with the single crystal perturbation function, as written as the equation (3.50):

$$G_{k_1,k_2}^{N_1,N_2}(t) = \sum_{M_a,M_b} \left(\begin{matrix} (-1)^{2I+M_a+M_b} \sqrt{(2k_1+1)(2k_2+1)} \begin{pmatrix} I & I & k_1 \\ M_a' & -M_a & N_1 \end{pmatrix} \\ \times \begin{pmatrix} I & I & k_2 \\ M_b' & -M_b & N_2 \end{pmatrix} \langle I, M_b|\Lambda(t)|I, M_a\rangle \langle I, M_b'|\Lambda(t)|I, M_a'\rangle^* \end{matrix} \right), \quad (3.50)$$

and also, in this form (equation (3.58)):

$$G_{k_1,k_2}^{N_1,N_2}(t) = \sum_{\substack{M_a, \\ M_b}} \left(\begin{matrix} (-1)^{2I+M_a+M_b} \sqrt{(2k_1+1)(2k_2+1)} \begin{pmatrix} I & I & k_1 \\ M_a' & -M_a & N_1 \end{pmatrix} \begin{pmatrix} I & I & k_2 \\ M_b' & -M_b & N_2 \end{pmatrix} \\ \times \sum_{N,N'} \langle N|I, M_b\rangle^* \langle N|I, M_a\rangle \langle N'|I, M_b'\rangle \langle N'|I, M_a'\rangle^* \exp\left(\frac{-i\left(E_N - E_{N'}\right)t}{\hbar} \right) \end{matrix} \right). \quad (3.58)$$

Proof of certain properties of $G_{k_1k_2}^{N_1N_2}(t)$:

$$G_{0,0}^{0,0}(t) = 1 \quad (3.75)$$

We first start with:

$$G_{0,0}^{0,0}(t) = \sum_{M_a,M_b} \left(\begin{matrix} (-1)^{2I+M_a+M_b} \begin{pmatrix} I & I & 0 \\ M_a & -M_a & 0 \end{pmatrix} \begin{pmatrix} I & I & 0 \\ M_b & -M_b & 0 \end{pmatrix} \\ \times \langle I, M_b|\Lambda(t)|I, M_a\rangle \langle I, M_b|\Lambda(t)|I, M_a\rangle^* \end{matrix} \right)$$

1) We note that due to the condition $M_a' - M_a + N_1 = 0$ & $M_b' - M_b + N_2 = 0$ for the corresponding 3j-symbols to be non-zero, which sets $M_a' = M_a$ & $M_b' = M_b$ in this case.
2) We make use of a special relationship [3,113]:

$$\begin{pmatrix} I & I & 0 \\ m & -m & 0 \end{pmatrix} = \frac{1}{\sqrt{2I+1}} (-1)^{I-m}$$

Thus, we have:

$$G_{0,0}^{0,0}(t) = \frac{1}{2I+1} \sum_{M_a,M_b} (\langle I, M_b|\Lambda(t)|I, M_a\rangle \langle I, M_b'|\Lambda(t)|I, M_a'\rangle^*)$$

As $\Lambda(t)$ is a unitary operator,

$$\sum_{M_a,M_b} (\langle I, M_b|\Lambda(t)|I, M_a\rangle \langle I, M_b'|\Lambda(t)|I, M_a'\rangle^*) = 2I+1,$$

And hence:

$$G_{0,0}^{0,0}(t) = 1.$$

$$N_1 + N_2 \in 2\mathbb{Z} \quad (3.76)$$

We exploit the checkerboard structure of our unitary matrix $\overleftrightarrow{U}$. We have for $m, m' \in \{-I, -I+1 \ldots, I-1, I\}$:

$$U_{m,m'} = 0,$$

if i) for integer I, $m + m' \in 2\mathbb{Z}$ or ii) for half-integer I, $m + m' \in 2\mathbb{Z} + 1$.
From equation (3.58), the expressions $M_b + N, M_a + N, M_b' + N$ & $M_a' + N$ has to be even (odd) if I is an integer (half-integer).
It immediately follows that the expressions $M_b + M_a, M_b' + M_a'$ has to be even (odd) if I is an integer (half-integer).
Further using the restriction provided by the 3j-symbols:

$$M_a' - M_a + N_1 = 0 \;\&\; M_b' - M_b + N_2 = 0$$

Or:

$$M_a' + M_b' - (M_a + M_b) + N_1 + N_2 = 0$$

Which forces:

$$N_1 + N_2 \in 2\mathbb{Z}.$$

$$G_{k_1,k_2}^{N_1,N_2}(t) = G_{k_2,k_1}^{N_2,N_1}(t) \tag{3.77}$$

We first interchange $k_1 \leftrightarrow k_2$ and $N_1 \leftrightarrow N_2$ in equation (3.50):

$$G_{k_2,k_1}^{N_2,N_1}(t) = \sum_{M_a,M_b} \left(\begin{array}{c} (-1)^{2I+M_a+M_b} \sqrt{(2k_1+1)(2k_2+1)} \begin{pmatrix} I & I & k_2 \\ M_a' & -M_a & N_2 \end{pmatrix} \\ \times \begin{pmatrix} I & I & k_1 \\ M_b' & -M_b & N_1 \end{pmatrix} \langle I, M_b|\Lambda(t)|I, M_a\rangle \langle I, M_b'|\Lambda(t)|I, M_a'\rangle^* \end{array} \right)$$

Next, we exchange $M_a \leftrightarrow M_b$ and $M_a' \leftrightarrow M_b'$:

$$G_{k_2,k_1}^{N_2,N_1}(t) = \sum_{M_a,M_b} \left(\begin{array}{c} (-1)^{2I+M_a+M_b} \sqrt{(2k_1+1)(2k_2+1)} \begin{pmatrix} I & I & k_2 \\ M_b' & -M_b & N_2 \end{pmatrix} \\ \times \begin{pmatrix} I & I & k_1 \\ M_a' & -M_a & N_1 \end{pmatrix} \langle I, M_a|\Lambda(t)|I, M_b\rangle \langle I, M_a'|\Lambda(t)|I, M_b'\rangle^* \end{array} \right)$$

We note:

1) From equation $(3.60b)$, $\Lambda(t)$ as an operator is symmetric. Hence:

$$\langle I, M_a|\Lambda(t)|I, M_b\rangle = \langle I, M_b|\Lambda(t)|I, M_a\rangle$$

We hence have:

$$G_{k_1,k_2}^{N_1,N_2}(t) = G_{k_2,k_1}^{N_2,N_1}(t)$$

$$G_{k_1,k_2}^{N_1,N_2}(t) = G_{k_1,k_2}^{-N_1,-N_2}(t) \tag{3.78}$$

We start with the expression of $G_{k_1,k_2}^{-N_1,-N_2}(t)$:

$$G_{k_2,k_1}^{N_2,N_1}(t) = \sum_{M_a,M_b} \left(\begin{array}{c} (-1)^{2I+M_a+M_b} \sqrt{(2k_1+1)(2k_2+1)} \begin{pmatrix} I & I & k_2 \\ M_a' & -M_a & -N_2 \end{pmatrix} \\ \times \begin{pmatrix} I & I & k_1 \\ M_b' & -M_b & -N_1 \end{pmatrix} \langle I, M_b|\Lambda(t)|I, M_a\rangle \langle I, M_b'|\Lambda(t)|I, M_a'\rangle^* \end{array} \right)$$

We interchange $M_a \leftrightarrow -M_a, M_b \leftrightarrow -M_b, M_a' \leftrightarrow -M_a', M_b' \leftrightarrow -M_b'$ to obtain:

$$G_{k_2,k_1}^{N_2,N_1}(t)$$
$$= \sum_{M_a,M_b} \left(\begin{array}{c} (-1)^{2I-M_a-M_b} \sqrt{(2k_1+1)(2k_2+1)} \begin{pmatrix} I & I & k_2 \\ -M_a' & M_a & -N_2 \end{pmatrix} \\ \times \begin{pmatrix} I & I & k_1 \\ -M_b' & M_b & -N_1 \end{pmatrix} \langle I, -M_b|\Lambda(t)|I, -M_a\rangle \langle I, -M_b'|\Lambda(t)|I, -M_a'\rangle^* \end{array} \right)$$

Using the time-reversal property of the 3j-symbol:

$$\begin{pmatrix} j_1 & j_2 & j_3 \\ -m_1 & -m_2 & -m_3 \end{pmatrix} = (-1)^{j_1+j_2+j_3}\begin{pmatrix} j_1 & j_2 & j_3 \\ m_1 & m_2 & m_3 \end{pmatrix}$$

$$G_{k_2,k_1}^{N_2,N_1}(t)$$

$$= \sum_{M_a,M_b}\left((-1)^{2I-M_a-M_b+(2I+k_1)+(2I+k_2)}\sqrt{(2k_1+1)(2k_2+1)}\begin{pmatrix} I & I & k_2 \\ -M_a' & M_a & -N_2 \end{pmatrix}\right.$$
$$\left.\times\begin{pmatrix} I & I & k_1 \\ -M_b' & M_b & -N_1 \end{pmatrix}\langle I,-M_b|\Lambda(t)|I,-M_a\rangle\langle I,-M_b'|\Lambda(t)|I,-M_a'\rangle^*\right)$$

We note:

1) $(2I+k_1)+(2I+k_2)$ is even, since k_1 & $k_2 \in 2\mathbb{Z}$ by the conservation of parity of the electromagnetic wave as seen in section 3.3.2.
2) We add $2(M_a+M_b)$ to the exponent of (-1) i.e., $(-1)^{2(M_a+M_b)} = 1$.
3) Equation $(3.60a)$ guarantees:
$$\langle I,-M_b|\Lambda(t)|I,-M_a\rangle = \langle I,M_b|\Lambda(t)|I,M_a\rangle$$

We hence have:

$$G_{k_1,k_2}^{N_1,N_2}(t) = G_{k_1,k_2}^{-N_1,-N_2}(t)$$

$$G_{k_1,k_2}^{N_1,N_2}(t) = \left(G_{k_1,k_2}^{N_1,N_2}(t)\right)^* \tag{3.79}$$

We start with $\left(G_{k_1,k_2}^{N_1,N_2}(t)\right)^*$:

$$\left(G_{k_1,k_2}^{N_1,N_2}(t)\right)^* = \sum_{M_a,M_b}\left((-1)^{2I+M_a+M_b}\sqrt{(2k_1+1)(2k_2+1)}\begin{pmatrix} I & I & k_1 \\ M_a' & -M_a & N_1 \end{pmatrix}\right.$$
$$\left.\times\begin{pmatrix} I & I & k_2 \\ M_b' & -M_b & N_2 \end{pmatrix}\langle I,M_b'|\Lambda(t)|I,M_a'\rangle\langle I,M_b|\Lambda(t)|I,M_a\rangle^*\right)$$

We interchange $M_a \leftrightarrow -M_a', M_b \leftrightarrow -M_b'$ to obtain:

$$\left(G_{k_1,k_2}^{N_1,N_2}(t)\right)^*$$

$$= \sum_{-M_a',-M_b'}\left((-1)^{2I-M_a'-M_b'}\sqrt{(2k_1+1)(2k_2+1)}\begin{pmatrix} I & I & k_1 \\ -M_a & M_a' & N_1 \end{pmatrix}\right.$$
$$\left.\times\begin{pmatrix} I & I & k_2 \\ -M_b & -M_b' & N_2 \end{pmatrix}\langle I,-M_b|\Lambda(t)|I,-M_a\rangle\langle I,-M_b'|\Lambda(t)|I,-M_a'\rangle^*\right)$$

Note:

1) A property of the 3j-symbol to be non-zero is the necessity of this condition: $M_a' - M_a + N_1 = 0$ & $M_b' - M_b + N_2 = 0$. Given that N_1 & N_2 are both fixed, we can simply sum over the unprimed terms or the primed terms. In this case, we take the primed terms.
2) We multiply the expression by $(-1)^{2(M_a'+M_b')} = 1$
3) We perform an odd permutation of the column to extract a phase factor [3,113]:
$$\begin{pmatrix} j_1 & j_2 & j_3 \\ m_1 & m_2 & m_3 \end{pmatrix} = (-1)^{j_1+j_2+j_3}\begin{pmatrix} j_2 & j_1 & j_3 \\ m_2 & m_1 & m_3 \end{pmatrix}$$
4) Equation $(3.60a)$ guarantees:
$$\langle I,-M_b|\Lambda(t)|I,-M_a\rangle = \langle I,M_b|\Lambda(t)|I,M_a\rangle$$
5) From 1), We switch back to summation along the unprimed M_a & M_b, and note that from the equation (3.76), $N_1+N_2 \in 2\mathbb{Z} \Rightarrow (-1)^{N_1+N_2} = 1$ to obtain:
$$G_{k_1,k_2}^{N_1,N_2}(t) = \left(G_{k_1,k_2}^{N_1,N_2}(t)\right)^*$$

Remark:
Regarding equation (3.58), we can derive another relationship for the matrix elements of $\overleftrightarrow{U}$, which is not immediately evident until equation (3.79) was stated and proven:

$$\langle N|I,M_B\rangle\langle N|I,M_A\rangle\langle N'|I,M_B-N_2\rangle\langle N'|I,M_a-N_1\rangle = \langle N'|I,M_B\rangle\langle N'|I,M_A\rangle\langle N|I,M_B-N_2\rangle\langle N|I,M_a-N_1\rangle$$

In this expression, N is interchanged with N' to eliminate the exponential factors.

$$G_{0,k_2}^{0,N_2}(t) = 0 \; if \; k_2 \neq 0 \tag{3.80}$$

$$G_{0,k_2}^{0,N_2}(t) = \sum_{M_a,M_b}\left((-1)^{2I+M_a+M_b}\sqrt{(2k_2+1)}\begin{pmatrix} I & I & 0 \\ M_a & -M_a & 0\end{pmatrix} \times \begin{pmatrix} I & I & k_2 \\ M_b' & -M_b & N_2\end{pmatrix}\langle I,M_b|\Lambda(t)|I,M_a\rangle\langle I,M_b'|\Lambda(t)|I,M_a'\rangle^*\right)$$

1) We make use of a special relationship [3,113] again:

$$\begin{pmatrix} I & I & 0 \\ m & -m & 0\end{pmatrix} = \frac{1}{\sqrt{2I+1}}(-1)^{I-m}$$

$$G_{0,k_2}^{0,N_2}(t) = \sum_{M_a,M_b}\left((-1)^{2I+M_a+M_b}\sqrt{\frac{(2k_2+1)}{2I+1}}(-1)^{I-M_a} \times \begin{pmatrix} I & I & k_2 \\ M_b' & -M_b & N_2\end{pmatrix}\langle I,M_b|\Lambda(t)|I,M_a\rangle\langle I,M_b'|\Lambda(t)|I,M_a\rangle^*\right)$$

And thus:

$$G_{0,k_2}^{0,N_2}(t) = \sum_{M_b}\left((-1)^{3I+M_b}\sqrt{\frac{(2k_2+1)}{2I+1}}\begin{pmatrix} I & I & k_2 \\ M_b' & -M_b & N_2\end{pmatrix} \times \sum_{M_a}\langle I,M_b|\Lambda(t)|I,M_a\rangle\langle I,M_b'|\Lambda(t)|I,M_a\rangle^*\right)$$

Further evaluation leads to:

$$G_{0,k_2}^{0,N_2}(t) = \sum_{M_b}\left((-1)^{3I+M_b}\sqrt{\frac{(2k_2+1)}{2I+1}}\begin{pmatrix} I & I & k_2 \\ M_b' & -M_b & N_2\end{pmatrix} \times \sum_{M_a}\langle I,M_b|\Lambda(t)|I,M_a\rangle\langle I,M_a|\Lambda(t)|I,M_b\rangle\right)$$

With $\sum_{M_a}|I,M_a\rangle\langle I,M_a| = \overleftrightarrow{Id}$ and $\Lambda(t)$ being an orthonormal operator:

$$G_{0,k_2}^{0,N_2}(t) = \sum_{M_b}\left((-1)^{3I+M_b}\sqrt{\frac{(2k_2+1)}{2I+1}}\begin{pmatrix} I & I & k_2 \\ M_b' & -M_b & N_2\end{pmatrix}\delta_{M_b,M_b'}\right)$$

$$= \sum_{M_b}\left((-1)^{3I+M_b}\sqrt{\frac{(2k_2+1)}{2I+1}}\begin{pmatrix} I & I & k_2 \\ M_b' & -M_b & N_2\end{pmatrix}\delta_{N_2,0}\right)$$

$$= \sum_{M_b}\left((-1)^{3I+M_b}\sqrt{\frac{(2k_2+1)}{2I+1}}\begin{pmatrix} I & I & k_2 \\ M_b' & -M_b & 0\end{pmatrix}\right)$$

But:

$$\sum_m (-1)^{j-m} \begin{pmatrix} j & j & J \\ m & -m & 0 \end{pmatrix} = \sqrt{2J+1}\delta_{J,0},$$

which implies that $G_{0,k_2}^{0,N_2}(t) = 0$ unless $k_2 \neq 0$.

$$G_{k_1,k_2}^{N_1,N_2}(t=0) = \delta_{k_1,k_2}\delta_{N_1,N_2} \tag{3.81}$$

This case has been treated in section 3.4.2 in the derivation of equation (3.64).

Appendix C: Explicit expression of the unitary matrix $\overleftrightarrow{U}$ for $I = 5/2$ as given by Butz.

In this appendix, we will mainly look at Butz's expression [23] of the unitary matrix $\overleftrightarrow{U}$ for $I = 5/2$ and the general expression for the coefficients of $G_{k_1,k_2}^{N_1,N_2}(t)$. Like the contents of appendix B, it is reproduced here (with permission) for ease of reference. Copyright is retained under Springer Nature.

We want to note that in Butz's paper, he followed the convention of the diagonalization of a matrix: Given a Hermitian matrix $\overleftrightarrow{A}$, there exists a unitary matrix $\overleftrightarrow{U}$ and a diagonal matrix $\overleftrightarrow{D}$ such that $\overleftrightarrow{D} = \overleftrightarrow{U}\overleftrightarrow{A}\overleftrightarrow{U}^{-1}$, as adopted in the earlier textbooks that mention TDPAC.

In our convention, we assume the following instead as in modern linear algebra textbooks: Given a Hermitian matrix $\overleftrightarrow{A}$, there exists a unitary matrix $\overleftrightarrow{U}$ and a diagonal matrix $\overleftrightarrow{D}$ such that $\overleftrightarrow{D} = \overleftrightarrow{U}^{-1}\overleftrightarrow{A}\overleftrightarrow{U}$.

The expression for the unitary matrix $\overleftrightarrow{U}$ for $I = 5/2$, according to Butz's [23], is written as:

$$\overleftrightarrow{U} = \begin{bmatrix} a_{5/2} & 0 & a_{1/2} & 0 & a_{3/2} & 0 \\ 0 & c_{3/2} & 0 & c_{1/2} & 0 & c_{5/2} \\ b_{5/2} & 0 & b_{1/2} & 0 & b_{3/2} & 0 \\ 0 & b_{3/2} & 0 & b_{1/2} & 0 & b_{5/2} \\ c_{5/2} & 0 & c_{1/2} & 0 & c_{3/2} & 0 \\ 0 & a_{3/2} & 0 & a_{1/2} & 0 & a_{5/2} \end{bmatrix}, \qquad (C1)$$

$$\overleftrightarrow{U}^T = \begin{bmatrix} a_{5/2} & 0 & b_{5/2} & 0 & c_{5/2} & 0 \\ 0 & c_{3/2} & 0 & b_{3/2} & 0 & a_{3/2} \\ a_{1/2} & 0 & b_{1/2} & 0 & c_{1/2} & 0 \\ 0 & c_{1/2} & 0 & b_{1/2} & 0 & a_{1/2} \\ a_{3/2} & 0 & b_{3/2} & 0 & c_{3/2} & 0 \\ 0 & c_{5/2} & 0 & b_{5/2} & 0 & a_{5/2} \end{bmatrix}, \qquad (C2)$$

with:

$$a_{5/2} = \frac{1}{N_{5/2}}\left(\frac{1 - 18\eta^2}{(8 + E_{\pm 5/2})(2 + E_{\pm 5/2})}\right), \qquad (C3.1)$$

$$a_{3/2} = \frac{1}{N_{3/2}}\left(\frac{-\eta^2\sqrt{180}}{(8 + E_{\pm 3/2})(10 - E_{\pm 3/2})}\right), \qquad (C3.2)$$

$$a_{1/2} = \frac{1}{N_{1/2}}\left(\frac{-\eta\sqrt{10}}{(10 - E_{\pm 1/2})}\right), \qquad (C3.3)$$

$$b_{5/2} = \frac{1}{N_{5/2}}\left(\frac{\eta\sqrt{10}}{(8 + E_{\pm 5/2})}\right), \qquad (C3.4)$$

$$b_{3/2} = \frac{1}{N_{3/2}}\left(\frac{\eta\sqrt{18}}{(8+E_{\pm 3/2})}\right), \tag{C3.5}$$

$$b_{1/2} = \frac{1}{N_{1/2}}, \tag{C3.6}$$

$$c_{5/2} = \frac{1}{N_{5/2}}\left(\frac{\eta^2\sqrt{180}}{(8+E_{\pm 5/2})(2+E_{\pm 5/2})}\right), \tag{C3.7}$$

$$c_{3/2} = \frac{1}{N_{3/2}}\left(\frac{1-10\eta^2}{(8+E_{\pm 3/2})(10-E_{\pm 3/2})}\right), \tag{C3.8}$$

$$c_{1/2} = \frac{1}{N_{1/2}}\left(\frac{\eta\sqrt{18}}{(2+E_{\pm 1/2})}\right), \tag{C3.9}$$

with the normalization constants:

$$N_x = \sqrt{a_x^2 + b_x^2 + c_x^2}; x = 1/2, 3/2, 5/2, \tag{C3.10}$$

and the energies $E_{\pm 1/2}, E_{\pm 3/2}, E_{\pm 5/2}$ defined as per equation $(2.60a - 2.60c)$.

Butz has constructed $(C3.1 - C3.10)$ to avoid problems of the type "division by zero". It is also noted that $\lim_{\eta\to 0} \overleftrightarrow{U} = \overleftrightarrow{Id}$, which is consistent with the diagonalization of $\overleftrightarrow{H}$ from equation $(2.56a)$ when $\eta = 0$.

Note that in general, this class of $\overleftrightarrow{H}$ (for a general integer or half-integer I) is called a bisymmetric matrix [114], in which there, for half-integer I, there exists a standard method (such as the one outlined in [114]) in which transforms $\overleftrightarrow{H}$ of dimension $2n \times 2n, n \in \mathbb{Z}$, into an orthogonally similar matrix with two $n \times n$ blocks on its diagonal.

We then recall the perturbation function $G^{N_1,N_2}_{k_1,k_2}(t)$ and equations $(4.1a - 4.1i)$. Butz has calculated the complicated mess of the $S(m,m')$ for $m,m' \in \left\{\frac{1}{2},\frac{3}{2},\frac{5}{2}\right\}$ [23], in which we will reproduce here (with permission) for convenience's sake.

First, we reproduce Table 2 of [23] and state that the terms inside each of these $G^{N_1,N_2}_{k_1,k_2}(t)$ contains expressions like $X_k(m,m')$, where X stands for the letter $A-G$, and $k \in \{2,4\}$. They represent the coefficients for $S(m,m')$, i.e., $S(m,m') = X_k(m,m')$. From this point on, we drop off the arguments (m,m') for brevity.

$G^{0,0}_{2,2}: \frac{1}{7}A_2^2$	$G^{0,0}_{2,4}: \frac{1}{7}A_2A_4$	$G^{0,0}_{4,4}: \frac{1}{7}A_4^2$
$G^{2,0}_{2,2}: \frac{1}{14}A_2(D_2+E_2)$	$G^{2,0}_{2,4}: \frac{1}{14}A_4(D_2+E_2)$ $G^{0,2}_{2,4}: \frac{1}{14}A_2(D_4+E_4)$ $G^{0,4}_{2,4}: \frac{1}{\sqrt{14}}A_2(F_4+G_4)$	$G^{2,0}_{4,4}: \frac{1}{14}A_4(D_4+E_4)$ $G^{4,0}_{4,4}: \frac{1}{\sqrt{14}}A_4(F_4+G_4)$

$G_{2,2}^{1,1}: \frac{1}{7}(5B_2^2 + 2C_2^2)$ $G_{2,2}^{1,-1}: \frac{2\sqrt{10}}{7} B_2 C_2$	$G_{2,4}^{1,1}: \frac{\sqrt{10}}{7}(B_2^2 - C_4^2)$ $G_{2,4}^{1,-1}: \frac{3}{7} B_2 C_4$ $G_{2,4}^{1,3}: \frac{\sqrt{5}}{\sqrt{7}} B_2 B_4$ $G_{2,4}^{1,-3}: \frac{\sqrt{2}}{\sqrt{7}} C_2 B_4$	$G_{4,4}^{1,1}: \frac{1}{7}(2B_2^2 + 5C_4^2)$ $G_{4,4}^{1,-1}: \frac{2\sqrt{10}}{7} B_2 C_4$ $G_{4,4}^{1,3}: \frac{\sqrt{2}}{\sqrt{7}} B_2 B_4$ $G_{4,4}^{1,-3}: \frac{\sqrt{5}}{\sqrt{7}} C_4 B_4$
$G_{2,2}^{2,2}: \frac{1}{14}(D_2^2 + E_2^2)$ $G_{2,2}^{2,-2}: \frac{1}{7} D_2 E_2$	$G_{2,4}^{2,2}: \frac{1}{14}(D_2 D_4 + E_2 E_4)$ $G_{2,4}^{2,-2}: \frac{1}{14}(D_2 E_4 + E_2 D_4)$ $G_{2,4}^{2,4}: \frac{1}{\sqrt{14}}(D_2 F_4 + E_2 G_4)$ $G_{2,4}^{2,-4}: \frac{1}{\sqrt{14}}(E_2 F_4 + D_2 G_4)$	$G_{44}^{22}: \frac{1}{14}(D_4^2 + E_4^2)$ $G_{4,4}^{2,-2}: \frac{1}{7}(D_4 E_4)$ $G_{4,4}^{2,4}: \frac{1}{\sqrt{14}}(D_4 F_4 + E_4 G_4)$ $G_{4,4}^{2,-4}: \frac{1}{\sqrt{14}}(E_4 F_4 + D_4 G_4)$
		$G_{4,4}^{3,3}: B_4^2$ $G_{4,4}^{3,-3}: 0$ $G_{4,4}^{4,4}: F_4^2 + G_4^2$ $G_{4,4}^{4,-4}: 2F_4 G_4$
$G_{22}: \frac{1}{35}(A_2^2 + 10\,B_2^2 + 4C_2^2 + D_2^2 + E_2^2)$	$G_{44}: \frac{1}{63}(A_4^2 + 4B_2^2 + 10B_4^2 + 10C_4^2 + D_4^2 + E_4^2 + 14F_4^2 + 14G_4^2)$	

Table C1: The $G_{k_1,k_2}^{N_1,N_2}(t)$ contains the coefficients $S(m,m') = X_k(m,m')$ as reflected in equations $(4.1a - 4.1i)$. The meaning of like $X_k(m,m')$, where X stands for the letter $A - G$, and $k \in \{2,4\}$, is found in table C2. We drop off the arguments (m,m') for brevity. The following table was reproduced with permission as Table 2 from [23], with copyright retained under Springer Nature.

We define the X_k's in Table C2, with reference to equations $(C3.1 - C3.10)$:

$A_2 = \frac{1}{\sqrt{3}}(5a_m a_{m'} - 4b_m b_{m'} - c_m c_{m'})$	$A_4 = a_m a_{m'} + 2b_m b_{m'} - 3c_m c_{m'}$
$B_2 = a_m c_{m'} - c_m a_{m'}\ (= F_4 - G_4)$	$B_4 = a_m b_{m'} - b_m a_{m'}$
$C_2 = c_m b_{m'} - b_m c_{m'}$	$C_4 = b_m c_{m'} - c_m b_{m'}\ (= -C_2)$
$D_2 = 3b_m c_{m'} + \sqrt{5} a_m b_{m'}$	$D_4 = 3a_m b_{m'} - \sqrt{5} b_m c_{m'}$
$E_2 = 3c_m b_{m'} - \sqrt{5} b_m a_{m'}$	$E_4 = 3b_m a_{m'} - \sqrt{5} c_m b_{m'}$
	$F_4 = a_m c_{m'}$
	$G_4 = c_m a_{m'}$

Table C2: The meaning of X_k's, with reference to equations $(C3.1 - C3.10)$. Reproduced with permission as equation 79 from [23], with copyright retained under Springer Nature.

After several calculations, Butz will arrive at what he deemed as a final form:

$$5G_{22}(t) + 9G_{44}(t) = 2 + 4\cos(\omega_1 t) + 4\cos(\omega_2 t) + 4\cos(\omega_3 t) \qquad (C4)$$

Further details that are not necessarily needed for the understanding of the theoretical portion of TDPAC spectroscopy is contained in Butz's paper [23].

Appendix D: Geometry between the Different Detector Planes.

The contents in Appendix E have been communicated and published in [2]. They are re-communicated, some ab-verbatim, in this thesis as:

Section of this thesis	Reproduced from [2] under section
Appendix D	Appendix B: Geometry between the Different Detector Planes

This work leads us to ask, what is the relationship between the angles θ and ϕ that correspond to the different detector planes?

Note that, given a perfect sample and perfect detectors and considering the symmetry corresponding to the angles θ and ϕ of each detector plane, we obtain an equivalence of the angles, whereby the following equivalent angles of θ and ϕ generate the same $R(t)$:

$$\theta = \theta \bmod 90°,$$

$$\phi = \phi \bmod 45°.$$

We use the Euler rotations $R_i(\theta)$, which is the matrix associated with the rotation of an object anticlockwise around axis i ($i \in \{x, y, z\}$) by the angle θ. Explicitly, these matrices are

$$R_x(\theta) = \begin{pmatrix} 1 & 0 & 0 \\ 0 & \cos(\theta) & -\sin(\theta) \\ 0 & \sin(\theta) & \cos(\theta) \end{pmatrix},$$

$$R_y(\theta) = \begin{pmatrix} \cos(\theta) & 0 & \sin(\theta) \\ 0 & 1 & 0 \\ -\sin(\theta) & 0 & \cos(\theta) \end{pmatrix},$$

$$R_z(\theta) = \begin{pmatrix} \cos(\theta) & -\sin(\theta) & 0 \\ \sin(\theta) & \cos(\theta) & 0 \\ 0 & 0 & 1 \end{pmatrix}.$$

Now, assume that we have the angles θ_1, ϕ_1 for the $R(t)$ signal that corresponds to the $x - y$ detector plane, θ_2, ϕ_2 for the $y - z$ plane, and θ_3, ϕ_3 for the $x - z$ plane. Since this proof may be applied between any combination of detector planes, we need only show the relationship between θ_1, ϕ_1 and θ_2, ϕ_2 (i.e., for the combination of $x - y$ and $y - z$ planes).

For the angles $\theta_j, \phi_j, j \in \{1,2,3\}$ corresponding to the three different detector planes to make sense, we would need to have the "defining axis" corresponding to each θ_j and ϕ_j. A "defining axis" means that if the vector that is free to rotate by θ about a mutually perpendicular axis is aligned with said defining axis, then we set $\theta = 0°$.

The above convention means that the defining axes of $\theta_1, \theta_2, \theta_3$ are the z, x, and y axes, respectively, and the defining axes of ϕ_1, ϕ_2, ϕ_3 are the x, y, and z axes, respectively. Note that, by freedom of choice, we can also equivalently set the defining axes of ϕ_1, ϕ_2, ϕ_3 to be the y, z, and x axes, respectively.

Note also that, in general, the Euler rotations of two angles (with possibly the same magnitude) about two different axes, say $R_i(\theta)$ and $R_{i'}(\phi)$, do not commute [i.e., $R_i(\theta)R_{i'}(\phi) \neq R_{i'}(\phi)\, R_i(\theta)$]. To fix this issue, we introduce the order of rotations such that, for each detector plane with the angles θ, ϕ, we first do the Euler rotation corresponding to the angle ϕ, and then do the Euler rotation corresponding to the angle θ so that the latter does not affect the former. This assertion can be shown by noting that if the normal of the sample $\hat{n}_i$ is perpendicular to the detector plane (i.e., $\theta = 0°$), then the rotation of the sample by an angle ϕ around axis i does not affect $\hat{n}_i$:

$$R_i(\varphi)\hat{n}_i(\theta = 0) = \hat{n}_i(\theta = 0).$$

Note, however, that Euler rotations of two different angles about the same axis do commute: $R_i(\theta)R_i(\phi) = R_i(\theta + \phi)$.

We now derive the explicit relationship between two pairs of angles θ_1, ϕ_1 and θ_2, ϕ_2 corresponding to the $x - y$ and $y - z$ detector planes for a sample with a fixed orientation.

We assume that the sample is an infinitely thin sheet of paper with 1-unit-thick square edges and positioned in such a way that the corners of the sample occupy the spot

$$\left\{\pm\begin{pmatrix}1\\0\\0\end{pmatrix}, \pm\begin{pmatrix}0\\1\\0\end{pmatrix}\right\}.$$

This configuration means that the normal $\hat{n}_1$ to the sample is

$$\hat{n}_1(\theta_i = 0) = \begin{pmatrix}0\\0\\1\end{pmatrix}.$$

In the $x - y$ detector plane, this would correspond to the angle $\theta_1 = 0°$ and $\phi_1 = 0°$.

A sample rotating by the finite angle ϕ_1 means that sample must rotate anticlockwise ϕ_1 degrees about the z-axis. We keep track of the changes made to the orientation of the sample parallel to the detector plane by defining the initial value of two vectors $\hat{a}_1$ and $\hat{b}_1$ to be

$$\hat{a}_1(\phi_1 = 0°) = \begin{pmatrix}1\\0\\0\end{pmatrix}, \hat{b}_1(\phi_1 = 0°) = \begin{pmatrix}0\\1\\0\end{pmatrix}.$$

The rotation of the sample by a finite angle ϕ_1 about the z-axis corresponds to the transformation of vectors $\hat{a}_1$ and $\hat{b}_1$ by the Euler rotation $R_z(\phi_1)$:

$$\hat{a}_1(\phi_1) = R_z(\phi_1)\hat{a}_1(\phi_1 = 0°) = \begin{pmatrix}\cos(\phi_1)\\\sin(\phi_1)\\0\end{pmatrix},$$

$$\hat{b}_1(\phi_1) = R_z(\phi_1)\hat{b}_1(\phi_1 = 0°) = \begin{pmatrix}-\sin(\phi_1)\\\cos(\phi_1)\\0\end{pmatrix}.$$

As mentioned above, $R_z(\phi_1)$ acting on $\hat{n}_1(\theta_i = 0)$ does nothing:

$$R_z(\phi_1)\hat{n}_1(\theta_1 = 0) = \hat{n}_1(\theta_1 = 0).$$

Next, we rotate the sample at a finite angle θ_1 either about the x-axis or the y-axis. Note that, through Euler's rotation theorem, the composition of two such Euler rotations $R_i(\theta_j)$ is also a rotation. This closure of composition means that the Euler rotations form a group [precisely, the $SO(3)$ group], and we can change the orientation of a sample just by applying three specific Euler rotations.

Nevertheless, given that we have established the symmetry corresponding to the angles θ, ϕ of each detector plane and the equivalence of the angles θ, ϕ, we can identify the common axis of the two detector planes (in our case, it is the y-axis), and rotate the sample by the finite angle θ_1 about the abovementioned axis (i.e., the y-axis) to simplify the problem at hand.

Therefore, rotation of the sample by the finite angle θ_1 about the y-axis corresponds to the transformation of vectors $\hat{a}_1(\theta_1 = 0, \phi_1)$, $\hat{b}_1(\theta_1 = 0, \phi_1)$, and $\hat{n}_1(\theta_1 = 0)$ by the Euler rotation $R_y(\theta_1)$:

$$\hat{a}_1(\theta_1, \phi_1) = R_y(\theta_1)\hat{a}_1(\theta_1 = 0, \phi_1) = \begin{pmatrix} \cos(\theta_1)\cos(\phi_1) \\ \sin(\phi_1) \\ -\sin(\theta_1)\cos(\phi_1) \end{pmatrix},$$

$$\hat{b}_1(\theta_1, \phi_1) = R_y(\theta_1)\hat{b}_1(\theta_1 = 0, \phi_1) = \begin{pmatrix} -\cos(\theta_1)\sin(\phi_1) \\ \cos(\phi_1) \\ \sin(\theta_1)\sin(\phi_1) \end{pmatrix},$$

$$\hat{n}_1(\theta_1) = R_y(\theta_1)\hat{n}_1(\theta_1 = 0) = \begin{pmatrix} \sin(\theta_1) \\ 0 \\ \cos(\theta_1) \end{pmatrix}.$$

We now shift our perspective from the $x - y$ detector plane to the $y - z$ detector plane and define:

$$\hat{n}_2(\theta_2 = 0) = \begin{pmatrix} 1 \\ 0 \\ 0 \end{pmatrix},$$

$$\hat{a}_2(\phi_1 = 0°) = \begin{pmatrix} 0 \\ 1 \\ 0 \end{pmatrix}, \hat{b}_2(\phi_1 = 0°) = \begin{pmatrix} 0 \\ 0 \\ 1 \end{pmatrix}.$$

The rotation of the sample by a finite angle of ϕ_2 about the x-axis corresponds to the transformation of vectors $\hat{a}_2$ and $\hat{b}_2$ by the Euler rotation $R_x(\phi_2)$:

$$\hat{a}_2(\phi_2) = R_x(\phi_2)\hat{a}_2(\phi_2 = 0°) = \begin{pmatrix} 0 \\ \cos(\phi_2) \\ \sin(\phi_2) \end{pmatrix},$$

$$\hat{b}_2(\phi_2) = R_x(\phi_2)\hat{b}_2(\phi_2 = 0°) = \begin{pmatrix} 0 \\ -\sin(\phi_2) \\ \cos(\phi_2) \end{pmatrix}.$$

Note that applying $R_x(\phi_2)$ to $\hat{n}_2(\theta_2 = 0)$ does nothing:

$$R_x(\phi_2)\hat{n}_2(\theta_2 = 0) = \hat{n}_2(\theta_2 = 0).$$

Next, we rotate the sample at a finite angle θ_2 about the y-axis, which corresponds to the transformation of vectors $\hat{a}_2(\theta_2 = 0, \phi_1)$, $\hat{b}_2(\theta_2 = 0, \phi_1)$ and $\hat{n}_2(\theta_2 = 0)$ by the Euler rotation $R_y(\theta_2)$:

$$\hat{a}_2(\theta_2, \phi_2) = R_y(\theta_2)\hat{a}_2(\theta_2 = 0, \phi_2) = \begin{pmatrix} \sin(\theta_2)\sin(\phi_2) \\ \cos(\phi_2) \\ \cos(\theta_2)\sin(\phi_2) \end{pmatrix},$$

$$\hat{b}_2(\theta_2, \phi_2) = R_y(\theta_2)\hat{b}_2(\theta_2 = 0, \phi_2) = \begin{pmatrix} \sin(\theta_2)\cos(\phi_2) \\ -\sin(\phi_2) \\ \cos(\theta_2)\cos(\phi_2) \end{pmatrix},$$

$$\hat{n}_2(\theta_2) = R_y(\theta_2)\hat{n}_2(\theta_2 = 0) = \begin{pmatrix} \cos(\theta_2) \\ 0 \\ -\sin(\theta_2) \end{pmatrix}.$$

What remains is to determine the relationship between (θ_1, ϕ_1) and (θ_2, ϕ_2) such that

$$\hat{a}_1(\theta_1, \phi_1) = \hat{a}_2(\theta_2, \phi_2),$$

$$\hat{b}_1(\theta_1, \phi_1) = \hat{b}_2(\theta_2, \phi_2),$$

$$\hat{n}_1(\theta_1) = \hat{n}_2(\theta_2).$$

We can reduce this set of equations to

$$\cos(\theta_2) = \sin(\theta_1),$$

$$-\sin(\theta_2) = \cos(\theta_1),$$

$$\cos(\phi_2) = \sin(\phi_1),$$

$$-\sin(\phi_2) = \cos(\phi_1).$$

By using specific trigonometric identities ($0 \leq \alpha \leq 90°$),

$$\cos(\alpha) = \sin(90° - \alpha),$$

$$\sin(\alpha) = \cos(90° - \alpha),$$

$$\cos(\alpha) = \cos(-\alpha),$$

$$\sin(\alpha) = -\sin(\alpha),$$

The solutions are

$$\theta_2 = \theta_1 - 90° = -(90° - \theta_1),$$

$$\phi_2 = \phi_1 - 90° = -(90° - \phi_1).$$

In physical terms, rotating the sample by the angle ϕ_1 about the z-axis and then by θ_1 about the y-axis in the $x - y$ plane (frame) of reference corresponds to rotating the sample by the angle of $\phi_1 - 90°$ about the x-axis and then by $\theta_1 - 90°$ about the y-axis in the $y - z$ plane (frame) of reference.

The following sequences detail the transformation of the following pair of unit vectors from $\{\hat{a}_1, \hat{b}_1, \hat{n}_1\}$ to $\{\hat{a}_2, \hat{b}_2, \hat{n}_2\}$ by the following Euler rotations:

$$\hat{a}_1 = \begin{pmatrix}1\\0\\0\end{pmatrix} \xrightarrow{R_z(\phi_1)} \begin{pmatrix}\cos(\phi_1)\\ \sin(\phi_1)\\ 0\end{pmatrix} \xrightarrow{R_y(\theta_1)} \begin{pmatrix}\cos(\theta_1)\cos(\phi_1)\\ \sin(\phi_1)\\ -\sin(\theta_1)\cos(\phi_1)\end{pmatrix} \xrightarrow{R_y(90°-\theta_1)} \begin{pmatrix}0\\ \cos(\phi_2)\\ \sin(\phi_2)\end{pmatrix} \xrightarrow{R_x(90°-\phi_1)} \begin{pmatrix}0\\1\\0\end{pmatrix} = \hat{a}_2,$$

$$\hat{b}_1 = \begin{pmatrix}0\\1\\0\end{pmatrix} \xrightarrow{R_z(\phi_1)} \begin{pmatrix}-\sin(\phi_1)\\ \cos(\phi_1)\\ 0\end{pmatrix} \xrightarrow{R_y(\theta_1)} \begin{pmatrix}-\cos(\theta_1)\sin(\phi_1)\\ \cos(\phi_1)\\ \sin(\theta_1)\sin(\phi_1)\end{pmatrix} \xrightarrow{R_y(90°-\theta_1)} \begin{pmatrix}0\\ -\sin(\phi_2)\\ \cos(\phi_2)\end{pmatrix} \xrightarrow{R_x(90°-\phi_1)} \begin{pmatrix}0\\0\\1\end{pmatrix} = \hat{b}_2,$$

$$\hat{n}_1 = \begin{pmatrix}0\\0\\1\end{pmatrix} \xrightarrow{R_z(\phi_1)} \begin{pmatrix}0\\0\\1\end{pmatrix} \xrightarrow{R_y(\theta_1)} \begin{pmatrix}\sin(\theta_1)\\ 0\\ \cos(\theta_1)\end{pmatrix} \xrightarrow{R_y(90°-\theta_1)} \begin{pmatrix}1\\0\\0\end{pmatrix} \xrightarrow{R_x(90°-\phi_1)} \begin{pmatrix}1\\0\\0\end{pmatrix} = \hat{n}_2.$$

The symmetry of our TDPAC design allows us only to detect the magnitude of θ_j, ϕ_j of each set of detector angles for the three planar configurations. In sum, the following relations must hold:

$$|\theta_1| + |\theta_2| = |\theta_1| + |\theta_3| = 90°,$$

$$|\varphi_1| + |\varphi_2| = |\varphi_1| + |\varphi_3| = 90°.$$

In practice, the above conditions cannot be achieved because, for example, the crystal is not perfect or infinitesimally thin, or the average depth of the implantation may vary statistically. Therefore, we allow our θ, ϕ to be free for each detector plane, but we try to ensure that $|\theta_1| + |\theta_{2,3}|$ and $|\varphi_1| + |\varphi_{2,3}|$ remain as close as possible to $90°$.

Appendix E: Literature Review of Ion Implantation Damage to the Host Semiconductor.

The contents in Appendix E have been communicated and published in [2]. They are re-communicated, some ab-verbatim, in this thesis as:

Section of this thesis	Reproduced from [2] under section
Appendix E	Appendix A.1: Literature Review of Ion Implantation Damage to the Host Semiconductor

While this paper mainly centres on the comparison between the γ−γ and e−γ ^{181}Ta(TiO_2) TDPAC signal acquired from the well-defined substitutional site of ^{181}Ta probes in the TiO_2 matrix, some questions may arise pertaining to the effect of the ion implantation of the $80\ keV$ ^{181}Hf isotope on the lattice structure of the single crystal TiO_2. In particular, readers might want to understand the extent of thermal annealing after the ion implantation, which is said to restore the lattice structure of TiO_2 (now implanted with ^{181}Hf$\rightarrow$^{181}Ta probe at parts per billion number density).

In the review paper "Ion implantation in Semiconductors, Part 1" by Gibbons [115], the contribution to the stopping range of the implanted ions comes from both the individual stopping power of the nuclei and the electron cloud of the atoms in the single crystal semiconductor such as silicon and our case, TiO_2. Models such as the LSS theory and the Lindhard model were elaborated in detail, and comparisons between experiments and theory (particularly the range distribution of implanted ions in single crystal silicon) were also discussed. It was found that the Lindhard model qualitatively agrees with the stopping range of ^{32}P implanted ions in single crystal silicon in the range of 400 to 1200 Å, with the direction of the incident ion beam parallel to the major crystal axis of single crystal silicon.

As discussed in Chapter 6 of this thesis, we used SRIM 2013 [88], which uses the Monte Carlo method [116] (effectively the assumption of binary collision approximation) with the random sampling (layer and type of atom/ion, respecting the stoichiometric ratio of the atoms/ions in the target material) of the impact parameters of the following atom/ion in the target material (layer and type, with the probability distribution respecting the stoichiometric ratio of the atoms/ions in the target material).

Four years later, in the subsequent review paper "Ion implantation in Semiconductors, Part 2" by Gibbons [117], efforts to understand the type of damage to the lattice structure of the semiconductor, and its rejuvenation by sufficient thermal annealing, were discussed. Using silicon as his choice semiconductor, he mentioned that if the energy (after a series of prior collisions) of the incoming implanted ion is higher than the displacement threshold energy (defined as the energy needed to break the bonds of a said native ion from its nearest neighbours in the lattice of the host material) of that said native ion, the native atom will be displaced from the lattice site. Furthermore, the mentioned displaced native ions could be considered a second projectile, which will cause more collisions with other native ions of the

host material. The above factor causes the formation of what is commonly termed “damage clusters”.

A library of the type of damage to the lattice structure of the host material is discussed, mainly (1) The Frankel defect (removing a native ion from its lattice site and placing it in a nearby interstitial position), (2) The location of the implanted ion in the host material, be it substitutional or interstitial, (3) Dislocation lines and loops, which are caused by the clustering of the point (Frankel) defects onto a lattice plane, were also discussed in detail. (4) Vacancy and interstitial platelets (caused by the agglomeration of the vacant lattice site and the interstitial ions, respectively) were also mentioned. It serves as a site for the adsorption of “wrongly-sized” implanted ions in the host material.

Furthermore, Gibbons separated cases of damage caused by heavy, intermediate, and light ions. Since ^{181}Hf is a very heavy ion (its atomic weight is more than three times the corresponding native Ti ion in our single crystal TiO_2), we would focus on the case of heavy ions.

Gibbons mentioned that heavy ions implanted into a non-channelling direction in single crystal silicon would produce heavily disordered damage clusters that contain both simple Frankel defects and sparse areas, with their properties being more like a polycrystalline solid. Furthermore, if the implanted ion dose is large enough, then the single crystal silicon can be made polycrystalline.

Gibbons has also provided many experiments to understand the annealing process of the damaged silicon caused by the ion implantation process, over varying implantation energies, and the type of implanted ion. Of particular interest to this study is that if the silicon is made polycrystalline from the surface to a certain depth caused by the path of the implanted ion, then thermal annealing of 30 min with a temperature of $923\ K$ in the air will make the silicon roughly single crystal again, though with micro twins and stacking faults. However, dislocation loops and lines will still exist unless the silicon is subjected to further annealing for several hours at a temperature of $1273\ K$ in a vacuum. Vacancy platelets will degrade into dislocation loops under thermal annealing of 30 min at a temperature of $873\ K$.

Appendix F: Proof of the Copyright Licenses Agreement.

Copyright Agreement A: For Reference [3]:

CCC Marketplace™

This is a License Agreement between Ian Chang Jie Yap ("User") and Copyright Clearance Center, Inc. ("CCC") on behalf of the Rightsholder identified in the order details below. The license consists of the order details, the Marketplace Order General Terms and Conditions below, and any Rightsholder Terms and Conditions which are included below.

All payments must be made in full to CCC in accordance with the Marketplace Order General Terms and Conditions below.

Order Date	09-Aug-2022	Type of Use	Republish in a thesis/dissertation
Order License ID	1256155-1		
ISBN-13	9780471954798	Publisher	John Wiley
		Portion	Chapter/article

LICENSED CONTENT

Publication Title	Nuclear Condensed Matter Physics : Nuclear Methods and Applications	Country	United Kingdom of Great Britain and Northern Ireland
Author/Editor	Schatz, Günter., Weidinger, Alois.	Rightsholder	John Wiley & Sons - Books
		Publication Type	Book
Date	06/03/1996		
Language	English, German		

REQUEST DETAILS

Portion Type	Chapter/article	Rights Requested	Main product
Page range(s)	3-14, 21-32, 63-85	Distribution	Worldwide
Total number of pages	47	Translation	Original language of publication
Format (select all that apply)	Electronic	Copies for the disabled?	No
Who will republish the content?	Academic institution	Minor editing privileges?	Yes
Duration of Use	Life of current edition	Incidental promotional use?	No
Lifetime Unit Quantity	Up to 499	Currency	EUR

NEW WORK DETAILS

Title	A particular EFG temperature dependence for 181Ta(TiO2): An electron-gamma TDPAC Study	Institution name	University of Goettingen, Faculty of Physics
		Expected presentation date	2022-10-31
Instructor name	Ian Yap Chang Jie c/o Hans Hofsaess		

ADDITIONAL DETAILS

The requesting person / organization to appear on the license	Ian Chang Jie Yap

REUSE CONTENT DETAILS

Title, description or numeric reference of the portion(s)	Electromagnetic Properties and Nuclear Decay, Hyperfine interactions and Perturbed Angular Correlations	Title of the article/chapter the portion is from	N/A
		Author of portion(s)	Schatz, Günter.; Weidinger, Alois.
Editor of portion(s)	N/A	Publication date of portion	1996-06-03
Volume of serial or monograph	N/A		
Page or page range of portion	3-14,21-32,63-85		

Copyright Agreement B: For Reference [23]:

SPRINGER NATURE LICENSE TERMS AND CONDITIONS

Aug 18, 2022

This Agreement between Mr. Ian Yap ("You") and Springer Nature ("Springer Nature") consists of your license details and the terms and conditions provided by Springer Nature and Copyright Clearance Center.

License Number	5371900529745
License date	Aug 18, 2022
Licensed Content Publisher	Springer Nature
Licensed Content Publication	Hyperfine Interactions
Licensed Content Title	Analytic perturbation functions for static interactions in perturbed angular correlations of ®rays
Licensed Content Author	T. Butz
Licensed Content Date	Jan 1, 1989
Type of Use	Thesis/Dissertation
Requestor type	academic/university or research institute
Format	electronic
Portion	Text extract
Number of text extracts	5
Will you be translating?	no
Circulation/distribution	1 - 29
Author of this Springer Nature content	no
Title	A particular EFG temperature dependence for 181Ta(TiO2): An electron-gamma TDPAC Study
Institution name	University of Goettingen, Faculty of Physics
Expected presentation date	Oct 2022
Portions	I am going to paraphrase relevant sections of Chapter 2), Chapter 4 and Chapter 4.3d. This constitute a major part of my literature review for which my TDPAC results for 181Ta(TiO2) is based.
Requestor Location	Mr. Ian Yap Grisebachstrasse 7 234 Göttingen, other 37077 Germany Attn: Mr. Ian Yap
Total	**0.00 USD**
Terms and Conditions	

Copyright Agreement C: For Reference [46]:

AIP PUBLISHING LICENSE
TERMS AND CONDITIONS

Aug 11, 2022

This Agreement between Mr. Ian Yap ("You") and AIP Publishing ("AIP Publishing") consists of your license details and the terms and conditions provided by AIP Publishing and Copyright Clearance Center.

License Number	5366161367933
License date	Aug 11, 2022
Licensed Content Publisher	AIP Publishing
Licensed Content Publication	Review of Scientific Instruments
Licensed Content Title	A compact digital time differential perturbed angular correlation-spectrometer using field programmable gate arrays and various timestamp algorithms
Licensed Content Author	Markus Jäger, Kornelius Iwig, Tilman Butz
Licensed Content Date	Jun 1, 2011
Licensed Content Volume	82
Licensed Content Issue	6
Type of Use	Thesis/Dissertation
Requestor type	Student
Format	Electronic

Portion	Photograph/Image
Number of Photographs/Images	1
Will you be translating?	No
Title	A particular EFG temperature dependence for 181Ta(TiO2): An electron-gamma TDPAC Study
Institution name	University of Goettingen, Faculty of Physics
Expected presentation date	Oct 2022
Portions	Figure 1
Requestor Location	Mr. Ian Yap Grisebachstrasse 7 234 Göttingen, other 37077 Germany Attn: Mr. Ian Yap
Total	0.00 USD

Copyright Agreement D: For Reference [65]:

AIP PUBLISHING LICENSE
TERMS AND CONDITIONS

Aug 16, 2022

This Agreement between Mr. Ian Yap ("You") and AIP Publishing ("AIP Publishing") consists of your license details and the terms and conditions provided by AIP Publishing and Copyright Clearance Center.

License Number	5370891075724
License date	Aug 16, 2022
Licensed Content Publisher	AIP Publishing
Licensed Content Publication	Journal of Applied Physics
Licensed Content Title	Ion implantation in titanium dioxide thin films studied by perturbed angular correlations
Licensed Content Author	Juliana Schell, Doru C. Lupascu, Artur Wilson Carbonari, et al
Licensed Content Date	Apr 14, 2017
Licensed Content Volume	121
Licensed Content Issue	14
Type of Use	Thesis/Dissertation
Requestor type	Student
Format	Print and electronic

Portion	Figure/Table
Number of figures/tables	1
Will you be translating?	No
Title	A particular EFG temperature dependence for 181Ta(TiO2): An electron-gamma TDPAC Study
Institution name	University of Goettingen, Faculty of Physics
Expected presentation date	Oct 2022
Portions	Figure 4
Requestor Location	Mr. Ian Yap Grisebachstrasse 7 234 Göttingen, other 37077 Germany Attn: Mr. Ian Yap
Total	0.00 EUR

References

1. SSP ISOLDE-CERN Collaboration. Available Online: https://espace.cern.ch/ISOLDE-SSP/default.aspx (accessed on 21 August 2022).
2. Yap, I.C.J.; Schell, J.; Dang, T.T.; Noll, C.; Beck, R.; Köster, U.; Mansano, R.; Hofsäss, H.C. Room-Temperature 181Ta(TiO2): An e-γ TDPAC Study. Crystals 2022, 12, 946. https://doi.org/10.3390/cryst12070946
3. Schatz, G.; Weidinger, A. *Nuclear Condensed Matter Physics: Nuclear Methods and Applications*; Wiley: Chichester, UK, **1996**; pp. 3–32, 63–99, ISBN 0 471 95479 9.
4. CP-PAW home website designed by Blöchl P. Available Online: https://cppaw.org/doku.php?id=start (accessed on 21 August 2022).
5. The ISOLDE facility. Available Online: https://isolde.cern/isolde-facility (accessed on 29 August 2022).
6. The Bonn Isotope Separator. Available online: https://isosep.hiskp.uni-bonn.de/ (accessed on 29 August 2022).
7. Sullivan, N. A. H. "Radiation safety at ISOLDE." *CERN Technical Inspection and Safety Commission (TIS)*, **1993** (CERN/TIS/RP/93-13), S. 15, Figure 2. Available Online: https://de.wikipedia.org/wiki/Datei:ISOLDE_Schema.png (accessed on 21 August 2022)
8. Johnston, K.; Schell, J.; Correia, J.G.; Deicher, M.; Gunnlaugsson, H.P.; Fenta, A.S.; David-Bosne, E.; Costa, A.R.G.; Lupascu, D.C. "The solid state physics programme at ISOLDE: Recent developments and perspectives. *J. Phys. G Nucl. Part. Phys.* **2017**, *44*, 104001, https://doi.org/10.1088/1361-6471/aa81ac.
9. Freitag, K. A facility for ion implantation in samples colder than 0.5 K. *Radiat. Eff.* **1979**, *44*, 185; https://doi.org/10.1080/00337577908245993.
10. Nukleare Festkörperphysik -Arbeitsgruppe Vianden-. Available Online: https://tdpac.hiskp.uni-bonn.de/pac/ (accessed on 21 August 2022).
11. Forker, M.; Krien, K.; Reuschenbach, F. e^-−γ TDPAC measurements of the magnetic and electric hyperfine interaction of ^{181}Ta implanted in terbium. *Hyperfine Interact.* **1981**, *9*, 255–259. https://doi.org/10.1007/BF01020927.
12. Krien, K.; Forker, M.; Reuschenbach, F.; Trzcinski, R. "The magnetic hyperfine field and the electric field gradient at ^{181}Ta impurities in Gd metal. *Hyperfine Interact.* **1979**, *7*, 19–27. https://doi.org/10.1007/BF01021489.
13. Soares, J.C.; Krien, K.; Freitag, K. Magnetic hyperfine fields at Ta in Co and Fe hosts measured by the e^-−γ time-differential perturbed angular-correlation method. *Hyperfine Interact.* **1975**, *1*, 45–53. https://doi.org/10.1007/BF01022441.
14. Krien, K.; Bibiloni, A.G.; Freitag, K.; Soares, J.C.; Vianden, R. Measurements of the Magnetic Hyperfine Fields at Hg in Fe, Co, and Ni Hosts by the e^-−γ Time-Differential Perturbed-Angular-Correlation Method. *Phys. Rev. B* **1973**, *8*, 2248. https://doi.org/10.1103/PhysRevB.8.2248.
15. Schell, J.; Schaff, P.; Lupascu, D.C. Perturbed angular correlations at ISOLDE: A 40 years young technique. *AIP Adv.* **2017**, *7*, 105017. https://doi.org/10.1063/1.4994249.
16. Marques, J.G.; Correia, J.G.; Melo, A.A.; da Silva, M.F.; Soares, J.C. ISOLDE Collaboration (CERN). A four-detector spectrometer for e^-γ PAC on-line with the ISOLDE-CERN isotope separator. *Nucl. Instrum. Methods Phys. Res. Sect. B* **1995**, *99*, 645–648. https://doi.org/10.1016/0168-583X(94)00591-5.
17. Kleinheinz, P.; Samuelsson, L.; Vukanović, R.; Siegbahn, K. A four-detector electron directional correlation spectrometer. *Nucl. Instrum. Methods.* **1965**, *32*, 1–27. https://doi.org/10.1016/0029-554X(65)90466-0.

18. Barbosa, M.B.; Correia, J.G.; Lorenz, K.; Vianden, R.; Araújo, J.P. Studying electronic properties in GaN without using electrical contacts using γ−γ vs e^-−γ Perturbed Angular Correlations. *Sci. Rep.* **2019**, *9*, 15734. https://doi.org/10.1038/s41598-019-52098-5.
19. Nouredine, Z. *Quantum Mechanics, Concepts and Applications*, 2nd ed., John Wiley & Sons: Jacksonville, Jacksonville, USA, 2009. ISBN 9 780 470 02679 3
20. Casimir element. Available Online: http://www.scientificlib.com/en/Mathematics/LX/CasimirElement.html (accessed on 21 August 2022).
21. Griffiths, D. J. *Introduction to Electrodynamics*, 4th ed., Cambridge University Press: Cambridge, United Kingdom, 2017. ISBN 9 781 108 42041 1
22. Savage, M. "Quadrupole Interactions," 19 October 1999. Available Online: http://www.int.washington.edu/users/mjs5/Class_560/lec560_4/node4.html (accessed on 21 August 2022).
23. Butz, T. Analytic perturbation functions for static interactions in perturbed angular correlation of γ rays. *Hyperfine Interact.* **1989**, *52*, 189–228. https://doi.org/10.1007/BF02651311.
24. Kaufmann, E. N.; Vianden, R. J. The Electric Field Gradient in Noncubic Metals. *Reviews of Modern Physics* **1979**, *51*, 161–214. https://doi.org/10.1103/RevModPhys.51.161.
25. Gerdau, E.; Wolf, J.; Winkler H.; Braunsfurth J. Quadrupole interaction of 181-Ta in Hf compounds. *Proceedings of the Royal Society A*. **1969**, *311*, 197-206.
26. Steffen, R.M.; Alder, K. Chapter 13: "Extranuclear perturbations of angular distributions and correlations". In *The Electromagnetic Interaction in Nuclear Spectroscopy*, 1st ed.; Hamilton, W.D., Ed.; North-Holland Publishing Company Ltd.: Oxford, UK, 1975; pp. 583–643, ISBN 0 720 40275 1.
27. Jackson, J. D. *Classical Electrodynamics*, 3rd ed., John Wiley & Sons: Hoboken, New Jersey, USA, 2001. ISBN: 9 780 471 30932 1
28. Young, P. Helmholtz's and Laplace's Equations in Spherical Polar Coordinates: Spherical Bessel Functions. UC Santa Cruz, 23 October 2009. Available Online: http://physics.ucsc.edu/~peter/116C/helm_sp.pdf (accessed on 21 August 2022).
29. Frauenfelder, H.; Steffen, R.M. "Chapter I: The Influence of Extranuclear Fields on Angular Correlations" In *Perturbed Angular Correlations*, Karlsson, E.; Matthias, E.; Siegbahn, K., Eds.; North-Holland Publishing Company Ltd: North-Holland, Amsterdam, 1964 pp. 3–89.
30. Frauenfelder, H.; Steffen, R.M. "Chapter XIX: Angular Correlations." In *Alpha-, Beta- and Gamma-ray Spectroscopy*, vol 2.; Siegbahn, K., Ed.; North-Holland Publishing Company Ltd: North-Holland, Amsterdam, 1965; pp. 997.
31. Barbosa, M. Implementation of "ab initio" Perturbed Angular Correlation Observables for Analysis of Fluctuating Quadrupole Interactions. M.Sc. Thesis, University of Porto, Porto, Portugal, 2010.
32. Yamazaki, T. Tables of Coefficients for Angular Distribution of Gamma Rays from Aligned Nuclei. *Nucl. Data Sheets Sec. A*, **1967**, *3*, 1–23. https://doi.org/10.1016/S0550-306X(67)80002-8.
33. Ferguson, A. J. *Angular Correlation Methods in Gamma-Ray Spectroscopy*; North-Holland Publ. Company: Amsterdam, Netherlands, **1965**, ISBN 9 781 114 56774 0.
34. Weisstein, E. W. *Wigner 3j-Symbol*. **2004**. Available Online: https://mathworld.wolfram.com/Wigner3j-Symbol.html (accessed on 21 August 2022).
35. Weisstein, E. W. "*Spherical Harmonic Addition Theorem.*," **2004**. Available Online: https://mathworld.wolfram.com/SphericalHarmonicAdditionTheorem.html (accessed on 21 August 2022).

36. Wegner, D. Calculated Perturbed Angular Correlations for ^{111}In Doped Cubic Single Crystals. *Hyperfine Interactions* **1985**, *23*, 179–210. https://doi.org/10.1007/BF02058076.
37. Mottner, P.; Butz, T. The Nuclear Quadrupole Interaction of ^{187}W (β−) ^{187}Re in a 2H-WS_2 Single Crystal. *Chemical Physics* **1990**, *147*, 199–204. https://doi.org/10.1016/0301-0104(90)85035-U.
38. Mendoza-Zélis, L. A.; Bibiloni, A. G.; Caracoche, M. C.; Lopéz-García, A. R.; Martínez, J. A.; Mercader, R. C.; Pasquevich, A. F. Temperature Dependence of the Electric Field Gradient at Ta Nuclei in Hafnium Pyrovanadate. *Hyperfine Interactions* **1977**, *3*, 315–320. https://doi.org/10.1007/BF01021562.
39. Rose, M.E. The Analysis of Angular Correlation and Angular Distribution Data. *Phys. Rev.* **1953**, *91*, 610. https://doi.org/10.1103/PhysRev.91.610.
40. Lorenz, K. Implantationsstudien an Gruppe-III-Nitriden. Ph.D. Thesis, Universität Bonn, Bonn, Germany, 2002.
41. Nédélec, R. Seltene Erden in GaN und ZnO untersucht mit der PAC-Methode. Ph.D. Thesis, Universität Bonn, Bonn, Germany, 2007
42. Yates, M. J. L. "Appendix 9: Finite Solid Angle Corrections." In *Alpha-, Beta- and Gamma-ray Spectroscopy*, vol 1.; Siegbahn, K., Ed.; North-Holland Publishing Company Ltd: North-Holland, Amsterdam, 1965; pp. 1691.
43. Correia, J.G. (C2TN, DECN, Instituto Superior Técnico, Universidade de Lisboa, Lisboa, Portugal) & (European Organization for Nuclear Research (CERN), 1211 Geneva, Switzerland). Personal communication: "Details for γ A_{kk} coefficients. Obtained with program multiAkk (J.G. Correia and J.G. Marques) that generates angular correlation coefficients $(b_k)A_{kk'}(b_{k'})$. Multiple gamma - gamma and electron-gamma nuclear cascades are based on references [44,45]. The program further includes gamma finite size (gamma) attenuations coefficients $Q_{kk'}$ which were analytically calculated based on reference [39].
44. Hager, R.S.; Seltzer, E.C. Internal conversion tables, part II: Directional and polarization particle parameters for Z = 30 to Z = 103. *Nucl. Data Sheets A* **1968**, *4*, 397–641. https://doi.org/10.1016/S0550-306X(68)80017-5, https://doi.org/10.1016/S0550-306X(68)80018-7, https://doi.org/10.1016/S0550-306X(68)80019-9,
45. Hager, R.S.; Seltzer, E.C. Internal conversion tables, part I: K-, L-, M- Shell conversion coefficients for Z = 30 to Z = 103. *Nucl. Data Sheets A* **1968**, *4*, 1–235. https://doi.org/10.1016/S0550-306X(68)80002-3.
46. Jäger, M.; Iwig, K.; Butz, T. A compact digital time differential perturbed angular correlation-spectrometer using field programmable gate arrays and various timestamp algorithms. *Rev. Sci. Instrum*. **2011**, *82*, 065105. https://doi.org/10.1063/1.3599417.
47. Nukleare Festkörperphysik -Arbeitsgruppe Vianden-. English Version. Available Online: https://tdpac.hiskp.uni-bonn.de/pac/ (accessed on 21 August 2022- Click on "English Version").
48. Beuzekom, M. Appendix A in *Identifying fast hadrons with silicon detectors*. Ph.D. Thesis, University of Groningen, Groningen, Netherlands, 2006.
49. Saint Gobain $LaBr_3$ Scintillation Crystal. Available Online: https://www.crystals.saint-gobain.com/radiation-detection-scintillators/crystal-scintillators/lanthanum-bromide-labr3 (accessed on 21 August 2022).
50. Schell, J.; Schmuck, M.; Efe, İ.; Dang, T. T.; Gonçalves, J. N.; Lewin, D.; Castillo, M. E.; Shvartsman, V. V.; Costa, Â. R.; Köster, U.; et al. Strong Magnetoelectric Coupling at an Atomic Nonmagnetic Electromagnetic Probe in Bismuth Ferrite. *Phys. Rev. B* **2022**, 105 ,094102. https://doi.org/10.1103/PhysRevB.105.094102 (Supplemental Material).

51. Kleinheinz, P.; Samuelsson, L.; Vukanović, R.; Siegbahn, K. A four-detector electron directional correlation spectrometer. *Nucl. Instrum. Methods.* **1965**, *32*, 1–27. https://doi.org/10.1016/0029-554X(65)90466-0.
52. Marques, J.G.; Correia, J.G.; Melo, A.A.; da Silva, M.F.; Soares, J.C. ISOLDE Collaboration (CERN). A four-detector spectrometer for e⁻γ PAC on-line with the ISOLDE-CERN isotope separator. *Nucl. Instrum. Methods Phys. Res. Sect. B* **1995**, *99*, 645–648. https://doi.org/10.1016/0168-583X(94)00591-5.
53. Greenwood, N.N.; Earnshaw, A. Chapter 21: "Titanium, Zirconium and Hafnium". In *Chemistry of the Elements*, 2nd ed.; Butterworth Heinemann, Oxford, UK, 1998; pp. 954–975, ISBN 0 750 63365 4.
54. Hanaor, D.A.H.; Sorrell, C.C. Review of the anatase to rutile phase transformation. *J. Mater. Sci.* **2011**, *46*, 855–874. https://doi.org/10.1007/s10853-010-5113-0.
55. Fujishima, A.; Honda, K. Electrochemical Photolysis of Water at a Semiconductor Electrode. *Nature* **1972**, *238*, 37–38. https://doi.org/10.1038/238037a0.
56. Hanaor, D.A.H.; Sorrell, C.C. Sand Supported Mixed-Phase TiO_2 Photocatalysts for Water Decontamination Application. *Adv. Eng. Mater.* **2014**, *16*, 248–254. https://doi.org/10.1002/adem.201300259.
57. Dumbuya, H.; Grimes, P.E.; Lynch, S.; Ji, K.; Brahmachary, M.; Zheng, Q.; Bouez, C.; Wangari-Talbot, J. Impact of iron-oxide containing formulations against visible light-induced skin pigmentation in skin of color individuals. *J. Drugs Dermatol.* **2020**, *19*, 712–717. https://doi.org/10.36849/jdd.2020.5032.
58. Gázquez, M.J.; Moreno, S.M.P.; Bolívar, J.P. Chapter 9: "TiO_2 as white pigment and valorization of the waste coming from its production". In *Metal Oxides Series: Titanium Dioxide (TiO_2) and Its Applications*, 1st ed.; Parrino, F., Palmisano, L., Eds.; Elsevier Academic Press: Amsterdam, The Netherlands, 2021; pp. 311–335, ISBN 9 780 12819 960 2.
59. Adams, J.M.; Catchen, G.L. Anomalous crystal chemistries of the $^{111}In \rightarrow {}^{111}Cd$ and $^{181}Hf \rightarrow {}^{181}Ta$ probes in rutile TiO_2 studied using perturbed-angular-correlation spectroscopy. *Phys. Rev. B* **1994**, *50*, 1264. https://doi.org/10.1103/PhysRevB.50.1264.
60. Darriba, G.N.; Errico, L.A.; Eversheim, P.D.; Fabricus, G.; Rentería, M. First-principles and time-differential γ−γ perturbed-angular-correlation spectroscopy study of structural and electronic properties of Ta-doped TiO_2 semiconductor. *Phys. Rev. B* **2009**, *79*, 115213. https://doi.org/10.1103/PhysRevB.79.115213; Erratum in *Phys. Rev. B* **2011**, *84*, 239903. https://doi.org/10.1103/PhysRevB.84.239903.
61. Das, S.K.; Thakare, S.V.; Butz, T. The nuclear quadrupole interaction at ^{111}Cd and ^{181}Ta sites in anatase and rutile TiO_2: A TDPAC study. *J. Phys. Chem. Solids* **2009**, *70*, 778–781. https://doi.org/10.1016/j.jpcs.2009.03.008.
62. Banerjee, D.; Das, S.K.; Thakare, S.V.; Nabhiraj, P.Y.; Menon, R.; Bhandari, R.K.; Krishnan, K. Study of surface-bulk mass transport and phase transformation in nano-TiO_2 using hyperfine interaction technique. *J. Phys. Chem. Solids* **2010**, *71*, 983–987. https://doi.org/10.1016/j.jpcs.2010.04.005.
63. Banerjee, D.; Das, S.K.; Thakare, S.V. Simultaneous measurement of electric field gradient both at ^{111}Cd and ^{181}Ta sites in a single perturbed γ−γ angular correlation measurement. *J. Radioanal. Nucl. Chem.* **2017**, *313*, 677–682. https://doi.org/10.1007/s10967-017-5301-3.
64. Banerjee, D.; Guin, R.; Das, S.K.; Thakare, S.V. Effect of γ-dose on the crystal structure and leaching behavior of TiO_2 matrix labeled with $^{181}Hf/^{181}Ta$ tracer. *J. Radioanal. Nucl. Chem.* **2011**, *290*, 119–121. https://doi.org/10.1007/s10967-011-1155-2.
65. Schell, J.; Lupascu, D.C.; Carbonari, A.W.; Mansano, R.D.; Ribeiro Junior, I.S.; Dang, T.T.; Anusca, I.; Trivedi, H.; Johnston, K.; Vianden, R. Ion implantation in titanium dioxide thin

films studied by perturbed angular correlations. *Int. J. Appl. Phys.* **2017**, *121*, 145302. https://doi.org/10.1063/1.4980168.
66. Schell, J. Investigation of Hyperfine Parameters in Pure and 3D Transition Metal Doped SnO_2 and TiO_2 by Means of Perturbed Gamma–Gamma Angular Correlation Spectroscopy. Ph.D. Thesis, São Paulo University, São Paulo, Brazil, 2015.
67. Martucci, T.; Ramos, J.M.; Carbonari, A.W.; Silva, A.S.; Saxena, R.N. Investigation of electric quadrupole interaction in TiO_2 by means of perturbed gamma-gamma angular correlation spectroscopy. In Proceedings of the 2011 International Nuclear Atlantic Conference, Belo Horizonte, Brazil, 24–28 October 2011. Available online: https://inis.iaea.org/collection/NCLCollectionStore/_Public/43/046/43046289.pdf (accessed on 21 August 2022).
68. Dimesso, L. Pechini Processes: An Alternate Approach of the Sol–Gel Method, Preparation, Properties, and Applications. In *Handbook of Sol-Gel Science and Technology*, 1st ed.; Klein, L., Aparicio, M., Jitianu, A., Eds.; Springer: Cham, Switzerland, 2018; pp. 1–22, ISBN 978 3 319 19454 7. https://doi.org/10.1007/978-3-319-19454-7_123-1.
69. Ribeiroa, P.C.; Figueiredo de Melo da Costa, A.C.; Goldschmidt Aliaga Kiminami, R.H.; Sasaki, J.M.; Lira, H.L. Synthesis of TiO_2 by the Pechini Method and Photocatalytic Degradation of Methyl Red. *Mater. Res.* **2013**, *16*, 468–472. https://doi.org/10.1590/S1516-14392012005000176.
70. Schell, J.; Zyabkin, D.; Lupascu, D.C.; Hofsäss, H.C.; Karabasov, M.O.; Welker, A.; Schaaf, P. A hyperfine look at Titanium Dioxide. *AIP Adv.* **2019**, *9*, 085208. https://doi.org/10.1063/1.5097459.
71. Aroyo, M.I. (Editor); Vol. A, ch. 7.1: Space Group 136. In *International Tables for Crystallography, Volume A, 6th Edition, Space-group Symmetry*; Wiley: Chichester, UK, 2006, ISBN: 978-0-470-97423-0. Available online: https://it.iucr.org/Ab/ch7o1v0001/sgtable7o1o136/ (accessed on 4 April 2022).
72. Rutile (TiO_2, C4) Structure: A2B_tP6_136_f_a. In *Encyclopedia of Crystallographic Prototypes*; Available online: http://aflowlib.org/prototype-encyclopedia/A2B_tP6_136_f_a.html (accessed on 4 April 2022).
73. Titanium Dioxide (Rutile) TiO_2, Shinkosha. Available Online: https://www.shinkosha.com/english/product/epi_substrate/epi_substrate_03/ (accessed on 29 June 2022).
74. Maity, P.; Mohammed, O.F.; Katsiev, K. Study of the Bulk Charge Carrier Dynamics in Anatase and Rutile TiO_2 Single Crystals by Femtosecond Time Resolved Spectroscopy. *J. Phys. Chem. C* **2018**, *122*, 8925–8932. https://doi.org/10.1021/acs.jpcc.8b00256.
75. Grundmann, M. Chapter 8: "Transport" and Chapter 10: "Recombination" In *The Physics of Semiconductors: An Introduction Including Nanophysics and Applications*, 3rd ed.; Springer International Publishing: Cham, Switzerland, 2016; pp. 278–281, 343–346, ISBN 978-3-319-23879-1.
76. Gehring, A.; Selberherr, S. Chapter 9: ""Tunnelling Models for Semiconductor Device Simulation" In *Handbook of Theoretical and Computational Nanotechnology*; American Scientific Publishers: Valencia, California, USA, 2006; Volume 10. Available online: https://www.iue.tuwien.ac.at/pdf/ib_2006/BC2006_Gehring_1.pdf (accessed on 29 June 2022).
77. Woolcot, T.; Teobaldi, G.; Pang, C.L.; Beglitis, N.S.; Fisher, A.J.; Hofer, W.A.; Thornton, G. Scanning Tunneling Microscopy Contrast Mechanisms for TiO_2. *Phys. Rev. Lett*. **2012**, *109*, 156105. https://link.aps.org/doi/10.1103/PhysRevLett.109.156105.

78. Adachi, Y.; Brndiar, J.; Wen, H.F.; Zhang, Q.Z.; Miyazaki, M.; Thakur, S.; Sugawara, Y.; Sang, H.Q.; Li, Y.J.; Štich, I.; et al. Electron dynamics of tip-tunable oxygen species on TiO2 surface. *Commun. Mater.* **2021**, *2*, 71. https://doi.org/10.1038/s43246-021-00176-5.
79. Thomas, A.G.; Flavell, W.R.; Mallick, A.K.; Kumarasinghe, A.R.; Tsoutsou, D.; Khan, N.; Chatwin, C.; Rayner, S.; Smith, G.C. Comparison of the electronic structure of anatase and rutile TiO_2 single-crystal surfaces using resonant photoemission and x-ray absorption spectroscopy. *Phys. Rev. B* **2007**, *75*, 035105. https://link.aps.org/doi/10.1103/PhysRevB.75.035105.
80. Zhu, H.X.; Zhou, P.X.; Li, X.; Liu, J.-M. Electronic structures and optical properties of rutile TiO_2 with different point defects from DFT+U calculations. *Phys. Lett. A* **2014**, *378*, 2719–2724, https://doi.org/10.1016/j.physleta.2014.07.029.
81. Perron, H.; Domain, C.; Roques, J.; Drot, R.; Simoni, E.; Catalette, H. Optimization of accurate rutile TiO_2 (110), (100), (101) and (001) surface models from periodic DFT calculations. *Theor. Chem. Acc.* **2007**, *117*, 565–574. https://doi.org/10.1007/s00214-006-0189-y.
82. Rühle, S.; Cahen, D. Electron Tunnelling at TiO_2/Substrate Interface Can Determine Dye-Sensitized Solar Cell Performance. *J. Phys. Chem. B* **2004**, *108*, 17946–17951. https://doi.org/10.1021/jp047686s.
83. Schell, J.; Lupascu, D.C.; Correia, J.G.; Carbonari, A.W.; Deicher, M.; Barbosa, M.B.; Mansano, R.D.; Johnston, K.; Ribeiro, I.S., Jr. ISOLDE collaboration "In and Cd as defect traps in titanium dioxide". *Hyperfine Interact.* **2017**, *238*, 2. https://doi.org/10.1007/s10751-016-1373-7.
84. Wu, S.-C. Nuclear Data Sheets for A = 181. *Nucl. Data Sheets* **2005**, *106*, 367–600. https://doi.org/10.1016/j.nds.2005.11.001.
85. Nagl, M.A.; Barbosa, M.B.; Vetter, U.; Correia, J.G.; Hofsäss, H.C. A new tool for the search of nuclides with properties suitable for nuclear solid-state physics based on the Evaluated Nuclear Structure Data Files. *Nucl. Instrum. Methods Phys. Res. A* **2013**, *726*, 17–30. https://doi.org/10.1016/j.nima.2013.05.045.
86. Lupascu, D.C.; Habenicht, S.; Lieb, K.-P.; Neubauer, M.; Uhrmacher, M.; Wenzel, T. Relaxation of electronic defects in pure and doped La_2O_3 observed by perturbed angular correlations. *Phys. Rev. B* **1996**, *871*, 871. https://doi.org/10.1103/PhysRevB.54.871.
87. Crystals GmbH. Available online: https://crystal-gmbh.com/ (accessed on 18 January 2022).
88. Ziegler, J.F. SRIM-2013 software package. Available online: http://www.srim.org/ (accessed on 29 August 2022).
89. Rutile Mineral Data. Available online: http://webmineral.com/data/Rutile.shtml#.YeYHc_7MIQ9 (accessed on 18 January 2022).
90. Raghavan, R.S.; Raghavan, P. A new method for differential perturbed angular correlation measurements. *Nucl. Instrum. Methods* **1971**, *92*, 435–437. https://doi.org/10.1016/0029-554X(71)90421-6.
91. Horta, J.; Silva, D. Interlude, Copyright (2000–2002) from Leipzig University © JL. Available for download via the repository https://doi.org/10.5281/zenodo.6789196.
92. Correia, J.G. GFit19 Software, 2019. Based on reference [93], and available either upon request to author: joao@cern.ch, or via the repository https://doi.org/10.5281/zenodo.6789196.
93. Barradas, N.P. NNFit Program,1992. Includes a PAC MANual published independently in Lisbon, Portugal, 1992, and cited formally as reference [94].

94. Barradas N. P.; Rots, M.; Melo, A. A.; Soares, J. C. Magnetic anisotropy and temperature dependence of the hyperfine fields of ^{111}Cd in single-crystalline cobalt. *Phys. Rev. B* **1993**, *47,* 8763. https://doi.org/10.1103/PhysRevB.47.8763.
95. *Nightmare (MDI)*, Version RC 3 (1.2.0.247); Copyright (2005–2010) from the group Reiner Vianden and (2008–2010) Ronan Nédélec; Bonn University, North Rhine-Westphalia, Germany, 2010. Available for download via the repository https://doi.org/10.5281/zenodo.6789196.
96. Correia, J.G. (C2TN, DECN, Instituto Superior Técnico, Universidade de Lisboa, Lisboa, Portugal) & (European Organization for Nuclear Research (CERN), 1211 Geneva, Switzerland). Personal communication: "Qk(e^-) anisotropy attenuation coefficients consider electron (back)scattering on sample and spectrometer geometry acceptance solid angle determined with the esP2P4 program that was built on purpose and integrates modified versions of Penelope and penEasy programs. With reference as [97]:
97. Baró, J.; Sempau, J.; Fernández-Varea, J.M.; Salvat, F. PENELOPE: An algorithm for Monte Carlo simulation of the penetration and energy loss of electrons and positrons in matter. *Nucl. Instrum. Methods Phys. Res. Sect. B* **1995**, *100*, 31–46. https://doi.org/10.1016/0168-583X(95)00349-5.
98. Empyrean, the Intelligent Diffractometer by Malvern Panalytical. Available online: https://www.malvernpanalytical.com/en/products/product-range/empyrean-range/empyrean (accessed on 17 June 2022).
99. Guo, X.Y.; Xu, D.P.; Ding, Z.H.; Su, W.H. Preparation and Raman Spectrum of Rutile Single Crystals using Floating Zone Method. *Chin. Phys. Lett.* **2006**, *23*, 1645. https://doi.org/10.1088/0256-307X/23/6/080.
100. Müller, G.; Friedrich, J. Crystal Growth, Bulk: Methods. In *Encyclopedia of Condensed Matter Physics*, 1st ed.; Bassani, F., Liedl, G.L., Wyder, P., Eds.; Elsevier Academic Press: Amsterdam, The Netherlands, 2007; pp. 269–270, ISBN 978 0 12 369401 0.
101. Wenzel, T., Bartos, A., Lieb, K.P., Uhrmacher, M. and Wiarda, D. (1992), Hyperfine interactions of 111Cd in TiO2 (Rutile) studied by perturbed angular correlations. Ann. Phys., 504: 155-163. https://doi.org/10.1002/andp.19925040302
102. Christiansen, J., Heubes, P., Keitel, R., Klinger, W., Loeffler, W., Sandner, W., & Witthuhn, W. (1976). Temperature dependence of the electric field gradient in noncubic metals. Zeitschrift F r Physik B Condensed Matter and Quanta, 24(2), 177-187. https://doi:10.1007/bf01312998
103. Haas, H.; Zyabkin, D.; Schell, J.; Dang, T.T.; Yap, I.C.J.; Michelon, I.; Gaertner, D.; Gerami, A.M.; Noll, C.; Beck, R. Confirming the Unusual Temperature Dependence of the Electric-Field Gradient in Zn. Crystals 2022, 12, 1064. https://doi.org/10.3390/cryst12081064
104. Haas, H. Temperature Dependence of Electric-Field Gradient in Zn and Cd: Ending the $T^{3/2}$ "Myth". Manuscript to Be Submitted to Physical Review B. Available online: https://indico.cern.ch/event/1182057/ (accessed on 3 July 2022).
105. Butz, T., Vianden, R. The temperature dependence of the nuclear quadrupole interaction of 44Ti(EC)44Sc in rutile. Hyperfine Interact 221, 99–103 (2013). https://doi.org/10.1007/s10751-012-0675-7
106. Blöchl, P. E. Projector Augmented-Wave Method. *Phys. Rev. B* **1994**, *50*, 17953–17979. https://doi.org/10.1103/PhysRevB.50.17953.
107. Petrilli, H. M.; Blöchl, P. E.; Blaha, P.; Schwarz, K. Electric-Field-Gradient Calculations Using the Projector Augmented Wave Method. *Physical Review B* **1998**, *57*, 14690–14697. https://doi.org/10.1103/PhysRevB.57.14690.

108. Kanert, O.; Kolem, H. The Unusual Temperature Dependence of the Electric Field Gradient at Titanium Sites in Rutile (TiO_2). *J. Phys. C Solid. State. Phys.* **1988**, *21*, 3909–3916. https://doi.org/10.1088/0022-3719/21/21/013
109. Power Diffraction Data of Rutile. Available online: https://rruff.info/repository/sample_child_record_powder/by_minerals/Rutile__R060745-1_Powder_Cell_Refinement_Output_Data__6282.txt; in https://rruff.info/Rutile/R060745 (accessed on 18 June 2022).
110. RRUFF™ Project. Available online: https://rruff.info/about/about_general.php (accessed on 18 June 2022).
111. The "Cubic Formula". Available online: http://www.sosmath.com/algebra/factor/fac11/fac11.html (accessed on 18 August 2022).
112. Cardano, G.; Witmer, T. R. *Ars Magna or the Rules of Algebra*; Dover: New York, USA, **1993**, ISBN 9 780 486 67811 5.
113. Edmonds, A. R. Chapter 4. In *Angular momentum in quantum mechanics*; Princeton Univ. Press: Princeton, NJ, USA, **1957**. https://doi.org/10.1515/9781400884186.
114. Nouri, M. Bisymmetric, Persymmetric Matrices and Its Applications in Eigen-decomposition of Adjacency and Laplacian Matrices. *World Academy of Science, Engineering and Technology, International Journal of Mathematical, Computational, Physical, Electrical and Computer Engineering* **2012**, *6*, 766-769. https://zenodo.org/record/1061190. https://doi.org/10.5281/zenodo.1061190
115. Gibbons, J.F. Ion implantation in semiconductors—Part I: Range distribution theory and experiments. *Proc. IEEE* **1972**, *56*, 259–319. https://doi.org/10.1109/PROC.1968.6273.
116. Metropolis, N. The beginning of the Monte Carlo method. In *Los Alamos Sci* **1987**, *15*, 124-130. Volume is a Special Issue Dedicated to Stanislaw Ulam.; LANL publications: Los Alamos County, New Mexico, United States. Available online: https://library.lanl.gov/la-pubs/00326866.pdf (accessed on 11 April 2022).
117. Gibbons, J.F. Ion implantation in semiconductors—Part II: Damage production and annealing. *Proc. IEEE* **1972**, *60*, 1062–1096. https://doi.org/10.1109/PROC.1972.8854.